Development of a Phase–Sensitive Pulse Measurement Technique for Semiconductor Mode–Locked Lasers

by

Piotr Michał Stolarz

May 2012

A thesis submitted in fulfillment of the requirements
for the degree of Doctor of Philosophy (Ph.D.)
in the

School of Engineering
Electronics and Nanoscale Engineering Research Division

UNIVERSITY OF GLASGOW

Abstract

The ultrashort pulses emitted by passive semiconductor mode-locked lasers (PSMLLs) can be applied to a wide range of applications, including modern optical communication systems, optical sampling, security, imaging or sensing. For most of these applications, it is of critical importance to gather detailed information on the mode-locked laser (MLL) dynamics as well as on the temporal intensity and phase profiles of the pulses. The pulse formation in a PSMLL is in fact a very complex mechanism that is governed by the close interplay between a number of linear and nonlinear phenomena, influenced by various semiconductor parameters. The complete characterisation of the devices as a function of the laser driving parameters, geometry and semiconductor material structure has therefore the potential to provide a deeper understanding of the PSMLL behavior. As the available detectors are usually incapable of resolving the temporal structures of ultrashort pulses from the high repetition rate MLLs, a number of indirect measurement solutions have been developed for full pulse characterisation. However, these methods are designed for lasers with high-energy optical pulses or require pulse synchronisation or ultrafast modulation. This obviously restricts their suitability for the unsynchronised, low energy and high repetition rate pulses as those emitted by the mode-locked laser diodes. In this work, an extensive study of various dynamical regimes, such as mode-locking, self-pulsation and continuous-wave operations of the monolithically integrated AlGaInAs/InP MLLs is reported. The devices operate around 1.55 μm and emit optical pulses with sub-40 GHz repetition frequencies. The influence of the biasing conditions, laser geometry and semiconductor material on the lasers performance is analysed in detail. The complete characterisation includes the evaluation of both the phase and time profiles of pulses, using a sonogram system developed as part of this thesis. It is based on a self–referenced method, capable of ambiguity-free measurements of low power and sub-picosecond pulses. A sensitivity as low as 5 mW on the pulse peak power has been achieved through the design and fabrication of a two-photon absorption (TPA) detector, optimised for polarisation insensitivity and high nonlinear response. The traveling-wave operation enables the characterisation of high-repetition rate pulses and minimises the amount of introduced dispersion. The sonogram system has been successfully employed to study the evolution of the temporal intensity and group delay profiles as a function of the laser biasing conditions and for different device geometries. The obtained results indicate a prevailing positive chirp present in the pulses, which can be reduced by a careful adjustment of the device biasing. The minimum pulse width emitted from the investigated MLLs and measured with the sonogram technique was $\sim$500 fs.

Declaration

Unless otherwise acknowledged, the content of this thesis is the original and sole work of the author. No portion of this has been submitted by the author in support of any application for any degree or qualification, at this or any other university or institute of learning. The views expressed in this thesis are those of the author, and not necessarily those of the University of Glasgow.

Piotr Michał Stolarz

Copyright

Acknowledgements

Firstly, I would like to thank my supervisor, Dr. Marc Sorel, for his enormous support, encouragement and continuous involvement in my project. It has been a great pleasure to pursue my degree under Marc's guidance, who was always able to create an extremely friendly and enthusiastic work environment. I guess that some occasional group meetings in the GU pub helped build up such a brilliant atmosphere.

Obviously, these meetings could never be missed by my hungarian *bratanek*, Gábor, who was always there to scrupulously take minutes and bombard us with his never ending ideas. Together with Sandor, Gábor set up the Hungarian Chapter, which made a massive impact on the Optoelectronics Group, not only thanks to their great research but also trough the number of empty *pálinka* bottles and the amount of home-made *kolbász*. Gábor, thanks for being my guide, lab mate and, simply, friend! A special acknowledgement goes to Steven, who has also been a great lab mate and friend. Stevie, our Friday lunch in Little Italy has become a permanent routine for many of us.

Now, it's time for the Italian Chapter of the opto-group. Massive thanks are sent to Marco, who came to visit our department for a short project a few years ago, and forgot to go back home since then. I guess it was the Opto-Teddy episode that made him feel at home. Special thanks go to Vincenzo, a good pal and a holiday companion. Also, great cheers to my office mates: Giuseppe, Antonio and Laura. To conclude with the Italians, I would like to mention Carla, Piero, Oberdan, Andrea, Giangiacomo, and Stefano.

I also thank the rest of the Phd students and research colleagues with which I had a pleasure to work and socialize: Michael, Moss, Salah, Sankar, Leo, Philippe, Barry, Dave, Olek, Lianping, Corrie, Julien, Salvador, Chidi, Bruno, Shahid, Jehan, Masoud, Cheng, Usman ...and others. Special appreciation should go to the fantastic technical staff in the James Watt Nanofabrication Centre and the Rankine Building, especially to Bill, thanks to whom working in the opto-labs was so much easier! The financial support from the UK Engineering and Physical Sciences Research Council is also gratefully acknowledged.

My warmest thanks and recognition are sent to my parents, from whom I have always been receiving endless love, support, and encouragement. This is thanks to you that I was able to achieve this goal. Also, my deep appreciation goes to my brother, Marcin, sister-in-law, Agnieszka, niece, Weronika, and nephew, Michał. Also, to the rest of my family and friends, thank you all for being there! I would also like to remember Michał, who had always been for me an example of a good man and scientist.

Contents

List of Figures

To my family.

Chapter 1

Introduction

The work described in this thesis forms a part of the Engineering and Physical Sciences Research Council (EPSRC) funded project, *High Power, High Frequency Mode–locked Semiconductor Lasers* [1]. The aims of this project are focused on the development of monolithic semiconductor mode-locked lasers (SMLLs) to generate ultrashort optical pulses with high peak power levels (from a few Watts to several tens of Watts) and high repetition rates (from tens to hundreds of GHz). The main spectral emission regions of interest are 700–850 nm and 1550 nm, with applications in security, imaging, sensing and communication systems.

The main aim of this PhD project was to characterise passive SMLLs emitting picosecond and sub-picosecond pulses at 1550 nm, with repetition frequencies at ∼40 GHz. Within the context of the EPSRC project, this study intended to improve the understanding of the developed devices and deliver experimental feedback for their optimisation. The PhD project consists of two main components:

1. Investigation of the dynamical behaviour of SMLLs, by performing an extensive study of the properties of the lasers in various operating regimes.
2. Development and implementation of measurement tools capable of phase sensitive characterisation of the optical pulses from the SMLLs.

While the former task was accomplished with standard diagnostic measurement tools, such as radio-frequency (RF), optical spectrum (OS) and second-harmonic generation (SHG) autocorrelation, the second objective required the development of a highly sensitive detection scheme, due to inherently low energy and high repetition rates of the emitted optical pulses.

1.1 Project Motivation

Pulse formation in a semiconductor passive mode-locked laser (PMLL) is a very complex mechanism that is governed by the close interplay between numerous linear and nonlinear phenomena. It is influenced by a large number of semiconductor device parameters, such as the chromatic dispersion, self-phase modulation (SPM), gain and absorption of the material, the saturation levels, carrier recovery times, and gain/refractive index coupling in both the gain and absorption sections [2, 3]. The detailed characterisation of the pulses has therefore a potential to provide a deeper understanding of these mechanisms and thus to contribute to the improvement of the laser system stability under mode-locking (ML) operation. This in turn allows the optimisation of the optical cavity geometry and semiconductor material structure for tailorable ML performance. Furthermore, a precise insight into the intensity and phase profiles of the pulses is required for maximising the performance in the final application areas.

The fundamental challenge in the analysis of SMLLs is the lack of pulse diagnostic tools which could be applicable to these devices. Despite the continuously increasing capabilities of modern photodetectors and time-domain oscilloscopes, their response bandwidth is not sufficient for a detailed measurement of the high-repetition-rate, ultrashort pulse structures. This stimulated a rapid development of laser pulse diagnostic techniques, leading to the creation of a wide research field of ultrafast metrology. Depending on the properties of an examined ML system the pulse measurement methods may use different indirect procedures, e.g. decorrelation, interferometry, spectrography or tomography. However, as explained later in greater detail, most of the ultrafast metrology techniques are not suitable to characterise high repetition rate, unsynchronised, and low energy pulses, such as those emitted by SMLLs. In particular, there are no commercially available tools for the phase sensitive measurement of pulses with energies as low as a few tens of fJ, typical of the semiconductor devices. Hence, little has been done to investigate the mechanisms behind pulse formation and pulse phase profile in the semiconductor lasers.

Furthermore, there is a limited understanding of the properties of SMLLs in various dynamical regimes of operation. Most of the research work on SMLL characterisation usually exploits the intensity autocorrelation and the optical spectrum for the mode-locking quality assessment, however, it does not deliver any systematic study on the optimisation of ML operation. Such an analysis requires the simultaneous acquisition of output power, RF spectra (at both high and low frequencies), high resolution optical spectra, and intensity autocorrelations, combined with the phase sensitive pulse characterisation, performed at a wide range of external biasing conditions and laser geometries. A demand for these studies forms the main motivation behind this research,

which aims at providing better understanding of dynamical properties of semiconductor mode-locking devices, and a deeper insight into the optical pulse structures. Lasers fabricated on two different material systems and with various absorber lengths were thoroughly examined and compared within a broad range of biasing conditions, namely the gain section forward current and the saturable absorber reverse voltage. Furthermore, the issue of phase sensitive pulse measurements was addressed by extending the capability of an existing pulse diagnostic technique in order to make it applicable to optical pulses emitted by low power, passively ML semiconductor lasers.

1.2 Mode-Locking

ML is a method for producing ultrashort and high repetition rate optical pulses by introducing an intensity dependent loss element into the laser cavity. In the frequency domain, ML corresponds to a fixed frequency phase relationship between longitudinal modes of the cavity. If, for simplicity, only a single transverse mode oscillating at $N = 2m + 1$ longitudinal modes is considered, then the time-domain electric field, E(t), in the laser cavity can be expressed as:

$$E(t) = \sum_{n=-m}^{m} E_n e^{i[(\omega_0 + n\frac{2\pi}{t_r})t + \varphi_n]}, \tag{1.1}$$

where E_n, φ_n, ω_0, t_r and m are the electric field and phase of the nth mode, frequency of the mode at the gain bandwidth curve center, resonator round-trip time, and integer value, respectively [4]. With no mutual relationship between the modes, the laser output fluctuates randomly. In mode-locking the phases of the modes are equal. If, for simplicity, E_n=E_0 and φ_n=0 are assumed, the total electric filed can be expressed as:

$$E(t) = E_0 \sum_{n=-m}^{m} e^{i(\omega_0 + n\frac{2\pi}{t_r})t}, \tag{1.2}$$

The output intensity, I(t), can be calculated as:

$$I(t) = E(t)E^*(t) = E_0^2 \frac{sin^2(N\pi t/t_r)}{sin^2(\pi t/t_r)}. \tag{1.3}$$

As a result of the interference between the fixed equidistant longitudinal modes, the generated output forms a stationary waveform in time and space. Depending on the technique employed to achieve such condition, ML can be divided into active or passive. In active mode-locking (AML) an external source modulates losses in the gain medium, at a frequency that is synchronised to the cavity round-trip frequency. However, the synchronous mode-locking is limited in terms of the maximum repetition rates

achievable, as the upper-state lifetime needs to be shorter than the inverse pulse repetition rate of the laser. In the passive technique, no external modulator is needed, as an intra-cavity saturable absorber (SA) modulates the losses in the cavity. ML may be also achieved with synchronous pumping, in which the pump source of the laser is modulated. It is also possible to combine active and passive techniques into hybrid ML. In this project we will concentrate on passive mode-locking (PML), as this technique can provide ultra-short pulses, as well as ultra-high repetition rates without the need for expensive high-frequency electronics and device packaging.

In monolithic PML devices, the pulses are generated through a dynamic interplay between the gain in the continuously pumped amplifier section and the saturation of the reverse-biased SA. More advanced designs may include additional components, such as a passive waveguide extension, phase tuning segment or grating section. Pulse formation in PML starts with randomly uncorrelated mode phase profiles that are shaped by the absorber, which, due to its nonlinear absorption characteristics, is more transparent to high intensity spikes than to the weaker intensity components. The spikes experience less loss and begin to increase in amplitude. This process repeats at every cavity round-trip until a steady-state operation with a single pulse in the cavity is achieved. Under steady-state the pulse is shaped by the absorber in a narrow time window, in which the net gain exceeds the losses, as illustrated in Fig. 1.1. The pulse shaping mechanism

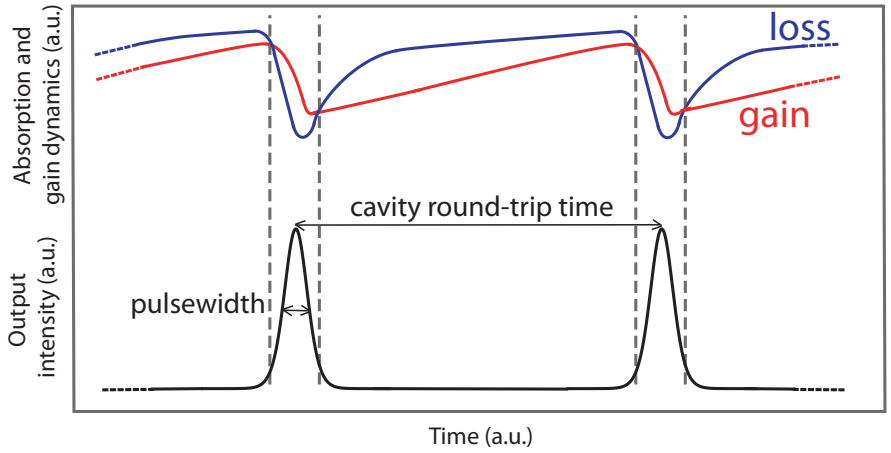

FIGURE 1.1: Temporal evolution of gain, losses and optical power in a passive ML device.

relies on the relative instantaneous levels of the net gain and loss in the cavity and can be explained as follows: The leading edge of a pulse entering the SA experiences loss, as the absorber is not initially saturated and has its full absorption capabilities. However, an increasing pulse intensity begins to bleach it, and from some point the pulse begins to experience amplification. This, on the other hand, triggers gain depletion (or gain saturation). In order to achieve ML condition, the gain needs to saturate slower than the absorber (absorber saturation energy $<$ gain saturation energy) [5]. On the trailing

edge, where the pulse intensity decreases, the absorber begins to recover, while the gain is still being depleted. From the point where the gain and loss characteristics cross, the pulse experiences loss, which further sharpens the trailing edge. In order to correctly "close" the net gain window until the arrival of the next pulse, the absorber recovery time must be faster than that of the gain (New's background stability criterion) [6].

1.3 Semiconductor Lasers as a Source of Ultrashort Optical Pulses

Semiconductor laser diodes (LDs) are strong competitors among the sources of light modulated at microwave frequencies, thanks to the possibility of direct electrical pumping, mature fabrication techniques, compactness and high integrating potential. Due to inherently short cavity length of semiconductor lasers, they may operate at fundamental frequencies exceeding hundreds of gigahertz. Even higher repetition rates, exceeding 1 THz may be obtained with harmonic ML [7].

1.3.1 Applications and Requirements

SMLLs emitting ultrashort pulses are of interest in a wide range of applications, including modern optical communication systems, security, imaging or sensing, thanks to their compactness, efficiency and low cost [8]. Regarding the EPSRC-project, the main field of interest for the developed devices are the THz generation and communication systems. These two applications, however, impose different requirements on the ultrashort pulse sources. The THz generation needs:

- THz pulse repetition rates or ultrashort pulses (below 100 fs);
- Ultra-high peak powers for efficient THz conversion ($\sim$1 kW) [9].

On the other hand, the optical communication systems emphasise the need for high quality optical pulse train and precisely controlled pulse properties. The SMLLs have proven their applicability in optical sampling measurement systems with picosecond resolution, such as those used in recovery dynamics and eye-pattern measurements [10]. They also have been investigated as the potential sources for optical time-division multiplexing (OTDM) [11]. However, they need to satisfy strict requirements imposed on the light sources by the OTDM standards, such as:

- Low temporal full-width half maximum (FWHM) values for proper separation between the adjacent pulses ($\leq 0.3 \cdot B^{-1}$, where B is the aggregate bit rate) [12];

- High repetition rates (currently up to 40 GHz) locked to the standard values (9.953 GHz, 19.906 GHz and 39.813 GHz);
- Low pedestal and high extinction ratio (strong suppression of trailing pulses);
- Low timing jitter (less that 1/12 of the switching window width) and low amplitude noise;
- Preferably sech^2-shaped and close to transform-limit pulses;
- Long term stability and reliability.

Furthermore, recent progress in stabilised, ultra-low noise SMLLs may provide the required performance for optical frequency metrology, x-ray and attosecond pulse generation, remote sensing applications and other optical systems, such as optical-code division multiple access (OCDMA), dense wavelength division multiplexing (DWDM), phase-shift keying (PSK) and quadrature-amplitude modulation (QAM) technologies [13].

1.3.2 Problematic Issues

In order to obtain the capability to produce optical pulses of specific properties, devices with fine control of nonlinearities, such SPM, self-focusing and defocusing, gain recovery, or saturable absorption have to be designed. These phenomena are of concern in SMLLs due to their inherently small cross-sectional area and also direct interaction between the injected carriers, the optical field and the refractive index. These effects may be handled to some extent with integrated cavity mode-locked laser (MLL), comprising of the gain, SA, phase and grating sections [14].

The minimum pulse width theoretically obtainable in a monolithic SMLL is limited by the finite gain bandwidth, and for 1.55 μm stays between 50 fs and 100 fs [15]. However, experimentally measured pulses are usually much longer, due to unbalanced dispersion effects and pulse shaping mechanisms, mainly the gain saturation. It is caused by the photon depletion of carriers, but also by other nonlinear phenomena triggered by finite scattering times, such as carrier heating and spectral hole-burning. Also, the SPM may impose a significant effect on the pulse width, however, an overall influence of this phenomenon depends on the level of broadening and narrowing in the gain and absorber sections, respectively [16]. The major requirement for ML operation is a strong saturation and shorter carrier lifetime in the absorber, compared to the gain section. Unfortunately, these conditions coincide with the optimum parameters for the intensity self-pulsation (SP), which can hinder or even completely suppress the ML. This

phenomenon is very common in SMLLs and can affect ML over wide range of biasing conditions [17]. SP can be minimised or virtually avoided by the optimisation of the laser material structure, laser geometry and the biasing parameters. The effects of such measures will be extensively presented in this work.

1.4 Ultrashort Optical Pulses

An ultrashort laser pulse is a propagating electromagnetic wave packet, which can be characterised by measurable quantities directly linked with the electric field [18]. The electric field may be described both in the time and the frequency domains. The time domain representation relates the real electric field, E(t), with the electric field envelope, $\varepsilon(t)$, the carrier to envelope phase, φ_0, the time dependent phase, $\varphi(t)$, and the average carrier frequency, ω_l:

$$E(t) = \frac{1}{2}\varepsilon(t)\ e^{i\varphi_0}\ e^{i\varphi(t)}e^{i\omega_l t} + c.c. \tag{1.4}$$

The complex spectrum of the field, $\tilde{E}(\Omega)$, may be obtained from the time dependent field through the complex Fourier transform:

$$\tilde{E}(\Omega) = \mathcal{F}\{E(t)\} = \int_{-\infty}^{\infty} E(t)\ e^{-i\Omega(t)}dt = |\tilde{E}|e^{i\Phi(\Omega)} \tag{1.5}$$

where $|\tilde{E}|$ and $\Phi(\Omega)$ denote the spectral amplitude and the spectral phase respectively. The instantaneous frequency of an optical pulse, ω, is also an essential parameter in optical pulse characterisation, as it indicates if the pulse is chirped, i.e. if the carrier frequency varies in time within the pulse envelope:

$$\omega(t) = \omega_l + \frac{d}{dt}\varphi(t). \tag{1.6}$$

It is essential to detect any time variation of the phase in order to identify the chirp. If $d^2\varphi/dt^2 < 0$, the pulse is down-chirped as the carrier frequency decreases with time. In the opposite case, the pulse is deemed to be up-chirped. Besides any potential variations in ω, the pulse characterisation aims at determining the pulse intensity profiles. Several standard waveforms are used to approximate ultrashort laser pulse shapes. The most typical are the Gaussian, hyperbolic-secant-squared ($sech^2$) and Lorentzian waveforms.

A convenient parameter describing an optical pulse is the temporal duration, τ_p, usually defined as the FWHM of the intensity profile. Its counterpart in the frequency domain is the spectral width, ($\Delta\omega_p$), which relates to the FWHM of the pulse spectrum. Both parameters are mutually linked through the time-bandwidth product (TBP) product, c_B:

$$\Delta\omega_p\tau_p = 2\pi c_B \tag{1.7}$$

The TBP depends on the pulse shape as well as the pulse chirp. In the case of a non-chirped pulse, called *transform-limited*, the TBP takes its minimum value. Table 1.1 summarises the parameters of the most common waveforms used to describe ultrashort laser pulses [18]. It is worth noting that the "real" pulses usually have more complicated profiles, and proper pulse description demands advanced measurement set-ups.

TABLE 1.1: Parameters of standard unchirped ultrashort laser pulses.

Shape	Intensity profile I(t)	τ_p	Spectral profile $\tilde{I}(\Omega)$	$\Delta\omega_p$	c_B
Gaussian	$e^{-2(t/\tau_G)^2}$	$1.177\tau_G$	$e^{\frac{((\Omega-\omega_l)\tau_G)^2}{2}}$	$2.355/\tau_G$	0.441
Sech^2	$sech^2(t/\tau_s)$	$1.763\tau_s$	$sech^2\frac{\pi(\Omega-\omega_l)\tau_s}{2}$	$1.122/\tau_s$	0.315
Lorentzian	$[1+(t/\tau_L)^2]^{-2}$	$1.287\tau_L$	$e^{-2\lvert(\Omega-\omega_l)\rvert\tau_L}$	$0.693/\tau_L$	0.142

1.4.1 Concepts for Representation of Optical Pulses

Pulsed sources usually produce an ensemble of pulses which cannot be represented with a simple field expression, as shown in Eq. 1.4. Instead, the pulse trains consist of randomly varying pulses, hence, the experimental outcome is rather a probability distribution of the optical field. Analytically, the simplest description of such an ensemble is the non-stationary two-time correlation function, $\text{C}(t_1, t_2)$, as introduced in [19] and presented in Eq. 1.8:

$$C(t_1, t_2) =< E(t_1) \cdot E^*(t_2) >, \tag{1.8}$$

where the brackets represent the averaging over the pulse ensemble, and E(t) is a real electric field. A knowledge of this function is useful to assess the statistical variations in a pulse train, usually expressed with a temporal coherence degree. However, in practical pulse characterisation systems it is difficult to measure the correlation function and the issue of pulse-to-pulse fluctuations is usually ignored. Instead, an ensemble of identical pulses is assumed, which simplifies the inversion algorithms employed to retrieve the pulse field.

The other common approach to represent the optical pulse is the two-dimensional chronocyclic (time-frequency) phase space, which is a variation of the correlation function. An example of this representation is a chronocyclic Wigner distribution function [20]. It is defined as a Fourier transform of the mutual temporal intensity of a complex electric field:

$$W(t,\omega) = \int E(t+\frac{t'}{2}) \cdot E^{\star}(t-\frac{t'}{2}) e^{i\omega t'} dt'. \tag{1.9}$$

The Wigner function allows for the retrieval of the complex field of the optical pulse, except the carrier to envelope component, φ_0. The equivalent spectral representation of the electric field, $\tilde{E}(\omega)$, can be expressed as a Fourier transform of the mutual spectral intensity:

$$W(t,\omega) = \frac{1}{2\pi} \int \tilde{E}(\omega+\frac{\omega'}{2}) \cdot \tilde{E}^{\star}(\omega-\frac{\omega'}{2}) e^{-i\omega' t} d\omega'. \tag{1.10}$$

Due to several properties of the Wigner function it usually a preferable concept applied in practical pulse diagnostic techniques. Also, this research will use a modification of the Wigner function to analyse the experimental time-frequency traces representing laser pulses. The most crucial properties of the function, directly applicable to "real" measurements are as follows:

- The temporal, $I(t)$, and spectral, $\tilde{I}(\omega)$, pulse intensities can be obtained by calculating the following marginals:

$$I(t) = \mid E(t) \mid^2 = \frac{1}{2\pi} \int W(t,\omega) d\omega \tag{1.11}$$

  and

$$\tilde{I}(\omega) = \mid \tilde{E}(\omega) \mid^2 = \int W(t,\omega) dt. \tag{1.12}$$

- The Wigner function integral over the whole phase space corresponds to the pulse energy.

- A measurement of a chronocyclic intensity corresponds to a measurement of the complex electric field of an optical pulse. It can be obtained through measurement of spectrally-resolved SHG cross-correlations, provided the correlation is performed with a known pulse.

- An inversion of chronocyclic intensity constructed with the spectrally-resolved SHG autocorrelation does not yield a unique solution for the complex pulse field.

- The requirement for a well-characterised pulse can be overcome by breaking the symmetry of the correlation function. It can be accomplished through spectral filtering of the pulse replica with a well-characterised and band-pass filter, with a stop-band much narrower than the spectral variations of the pulse.

Even though the the Wigner distribution is a real function, it can sometimes take negative values, which are impossible to be measured experimentally. However, the practical measurements of the ultrashort pulses yield only double convolutions of two Wigner functions, which always stay positive [20].

1.5 Ultrashort Optical Pulse Measurements Techniques

Due to inherently short pulses emitted by the MLLs the direct measurement of their intensity, even with fast photodetectors, is not possible. Furthermore, the characterisation with a fast square-law photodetectors could only provide information on pulse temporal intensity, without any insight into its phase profile. Hence, various indirect methods, which allow one to use "slow" photodetectors to measure the optical pulses have been developed. The most important concept of these methods relies on using the pulse itself as a fast "event" and combining it with an instantaneously responding medium. Such an arrangement can produce a time trigger as quick as the pulse being examined. The instantaneous (or quasi-instantaneous) processes are usually implemented in a nonlinear optical medium, although linear systems can also be used to measure the optical fields. Basically, there are four classes of ultrashort pulse diagnostic methods: decorrelation, the spectrographic, tomographic and the interferometric techniques. The general concept and features of each method will be presented, and the advantages and disadvantages of the approaches will be highlighted. Finally, the choice of the measurement technique chosen for this research will be explained.

1.5.1 Decorrelation Techniques

For the purpose of laser pulses measurement in the early stages of ultrashort metrology, nonlinear detection was widely adopted. In the autocorrelation, which is the most popular and simplest arrangement, the pulse replicas are mixed in a nonlinear medium and the resulting product is measured with an integrating detector as a function of the relative delay between the pulses (Fig. 1.2). Usually, a second-order non-linearity, such

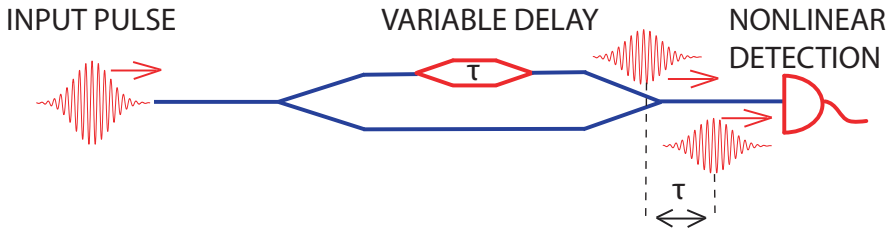

FIGURE 1.2: Principle of operation of an autocorrelation measurement.

as SHG combined with a photomultiplier tube (PMT) is used. However, the SHG is not an efficient process and requires high power levels. The efficiency is even lower if broad-bandwidth sources are used, as crystals as thin as a few micrometers need to be used to reduce dispersion and satisfy phase matching conditions [21]. The conversion taking place in a crystal is sensitive to the instantaneous intensities of the incident light, so it distinguishes between the relative position between the pulses. Hence, a measurement of the second harmonic (SH) signal as a function of the delay between the pulse replicas can yield information on the pulse duration.

The autocorrelation set-up can take one of the two basic configurations, as illustrated in Fig. 1.3. In a non-collinear arrangement (Fig. 1.3(a)) two beams spatially overlap only in a precise location in the crystal, which produces the electric field given by Eq. 1.13. The intensity of the cross-term field, E^{SHG}, is proportional to the product of the beam intensities. A slow detector cannot temporally resolve it, so it produces a response, $A^2(\tau)$, being the time integral of the doubled-frequency intensity, as presented in Eq. 1.14 [22]:

$$E^{SHG}(t,\tau) \propto E(t)E(t-\tau), \tag{1.13}$$

$$A^2(\tau) = \int_{-\infty}^{\infty} I(t)I(t-\tau)dt. \tag{1.14}$$

In addition to the E^{SHG} field, the $E^2(t)$ and $E^2(t-\tau)$ electric fields are generated in the crystal. However, they are spatially separated from the cross-term signal, hence, can be prevented from entering the integrating detector.

This configuration, known as the intensity autocorrelation (IAC), does not provide any insight into the phase profile, nor does it uniquely determine the pulse shape, and therefore yields only an estimation of the pulse duration (Fig. 1.4 (c)). Pulses with complicated intensities may generate an autocorrelation response which is sensitive only to the slowly varying envelope of their structures. As the complexity of a pulse increases, i.e. the slowly varying intensity envelope becomes affected by some additional substructures, the IAC response takes the shape of a pedestal with a central peak, called the *coherence spike* [22]. Such effect may also occur in the case of a unstable train of pulses, as the detector averages over several pulses with varying separation. The SHG signal introduces time reversal ambiguity, as it is symmetric and cannot distinguish between the pulse and its mirror image. Although there are some third-order nonlinearities, such as the polarisation-grating (PG), self-diffraction (SD), or third-harmonic generation (THG),

that can break this symmetry, their efficiencies are orders of magnitude lower than that of SHG, which is a major disadvantage in low energy pulse measurements.

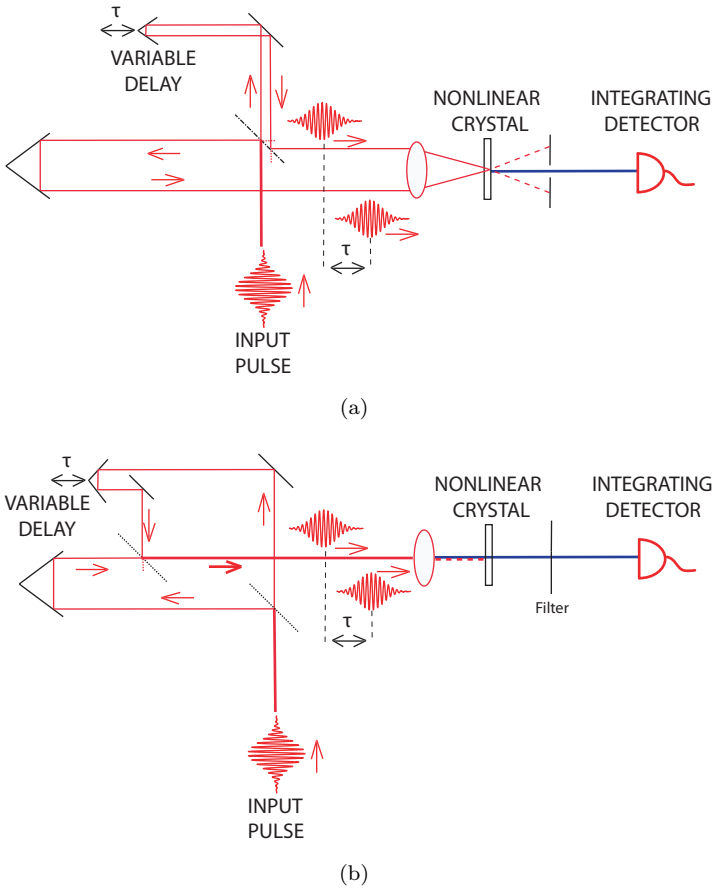

FIGURE 1.3: (a) Intensity and (b) interferometric autocorrelation set-ups - principle of operation

.

The second, collinear arrangement, (Fig. 1.3(b)) is called the interferometric autocorrelation or fringe-resolved autocorrelation (FRAC). Here, the two beams are kept collinear across the whole output arm of an interferometer, and across the whole length of the SHG crystal, so that the up-converted beams may interact coherently with each other, and an interference pattern is created. After filtering out the fundamental frequency, the detector yields the time-averaged signal, A^{FRAC}, proportional to the following function:

$$A^{FRAC}(\tau) = \int_{-\infty}^{\infty} |E(t) + E(t-\tau)|^4 dt. \tag{1.15}$$

This correlation function is composed of four components: a constant term yielding no information about the pulse, an intensity autocorrelation term and two field autocorrelation terms which, produce fringes as a function of delay between the input fields

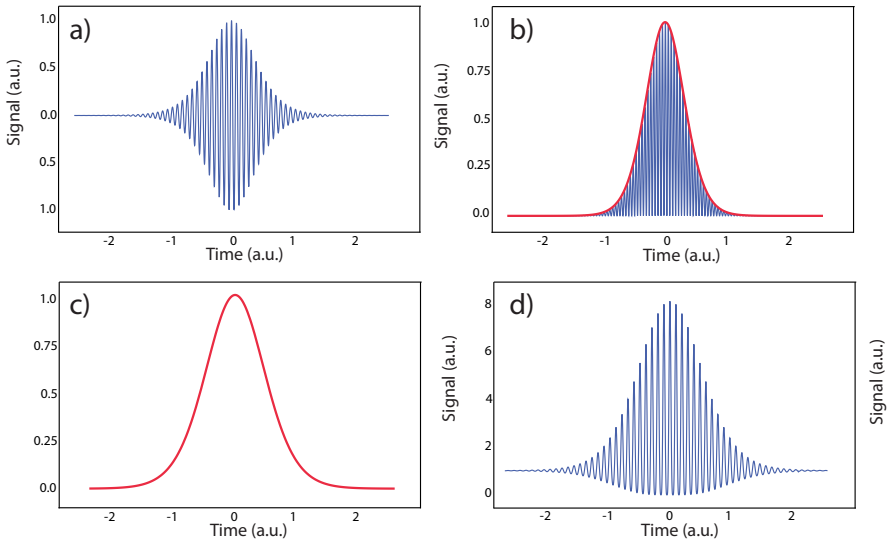

FIGURE 1.4: Example of the (a) real part of the electric field, (b) intensity and envelope, (c) SH intensity autocorrelation, and (d) SH interferometric autocorrelation of a sech^2 transform-limited optical pulse.

(Fig. 1.4 (d)). The field term oscillating at the fundamental frequency is the equivalent of the pulse spectrum, while the second one produces the double-frequency fringes and is sensitive to the pulse structure. There are several methods proposed in the literature which claim to resolve the pulse structure and remove time-ambiguity [23]. Naganuma *et al.* gave mathematical foundations for the pulse reconstruction, which do not require any pre-assumptions and use only the SHG FRAC trace and the pulse spectrum. Also, an iterative computer algorithm for pulse reconstruction was presented [24]. Another approach was proposed by Diels *et al.* [18], where the pulse reconstruction from an asymmetric SHG fringe-resolved trace is realised in a few iterations. A similar technique, called phase and intensity from correlation and spectrum only (PICASO), employs the measurement of the pulse spectrum and one or more nonlinear correlation traces [25]. Several versions of the PICASO method, with various correlator arrangement, detector type, and iterative retrieval algorithms were presented. The other important class of decorrelation approaches, called modified-spectrum auto-interferometric correlation (MOSAIC), utilises first and second-order interferometric and intensity traces [26]. By combining the second-order FRAC with the pulse spectrum, the IAC, or the linear detector field correlation, this method is capable of a complete pulse characterisation [27]. MOSAIC is claimed to be superior to the PICASO approach, because of its simplicity in the visual chirp interpretation [28]. Several variants of the method were presented, such as the envelope-MOSAIC, making use of the intensity autocorrelation; the hybrid-MOSAIC, utilising a linear detector; the retrieval-MOSAIC, with an enhanced pulse reconstruction iterative algorithm that minimised the root-mean-square (rms) error; and the unbalanced-MOSAIC, with unequal peak pulse amplitudes in the two arms of an

autocorrelator. Each variant exploits different advantages of the MOSAIC algorithm: the envelope-MOSAIC is useful for ultrashort low repetition rate pulses, the hybrid-MOSAIC enhances detection of both spectral dispersion and temporal chirp in pulses, the retrieval-MOSAIC minimises the numerical errors, and the unbalanced-MOSAIC can detect more clearly pulse asymmetry and the presence of multiple pulses [29].

1.5.2 Spectrographic and Sonographic Techniques

The concept of the spectrographic and sonographic techniques relies on simultaneous measurement of the pulse spectral and temporal intensity. The spectrogram image represents an assembly of the sequential pulse temporal slices spectra. The sonogram, on the other hand, measures the group delay of subsequent pulse spectral components. It can be demonstrated that both techniques are mathematically equivalent. The principles of operation of these two methods are schematically presented in Fig. 1.5. They both use time-stationary and time-non-stationary linear filters for the pulse processing. The response of a time-stationary filter (TSF) is independent of the arrival time of the test pulse. Examples of a TSF are a spectrometer, a delay line or a dispersive element. By contrast, the signal generated by a time-non-stationary filter (TNSF) – such as a time-gate or a phase modulator – depends on the pulse timing.

In the spectrogram, the optical signal is first processed using a time gate that has a response comparable with the measured pulse, after which it is resolved spectrally with a high resolution spectrometer (Fig. 1.5 (a)). The order of the filter types is inverted in the sonogram, in which the pulse first undergoes a spectral filtering (low-resolution) and is then temporally resolved with a fast time-gate (Fig. 1.5 (b)). In both cases, the final signal is measured with an integrating detector.

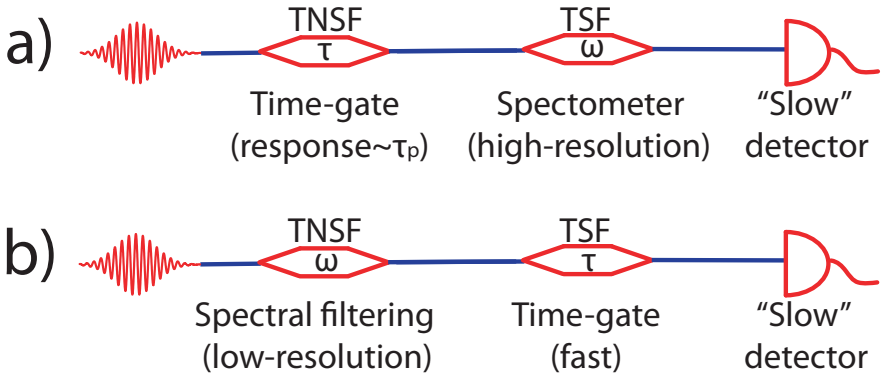

FIGURE 1.5: The schematic representation of (a) spectrography and (b) sonography pulse measurement methods.

The spectrography and sonography can be better understood with the reference to the phase space representation of optical pulses, as described by the Wigner function. However, due to the limited temporal resolution of the former method and a low-resolution of the latter approach, the Wigner function is smoothed and the experimental traces are rather described by the functions called the Gabor spectrogram, Sp_G (Eq. 1.16), and the Gabor sonogram, So_G (Eq. 1.17) [30]:

$$Sp_G(\Omega,\tau) = |\int E(t)N(t-\tau)e^{i\omega t}dt|^2, \tag{1.16}$$

$$So_G(\Omega,\tau) = |\int \frac{1}{2\pi}\tilde{E}(\omega')\tilde{S}(\omega'-\Omega)e^{-i\omega' t}d\omega'|^2, \tag{1.17}$$

where N and $\tilde{S}$ are the time and spectral gate functions, respectively. A knowledge of these functions allows for retrieving a pulse field by processing the traces with an iterative algorithm.

Due to the requirements for fast (spectrogram) and very fast (sonogram) time-shutter, practical approaches make use of nonlinear optics in order to realise adequate time gate functions. This however, implies the need for an iterative nonlinear deconvolution algorithm, which is more challenging in terms of producing a unique solution.

1.5.2.1 Practical Implementations of Spectrogram

The practical and most popular implementation of a spectrogram is through resolving the spectra of a SHG intensity autocorrelation signal. Such an approach was presented by Kane and Trebino [31], and is called frequency-resolved optical gating (FROG). It is a very popular technique, as it produces accurate and usually unique phase retrieval results and leaves only some "trivial" ambiguities unsolved, e.g. the absolute phase factor or the time and frequency translation. The mathematical representation of the FROG spectrogram, Sp_E, is shown in Eq. 1.18, where a variable-delay gate function, $g(t)$, scans the pulse in the time domain [22].

$$Sp_E(\omega,\tau) = |\int_{-\infty}^{\infty} E(t)g(t-\tau)e^{(-i\omega t)}dt|^2 \tag{1.18}$$

In practical terms, the FROG incorporates an autocorrelator to introduce a variable delay between the pulse and its replica, which then acts as a time-domain gate in an instantaneous nonlinear optical medium, e.g. SHG, THG, PG or transient-grating (TG).

The product of the time-gate operation is next resolved spectrally with a spectrometer. The measured quantity is described by Eq. 1.19

$$I_{FROG}(\omega,\tau) = |\int_{-\infty}^{\infty} E_{sig}(t,\tau)e^{(-i\omega t)}dt|^2, \tag{1.19}$$

where $E_{sig}(t,\tau)$ is an autocorrelation signal depending on the type of the nonlinear medium. For instance, SHG will produce $E_{sig}(t,\tau) \propto E(t)E(t-\tau)$, while for the polarisation gate medium $E_{sig}(t,\tau) \propto E(t)|E(t-\tau)|^2$. An example of SHG FROG is presented in Fig. 1.6. Table 1.2 summarises the different types of FROG techniques and highlights their main features.

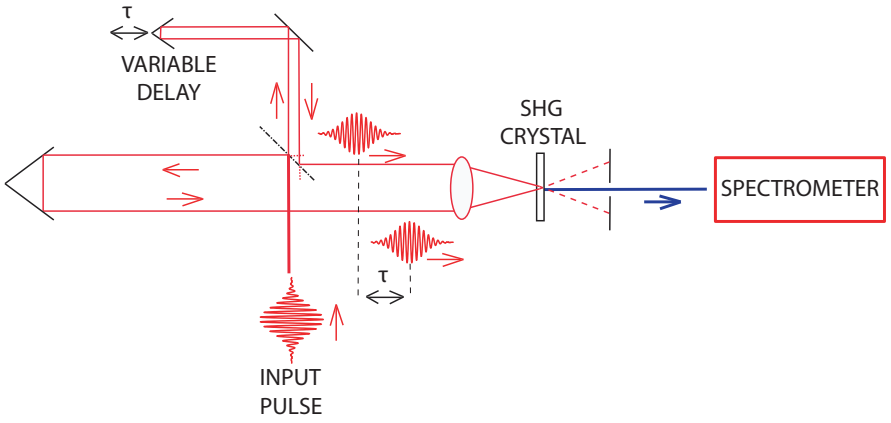

FIGURE 1.6: Schematic overview of a SHG FROG set-up.

As the FROG set-up is relatively complicated (while it requires a beam splitter, delay line, beam combing optics, spectrometer) and not always sensitive enough (due to low conversion efficiency of the thin nonlinear crystal) a simpler version, called grating-eliminated no-nonsense observation of ultrafast incident laser light e-fields (GRENOUILLE), has been developed [36]. It comprises a Fresnel biprism, which substitutes most of the autocorrelator's tasks, as it splits a wide beam into two beamlets that are next crossed at an angle in a thick SHG crystal. Crossing beamlets in different parts of the crystal (along one of its axes) corresponds to delaying one beam relative to the other.

Contrary to a very thin crystal, which has broadband phase-matching bandwidth and may generate the SH signal in any direction, a thick crystal loses the ability to create SH signal in any direction and it separates frequencies spatially like a spectrometer. With proper use of the input and output lenses, the spectrally and time resolved beams are mapped on a camera. Similar to the basic FROG configuration, the delay is mapped on one axis and the wavelengths are mapped on the perpendicular axis. The SH crystal needs to be thick enough in order to resolve the spectral structure of the laser pulse. However, the maximum thickness is limited by group velocity dispersion (GVD) which

TABLE 1.2: Summary of the FROG-based optical pulse measurement techniques.

Method	Advantages	Disadvantages
SHG FROG	• highest sensitivity: 1 pJ [22] • applicable to extremely short pulses [32] • easily implemented in mid-IR [33]	• time-direction (chirp sign) ambiguity • relative phase between the multiple pulses ambiguity
PG FROG	• clear representation of the chirp [34] • simple implementation • popular with chirped-pulse amplification systems [34]	• low sensitivity: 100 nJ [22] • polarisation-leakage background [35]
THG FROG	• large phase matching bandwidth • highest sensitivity (1 nJ) of all third-order nonlinearities FROG setups	• relative phase between the multiple pulses ambiguity • traces difficult to interpret
TG FROG	• no ambiguity • phase matched at all wavelengths [35] • background-free measurements	• low sensitivity: 10 nJ [22] • usually employed with UV pulses • three-beam operation

distorts the pulse. A sufficient group velocity mismatch (GVM) is required to spatially separate the SH and fundamental frequency pulses. On the other hand, the crystal thickness should not exceed the length causing a spread of the smallest temporal structure in the input pulse. These conditions can be satisfied for all but near single-cycle pulses, having a very wide spectrum. The GRENOUILLE is reported to accurately measure even highly structured pulses and allows for the full reconstruction of ultrashort laser pulses [22].

The GRENOUILLE trace is essentially a SHG FROG trace, hence it is affected by the same limitations. Furthermore, it works well only with pulses between 30 fs and 400 fs

and requires a beam of high spatial quality. Its big advantage is, however, the much thicker nonlinear crystal that substantially increases the sensitivity of the system.

1.5.2.2 Practical Implementations of Sonogram

A schematic representation of a practical sonogram arrangement is depicted in Fig. 1.7. The measured pulse is first split into two replicas. The first replica is temporally delayed, while the other undergoes spectral filtering. After being recombined, the replicas are sent to a nonlinear medium and the resulting product is measured with a slow detector. The full sonogram trace is completed by scanning the relative delay between the replica and the central frequency of the spectral filter. Due to broken symmetry between the two arms, the final trace is a clear representation of the pulse chirp, and is not affected by the time-direction ambiguity. The nonlinear detection mechanism can be constructed around

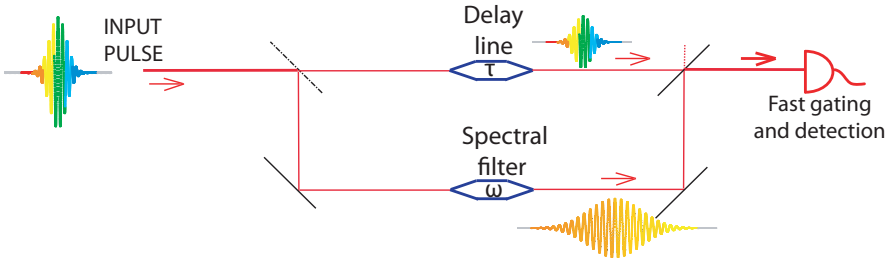

FIGURE 1.7: Schematic overview of a sonogram set-up

SHG [37] or two-photon absorption (TPA) [38] nonlinearities. TPA allows sensitivity improvement and, depending on the realisation of the TPA detection, can be applied to a wide range of ultrashort laser pulses. Further advantages of the TPA detection over the SHG will be discussed in Section 1.6.

1.5.3 Interferometric Techniques

In the interferometric techniques the pulse phase is retrieved from an intensity pattern produced by the field interference between the measured pulse and a well-characterised reference pulse (test-pulse-reference interferometry (TPRI)), or a pulse replica (self-reference interferometry (SRI)) [30]. Schematic examples of both approaches implemented in the spectral domain are presented in Fig. 1.8.

In the TPRI, the test pulse passes through a delay time, and is then combined with a reference pulse (Fig. 1.8 (a)). In the self-referenced approach, a beam splitter produces two pulse replicas, which undergo a temporal shift in a delay line or a spectral shift in a linear temporal phase modulator (Fig. 1.8 (b)). The recombined signals are finally resolved spectrally in both arrangements. Equivalent time-domain methods are

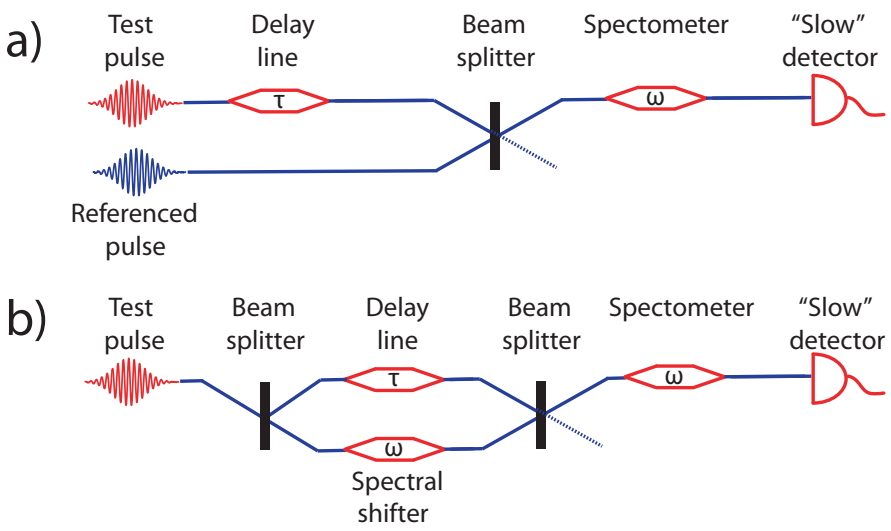

FIGURE 1.8: Schematic arrangement of a (a) test-pulse-reference and (b) self-reference spectral interferometry set-up.

also available for both techniques, however, they require fast detectors with sufficient temporal resolution to resolve the temporal beat pattern.

The spectral interferometry does not involve any nonlinearity, hence it can be used to measure extremely weak pulses. Characterisation of pulses as weak as 42 zJ has been reported with a spectral interferometry (SI) technique, called Temporal Analysis by Dispersive a Pair of Light E-fields (TADPOLE) [39].

However, the spectral interferometry is affected by several limitations:

- The self-referencing method requires a fast temporal modulator, which imposes a limit for its applicability with ultrashort and high repetition rate pulses.
- The interferometer must be very stable, otherwise the fringes would disappear.
- The reference pulses need to be well characterised, synchronised and spectrally aligned with the test pulses [22].
- The retrieved phase is related to the reference pulse phase profile.

A modification of SI, called spectral phase interferometry for direct electric field reconstruction (SPIDER), has been developed in order to measure pulses in a self-referenced fashion, without the need for a temporal modulator [40]. The principle of operation is based on a nonlinear mixing of a test pulses with a temporarily-stretched replica. After splitting in a beam-splitter, one replica is further divided into two delayed pulses, while the second one is strongly chirped in a pulse stretcher. Next, the pulses from both arms are mixed in a SHG crystal and the final interferometry pattern is resolved with a spectrometer.

An advantage of the SPIDER is that it is not affected by time-direction ambiguity, even if the lowest order non-linearity is used, and it does not require any iterative algorithm for phase retrieval. However, the SPIDER has also several disadvantages, such as:

- Lower sensitivity than a SHG FROG.
- Complicated and sensitive set-up.
- Unsuitability for long or complex optical pulses.
- Set-up configuration requires prior estimation of the pulse width and structure.

1.5.4 Temporal Imaging and Tomography Techniques

The concept of temporal imaging of ultrashort pulses stems from the analogy to an optical imaging system, which operates in the spatial domain [30]. Such systems can transform a small optical image in a way that it can be resolved with a detector of a limited spatial resolution. The light from a detected object first undergoes free space diffraction and then is refracted by the lens. After the second diffraction step, it forms a replica of the object on an image plane. A similar operation can be performed with an optical pulse in the time domain, where the temporal lenses transform the temporal intensity of the examined pulse into the spectrum. It can be realised with a temporal phase modulator, which shifts the frequency of successive temporal pulse slices by a different amounts. This has an analogy in a spectral domain in the form of a dispersive pulse stretcher, which temporally shifts the successive spectral pulse slices with different delays. In the time-frequency domain, on the other hand, such a pulse stretcher corresponds to spatial-domain diffraction. Hence, the combination of a temporal phase modulator and a dispersive stretcher allows to obtain a temporally magnified image of an ultrashort pulse, which can be next measured with a detector of limited time resolution. However, a drawback of this technique is the requirement for a temporal phase modulator with a response as fast as the measured pulses, which makes it difficult to implement with picosecond and sub-picosecond pulses

The tomography techniques employed in the ultrashort pulse metrology also have an analogy in the imaging applications. The concept of tomography is based on the reconstruction of an N-dimensional object from a number of data sets of lower dimension [30], e.g. reconstructing a three-dimensional form from a set of two-dimensional images. In ultrashort pulse metrology, the chronocyclic Wigner function is reconstructed from a number of its projections onto the chronocyclic phase space axes. This method is known as a "chronocyclic tomography" [41]. It can be also achieved by measuring a

number of projections of a rotated Wigner function on a single axis – for instance with a spectrometer measuring the frequency marginal of the function. Theoretically, such rotation can be realised with a series of spectral and temporal quadratic phase modulators. The technique is of a great interest in the ultrashort metrology, as it may measure complete Wigner functions, without the assumption of a coherent train of optical pulses. However, the practical implementations are extremely difficult due to stringent requirement imposed on the phase modulators, and therefore the method is used mainly with low-repetition-rate systems.

1.5.5 Discussion on the Pulse Measurement Techniques

The presented overview of the optical pulse characterisation techniques shows a wide range of available approaches. However, the applicability of each method depends on the properties of the investigated pulses and pulse ensemble. Characterisation of optical pulses emitted from the SMLLs examined in this work may be challenging due to a number of features, which greatly reduce the extent of the measurement approaches that can be used. Fig. 1.9 compares each full-pulse-retrieval technique against the typical properties of the pulse trains emitted by SMLLs. The characterised MLLs operate

MEASUREMENT TECHNIQUE	PULSE TRAIN FEATURE: Unsynchronised pulses	Pulse energy < 1 pJ	Sub-picosecond FWHM	Rep. rate: 40 GHz and higher	No reference pulses	Potentially complex pulses
Sonography (TPA)	✓	✓	✓	✓	✓	✓
Spectrography	✓		✓	✓	✓	✓
Self-referenced linear interferometry	✓	✓			✓	✓
Test-pulse-referenced linear interferometry		✓	✓	✓		✓
SPIDER	✓		✓	✓	✓	
Chronocyclic tomography		✓	✓		✓	✓
Temporal imaging		✓	✓		✓	✓

FIGURE 1.9: Applicability of pulse measurement techniques to SMLLs.

passively and emit picosecond and sub-picosecond optical pulses with repetition rates ∼40 GHz. Therefore, the synchronisation to the pulses and employment of a fast modulator is extremely difficult, which excludes the self-reference interferometry, temporal imaging and chronocyclic tomography. The pulses are also not accompanied by any well-characterised reference pulses, which is necessary in TPRI. The only SI technique

which could find application in those measurements is the SPIDER. However, the expected pulses are potentially of complex structure and can vary with the laser biasing parameters, which can be challenging for the SPIDER.

The most problematic issue is the inherently very low energy levels of the pulses produced by semiconductor LDs, as they can fall below 1 pJ. The linear techniques would be ideal but they are excluded because of the arguments discussed above. Therefore, the pulse detection needs to utilise a nonlinear phenomenon for the fast time gating. The most sensitive and popular spectrography technique, the SHG FROG is limited to 1 pJ of pulse energy due to the low efficiency of the SH crystals. However, the sensitivity can be largely increased by using TPA as the nonlinear detection mechanism. Even better is the sonography method, as it does not have time-direction ambiguity and the TPA detection can be implemented in a straightforward geometrical arrangement.

1.6 Two-photon Absorption

In the two-photon absorption an electron-hole pair is generated through the simultaneous absorption of two photons. The transition from the valence band to the conduction band is promoted by an intermediate, virtual energy level in the bandgap [42]. This is a non-resonant process, which occurs for photons of energy equal to $h\nu$, which satisfies the inequality:

$$\frac{E_g}{2} < h\nu, \tag{1.20}$$

where h, ν and E_g denote Planck's constant, the photon frequency and the band-gap energy, respectively [42]. The TPA simplifies the measurement set-up, as neither crystals nor sensitive detector such as a PMT [43] are required. TPA is a third-order non-linearity (χ^3) phenomenon that generates carriers, which can then be directly detected as a photocurrent. It is less polarisation sensitive compared to SHG and its photo-response is a quadratic function of the laser light intensity, I (Eq. 1.21) [18]. For instance, if the optical beam is guided through a semiconductor material (in the z-axis) with a TPA cross section equal to β_2, it experiences attenuation due to the TPA carrier excitation:

$$\frac{dI}{dz} = -\beta_2 I^2. \tag{1.21}$$

TPA has been widely used for ultrashort optical pulse characterisation and both, custom designed devices and commercially available devices, are described in the literature. For optical wavelengths of 1.55 μm, TPA-based pulse measurements have been reported with silicon avalanche [44] and non-avalanche [45] photodiodes, InGaAsP commercial

laser diodes [46], GaAs quantum-well (QW) waveguides detectors [42], GaAs photomultiplier tube [43], silicon waveguide detectors [47], and bulk [48] and QW InGaAsP [49] waveguides.

Due to the wide range of possible implementation of the TPA detection, it is crucial to choose a scheme that is best suited for the characterisation of the SMLL pulses. All the requirements imposed on such a detector, along with the proposed devices will be detailed in the next chapters of this thesis.

1.7 Organisation of the Chapters

The chapters are organised as follows:

Chapter 2 introduces the semiconductor material epilayers used to fabricate the MLLs and characterises their main features, e.g. the optical gain, the absorption spectra, and GVD.

Chapter 3 investigates the dynamical behaviour of ML devices and examines their performance at a range of biasing conditions, namely the SA reverse voltage and the gain section pump current. Also, the influence of the absorber length on the ML quality, as well as other dynamical regimes, is analysed.

Chapter 4 describes the concept of TPA detection selected for this research as well as design, fabrication and experimental test of the detectors.

Chapter 5 outlines the main features of the developed sonogram set-up and explains the pulse measurement routine. It verifies the suitability of the set-up and the embedded TPA detectors for characterisation of ultrashort pulses from the investigated SMLLs.

Chapter 6 presents the outcome of the sonogram characterisation of ultrashort pulses. It shows the evolution of the intensity and phase profiles of picosecond and sub-picosecond pulses emitted from various semiconductor devices over a wide range of biasing conditions.

Chapter 7 concludes the thesis and provides suggestions for future work.

Chapter 2

Al-quaternary Material Systems

This chapter reports on the characterisation of the laser material systems used for the fabrication of the SMLLs. The devices were based on two AlGaInAs material designs: a 5-QW commercially available epistructure and an improved design for high power operation.

In order to gain a deeper understanding of the device behaviour, several parameters of these material systems were experimentally investigated. The analysis includes a detailed study of the modal gain and absorption coefficient spectra for various biasing conditions, and the characterisation of the GVD in the laser waveguides along with the influence of numerous electro-optic (EO) effects.

It should be noted that the material characteristics presented in this chapter not only clarified some of the dynamical behaviours but were also crucial in providing experimental input data for the SMLL simulation work-package, which formed a part of the same EPSRC project [50].

2.1 Motivation for Al-quaternary Material

InGaAsP and AlGaInAs quaternary compounds are the two material systems, lattice-matched to InP, that are routinely used for optoelectronic devices operating around 1.55 μm. Historically, the former material system was preferred due to poor reliability of the latter compound, caused by the presence of aluminum. The early devices fabricated on the Al-quaternary systems were limited to low-temperature and low-power operation, especially due to the catastrophic optical mirror damage (COMD) [51]. However, recent progress in epitaxial growth techniques allowed the AlGaInAs compound to compete

with its P-quaternary counterpart in terms of performance and reliability. There are several attributes which make the Al-quaternary desirable for high-power applications:

1. Higher T_0 and T_1 characteristic temperatures (i.e. lower degradation of threshold current and slope efficiency with the junction temperature), due to lower Auger recombination and inter-valence band absorption.

2. Higher gain coefficient, enabling lower active layer confinement and consequently lower optical losses.

3. Higher conduction band discontinuity and lower valence band discontinuity compared with InGaAsP materials improve extinction behaviour and reduce hole pile-up in multi-quantum-well (MQW) electro-absorption (EA) modulators. This improves the temperature range and increases the optical saturation intensity [52]. Also, better electron confinement prevents carrier overflow at high temperatures and improves current injection efficiency. This allows for the reduction of p-doping in the cladding layer, which results in lower optical losses.

4. Easier control of the growth processes with respect to the desired emission wavelength (more linear system).

2.2 Overview of the AlGaInAs Material Systems

The main difference between the two epitaxial structures used for the fabrication of the SMLLs is the number of quantum wells embedded in the active layer and the inclusion of a far field reduction layer. For clarity, the terms 5-QW and 3-QW will be used throughout the work to reference the two different materials. The 5-QW material is a commercially available [1] *p-i-n* laser wafer and its energy band diagram is shown in Fig. 2.1. The MQW AlGaInAs/InP wafer has a gain region consisting of five, 6 nm thick, compressively strained (12000 ppm) $Al_{0.07}Ga_{0.22}In_{0.71}As$ QWs, having a photoluminescence (PL) wavelength of 1530 nm, and six, 10 nm thick, tensile strained (-3000 ppm) $Al_{0.224}Ga_{0.286}In_{0.49}As$ barriers. On each side of the QWs, the core layers are formed by a 60 nm graded-index (GRIN) layer for enhancing the optical confinement, terminated by a 60 nm $Al_{0.423}Ga_{0.047}In_{0.53}As$ electron confinement layer. On the *p-side*, the structure is completed by a 50 nm thick InP transition layer, a 20 nm thick $Ga_{0.15}In_{0.85}As_{0.33}P_{0.67}$ wet etch stop layer, a 1600 nm thick InP upper cladding, a 50 nm $Ga_{0.29}In_{0.71}As_{0.62}P_{0.38}$ lattice-matched layer and, finally, a highly doped 200 nm thick $Ga_{0.47}In_{0.53}As$ cap layer. On the *n-side*, the structure is formed by a 10 nm thick graded composition (GC) layer

[1] IQE Ltd. – www.iqep.com

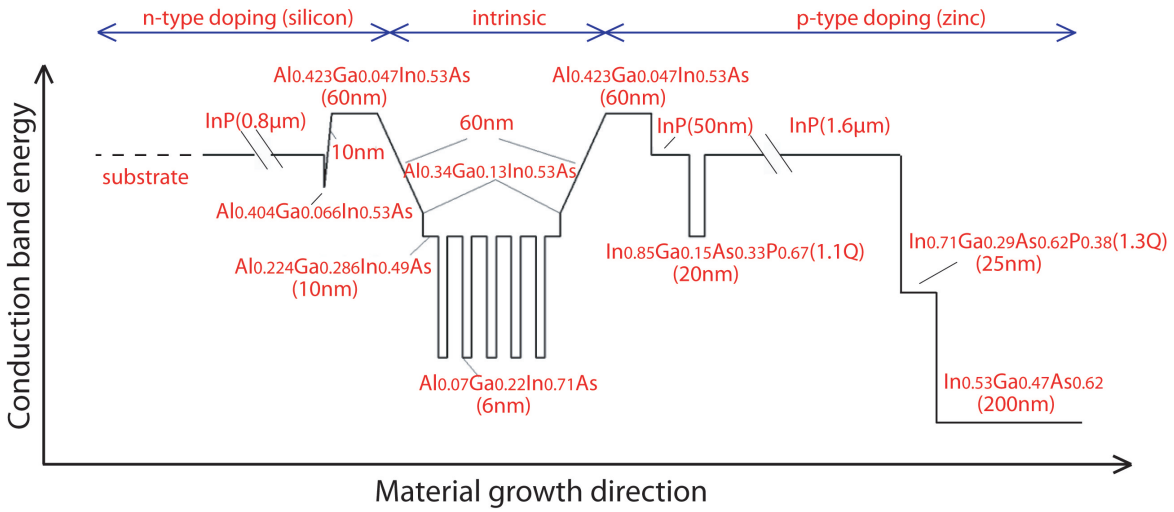

FIGURE 2.1: Conduction band diagram of the epitaxial layers in the 5-QW material design.

[53] with Al composition changing from 0.404 to 0.423, and a 800 nm thick InP buffer layer. The epitaxial structure was grown on an InP substrate via metal-organic chemical vapour deposition (MOCVD). The substrate and the epitaxial layers outside the GRIN structures were doped with Zn and Si, acting as p-type and n-type dopants, respectively. The second material structure is a 3-QW system, in principle based on the 5-QW design

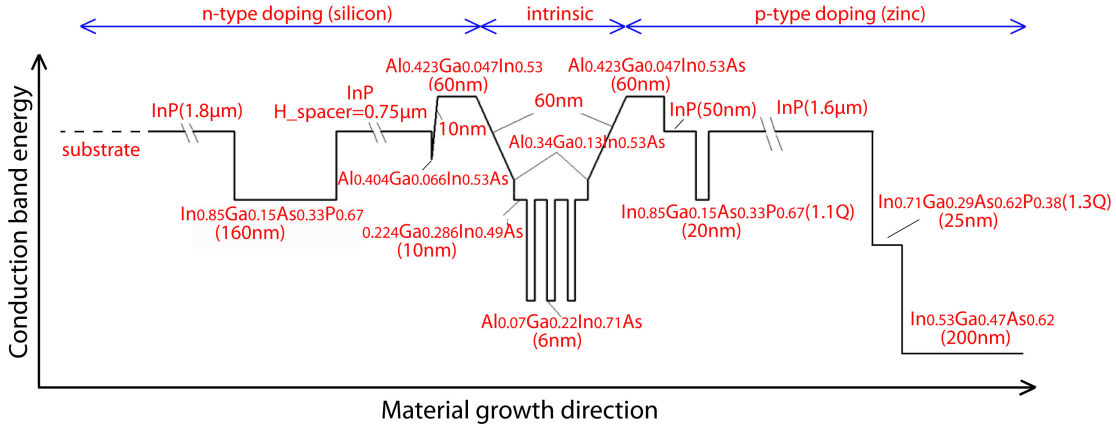

FIGURE 2.2: Conduction band diagram of the epitaxial layers in the 3-QW material design.

and optimised for high power operation by co-workers in the grant [54]. The conduction band diagram for this epistructure is displayed in Fig. 2.2. The main motivations for the modifications introduced in the 3-QW structure were:

1. to reduce the phase noise and timing jitter originating from the spontaneous emission and carrier fluctuations [55];

2. to improve ML operation, in terms of lower noise, better stability and shorter pulses;

3. to reduce the output divergence angle of the emitted light and make the far-field pattern more symmetric, to increase fibre coupling efficiency;

4. to increase the power emitted from the devices and minimise the possibility of COMD.

As the first two features are of utmost significance for this project, the effects of the material design on these laser performance criteria will be analysed next. The parameters affecting the phase noise, $\Delta\nu$, are summarised in Eq. 2.1 [56].

$$\Delta\nu = \frac{h\nu v_g^2 n_{sp}\alpha_m(\alpha_i + \alpha_m)(1+\alpha^2)}{8\pi P}, \tag{2.1}$$

where $\Delta\nu$ is the FWHM of the power spectrum of the laser, $h\nu$ is the photon energy, v_g is the group velocity, n_{sp} is the spontaneous emission factor, P is the output power per facet, α is the linewidth enhancement factor, and α_m and α_i are the mirror and internal losses, respectively. The relation between the rms timing jitter, σ_J, and phase noise can be expressed as:

$$\sigma_J = \frac{1}{2\pi f_L}(2\int_{f_{low}}^{f_{high}} L_1(f)df)^{1/2} \tag{2.2}$$

and

$$L_1(f) = L_n(f)/n^2, \tag{2.3}$$

where $L_n(f)$, f_L, f_{low}, and f_{high} are the phase noise power (per unit bandwidth) of the nth harmonic, the laser pulse repetition frequency, the low integration limit, and the high integration limits, respectively [57]. Eq. 2.1 shows that the phase noise can be reduced by either lowering the internal losses or increasing the pulse energy. Increased pulse energy and reduced power dissipation in the laser cavity results in the improved quality factor (Q-factor) of the optical resonator. This means that the oscillations take place within a smaller range of frequencies, which effectively leads to a lower phase noise. The first approach to reduce the phase noise can be realised by reducing the number of QWs or decreasing the overlap of the mode with the highly lossy p-doped cladding layer [54]. In order to increase the pulse energy the level of the saturated gain, E_{sat}, defined in Eq. 2.4, has to be raised.

$$E_{sat} = \frac{h\nu d}{\Gamma\frac{dg}{dN}}, \tag{2.4}$$

where d is the mode area, dg/dN is the differential gain, and Γ is the optical confinement factor. Again, this can be accomplished in two ways: either, by decreasing the differential gain through reduction of the number of the QWs in the gain medium [58], or by

maximising the d/Γ ratio. The latter approach can be implemented by reducing the number of QWs (lower Γ) or decreasing the overlap of the guided mode with the QWs.

All the solutions outlined above were implemented in the 3-QW design. The number of QWs was reduced to three, which decreased the cavity losses, and decreased both the differential gain and the optical confinement. Furthermore, the size of the guided mode was expanded by adding an additional $Ga_{0.15}In_{0.85}As_{0.33}P_{0.38}$ layer, 0.75μm below the bottom of the core structure. The position and thickness of this layer were optimised for the maximum d/Γ ratio with a single transverse mode operation [58]. The introduction of this layer also increases the near-field pattern (NFP), hence reduces the vertical divergence angle and the far-field pattern (FFP) of the output beam. The guided mode is being pulled towards the n cladding layer and its overlap with the p-doped cladding and cap layers is reduced. This allows for further reduction of the optical losses. The effects of these material modifications on the RF noise, timing jitter and the ML performance will be investigated in Chapter 3.

2.3 Material Characterisation

2.3.1 Gain and Absorption Measurements

An accurate evaluation of the gain and absorption of the active material is of paramount importance for the theoretical analysis of PMLLs. In fact, these parameters contribute substantially to the optical spectral behaviour under ML operation, to its dynamical stability, and to the optimum dimensions and biasing conditions of the gain and absorbing sections of the cavity.

For the gain and absorption measurements in the 5-QW material, there were two experimental methods implemented, namely the three-section and the Hakki-Paoli (HP) techniques. With the 3-QW system, only the latter technique was used, as it proved superior to the former approach in several aspects, as will be explained later. Both methods utilise the spontaneous emission of the lasers, which allows for the gain and absorption characterisation within a large wavelength range. Such a range is usually inaccessible from the commercially available tunable lasers, which could otherwise be used as the external probe sources. Furthermore, such measurements are extremely sensitive to the spectral purity of the tunable laser [59].

2.3.2 Gain and Absorption Measurements of the 5-QW Material System

2.3.2.1 Three-section Method

The three-section method utilises the amplified spontaneous emission (ASE) measurement, as described in [60] and [61]. A schematic of the three-section device is presented in Fig. 2.3. The device was fabricated by the author's colleague, Steven McMaster, using the same technology as for the SMLL devices [62]. The electrical contacts of the 500 μm long sections were separated by 20 μm gaps to allow independent biasing of each segment. The ASE is generated in Section 2 and collected at the front facet after propagating through Section 1. The analysis of the spectral profiles of the ASE as a function of different biasing conditions in Section 1 provides a precise evaluation of the gain and loss of the material. To prevent lasing and minimise back-reflections, Section 3 is biased

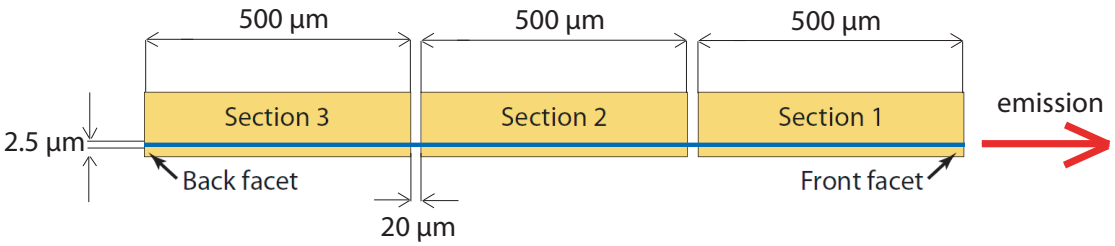

FIGURE 2.3: Schematic of the three-section device for the gain and absorption measurements.

with a reverse voltage of 3 V. The back-reflection has been further reduced by scribing through the waveguide close to the back facet. These additional losses prevent the cavity from lasing even at high current densities. Before being coupled into an optical spectrum analyser (OSA), the output light is directed through a polarising beam splitter (PBS), in order to separate the transverse electric (TE) and transverse magnetic (TM) polarisation states. The experimental work presented in this section focuses on the TE polarisation, i.e. the electric field is polarised in the plane of the QWs. This polarisation state dominates the emission from the MQW structures, due to the selection rule in the electron-hole recombination and the separation between the heavy and light holes [63]. Throughout the whole experiment the device temperature was maintained at 20 °C. The ASE emitted from a section of length L is equal to [64]:

$$P(L) \propto \frac{R_{sp}}{g_{net}}(e^{g_{net}L} - 1), \tag{2.5}$$

where R_{sp} is the recombination coefficient of spontaneous emission, and g_{net} is the net modal gain:

$$g_{net} = \Gamma g_{mat} - \alpha_i, \tag{2.6}$$

with Γ, g_{mat} and α_0 denoting the confinement factor, the material gain and the internal loss, respectively. It can be seen, that by varying the length of a pumped region, L, the modal absorption and the net modal gain can be evaluated. The three-section routine is as follows: Firstly, Section 1 is forward-biased with current density, J, Section 2 is left floating and the reference intensity, $I_{ref}(\lambda, J)$, emitted from the front facet is recorded with an OSA. Then, for the absorption measurements, Section 2 is forward-biased with J, while Section 1 is biased with the reverse voltage varying from 0 V to 3 V. In such an arrangement, the output intensity, $I_{out}(\lambda, V)$, depends on the initial emission from Section 2, which is equivalent to $I_{ref}(\lambda, J)$, and on the absorption, $\alpha(\lambda, V)$, of Section 1. This allows the losses to be deduced as:

$$\alpha(\lambda, V) = \frac{1}{L} \ln \left(\frac{I_{ref}(\lambda, J)}{I_{out}(\lambda, V)} \right). \tag{2.7}$$

As for the gain measurements, both sections are forward-biased with identical current densities and the ASE from the front facet, ($I_{out}(\lambda, J)$), is used for the net modal gain calculations:

$$g(\lambda, J) = \frac{1}{L} \ln \left[\left(\frac{I_{out}(\lambda, J)}{I_{ref}(\lambda, J)} \right) - 1 \right]. \tag{2.8}$$

The results of the material characterisation are summarised in Fig. 2.4 – Fig. 2.6. It can be observed, that the application of the reverse voltage changes the position of the SA band edge and triggers the exciton broadening. With increasing reverse bias the band edge absorption shifts towards lower energies (i.e. longer wavelengths). The variation of the band edge energy with an electric field perpendicular to the QW structure is known as the quantum confined Stark effect (QCSE) [65]. The field causes an offset in the confined energies inside the QW [66] and moves the holes and electrons to opposite ends of the QW. This leads to a reduction in the energy of the electron-hole pair [67]. An average shift of the band edge is estimated to be 1.7 THz.V^{-1} (9 nm.V^{-1}), although, the rate of change is not linearly proportional to the electric field.

This method, however, has one major limitation. It was noticed that the reference current used to pump Section 2, apart from influencing the level of maximum absorption, also shifts the position of the absorption peak. An example of such behaviour is presented in Fig. 2.5, where the absorption coefficient spectra for a range of pump current values in Section 2 at a constant voltage level in Section 1 are shown. The variations in the

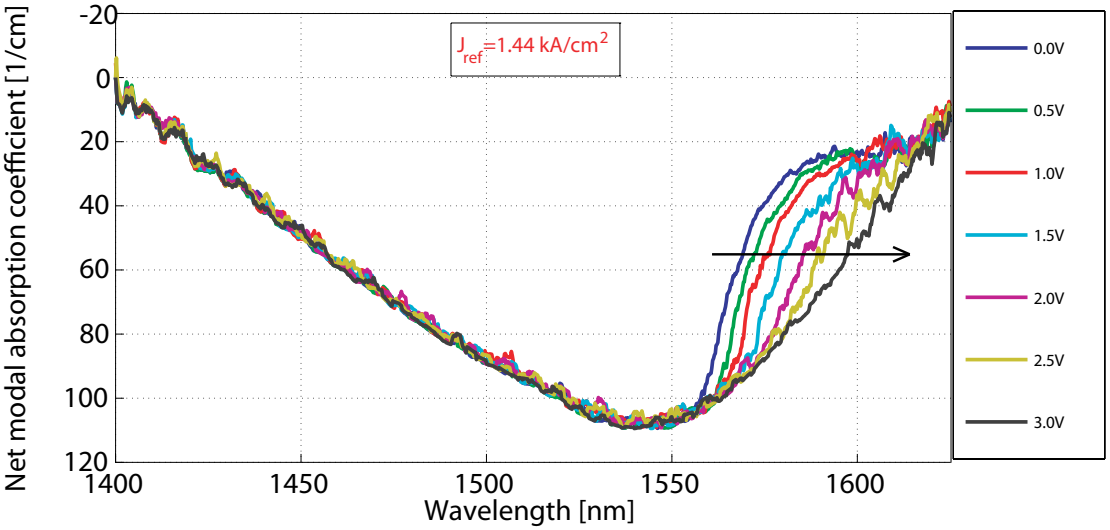

FIGURE 2.4: Modal absorption coefficient spectrum as a function of the reverse voltage obtained with the three-section method.

maximum absorption coefficient level can be explained by the fact that Section 1 is far too long to be saturated by the ASE generated in Section 2. In order to reach higher levels of saturation, a shorter (and hence easier to saturate) absorbing section should be used.

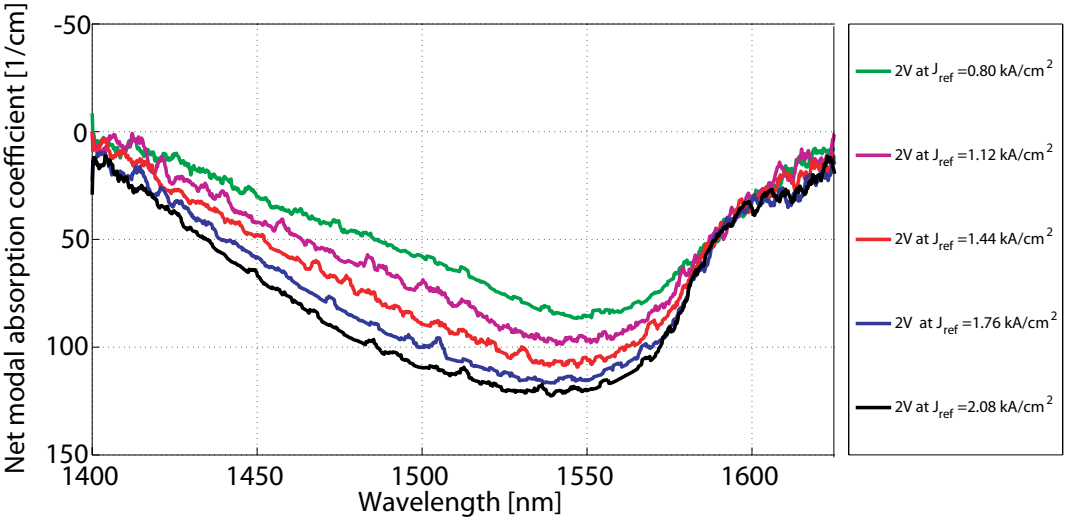

FIGURE 2.5: Net modal absorption coefficient spectrum at constant reverse voltage in the absorbing section as a function of the pump current in Section 2, measured with the three-section method.

Fig. 2.6 presents the evolution of the material gain with current density. The value of $\sim$-18 cm^{-1}, to which all the spectra converge for long wavelengths, indicates the internal losses. A continuous shift of the peak wavelength towards higher energies can be clearly noticed with increasing pumping. The carrier injection affects the spectral response of the system through two effects: bandgap renormalisation and band filling. Above the

lasing threshold the bandgap renormalisation reduces the energy gap, effectively moving the emission towards longer wavelengths. The band filling has the opposite effect and dominates below the threshold [68], [69]. Hence, the gain coefficient curves of Fig. 2.6 shift towards higher energies, as the device operates below threshold. With increasing carrier density the amplitude peak of the material gain increases up to $\sim 2\,\mathrm{kA/cm^2}$, above which it saturates.

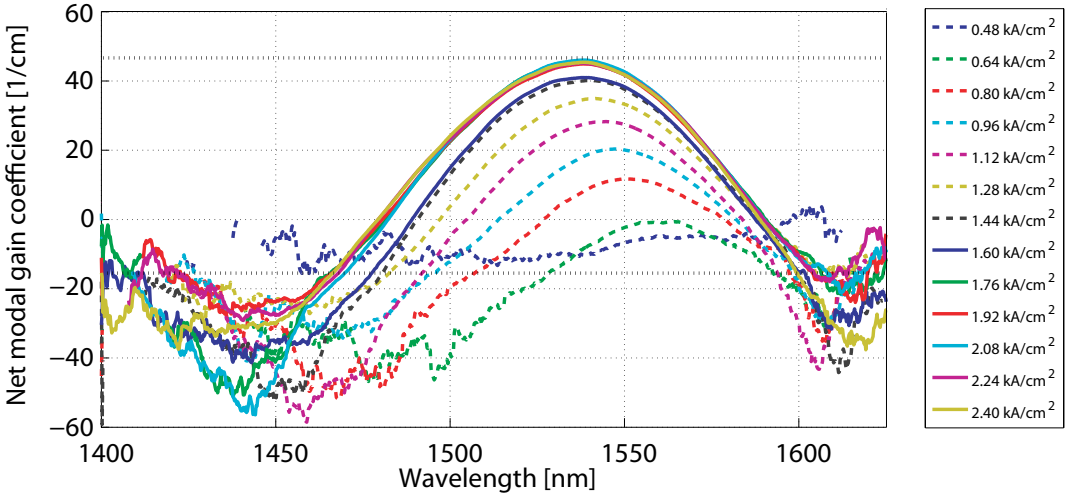

FIGURE 2.6: Modal gain coefficient spectrum as a function of the bias current obtained with the three-section method.

2.3.2.2 Hakki-Paoli Method

In order to verify the results of the gain and absorption measurement acquired by the three-section method, the experiment was repeated with an alternative technique, known as the HP method [70]. This approach extracts the gain/loss from the modulation depth of the ASE due to the Fabry-Pérot (FP) resonances of the laser cavity. As the method requires a high wavelength resolution [71], the measurements were performed with the Advantest Q8383 OSA, which has a high dynamic range of 60 dB and a spectral resolution of 10 pm. The device used in the experiments was a two-section SMLL, comprising a gain section and a saturable absorber, making up 3.3% of the total cavity length of L=1070 μm. Device layout details can be found in Section 3.1.1. Due to the limited sensitivity of the OSA and the small intensity of the spontaneous emission, the resolution bandwidth was set to 20 pm, which improves the signal-to-noise ratio on the OSA photodetector, while preserving the required accuracy to resolve the cavity modes. The measurement set-up is essentially the same as in the three-section method. The light emitted from the laser facet at the SA side is collimated in free-space, transmitted through the PBS for the polarisation selection, coupled back into the optical fibre, and finally sent to the OSA. The measurement procedure is as follows: In the first stage

the ASE spectra are recorded for various bias levels below threshold, with an equal current density in both sections. Next, the gain coeffiecient spectra corresponding to each current level are calculated using Eq. 2.9:

$$G_{net} = \Gamma g_{mat} - \alpha_i = \frac{1}{L} ln(\frac{S-1}{S+1}) + \frac{1}{2L} ln(\frac{1}{R1 \cdot R2}), \tag{2.9}$$

where

$$S = \sqrt{\frac{I_{MAX1} + I_{MAX2}}{2I_{MIN}}}, \tag{2.10}$$

and I_{MAX1},I_{MAX2}, I_{MIN}, R1, R2 are the peak intensities of successive cavity modes, the intensity of the intermediate valley, and the mirror reflectivity of the facets, respectively. The reflectivity of both cleaved, straight and uncoated facets is approximately equal to 0.32. The results of the gain characterisation are shown in Fig. 2.7, which shows the modal gain coefficient spectra of the dominant TE component for different injected current values. The gain coefficient demonstrates positive values for current densities above 0.78 kA/cm^2. This yields the possibility of obtaining lasing operation as soon as the modal gain matches the mirror losses.

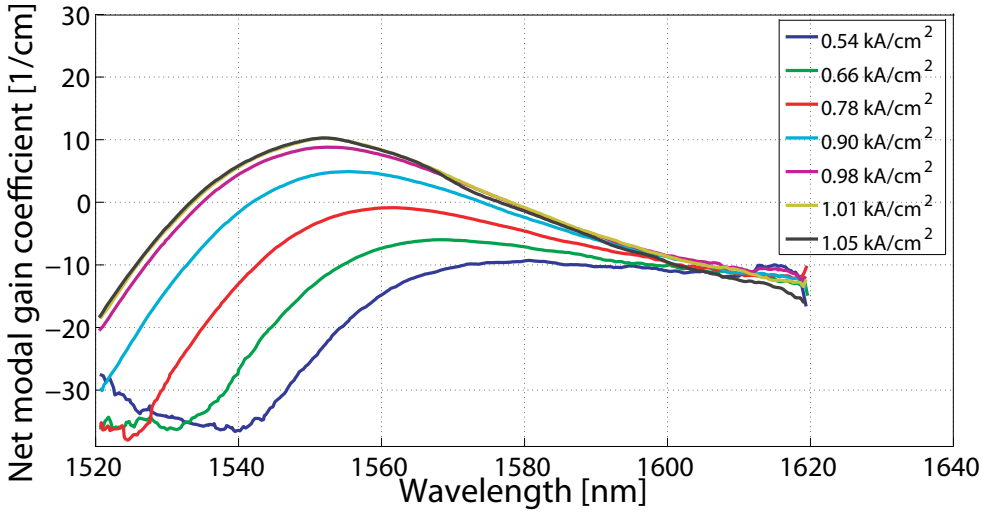

FIGURE 2.7: Modal gain coefficient spectrum of the 5-QW active material at different current density levels, obtained with the HP technique.

In the second stage, the amplified spontaneous emission is recorded with the SA section reverse-biased, while the current density in the gain section is maintained at a constant level of 1 kA/cm^2. The modified gain coefficient spectra, G'_{net}, are obtained by applying Eq. 2.9 to the measured traces. As the SA is no longer forward-biased, it acts as an absorber and influences the resulting spectra as follows:

$$G'_{net} = \frac{G_{net} L_G - A_{net} L_{SA}}{L_G + L_{SA}}, \tag{2.11}$$

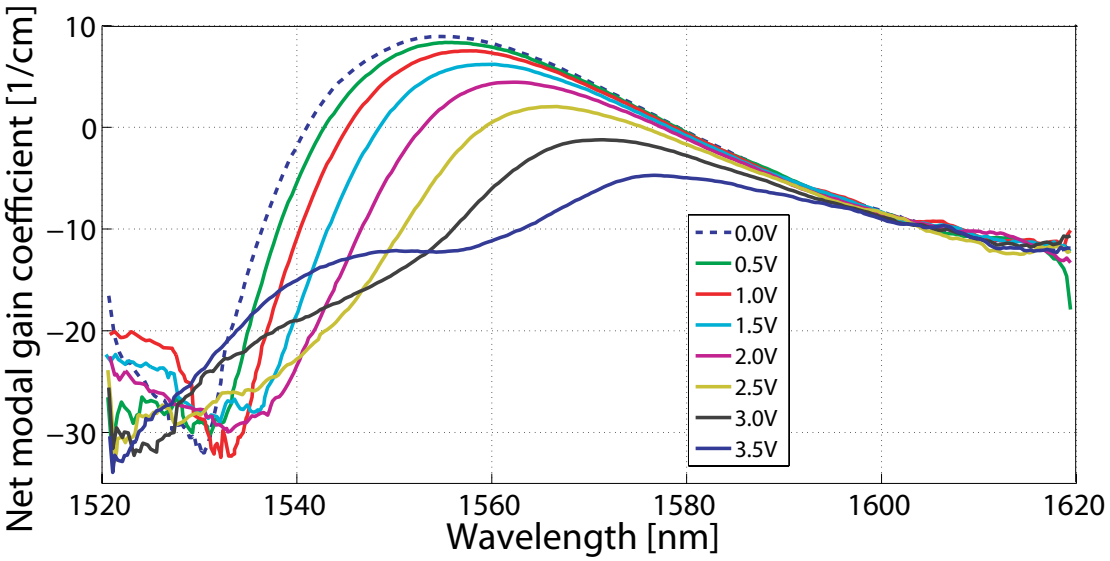

FIGURE 2.8: Modal gain coefficient spectrum of the 5-QW active material at different reverse voltage values applied to the SA section and the gain section current density of 1.0 kA/cm^2, obtained with the HP technique.

where A_{net} denotes the modal absorption coefficient spectrum, and L_G and L_{SA} are the lengths of the gain and absorption sections, respectively. Fig. 2.8 displays the calculated modal gain, G'_{net}, for absorber reverse bias voltages ranging from 0 V to 3.5 V.

By rearranging Eq. 2.11 A_{net} can be expressed as:

$$A_{net} = \frac{G_{net}L_G - G'_{net}(L_G + L_{SA})}{L_{SA}}. \tag{2.12}$$

Substituting the gain coefficient spectra, G_{net} and G'_{net}, into the equation, the modal absorption coefficient can be calculated for various reverse voltages.

The results of the absorption calculation are presented in Fig. 2.9 – 2.10. Similar to the three-section method, the level of saturation depends upon the reference intensity from the gain section. With the HP method, however, much higher saturation levels have been measured (over 800 cm^{-1}) due to the short length of the absorbing section. Also, the peak of the absorption coefficient spectra shifts towards shorter wavelengths with increasing reference current density (see Fig. 2.10). This is caused by carrier induced effects at increasing levels of photo-generated carriers. The QCSE is clearly evident in the obtained spectra and varies from 0.8 THz.V^{-1} (4 nm.V^{-1}) at low voltages to 1.7 THz.V^{-1} (9 nm.V^{-1}) at higher voltages.

As can be seen in Fig. 2.9, the maximum level of absorption coefficient shifts from 820 cm^{-1} at V_{SA}=0 V to 930 cm^{-1} at V_{SA}=-2.0 V. For higher values of reverse voltage the exciton peak rapidly broadens and the maximum absorption coefficient levels drop

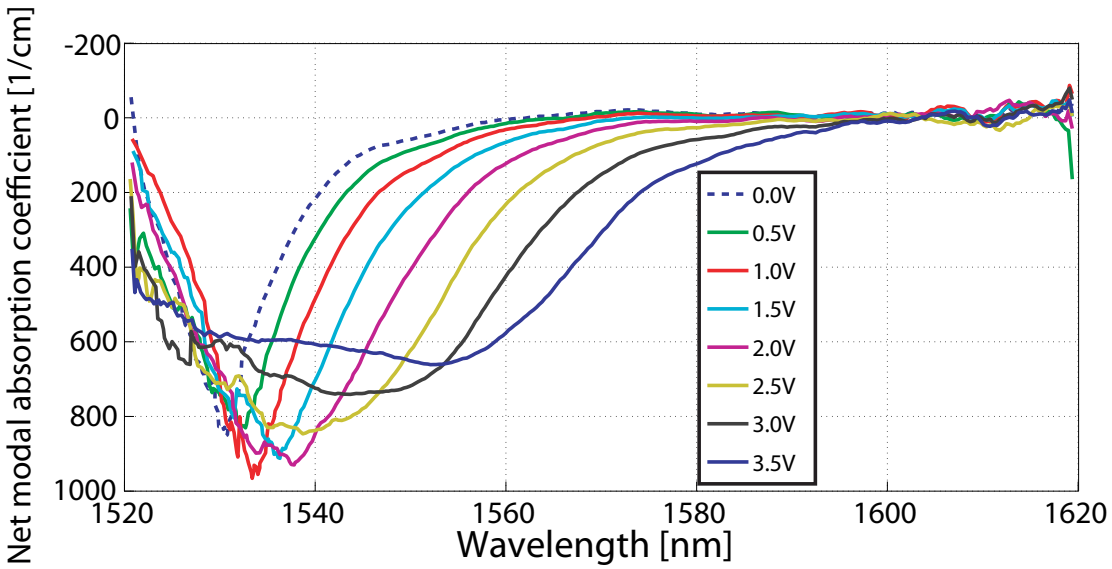

FIGURE 2.9: Computed modal absorption coefficient spectra of the 5-QW material at various reverse bias applied to the SA section and the current density in the gain section set to 1.0 kA/cm^2, obtained with the HP technique.

significantly (652 cm^{-1} at V_{SA}=-3.5 V). These effects are expected because of the reduction of the electron-hole wavefunction overlap [66]. The broadening of the exciton peak comes from the sum rule or the conservation of absorption, stating that the area under the absorption peak needs to stay constant (with higher order and forbidden transitions taken into account) [72]. The initial increase of the absorption peak with the applied voltage shows that not all the photogenerated carriers are effectively extracted by the external electric field. Also, the broadening of the absorption peak at these voltage levels is weak, which can be caused by the space charges broadening the exciton peak at low bias levels [73].

2.3.2.3 Comparison Between the Three-Section and Hakki-Paoli Methods

There are several differences between the results of the modal spectral absorption coefficient obtained with the two techniques:

1. The band edges from the three-section method are spectrally shifted by over 20 nm with respect to the band edge from the HP method.

2. The band edges from the HP technique are defined more clearly and the extent of the QCSE can be better assessed.

3. The variation of the peak absorption level with increasing voltage evident from the HP method is not observed with the three-section approach.

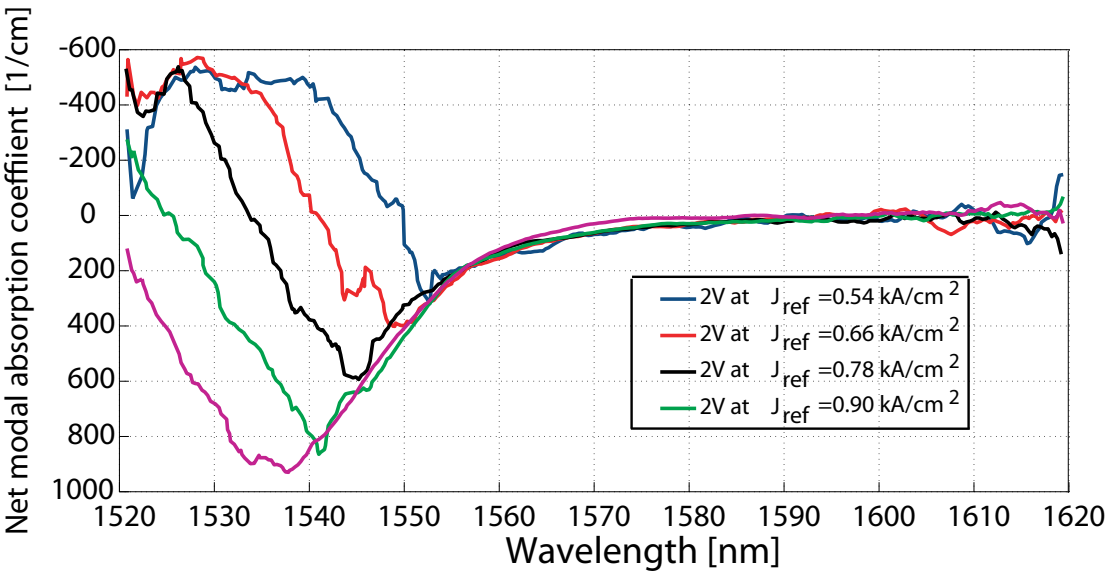

FIGURE 2.10: Computed modal absorption coefficient spectrum of the 5-QW system, with a constant SA reverse bias of 2 V and for a range of gain section current density levels.

The comparison between the modal gain coefficient spectra measured with the two methods, as presented in Fig. 2.6 and Fig. 2.7, shows that even though different values of the peak gain levels are obtained, similar trends in the spectra are evident. However, the HP technique delivers more accurate results for the modal absorption coefficient characterisation. Hence, this method has been chosen to investigate the properties of the second material system, based on the 3-QW design.

2.3.3 Gain and Absorption Coefficients Measurements of the 3-QW Material System

For the characterisation of the modal gain and absorption coefficients of the 3-QW material a standard SMLL comprising of a gain and a SA section was used. The total length of the cavity is equal to 1264 μm, with the absorber constituting $\sim$4 % of it (L_{abs}=50 μm.) The two sections are electrically separated by 10 μm gap between the p-contacts. The ridge waveguide is slightly narrower than in the 5-QW devices, with a width of 2 μm. Further details on the device layout can be found in Section 3.1.1.

The measurement procedure is identical to that used with the 5-QW material system. Firstly, the gain measurements are performed with both absorber and gain sections forward biased over a range of current densities below the lasing threshold. The outcome of this measurement is shown in Fig. 2.11. Injected current densities span from 0.29 kA/cm^2 to 1.12 kA/cm^2, above which the lasing modes begin to appear. The effects of the band filling due to increasing carrier densities in the QWs as the gain peak shifts from 1570 nm

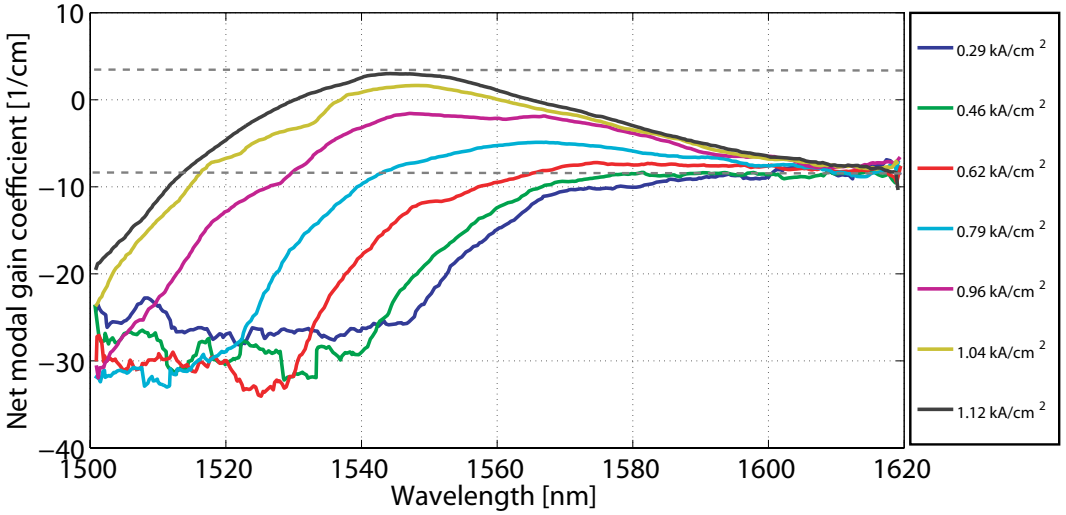

FIGURE 2.11: Modal gain coefficient spectra of the 3-QW active material at different current density values, obtained with the HP technique.

at the lowest pumping level to 1544 nm near the threshold can be observed. Also, gain clamping at a level of 3 cm^{-1} is evident from the modal gain coefficient spectra. The internal losses defined by the convergence point of the spectra at the long wavelength side are equal to 8.6 cm^{-1}. Next, the absorber section is reverse-biased and the refer-

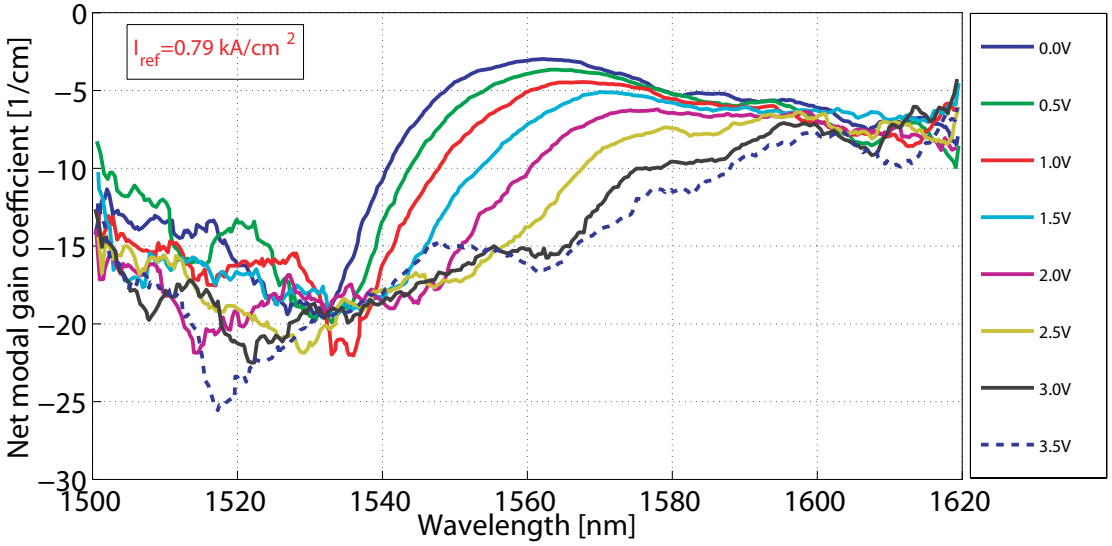

FIGURE 2.12: Reference spectra of the net modal gain coefficient for calculation of the modal absorption coefficient of the 3-QW active material with the HP technique.

ence spectra are measured, as displayed in Fig. 2.12. The reference spectra are recorded for each of the current density values presented in Fig. 2.11, and for reverse voltage values ranging from 0 V to 3.5 V. Eq. 2.12 is next used to calculate the modal absorption coefficient spectra, examples of which (for J_{ref}=0.79 kA/cm^2) are presented in Fig. 2.13. It can be seen that the peak absorption increases constantly from 100 cm^{-1} at 0 V to 220 cm^{-1} at 2 V, and clamps around that level at higher voltages. The QCSE is clearly

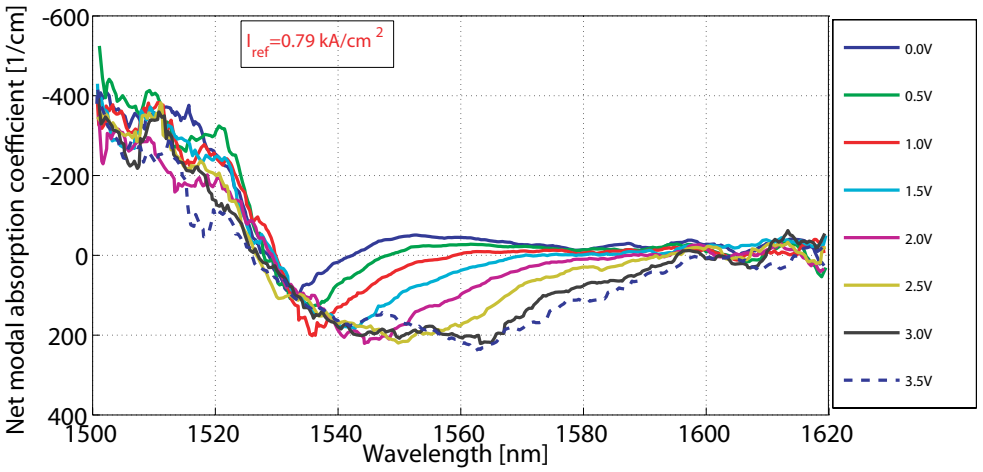

FIGURE 2.13: Computed modal absorption coefficient spectra of the 3-QW material at various reverse bias applied to the SA section and the gain section current density of 0.79 kA/cm^2.

evident, as the absorption peaks move and broaden with the increasing field, similar to those of the 5-QW material. The peak offset varies from 1.6 THz.V^{-1} (8 nm.V^{-1}) at the low voltage end to 3.4 THz.V^{-1} (12 nm.V^{-1}) between 2.5 V and 3.0 V. Interestingly, the shift between the last two voltage values is much smaller, and the absorption edges almost overlaps.

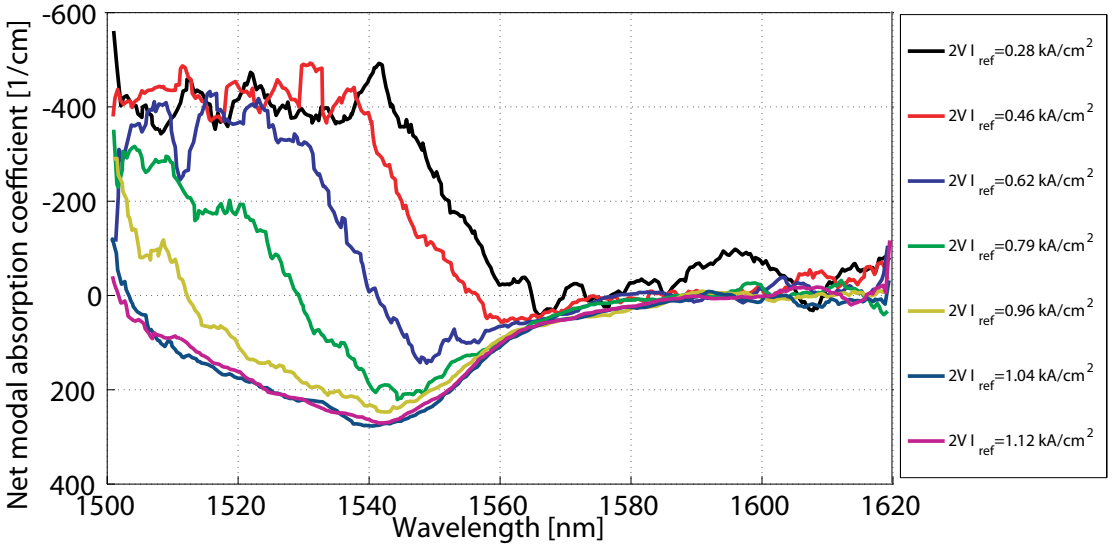

FIGURE 2.14: Computed modal absorption coefficient spectra of the 3-QW material system, with a constant SA reverse bias of 2 V and a various gain section current density.

Finally, the absorption coefficient spectra measured at a constant reverse voltage applied to the absorber section, and with varying reference current densities in the gain section, are shown in Fig. 2.14. The maximum absorption coefficient levels clamp around a value of 200 cm^{-1}. The absorption edges overlap with each other and, similar to the 5-QW

device, their position and amplitude depend on the current density level applied to the gain section.

The comparison of the gain and absorption coefficient spectra characterised with the HP method shows that the general trends and features of these spectra are similar for both laser material designs. However, absolute values of both the modal gain and the absorption coefficients, as well as the observed spectral shifts differ, and therefore some variations in the operational behaviour of the MLLs can be expected. The gain values recorded in the 3-QW material are considerably smaller than those measured with the 5-QW device for the same levels of current density. This is partially due to the lower number of quantum wells in the gain region as well as the modified shape of the mode, that results in the reduction of the confinement factor. For the same reasons and also due to minimised overlapping between the optical mode and the p-cladding layer, the internal losses are lower in the 3-QW system. The decreased level of saturated absorption in the 3-QW system may contribute to improved ML operation, e.g. lower noise, higher optical power, better stability, and larger ML biasing regions, as easier modulation of the absorber transparency can be achieved.

2.3.4 GVD in the Cavities of the Lasers

Another significant parameter that influences the behaviour of semiconductor ML devices is the group velocity dispersion. It contributes to the pulse shaping mechanism, and affects the overall chirp accumulated by the pulse. The GVD is defined as the second derivative of the phase constant, β, with respect to the frequency, ω, i.e. $d^2\beta/d\omega^2$. β is the real part of the complex propagation constant, $k = \beta + i\alpha$ [74], and is defined as a phase change per unit length for light propagating in a waveguide. The imaginary part of the propagation constant, α, is the absorption coefficient and represents optical gain (or loss) experienced by the optical mode. The complex amplitude, A(z, t), of light propagating along the waveguide axis z is described as

$$A(z,t) = A(z=0,t=0)e^{i(kz-\omega t)} = A(z=0,t=0)e^{-i(\omega t-\beta z)}e^{-\alpha z}. \tag{2.13}$$

The GVD can be derived from the effective refractive index, n_{eff}, or from the dispersion of the group index, n_g, as shown in Eq. 2.14 [75]:

$$GVD = \frac{dn_g}{d\lambda} = \lambda\frac{d^2n_{eff}}{d\lambda^2}, \tag{2.14}$$

where $n_{eff} = \beta c/\omega$. The effective group refractive index can be obtained from the longitudinal mode spacing in the laser cavity [76], as the frequency spacing, $\Delta\nu$, between

the Fabry-Perot modes corresponds to the inverse of the roundtrip time in the cavity of length L:

$$\Delta\nu = \frac{c}{2n_g L}. \tag{2.15}$$

Hence, n_g is related to the spectral separation between the modes, $\Delta\lambda$, the wavelength, λ, and the cavity length:

$$n_g = -\frac{\lambda^2}{2L\Delta\lambda} \tag{2.16}$$

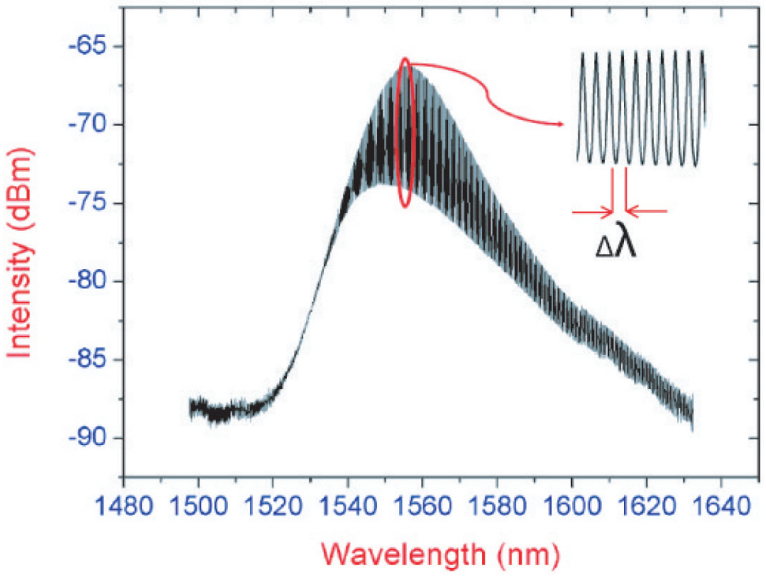

FIGURE 2.15: Exemplary spontaneous emission spectrum and the modal separation diagram.

The spontaneous emission spectra measured for the gain and absorption characterisation (HP method) were used to calculate the separation between the cavity modes. An example of the spontaneous emission spectrum along with the mode separation diagram is illustrated in Fig. 2.15.

Fig. 2.16 presents the third-order polynomials fitted to the mode spacing dependence on the wavelength, measured at various gain current levels below threshold. It can be observed that the spacing between consecutive longitudinal modes increases with increasing wavelength. As the pumping level reaches 1.12 kA/cm^2 the slope does not change anymore and the modal spacing shifts towards lower values – see Fig. 2.16 (a-b). This is even clearer in the graph presenting the group index profiles, as shown in Fig. 2.16 (c-d). The refractive index evolution is more complex in the 5-QW device,

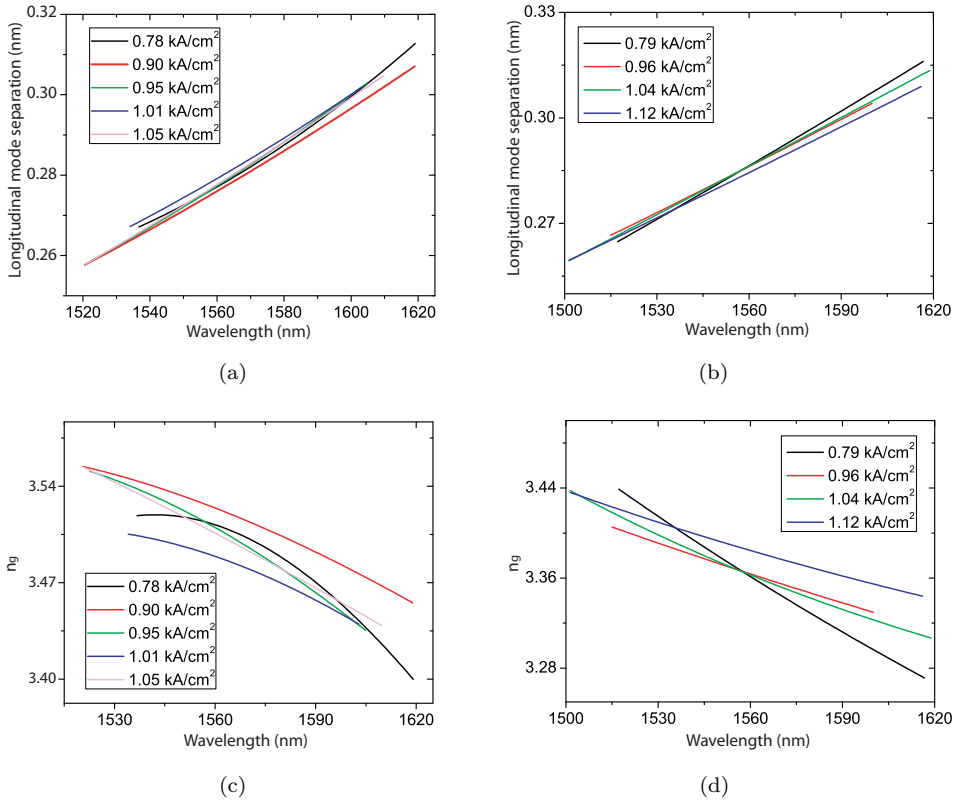

FIGURE 2.16: Spacing between the longitudinal modes in the laser cavity measured at a range of current densities, with (a) 5-QW and (b) 3-QW devices, and the group index for various current densities in the (c) 5-QW and (d) 3-QW devices.

for which the nonlinearity and slope of the refractive index characteristics strongly vary with the current density.

This complex behaviour is a consequence of the bandfilling, bandgap shrinkage and free-carrier absorption [77]. The bandfilling effect changes the level of absorption with respect to the unpumped material. It affects the energy levels close to the bandgap and weakens for energies well above it, effectively shifting the absorption edge. As the absorption and refractive index are correlated through the relations described by the Kramers-Kronig integrals [78], bandfilling inevitably modifies the refractive index spectra. The change in refractive index (Δn) is negative, near and below the bandgap, and becomes positive above it. The bandgap shrinkage comes from the mutual screening between electrons in the conduction band (as well as between holes in the valence band), which form a gas of interacting particles when current is injected. In terms of the refractive index variation, band-gap shrinkage always causes positive Δn, which is largest near the bandgap. The effect of free-carrier absorption is an intraband phenomenon, which manifests itself as an increase in the energy of free carriers within the energy band after photon absorption. This effect generates negative Δn and is proportional to the square of the wavelength.

All three carrier effects independently modify the refractive index spectra under current injection and their relative contribution changes as a function of the current density levels, with the bandfilling effect usually having a dominant impact. Besides the electro-optic effects, the refractive index is also influence by the active layer temperature increase induced by Joule heating due to the injection current. The refractive index change, Δn_T, for the III-V compounds is always positive [79] and depends on the increase in the temperature, ΔT, of the active layer accordingly to Eq. 2.17 [80].

$$\Delta n_T = (2 \sim 5) \times 10^{-4} \Delta T. \tag{2.17}$$

The average temperature of the active region, T_{act}, which increases linearly with the amount of the power, P_{act}, dissipated in the active guide depends on the effective thermal resistance, R_{th}, and can reach as high values as 400 K [81].

The group velocity dispersion spectra obtained through differentiation of the refractive index characteristics are shown in Fig. 2.17. In all the characteristics a negative GVD product, i.e. normal dispersion, can be observed. The only exception is the 5-QW characteristic taken at the current density of 0.78 kA/cm^2, where the blue-end of the spectrum exhibits anomalous dispersion. Due to a opposite sign of the curvatures of the group delay in the two materials, the GVD characteristics evolve in opposite ways in the 5-QW and 3-QW lasers, i.e. increasing for shorter wavelengths in the former device and decreasing in the latter one. This is probably due to the variations of the carrier induced effects between the two material systems as well as different dispersive properties of the devices waveguides (caused for instance by the unequal ridge waveguide widths). The presented results indicate that the contribution of the GVD to the overall pulse characteristics depends on the injected carrier density and on the spectral profiles of the emitted pulses.

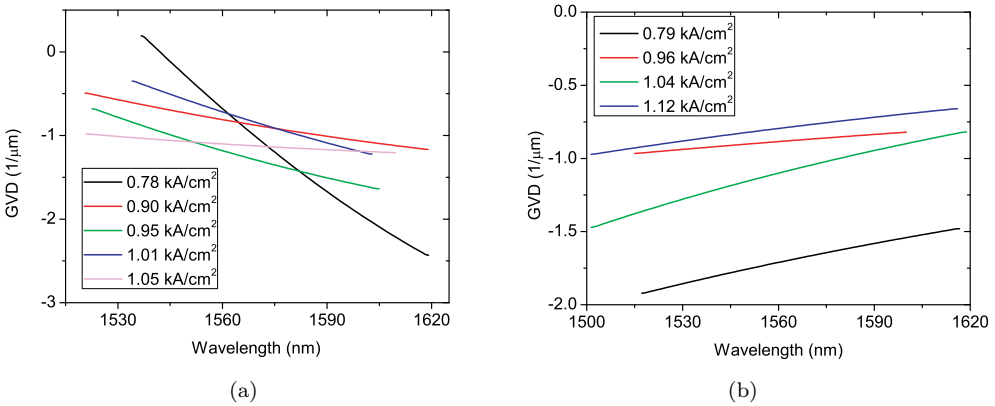

FIGURE 2.17: Group velocity dispersion profiles at various current densities in the (a) 5-QW and (b) 3-QW devices.

2.4 Chapter Summary

In this chapter, the basic characterisation of the laser material systems used in this work was presented. First, an overview of the epistructures used for the fabrication of the investigated SMLLs and the major differences between them were given. Next, two techniques for the modal gain and absorption coefficients characterisation were examined. The measurements confirmed that the HP method is more accurate than the three-section approach, and hence it has been employed for the complete evaluation of the gain and absorption spectra of both the 5-QW and 3-QW materials. The measurements were performed on standard SMLLs, with a short section acting as an absorber and a long section used as a spontaneous emission source. The obtained results showed different levels of the modal gain and absorption coefficients, which were considerably lower in the 3-QW structure. These measurements confirmed that the design modifications introduced in the 3-QW structure indeed affect the active material properties. The effects of several carrier induced phenomena, such as bandfilling, as well as the QCSE were also observed with varied biasing conditions. Finally, the dependence of the GVD on the current density was measured on the two material systems. The strong normal dispersion of the laser cavities indicated a significant correlation between the gain profile, the injected current and the refractive index, which needs to be taken into account in the evaluation of the devices under ML operation.

Chapter 3

Dynamics of Al-quaternary Mode-Locked Laser Diodes

In this chapter, the performance of the Al-quaternary SMLLs operating at a repetition rate close to 40 GHz is presented. First, an overview of the device geometry and a description of the experimental set–up employed for the measurements are given. Next, the characterisation based on a detailed analysis of the optical and RF spectra, as well as on the intensity autocorrelation traces, is performed. The various dynamical operating regimes of the devices, such as mode-locking, self-pulsation and continuous-wave operations are mapped as a function of the biasing parameters. For the biasing ranges in which ML operation is achieved, the quality of the ML is evaluated by measuring the phase noise, the temporal pulse width, the stability of the RF signal, and the extent of chirp accumulated in the optical pulses. The 3-QW devices are studied in greater detail because of their superior performance. Furthermore, the influence of the SA section length on the ML operation is investigated with these devices. The chapter concludes by comparing the performance of the different devices in terms of geometry and material.

3.1 Dynamical Characterisation Procedures

3.1.1 Examined Devices

Fig. 3.1 shows the layout of the characterised passive mode-locked lasers. A schematic diagram and an SEM image of the examined MLLs are also presented in Fig. 3.2. The devices were designed to operate with a sub-40 GHz repetition rate. The waveguide widths, d, of 2.5 μm and 2.0 μm were selected based on the trade-off between single-mode operation and low propagation losses in the 5-QW and 3-QW devices, respectively. The

absorber section was placed next to one of the facets and the electrical isolation between the gain and the SA sections was realised by a 10 μm wide gap, g, between the p-type metal contacts. The fabrication was performed by the author's colleagues, Lianping Hou and Gabor Mezosi, and details of this can be found in [54, 62, 82, 83].

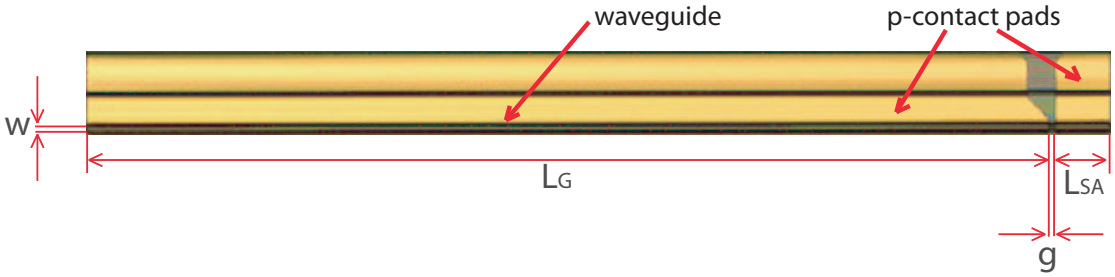

FIGURE 3.1: Layout of the mode-locking devices used in the work. The two section device comprises of a gain section of length L_g, a saturable absorber of length L_{SA}. A gap of width g is defined between the two p-contact sections for electrical insulation.

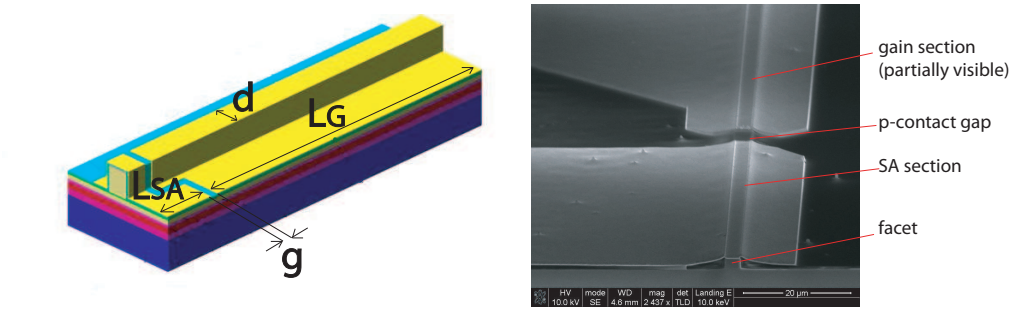

(a) (b)

FIGURE 3.2: Schematic diagram (a) and SEM image (b) of the SMLLs (courtesy of G. Mezosi).

The two-section devices fabricated on the two material structures were thoroughly characterised for a range of driving conditions. By scanning the values of gain current and SA reverse voltage applied to the lasers, several parametric contour maps were constructed. Such maps are useful tool for performing comparative studies between devices with different physical attributes. The analysis starts with two lasers fabricated in the 5-QW system, with differing SA length, L_{SA}, which constitutes 2.2 % and 3.1 % of the total cavity length. This is followed by the examination of six 3-QW lasers with the L_{SA} varying between 1 % and 6 %.

3.1.2 Experimental Set–up

The experimental set–up used to characterise the ML devices is presented in Fig. 3.3. The back side temperature of the laser sub-mount is controlled using a Peltier cell and set

to a constant temperature of 20°C. The light emitted from the facet at the gain section side is coupled into an AR-coated lensed fibre, mounted on a high resolution 5-axis micro-positioner and connected to a fibre pigtailed isolator. The optical signal is simultaneously distributed with fused fibre splitters into the intensity autocorrelator, the OSA and the RF analyser, (45 %, 10 % and 45 % of the total power, respectively). The electrical signal of the photodiode (45 GHz bandwidth) is amplified by a 50 GHz bandwidth RF amplifier. Before being coupled into the autocorrelator, the optical signal is amplified using an erbium-doped fibre amplifier (EDFA) and its polarisation is adjusted. Low dispersion (less than 35 fs/nm) of the EDFA ensures negligible pulse distortion of the amplification stage. The IAC measurements are performed with the background-free intensity autocorrelator (Femtochrome FR-130XL) [84], containing a PMT that records the intensity of the signal generated in the SHG crystal. The output power emitted from the opposite facet (SA side) is monitored with an InGaAs photodiode. All the devices driving the lasers, as well as the measurement apparatus, are remotely controlled with a PC, allowing for automatic and simultaneous acquisition of the recorded parameters. It should be noted at this stage that although the results presented in this Chapter were obtained with the lensed fibre coupled to the laser mirror located at the gain section side, the same results were recorded by measuring the light emitted from the SA-side facet, with no discrepancies observed between the two sides.

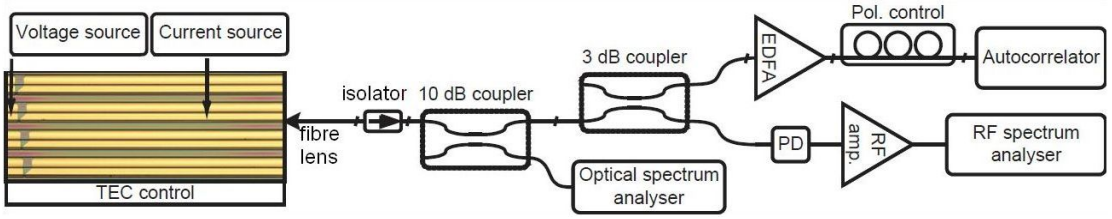

FIGURE 3.3: Schematic of the experimental setup for testing the SMLLs.

3.1.3 Monitored Parameters

The assessment of the properties of the investigated devices, with a particular focus on the ML region, is based on several monitored parameters. The recorded IAC, OSA and RF spectra were post-processed with Matlab and the following device properties were extracted:

1. SHG intensity autocorrelation:
    - FWHM of the autocorrelation peaks,
    - peak intensity of the traces.

2. Optical spectra:
   - peak wavelength,
   - FWHM,
   - modulation depth between the longitudinal modes.
3. Time-bandwidth product between the optical spectrum and intensity autocorrelation FWHM values.
4. RF spectra around the fundamental repetition rate:
   - peak frequency,
   - peak amplitude,
   - 10 dB width of the peak,
   - rms jitter
5. RF spectra at low frequencies (typically below 5 GHz):
   - peak frequency,
   - peak amplitude.
6. Output power.

Additionally, the following properties of the 3-QW devices were analysed:

- shape of the IAC traces,
- average photocurrent induced in the saturable absorber,
- peak power of the pulses.

The experimental results concerning the pulse profiles and the phase characteristics will be the subject of a detailed analysis and will be presented separately in Chapter 6.

3.2 5-Quantum Well Devices

3.2.1 Operating Regimes

The analysis of the autocorrelation traces, RF spectra, and optical spectra of the tested devices indicates a presence of several dynamical regimes, which, depending on the biasing conditions, dominate the emission or coexist with the other dynamics. For

instance, the main dynamical regimes encountered in the 3.1 % SA device are summarised in Fig. 3.4, which presents the optical and RF spectra as well as the IAC traces plotted for a constant V_{SA}=-2.6 V and several values of the gain current, scanned from threshold (I_{th}) up to 4·I_{th}.

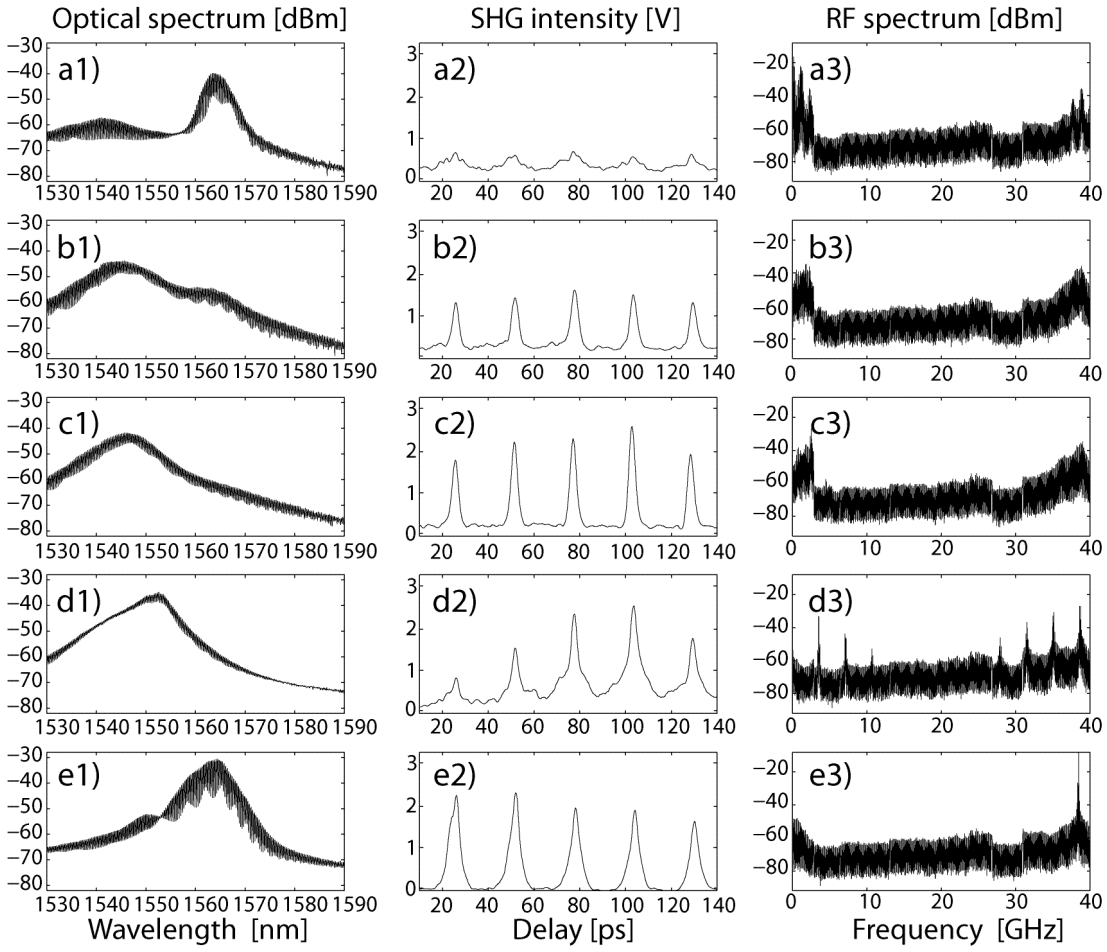

FIGURE 3.4: From left to right: optical spectra, IAC traces and RF spectra measured at various biasing conditions in the 3.1 % SA MLL. Rows a), b), c), d), e) correspond I_g of 42 mA, 52 mA, 56 mA, 80 mA and 118 mA, respectively. Saturable absorber is kept at a constant reverse voltage of V_{SA}=-2.6 V.

Close to the threshold (Fig. 3.4(a)), the IAC does not have any structure, and the RF spectrum displays a broad peak at the round-trip frequency, accompanied by broad and intense low-frequency noise. The OS indicates multimode operation around 1565 nm, which is close to the SA band-edge, although a second, wide and weak spectral component, blue-shifted by 20 nm with respect to the main peak is also evident. As the Ig is increased, this component begins to dominate the OS, the low-frequency components in the RF spectrum weakens, the repetition frequency RF peak broadens and the IAC trace begins to display shallow peaks, as presented in Fig. 3.4(b). Further increase of the gain current – Fig. 3.4(c) – results in the disappearance of the original optical component and lasing takes place solely in the blue-shifted region. This wavelength change

has a significant effect on the IAC trace, where much clearer and stronger pulses are observed. However, the persistence of the background signal between the pulses indicates incomplete ML operation, which is accompanied by SP, clearly visible in the RF spectrum around 2 GHz. With stronger pumping, as displayed in Fig. 3.4(d), the SP begins to prevail over the ML. The OS becomes wider, while its modulation depth decreases. Both the amplitude and the peak frequency from the SP contribution increase, which can also be identified in the IAC trace by the broad envelope superimposed on the ML pulses. At even higher gain current values the ML settles in, as presented in Fig. 3.4(e). The most striking feature of the ML at these gain current levels is that the central wavelength experiences a large red-shift by ∼20 nm, and lasing occurs around the original wavelength (except for the unavoidable red-shift due to Joule heating). The OS displays almost no trace of the blue-shifted component and the RF spectrum is free of any SP features.

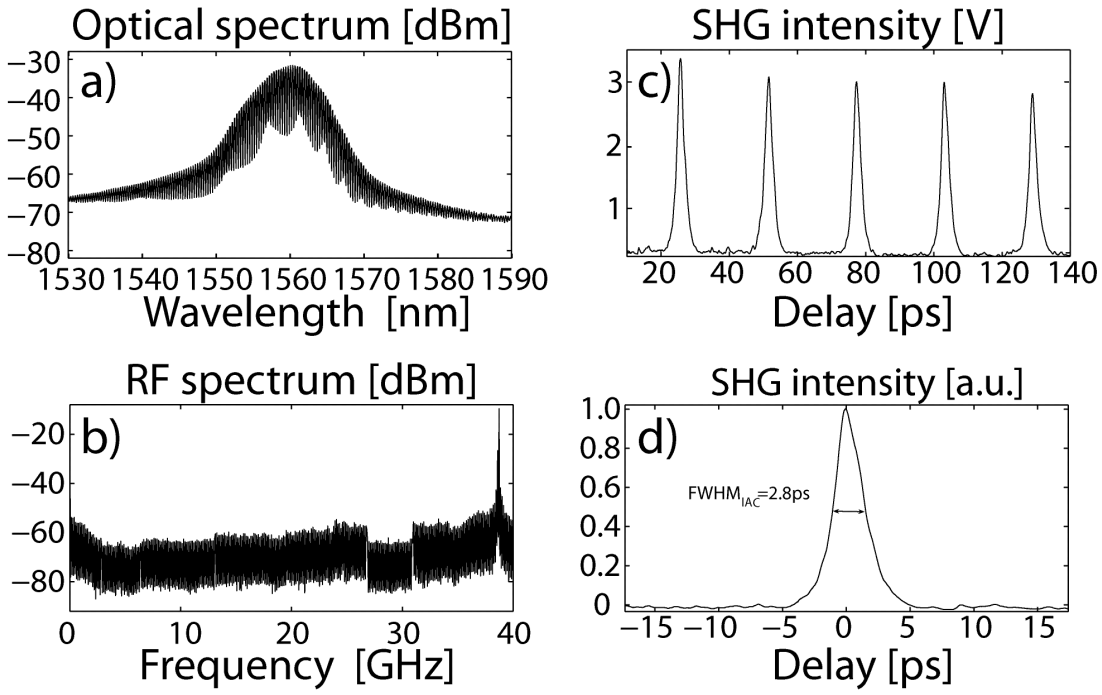

FIGURE 3.5: Optical, RF and IAC characteristics measured in the optimum ML range of the 5–QW SMLL with a 3.1 % SA. I_g=100 mA and V_{SA}=-3.2 V.

For comparison, the RF and optical spectrum, as well as the IAC traces from the optimum mode-locking region are shown in Fig. 3.5. At I_g=100 mA and V_{SA}=-3.2 V the emission is characterised by an almost symmetrical OS with a comb modulation of 12 dB, concentrated around 1560 nm, and with no evidence of a blue-shifted component. The IAC trace displays high intensity and pedestal-free peaks with an average FWHM of 2.8 ps. The RF spectrum confirms pure ML operation, as neither SP nor noise components are evident in the low frequency range.

The following sections will present a detailed analysis of all the monitored parameters performed within a wide range of the device biasing conditions. Also, the operating points presented in Fig. 3.4 and Fig. 3.5 will be identified on the parametric maps.

3.2.2 SHG Intensity Autocorrelation Measurements

The temporal width of an optical pulse can be estimated from second order IAC measurements. However, in order to determine the FWHM from an autocorrelation envelope, a specific pulse shape needs to be assumed. In fact, depending on the expected pulse profile, the deconvolution factor from the IAC width can take different values. The pulse shape that is usually used for fitting the experimental traces of pulses emitted from passive SMLLs is a sech^2 profile [85], for which the deconvolution factor is equal to 0.65. The sech^2 pulse shape is a solution to the Master equation usually used in analytical mode-locking theory [86], [87]. However, large deconvolution errors can occur when processing optical pulses with complex or non-symmetric intensity structures. Hence, only the non-deconvolved FWHM values of IAC traces will be presented in this Section. An example of the IAC pulse train is displayed in Fig. 3.6, with FWHM of the autocorrelation peak equal to 2.7 ps (temporal width of 1.75 ps with the sech^2 shape assumed). From the peak separation the repetition rate of the MLL can be deduced. In the trace of Fig. 3.6, the spacing of 25.78 ps corresponds to a pulse repetition frequency of 38.8 GHz.

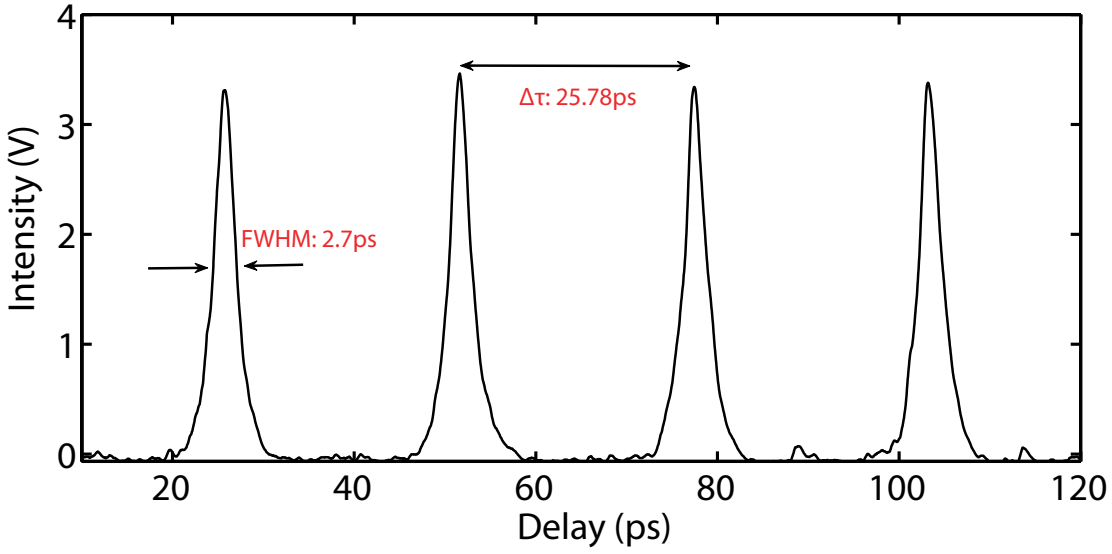

FIGURE 3.6: Example of the intensity autocorrelation trace measured on a 5-QW SMML with a 3.1 % SA (I_g=92 mA, V_{SA}=-3.2 V).

For both the 5-QW devices, i.e. with the 2.2 % and 3.1 % SA, IAC traces were recorded for a range of the SA reverse voltage gain section current. The parametric maps of

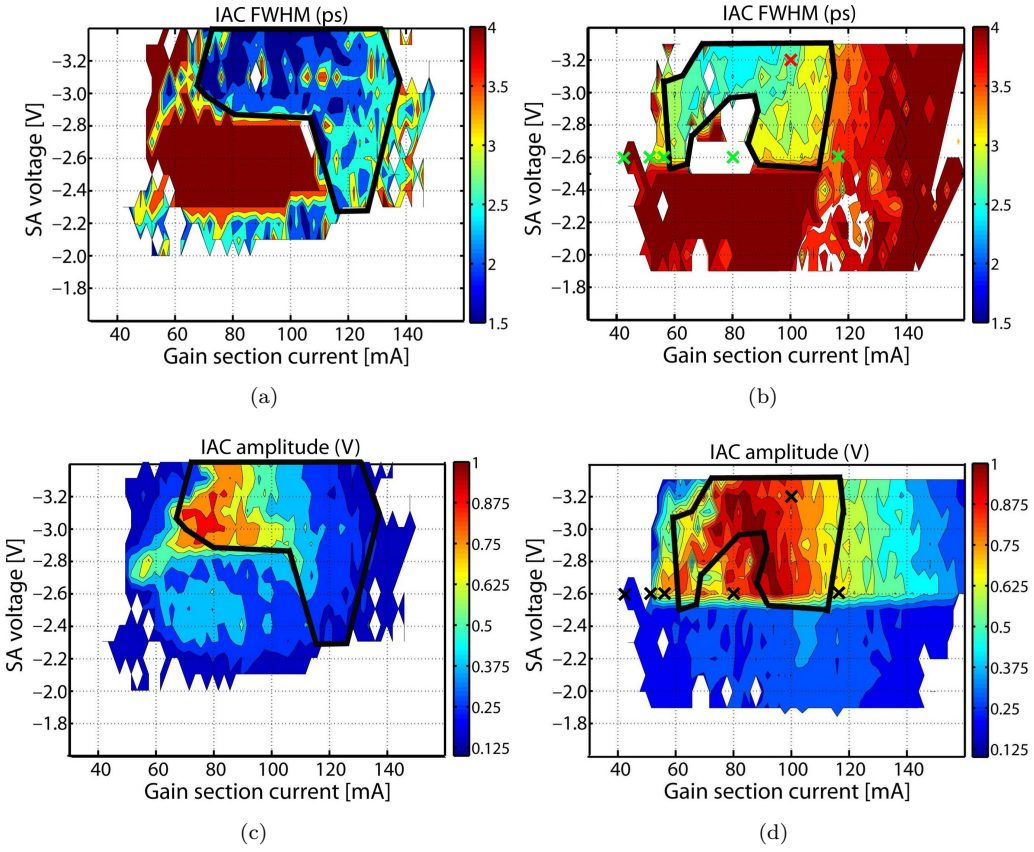

FIGURE 3.7: Parametric maps of the (a, b) IAC FWHM values and (c, d) the average amplitude (V) of IAC peaks measured on the (a, c) 5–QW SMLLs with 2.2 % SA (left column) and (b, d) 3.1 % SA (right column). The cross symbols identify the operating points presented in Section 3.2.1.

the autocorrelation FWHM values registered at each biasing point are presented in Fig. 3.7(a) – 3.7(b). The black contour lines encompass the biasing regions for which the autocorrelation width values stay below 3 ps. For easier comparison between various monitored parameters, these lines will be plotted in other parametric maps characterising the devices. To reject incomplete ML or noise present in the autocorrelation traces, a lower limit of 0.125 V and an upper threshold of 4 ps were applied to the normalised autocorrelation intensity and the autocorrelation width, respectively. It can be seen that the precursors of ML are already apparent around a SA reverse voltage of 2 V. At this voltage level the absorber recovery time is well below the cavity round-trip time [88], which allows for full recovery of the absorber between consecutive pulses. Pulses with the narrowest IAC traces were measured for a reverse voltage larger than 3 V, with widths as narrow as 1.5 ps, on the 2.2 % SA device. The device with shorter absorber emits much shorter pulses, which suggests that the conditions for optimum mode-locking are better satisfied for this SA length. Shorter absorber is probably easier saturated by the pulses traveling in the cavity and, hence, have a stronger influence on the pulse

shaping mechanism. Also, the decreased average losses in the absorber allow for higher optical intensities in the cavity and stronger modulation of the gain. The SA reverse voltage used in the experiments was kept above -3.4 V, as a stronger biasing resulted in deteriorated ML and induced excessive photocurrent values, which dramatically reduce the lifetime of the absorber. The regions of optimum ML expand from I_g=70 mA to I_g=130 mA for the device with the shorter absorber, and from I_g=60 mA to I_g=115 mA for the longer absorber. Above 115 mA the pulses deteriorate, as they gradually increase in width and reach 4 ps at around I_g=140 mA. This temporal pulse broadening is caused by the SPM and unstable mode-locking, triggered by the SA over-bleaching due to excessive power [89].

Another characteristic feature present in Fig. 3.7(a)-3.7(b) is a region of wide pulses in the bottom left part of the ML region. In this region the dynamical behaviour is dominated by self-pulsation operation. This is a strong detrimental effect in passive SMLLs, which is triggered by the carrier density fluctuations causing periodic modulation of the pulse train at frequencies typically below 10 GHz [90]. A similar behaviour was already described in [16], where the SP occurred at low gain currents and gradually gave way to ML at higher pumping levels. Also, the SA biasing has a substantial impact on the laser stability through the absorber recovery time, τ_{abs}. Larger SPs are induced by shorter τ_{abs} and a stronger absorber saturation as compared to the gain recovery time and gain saturation level, which coincides with the conditions for ML triggering [15], [91]. Furthermore, mode-locking requires the net gain modulation to be in phase with the photon density modulation and to lag behind the loss modulation, which also implies high probability of SP [17]. Consequently, the ML operation imposes specific requirements on the differential gain and effective lifetimes in the gain and absorber sections, as well as on the spontaneous emission lifetime, average photon density, and steady-state gain and absorption values. In order to avoid SP, a large intra-cavity photon density and a low threshold gain needs to be created. Photon density can be increased for instance by biasing the gain section with high currents, while the second requirement needs to be taken into consideration at the early stages of the material and device geometry design.

A second feature defining the ML quality is the amplitude of the autocorrelation pulses. Basically, the optimum ML, with narrow pulses and low noise levels would produce autocorrelation traces with high peak-to-pedestal ratios and high peak intensities. Fig. 3.7(c)-3.7(d) present the contour maps displaying the mean peak intensity values of six consecutive autocorrelation pulses measured on the 5-QW devices. The maps reveal that the vast majority of the regions inside the 3 ps-lines correspond to relatively low peak amplitudes. Above the gain current of 115 mA the autocorrelation peaks barely exceed the intensity threshold. For both the devices the amplitude changes as a function of the gain current and is not significantly affected by the SA bias. The intensities of IAC

peaks reach the highest values in the ML region adjacent to the SP region. This confirms that an excessive gain pumping results in deteriorated ML, which was already apparent from the FWHM maps, and that self-pulsation promotes the intensity of the measured autocorrelation signal.

3.2.3 Optical Spectrum Measurements

The stability of the mode-locking as well as a prediction of the minimum achievable optical pulse width can be deduced from the optical spectrum. Combined with the IAC, it is a useful tool for the estimation of the pulse chirp. An example of an optical spectrum under ML operation is presented in Fig. 3.8. An ideal pulse with a sech^2-shaped temporal intensity would also produce a frequency domain spectrum with a sech^2 envelope. However, SMLLs usually produce slightly asymmetric spectra, due to the non-symmetric curvature of the gain and absorption spectra, as well as SPM in the gain section. Furthermore, the pulse shaping mechanisms of the gain section and the absorber act differently on the temporal trailing and leading edges of a pulse [92], which also has a direct effect on the spectrum. Moreover, any other substructures present in the pulse spectrum may indicate noise, SPM or further undesired effects, e.g. self-pulsation. Additionally, the height of the mode-comb can be an indicator of the ML quality, with a stronger modulation of the OS suggesting better mode-locking.

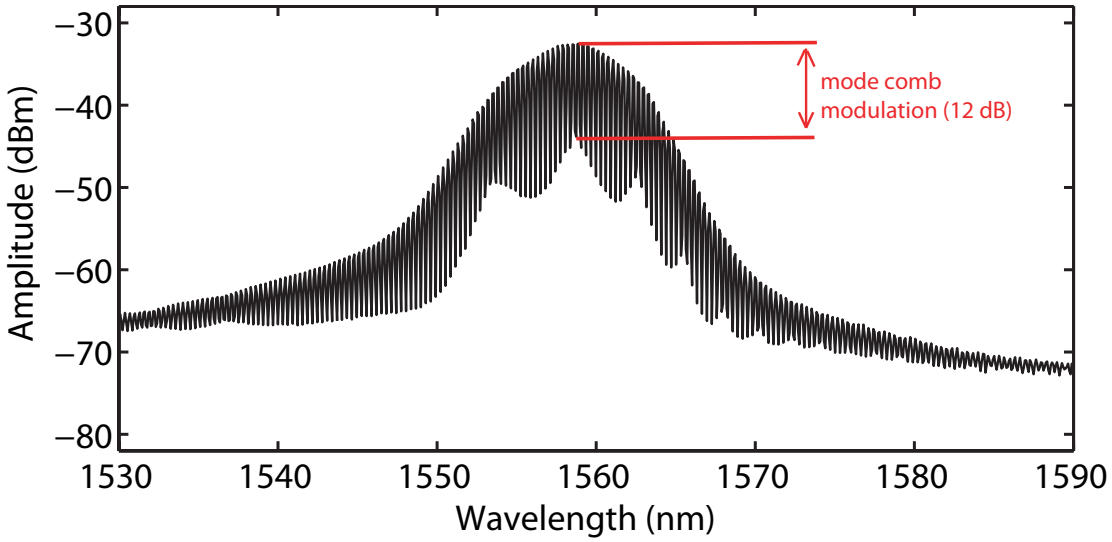

FIGURE 3.8: Example of the OS measured on the 5–QW SMML with a 3.1 % SA (I_g=92 mA, V_{SA}=-3.2 V).

The FWHM values of the optical spectra are mapped in Fig. 3.9(a) – 3.9(b). The typical widths registered in the region of the best ML range between 6 nm and 8 nm. The maximum FWHM values recorded in the experiments correspond to SP or mode-locking affected by SP, where double-peak spectra were measured. Similar to the IAC

traces, the optical spectra are more sensitive to a change in the gain section bias than in the SA voltage. The incomplete ML present at higher gain pumping levels and producing low intensity IAC is characterised by narrower spectral comb, indicating a temporal broadening of the pulses.

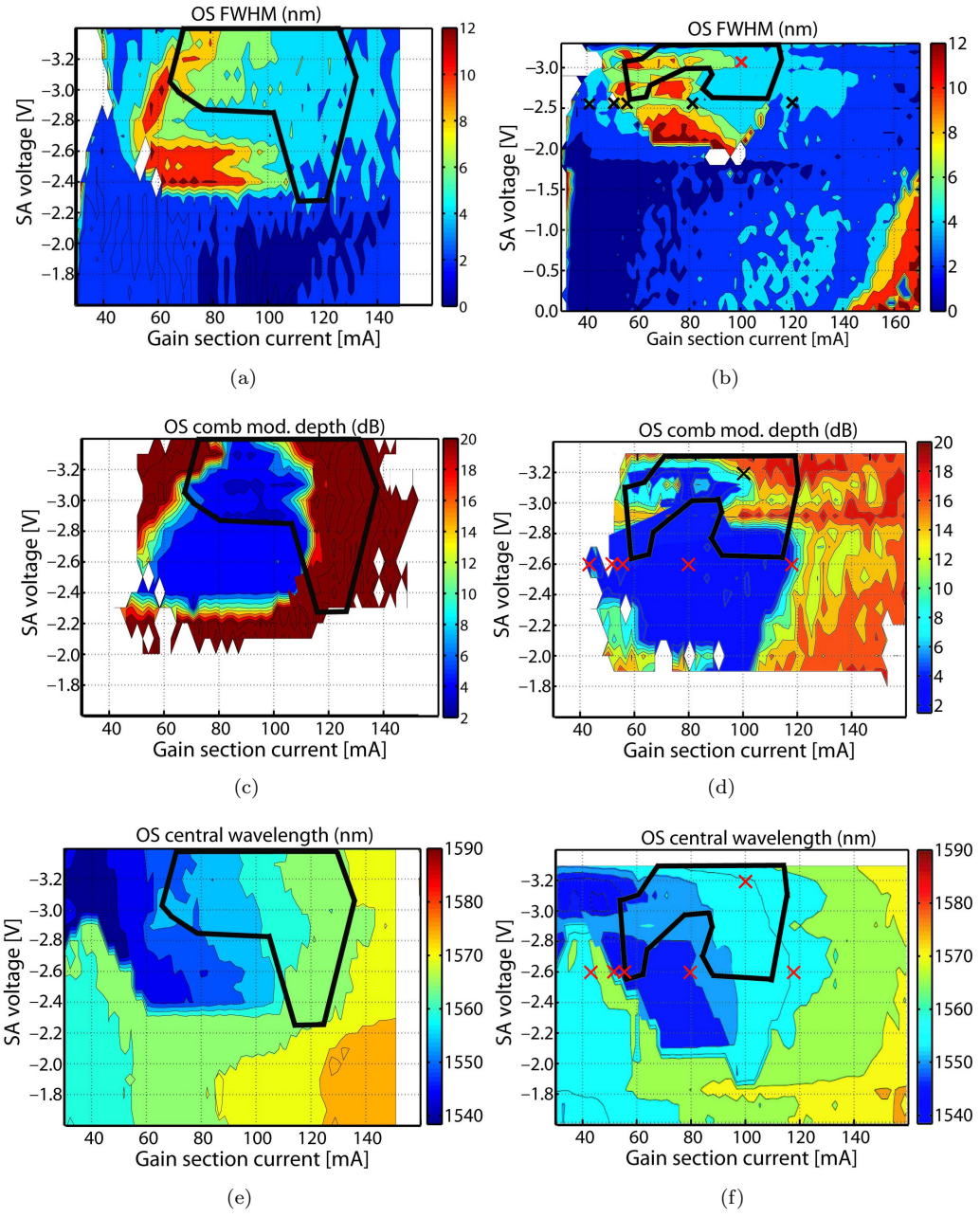

FIGURE 3.9: Parametric maps of the (a, b) FWHM (nm), (c, d) comb modulation depth (dB), and (e, f) central wavelength (nm) of the optical spectra measured on the 5–QW SMLLs with 2.2 % SA (left column) and (b) 3.1 % SA (right column).

Next, the spectra were analysed for their optical comb modulation depth. Fig. 3.9(c) – 3.9(d) display the parametric maps of the longitudinal modes modulation depth measured around the peak wavelengths. In order to minimise the error caused by the spectrum under-sampling, the resolution bandwidth of the OSA was set to 0.07 nm, corresponding to ∼5 samples taken per optical mode. However, the resolution error could not be completely avoided, the effect of which can be observed as a periodic modulation imposed on the low intensity optical spectrum envelope in Fig. 3.8. The spectra with the highest comb modulation within the contoured region occur at high gain current levels, mostly exceeding 100 mA. As already discussed, this region corresponds to temporally broad and spectrally narrow pulses. The low comb modulation present for weaker pumping is caused by self-pulsation, affecting the ML operation or even dominating it.

Finally, the spectra were analysed for their central wavelength. Results from Fig. 3.9(e) – 3.9(f) show that the optical emission in the ML region is concentrated around a wavelength of 1560 nm. When compared to the results presented in Fig. 2.7 and Fig. 2.9, the ML spectrum appears red-shifted with respect to the gain peak and centered around the SA absorption edge. Such a condition allows for deep modulation of the losses, which is a necessary requirement for the ML operation. However, when the device switches to the SP regime, a sudden jump of the peak lasing wavelength to the blue part of the spectrum can be observed. This transition between the mode-locking and self-pulsation regimes is clearly apparent in the spectral maps shown in Fig. 3.10. It can be noticed that the threshold current increases monotonously with the SA reverse voltage from I_{th}=26 mA at V_{SA}=0 V to I_{th}=41 mA at V_{SA}=-3.2 V. This increase is caused primarily by the higher losses due to stronger absorption, as was presented in Fig. 2.9. For low reverse bias, e.g. V_{SA}=-0.2 V, only a moderate red-shift following the gain peak is observed (Fig. 3.10 a). When the absorber biasing reaches $V_{SA} = -1.8$ V, SP and weak ML dynamics begin to modify the optical spectrum (Fig. 3.10 b). Further increase in the voltage triggers sudden spectral transitions, confirming a competition between the ML and SP operation (Fig. 3.10 c-d). The mode-locking at these voltage levels becomes free of SP only for gain currents exceeding 115 mA, where the pulses begin to be affected by the SPM. SA reverse voltages exceeding 3.0 V have to be applied in order to obtain SP-free pulses at relatively low I_g (Fig. 3.10 e-f). The graphs also confirm that the modulation between the comb modes are shallower in the region affected by self-pulsation.

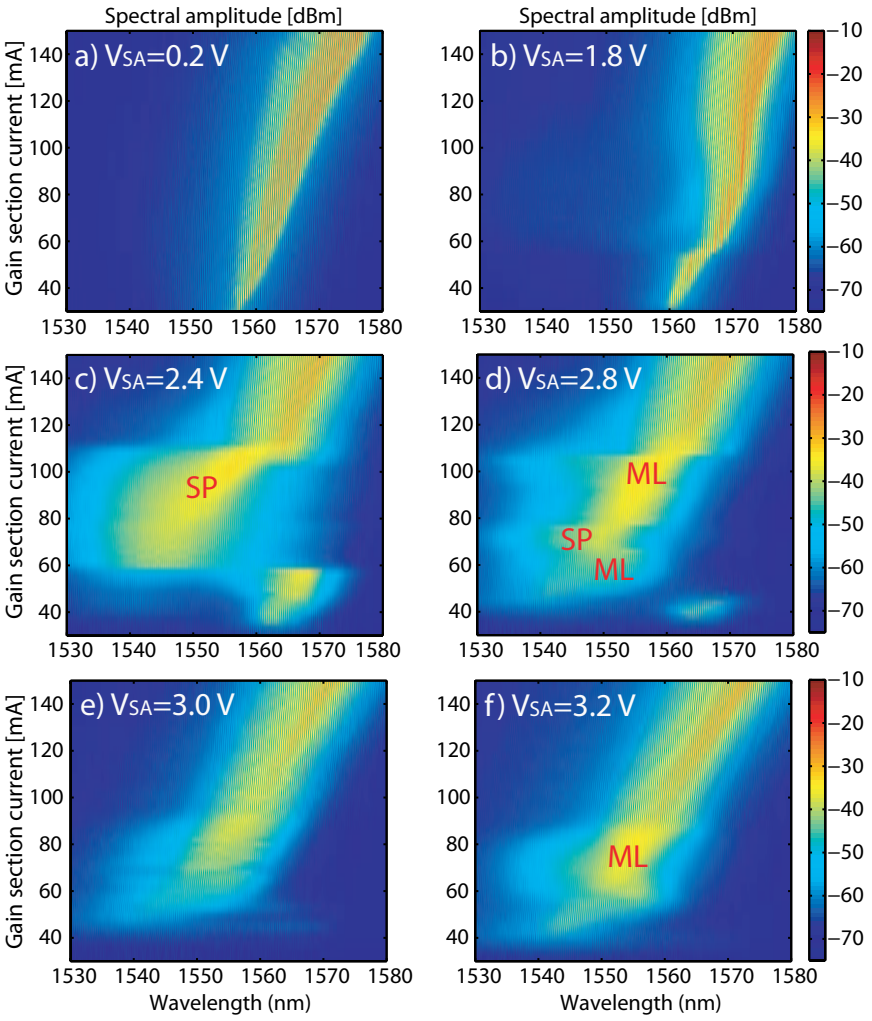

FIGURE 3.10: Spectral maps of the 5-QW SMML with a 3.1 % SA, captured at several values of the SA bias. Large central wavelength shifts can be observed as the device switches between the SP and the ML operational regimes.

3.2.4 Time-Bandwidth Product

The time-bandwidth product between the non-deconvolved widths of the IAC traces and the spectral FWHM are presented in Fig. 3.11. As was explained earlier, the non-deconvolved temporal width values are used in this analysis to avoid any assumption on the pulse shape at this stage of the characterisation. However, if a sech^2 pulse profile was used, the TBP of a transform-limited pulse would be equal to 0.315. With non-deconvolved pulses, this figure would rise to 0.485. In the case of a Gaussian pulse, these values would be 0.44 and 0.62. Clearly, none of the measured pulses reaches such low TBP levels, which proves that their phase profiles are to some extent affected by chirp or there are intensity substructures present in the temporal envelopes. From the TBP map of Fig. 3.11(a) it can be deduced that the bottom region of ML (below the SP region) on the 2.2 %-SA device produces the best quality pulses, with a TBP ∼0.7. The optical

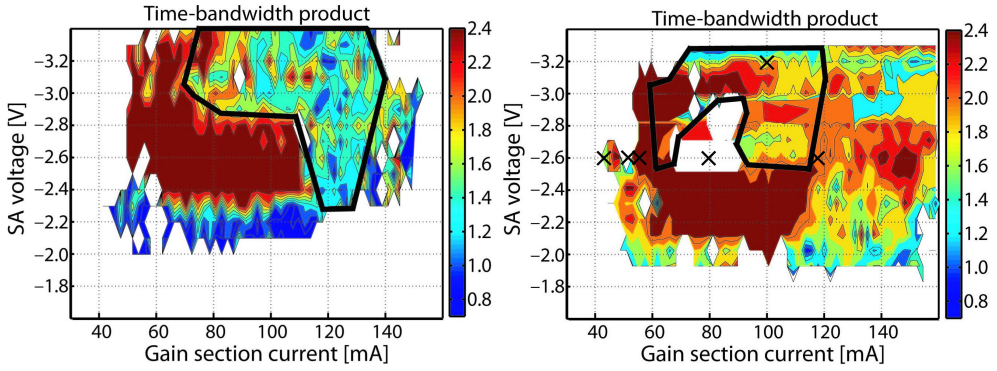

(a) (b)

FIGURE 3.11: Parametric time-bandwidth product maps measured on the 5-QW SM-LLs with (a) 2.2 % SA and (b) 3.1 % SA.

spectra of the pulses from this region are symmetric and deeply modulated. However, due to rather narrow optical spectrum envelopes (below 4 nm) these pulses are relatively broad (autocorrelation FWHM is around 2.5 ps). Therefore, low peak intensity values, and consequently, low autocorrelation signal levels are typical for this ML region. Mode-locking with shorter pulses was recorded above V_{SA}=-3.1 V and I_g ≈100 mA, with IAC widths as low as 1.5 ps, spectral FWHM of 6 nm and TBPs of ≈1.2. For the device with a longer SA, the region of the shortest pulses is concentrated around I_g=80 mA and V_{SA}=-3.2 V. The high value of TBP (≈1.2) of this region suggests considerable amount of chirp accumulated by pulses or incomplete phase locking between the laser modes. The best ML pulses in terms of all the performance indicators analysed so far are recorded around V_{SA}=-2.9 V and I_g=100 mA, with TBP below 1.0, autocorrelation FWHM of 2.8 ps, relatively high IAC intensity (over 3.0 V), deep frequency comb modulation (16 dB), and SP-free operation.

3.2.5 Radio Frequency Measurements

The RF spectrum of a mode-locking device not only delivers information about the stability of the pulse train, but also helps in assessing the quality of ML by providing evidence of possible noise or low frequency pulsation in the emitted signal. Hence, these spectral regions were studied and will be discussed in this section. The maps of the RF amplitude at the cavity round trip frequency for both devices are presented in Fig. 3.12(a) – 3.12(b). It is clear from both graphs that there is a direct relation between self-pulsation and RF peak amplitudes, as these increase with the gain current and weaken in the vicinity of a SP region. For the 2.2 % SA device the highest peaks are observed near the bottom limit of the ML region (i.e. in the region already discussed in Section 3.2.4), and on the high gain current side, outside the optimum ML region. In the

region which gives the best ML pulses, centered around V_{SA}=-3.2 V and I_g=100 mA, the RF peaks reach an amplitude of -35 dBm, i.e. ∼30 dB above the floor level. Similarly, for the device with a longer SA, the highest RF peak values are concentrated on the high gain current side of the ML region (and also well above it).

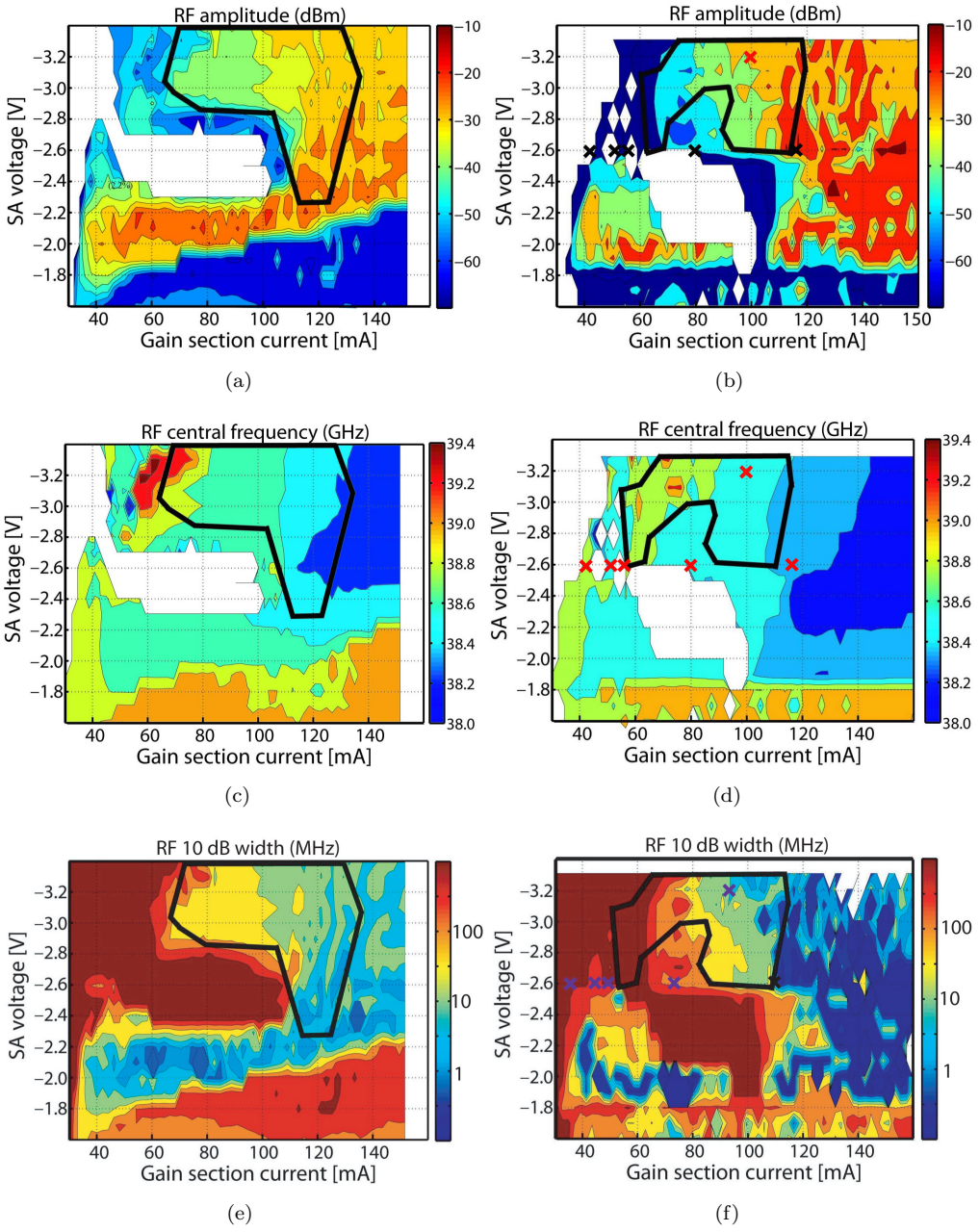

FIGURE 3.12: Parametric maps of the (a, b) the amplitude (dBm), (c, d) central frequency (GHz), and (e, f) 10 dB width (MHz) of the fundamental RF peak, measured on the 5–QW SMLLs with 2.2 % SA (left column) and (b) 3.1 % SA (right column).

Under the optimum mode-locking conditions both devices exhibit stable repetition rate at 38.8 GHz that increases monotonically with the gain current and is barely sensitive to the absorber bias (Fig. 3.12(c) – 3.12(d)). The repetition frequency increase is caused by

the plasma effects, which produces a negative group refractive index change. A detailed analysis of the influence of the driving conditions on the SMLLs fundamental repetition frequency will be presented in Section 3.3.4

Another significant parameter for the ML assessment is the linewidth of the RF peak. Fig. 3.12(e) – 3.12(f) present the 10 dB width of the fundamental frequency peaks. Both devices are characterised by a similar RF 10 dB-linewidth value, which in the optimum ML ranges remains between 1 MHz and 30 MHz. Much lower values, down to 100 kHz, are recorded outside the ML region, towards the high gain pumping side, where the multimode dynamics generates high-intensity and narrow-linewidth RF peaks. Further discussion of the RF-linewidth evolution with driving parameters and operational regimes will be presented in Section 3.3.4.

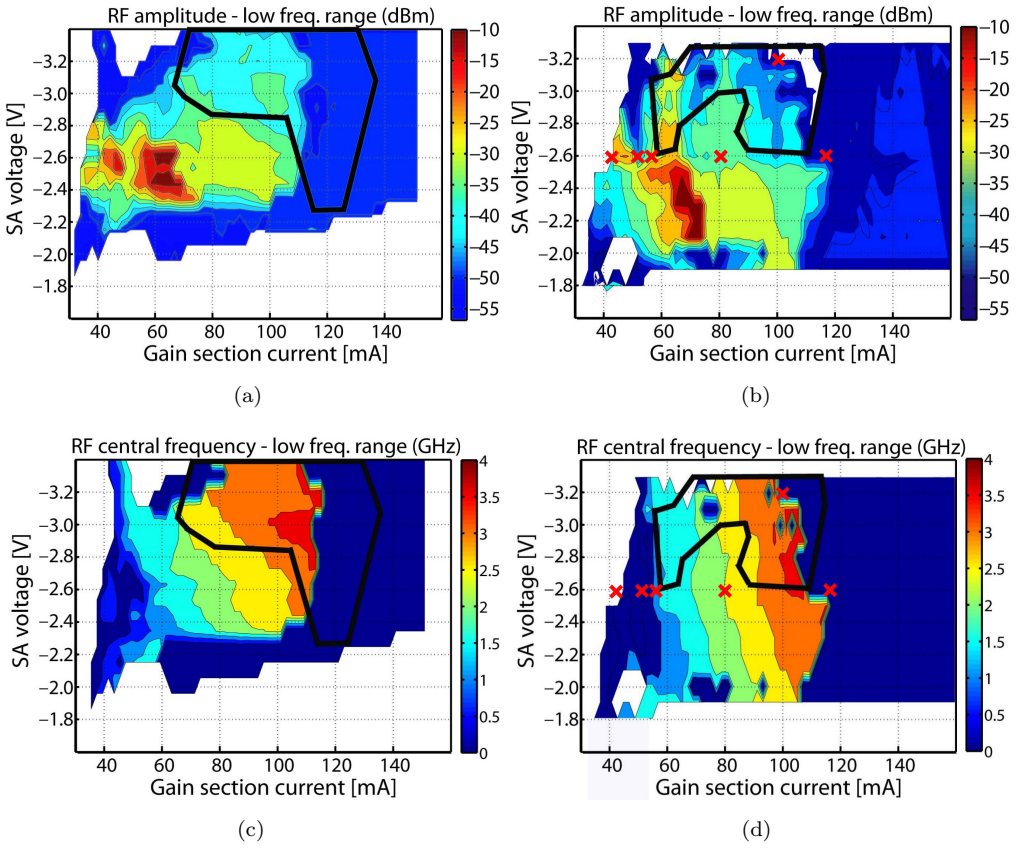

FIGURE 3.13: Parametric maps of the (a, b) amplitude (dBm) and (c, d) peak frequency (GHz) of the low frequency components, measured on the 5–QW SMLLs with (a, c) 2.2 % SA and (b, d) 3.1 % SA.

Finally, the RF spectrum from 0 GHz to 5 GHz is analysed. The main contributors to the RF signal in this frequency region are the SP and the low-frequency noise. Fig. 3.13 plots a distribution of the intensity and peak frequency of these spectral components. The regions with the highest low-frequency signal concentrate on the bottom left side

of the ML region. It can be clearly seen that there is a correlation between the presence of low-frequency peaks and self-pulsation, as the two regions overlap. The graphs also confirm the previous observations of a significant presence of SP even in the mode-locking region, which only reduces as the gain current is increased. The peak frequency depends mainly on the gain section current and it shifts from ∼0 GHz at threshold up to 3.5 GHz close to the high I_g edge of the SP region.

3.2.6 Jitter Measurements

Applications such as all-optical clock recovery and optical sampling systems, usually impose tight tolerances on the timing jitter parameters. Timing jitter is a statistical measure of a noisy signal and provides information about the deviation of the pulse-to-pulse arrival time in a pulse train. The mode-locked laser can be treated as a free-running noisy oscillator with oscillation concentrated around a mean value, τ_{avg}, and a Gaussian distribution characterised by a standard deviation, σ_c, called cycle-to-cycle jitter or rms cycle jitter [93]. The noise sources can be interpreted as the local oscillators operating around $1/\tau_{avg}$, which give rise to sidebands in the frequency domain signal, visualised as a phase-noise noise spectrum. The magnitude of the rms jitter is proportional to the square-root of the integrated power of the phase-noise sideband [94]. The integration limits in the frequency domain correspond to the measurement time in the time domain, hence the rms jitter can be interpreted as a standard deviation of the pulse arrival time recorded, with time integrals ranging between the reciprocals of the phase-noise integration limits.

The jitter performance of the investigated passively-running 2.2 % SA SMLL was tested within a range of typical biasing parameters. A Rohde & Schwarz FSV40 electrical signal analyser with a built-in phase noise utility, and a 40 GHz bandwidth photodiode were used to measure the single-sideband (SSB) phase noise on the quasi–40 GHz carrier. The measurements automatised with a LabView software were performed within the frequency range 10 kHz – 1 GHz, and next the rms jitter was calculated according to the ITU-T specified range for 40 GHz sources (20 kHz – 320 MHz). The measurement range exceeded the integration limits due to the fixed frequency ranges available in the phase-noise utility of the signal analyser. The rms timing jitter, σ_T, computed within the frequency limits f_u and f_d, is a function of the SSB curve, $S_{\phi_{RF}}$, as shown in Eq. 3.1 [95]:

$$\sigma_T(f_u, f_d) = \frac{T_R}{2\pi}\sqrt{\int_{f_d}^{f_u} S_{\phi_{RF}}(f)df}, \tag{3.1}$$

where T_R is a period of the pulse train.

Fig. 3.14(a) plots an example of the SSB characteristics measured at four different biasing points within the ML region. The rms jitter calculated from Eq. 3.1 with a lower frequency offset integration limit of 20 kHz is displayed in Fig. 3.14(b). Fig. 3.15 shows a distribution of the jitter values across the ML region. The typical levels are between 4 ps and 7 ps, and the lowest jitter values are concentrated at the lower boundary of the ML region as well as close to the low-I_g over the $V_{SA} \sim -3.0\,V$.

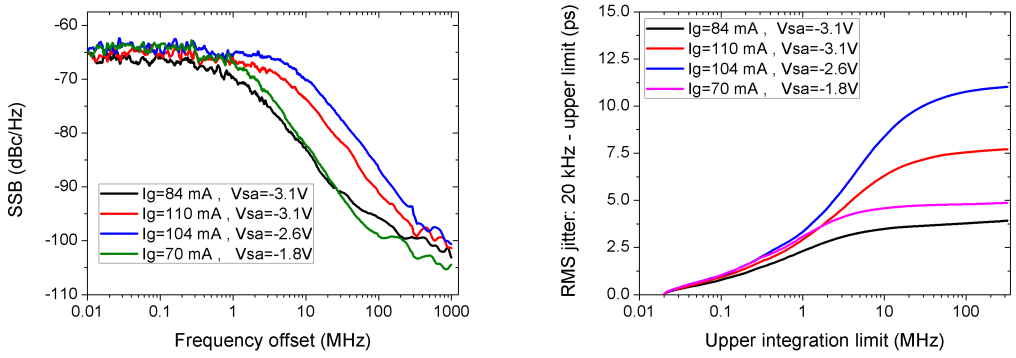

(a) (b)

FIGURE 3.14: (a) SSB phase noise spectra for various biasing conditions within the optimum ML region and (b) corresponding integrated rms jitter characteristics as a function of the upper integration limit, measured on the 5–QW SMLL with a 2.2 % SA.

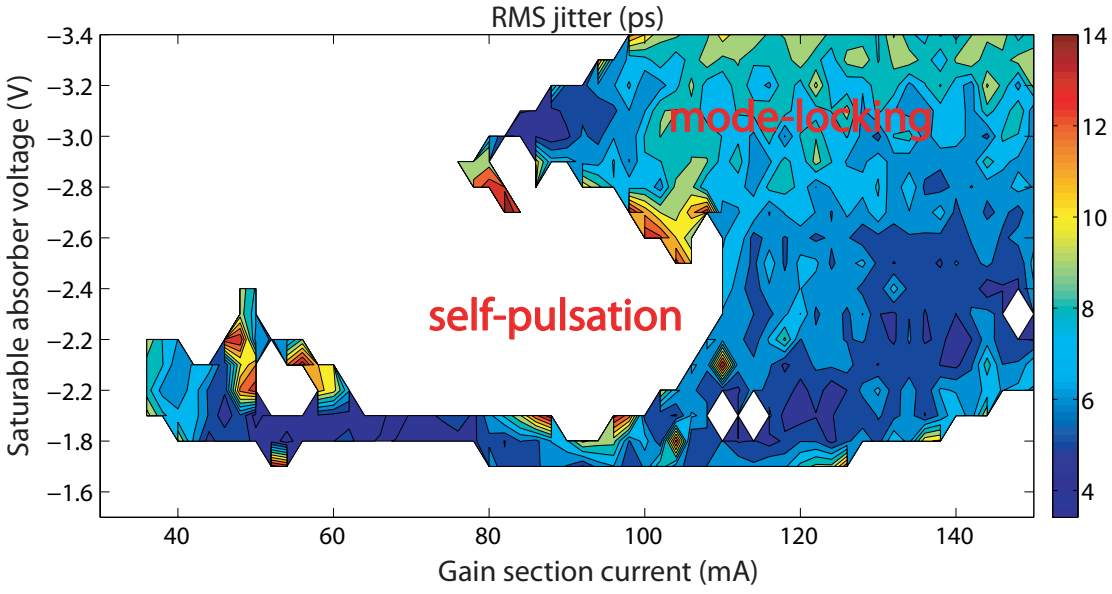

FIGURE 3.15: Parametric map of the rms jitter (ps) integrated in the frequency offset range of 20 kHz – 320 MHz, measured on a the 5–QW SMLL with a 2.2 % SA.

3.2.7 L-I Characteristics

In addition to the measurements described so far, the output intensity vs. gain current (L-I) characteristics were also measured for a range of SA bias values. The laser light was coupled directly to a broad area photodetector. A direct consequence of applying a reverse voltage to the absorber is an increase in the threshold current, as plotted in Fig. 3.16(a). With no voltage applied, i.e. V_{SA}=0 V, the threshold current is equal to 26 mA. Up to V_{SA}=-1.4 V the threshold only rises to 29 mA. However, higher voltage values trigger much larger changes in the absorption, and I_{th} grows more rapidly for V_{SA} exceeding -2 V, reaching 43 mA at V_{SA}=-3.0 V. Interestingly, above that value (V_{SA}=-3.2 V) the threshold current does not increase any more and even drops slightly. This behaviour can be explained by the spectral detuning between the bandgap of the saturable absorber and the gain section. Initially, the strongly blue-detuned SA is virtually transparent to the light and the threshold wavelength occurs close to the gain peak. The SA bandedge shifts towards longer wavelengths with increasing V_{SA}, which forces the threshold lasing to the red side of the gain peak (Fig. 3.10), consequently increasing the threshold current. However, at the highest absorber biasing levels, the lasing operation is again initiated at the gain peak, in order to overcome high losses caused by the close vicinity of the absorber bandedge, and the lasing threshold can be reached at a slightly lower gain section current [50].

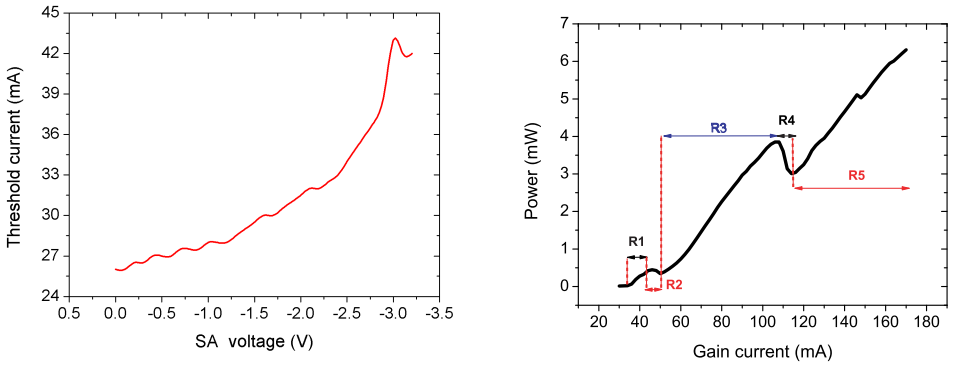

(a) (b)

FIGURE 3.16: (a) Development of the threshold current values with increasing SA voltage in the 3.1 % SA 5–QW SMLL, and (b) L-I characteristic at V_{SA}=-2.6 V.

The spectral instabilities described in Section 3.2.1, associated with different dynamical regimes present in the devices also have an impact on the L-I characteristics. For instance, Fig. 3.16 presents the L-I curve measured on the 3.1 % SA device biased at V_{SA}=-2.6 V. The development of laser dynamics at that V_{SA} level was already discussed in detail and shown in Fig. 3.4. Just above threshold the device operates with a single

spectral component (range R1 in Fig. 3.16) concentrated around 1565 nm. When the second, blue-shifted component appears (R2), the output power stagnates. Next, the emission is dominated by the SP (R3) with only weak ML pulses, and is spectrally centered around 1545 nm. The output power increases monotonically, until the transient region between the dynamic regimes (R4), where it suddenly drops until the ML operation takes over (R5). Here, the output power once more increases with I_g. However the curve is down-shifted with respect to the R3 range, due to higher losses in the ML regime, which is now centered closer to the absorber band-edge.

3.2.8 Summary of the 5-QW Devices

The performance of two SMLLs fabricated on the 5-QW laser material and operating with a repetition rate at around 39 GHz has been presented. The devices differ from each other in the length of the SA section, which were 25 μm and 35 μm (2.2 % and 3.1 % of the total cavity length, respectively). The lasers were tested for a wide range of external biasing conditions, and several mode-locking indicators were registered and compared. Both devices were influenced by self-pulsation, which affect their operation for absorber reverse bias values typically above -3.0 V and for gain currents ranging from threshold to 100 mA. On both MLLs, the SP decayed with stronger gain pumping. The device with a shorter SA exhibits a larger region of pure ML performance and also emits shorter pulses (autocorrelation FWHM as narrow as 1.5 ps). The narrowest pulses are obtained with the absorber reverse voltages exceeding 3.0 V, although, the higher reverse bias ($\geq$3.4 V) induces excessive photocurrent in the absorber section, which usually causes its failure. The pulses from the optimum ML region produce optical spectra with the 3 dB widths between 6 nm and 8 nm and the comb modulation of $\sim$12 dB. Spectral competition between the SP and ML is observed in the form of abrupt jumps of the emission wavelengths. These instabilities are particularly evident at relatively low V_{SA} levels and disappear with stronger SA biasing. The value of the rms timing jitter in the optimum ML biasing region of the 2.2 % SA laser stays around a level of 4 ps in the frequency offset range of 20 kHz – 320 MHz. The typical average power emitted from a single facet is between 2–6 mW, and is strongly dependent on the SA section bias.

3.3 3-Quantum Well Devices

As previously mentioned, the 3-QW devices were analysed more extensively than the 5-QW devices, with special attention paid to the dynamical behaviour as a function of the SA. It will be shown that this geometrical parameter plays an important role in the SMLLs operation, as it influences key properties of the devices, such as the gain and absorption saturation levels. The characterisation has been performed on six devices with the SA length changing from 1 % to 6 % of the total cavity length. For a more straightforward comparison between the devices, most of the maps displaying a particular parameter are plotted within the same gain current and SA voltage ranges and with an identical colour scale. The only exception is the device with a 6 % SA, which needs to be driven at higher I_g and V_{SA} in order to obtain the ML operation. The analysis begins with the time-domain measurements where the FWHM, intensity, and autocorrelation envelope shapes are studied. The sets of measurements are similar to what was presented for the 5-QW devices, as these provide a detailed and complete characterisation of the dynamical operation of the MLLs.

3.3.1 SHG Intensity Autocorrelation Measurements

Fig 3.17 displays the evolution of the autocorrelation FWHM for different absorber lengths. The black contour line in the graphs surrounds the regions in which the FWHM is below the value of 1.4 ps. The displayed mode-locking domains were restricted by a maximum FWHM value of 2.5 ps. The most striking feature apparent in Fig 3.17 is the expansion of the ML regions with increasing SA length. The most significant growth can be observed between the devices with SA=1 % and SA=2 %, where the region delimited by the contour line expands several times. The widths of the autocorrelation traces at low voltage levels are close to the limit of 2.5 ps, due to the relatively long recovery time of the absorber. Another feature characterising the evolution of the optimum ML regions with the SA length is that they tilt from an almost vertical orientation across the biasing region (e.g. 2 %-SA device) into a more horizontal one. Again, this feature stems from the higher losses induced by longer SAs, which requires higher gain pumping to sufficiently saturate the absorbers.

The autocorrelation traces peak amplitudes are illustrated in the same ML region as in Fig. 3.18. The region with the most intense peaks constantly shifts towards higher gain section pumping levels, but the general trend stays the same. The highest signals are registered at the low gain current edges of the ML regions, which are concentrated around a SA reverse bias in the range of 2–2.5 V. An interesting feature that is apparent from Fig. 3.18 is that the highest amplitudes of the autocorrelation peaks increase gradually

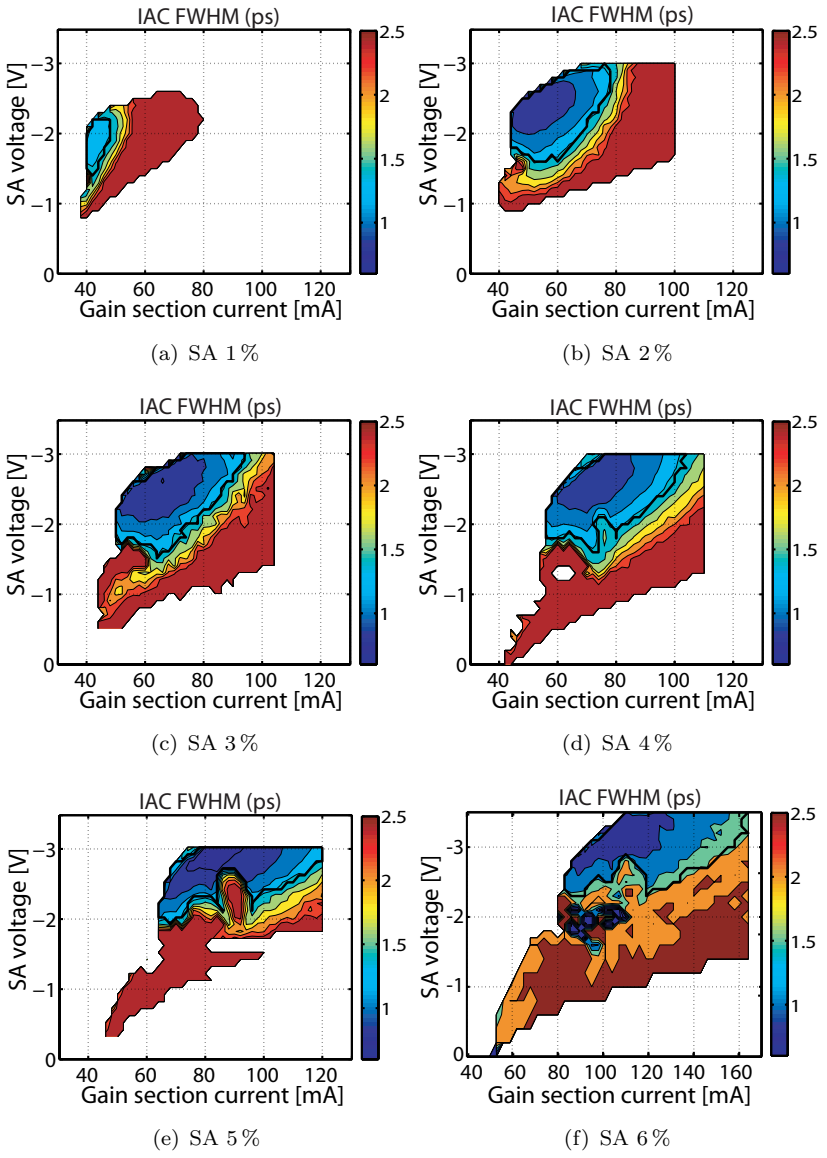

(a) SA 1 % (b) SA 2 %

(c) SA 3 % (d) SA 4 %

(e) SA 5 % (f) SA 6 %

FIGURE 3.17: FWHM (ps˙ of the intensity autocorrelation traces of the 3–QW material devices for various SA lengths.

with the absorber length, with the biggest changes recorded from SA=2 % to SA=3 %, and from SA=5 % to SA=6 %.

Even though the IAC is not capable of providing accurate insight into the pulse shape or phase profile, a non-ideal shape, e.g. affected by additional substructures or satellite pulses, often produces a SH intensity autocorrelation profile with a feature called the *coherence spike*. Example of such an autocorrelation trace is presented in Fig. 3.19(a). It consists of a narrow peak, situated in the middle of much wider "wings". However, the name of this structure may be somewhat confusing, as it is not related to the coherence time of the pulses (IAC is unable to resolve the phase). The coherence time,

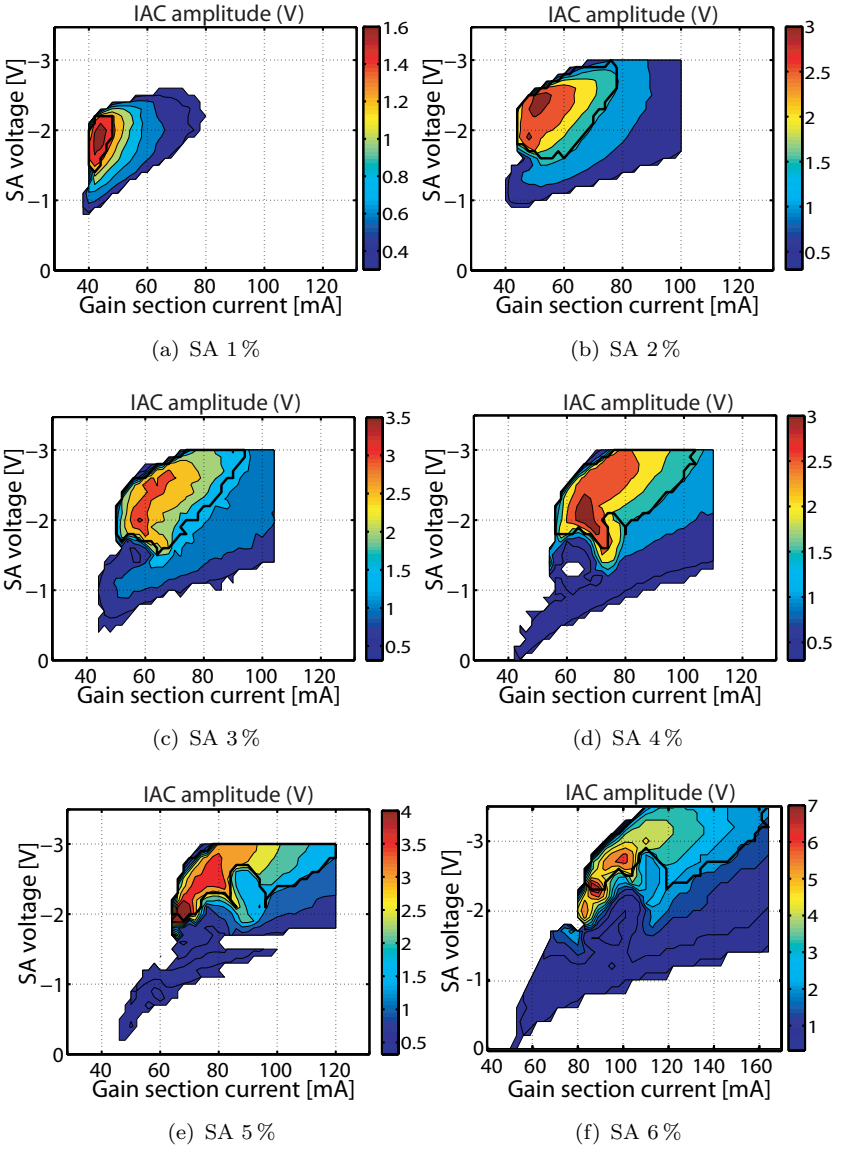

(a) SA 1 %

(b) SA 2 %

(c) SA 3 %

(d) SA 4 %

(e) SA 5 %

(f) SA 6 %

FIGURE 3.18: Amplitude (V) of the intensity autocorrelation traces of the 3–QW material devices for various SA lengths. The color scheme varies between the sub-figures.

though, could be estimated with the second-order FRAC measurements, and would be directly proportional to the width of the interferometric fringes envelope within the autocorrelation trace [96]. However, this method is usually insufficient for a full pulse phase characterisation, and therefore it was not used in this project. A more accurate, chirp sensitive method, called the *sonogram* was employed for the phase detection, and will be explained in Chapter 5 of this thesis.

In order to visualise the presence of the coherence spikes in the autocorrelation traces, the ratio between the width at 20 % and 50 % of the trace amplitude is evaluated and illustrated with a parameter referred to as *incoherence factor*. A threshold value of 2.25

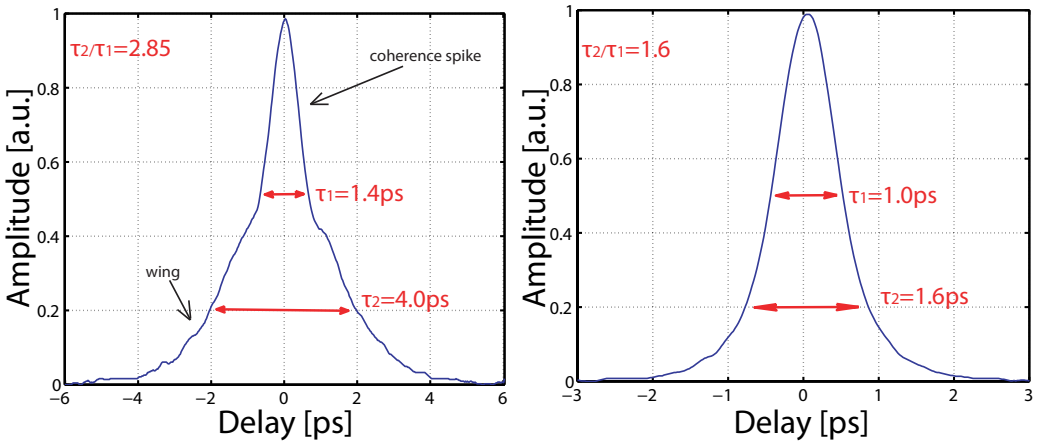

FIGURE 3.19: Examples of the autocorrelation traces (a) with and (b) without a coherence spike profile, measured with the 4 % SA device at V_{SA}=-2.2 V, I_g=96 mA and V_{SA}=-2.8 V, I_g=80 mA.

has been applied in order to assess the impact of the coherence spike on the autocorrelation traces (Fig. 3.19). If the width ratio stays below this level, the autocorrelation peak is classified as coherence-spike-free, and is assigned a incoherence factor value of 0. Otherwise, the factor is equal to 1. The procedure is repeated for each peak available in the autocorrelator delay following which an average value is calculated. The final results of the analysis are presented in Fig. 3.20. Obviously, such a simplified diagnosis is not error–free. For instance, there are two separate coherence-spike-free regions present in each map. The top left indicates optimum pulses as previously discussed, while the second domain only gives an impression of smooth pulses. In reality, the autocorrelation traces in this region deviate substantially from the shape produced by a Gaussian or sech^2 pulse. Instead, triangular-like envelopes are measured, which are more difficult to distinguish from good quality pulses with the incoherence-factor method. However, the incoherence factor maps can still be informative, as in conjunction with the contour lines, it can be seen how the FWHM measurements might be misleading. For instance, in Fig. 3.20(b), the region inside the contour plot extends far beyond the dark-blue region of coherence-spike-free pulses. If the laser driving parameters drift away from the optimum conditions (e.g. through excessive gain pumping), the pulse begins to spread unevenly. This is mostly evident in the lower part of its autocorrelation trace, and is usually overlooked in the FWHM measurements.

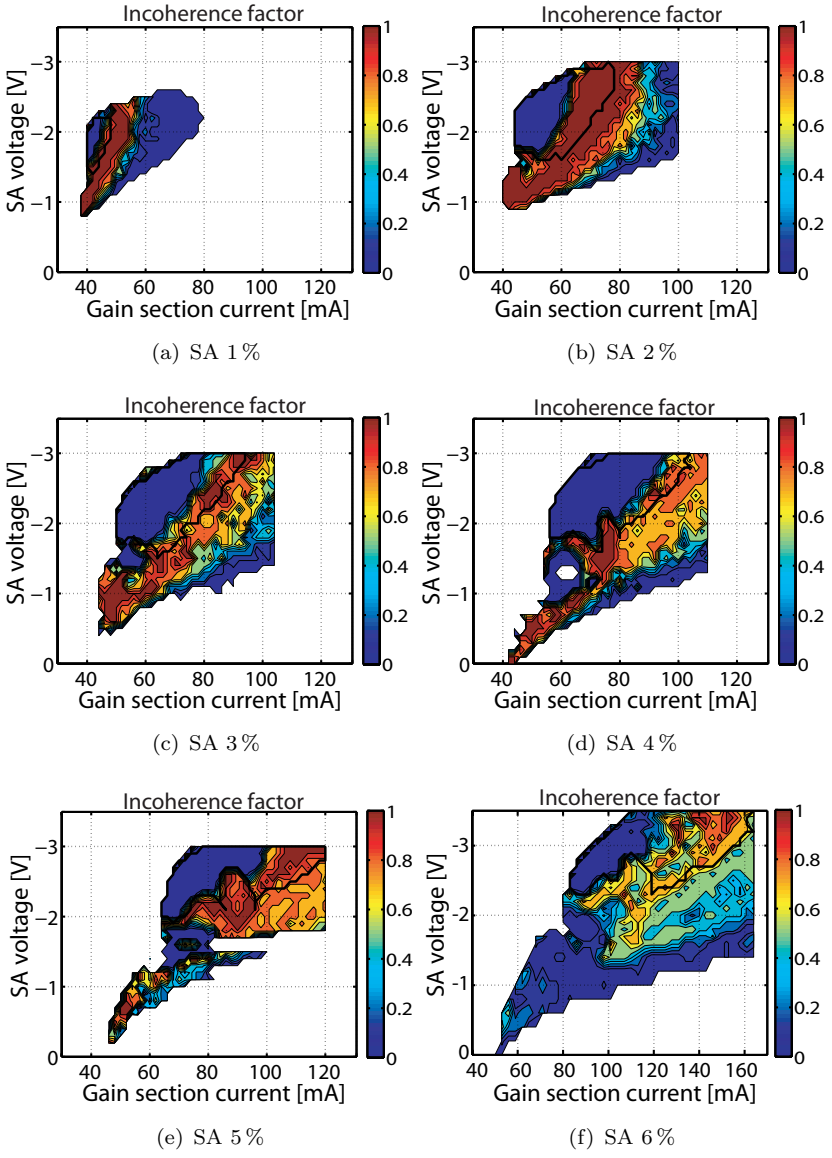

FIGURE 3.20: Incoherence factor maps of the intensity autocorrelation pulses of the 3–QW material devices for various SA lengths.

3.3.2 Optical Spectrum Measurements

The optical spectra were analysed over the full range of biasing conditions for each device. Fig. 3.21 presents a distribution of the spectral FWHM values. The inclusion of an upper limit of 14 nm in the plots eliminated large values caused by the presence of spontaneous emission spectral component or double-peak spectra. The global trend indicates an increase of spectral width with longer absorbers. The maximum values registered within the contour lines shift from 7 nm with SA=2 % to 12 nm with SA=6 %. Furthermore, the effect of intensifying self-pulsation, in the low gain current parts of the biasing regions, can also be observed. There are also sharp transitions in FWHM values

between the ML regions and the single-mode continuous wave operation. Interestingly, the widest spectra are localised near the high V_{SA} limits of the optimum ML regions, which is not necessarily where the shortest pulses were observed (Fig. 3.17). This is particularly evident for the short-SA devices, and it indicates that these spectrally wider pulses may be affected by stronger chirp than those at the low current edge of the ML regions.

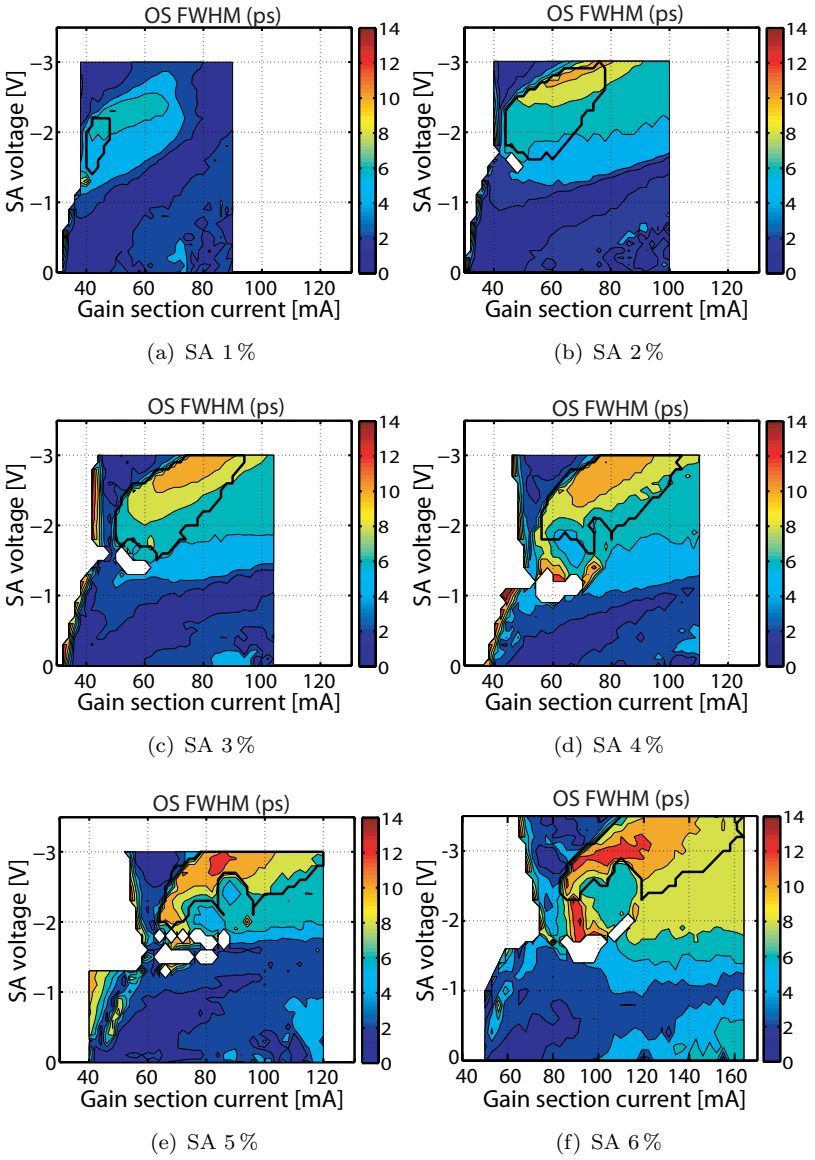

(a) SA 1 % (b) SA 2 %

(c) SA 3 % (d) SA 4 %

(e) SA 5 % (f) SA 6 %

FIGURE 3.21: FWHM (nm) of the optical spectra of the 3–QW material devices for various SA lengths.

A distribution of central wavelength in the optical spectra are presented in Fig. 3.22. It can be noticed that an increase in the absorber length induces a reduction of central wavelength in the optimum ML regions. It appears from these graphs that the central

wavelength follows the gain peak, which blue shifts with longer absorber. This is due to an increased threshold carrier density induced by the higher losses of the longer absorption section. Also, the ML regions extend over wider wavelength ranges. For instance, the contour plot in Fig. 3.22(b) spans over 4 nm, whereas in Fig. 3.22(e) it runs over 10 nm. The examples of OS evolution for various V_{SA} levels are presented in Fig. 3.23.

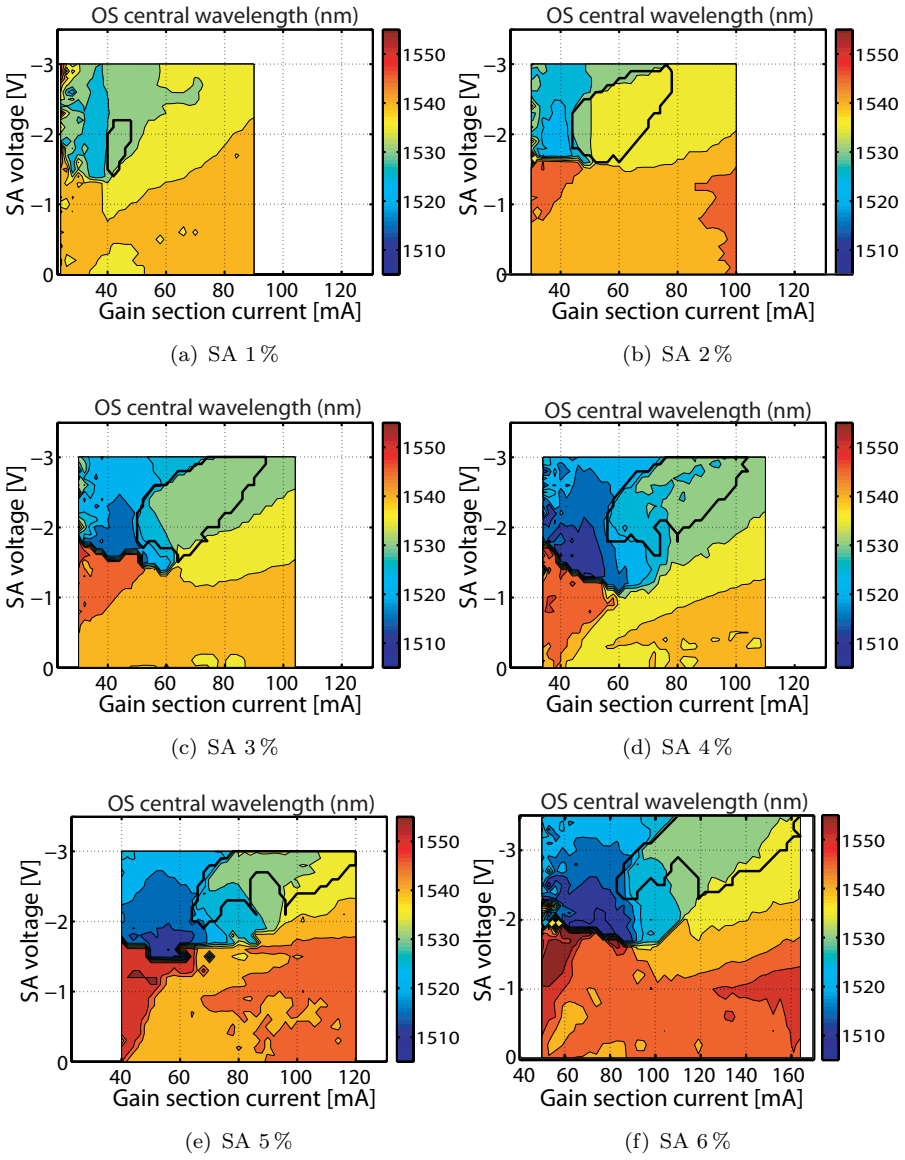

(a) SA 1 %

(b) SA 2 %

(c) SA 3 %

(d) SA 4 %

(e) SA 5 %

(f) SA 6 %

FIGURE 3.22: Peak wavelength (nm) of the optical spectra of the 3–QW material devices for various SA lengths.

At the lowest reverse voltage levels (e.g. at V_{SA}=-0.1 V) the emission is concentrated around a single spectral region ∼1540 nm. The spectrum is stable throughout the vast range of the gain section pumping, with some variations occurring close to the threshold. These instabilities intensify for higher V_{SA} and are strongest when the laser enters the SP region. This is evident in the spectral maps as the spectrum widens substantially

towards shorter wavelengths (∼1515 nm). When the SP entirely dominates the lasing operation (e.g. at V_{SA}=-1.7 V, I_g=60–70 mA), the spectral region is completely blue-shifted with respect to the ML region. The extent of this shift depends on the absorber biasing and typically decreases with V_{SA}. At very high values of the absorber voltage the lasing is usually SP-free and a sharp transition between the continuous-wave (CW) and ML regimes appears. For instance, at V_{SA}=-3.0 V and I_g ∼75 mA, where the ML starts, the spectral width increases from 2 nm to 10 nm within a gain current increment of only 4 mA.

Finally, the spectra were analysed for their mode-comb modulation depth. Fig. 3.24 shows that the OS modulation in the ML region is rather irregular with short SA lengths and stabilises on 4–6 % SA devices, with a typical value of ∼20 dB. The SP can be clearly identified as the dark-blue regions, which correspond to shallowly-modulated longitudinal mode comb (∼5 dB).

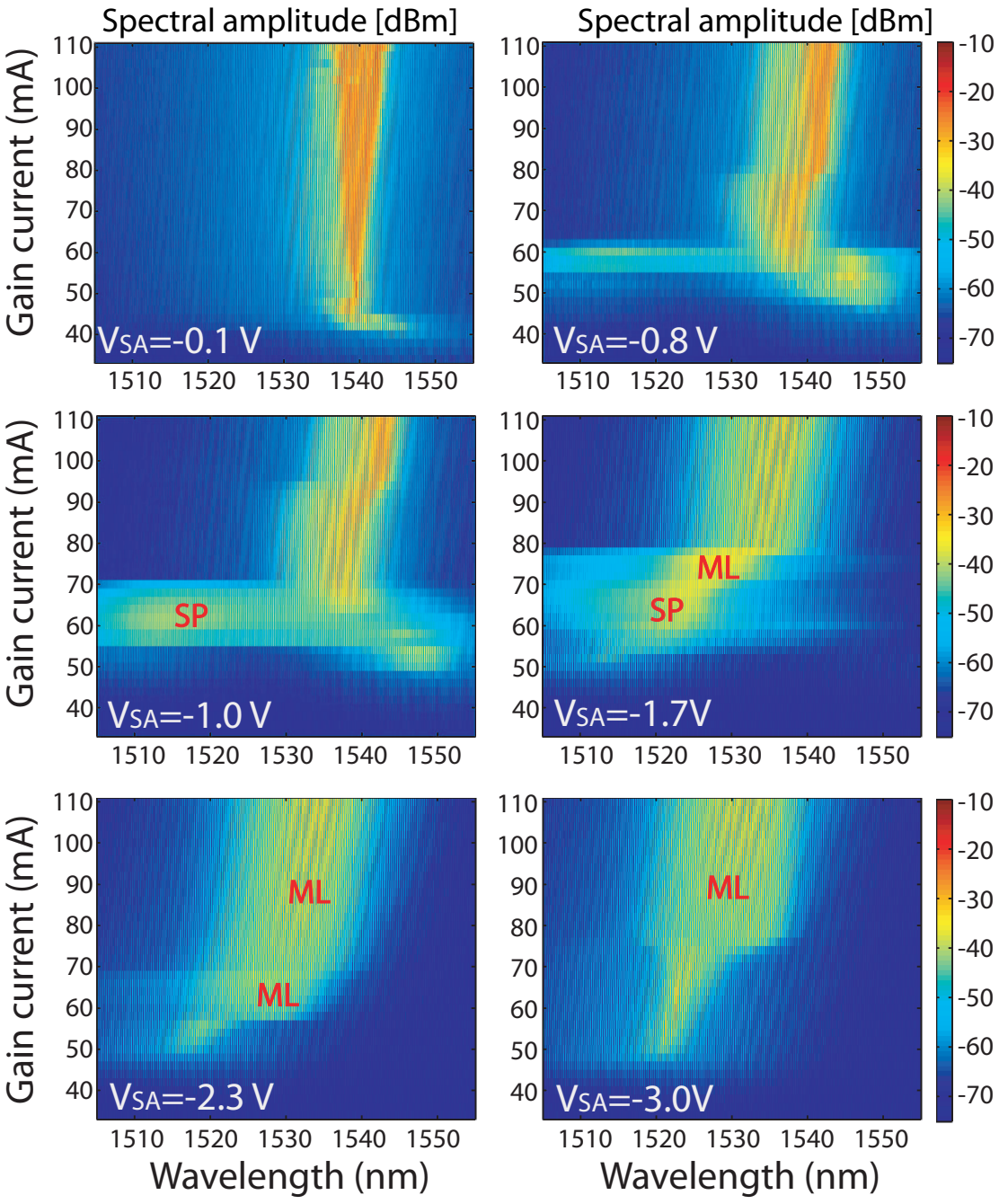

FIGURE 3.23: Spectral amplitude (dBm) maps measured on the 4 %-SA device at various levels of V_{SA}.

3.3.3 Time-Bandwidth Product

The TBP between the unconvoluted IAC widths and spectral FWHM values is plotted in Fig. 3.25. The TBP values displayed in the graphs are limited to the range of 0.5 – 2, which correspond approximately to the biasing regions shown in the previous autocorrelation-based maps (Fig. 3.17–Fig. 3.20). It can be noticed that the 2 % SA device has the widest region for which the TBP is below 1. The lowest values are registered

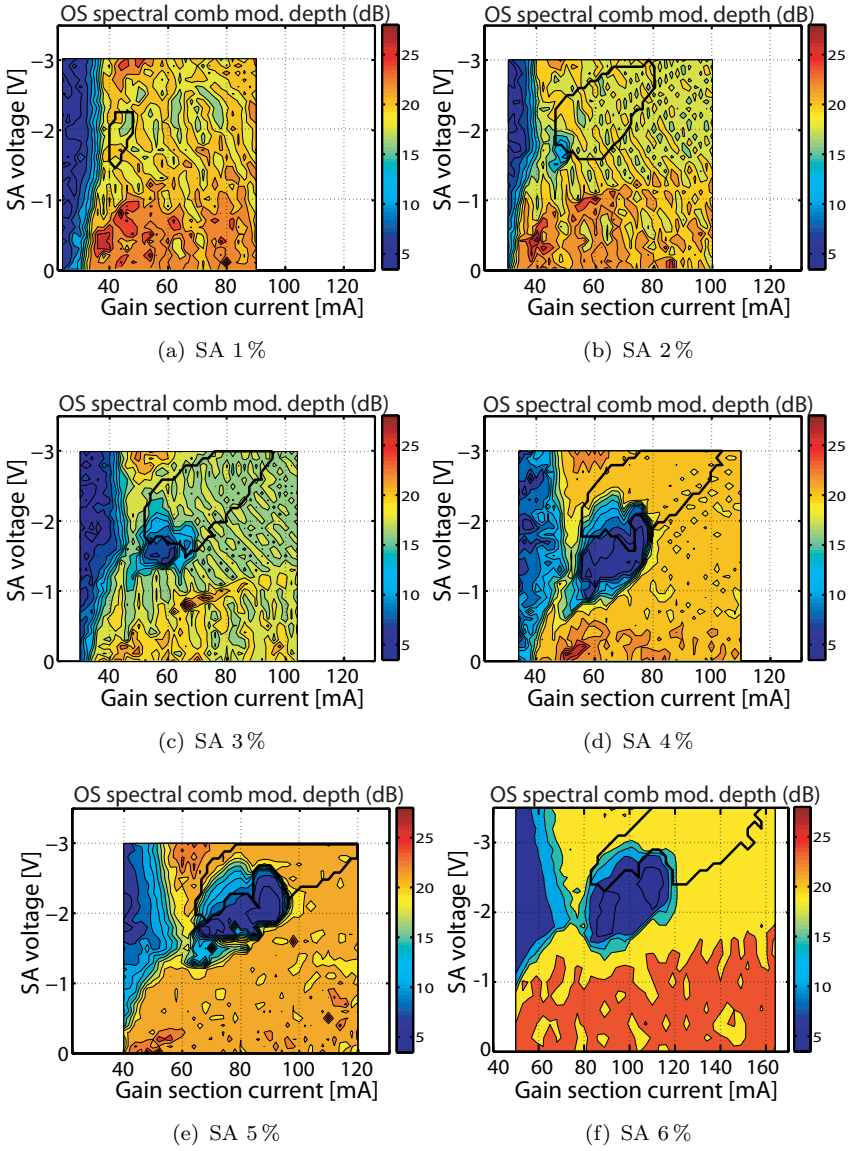

(a) SA 1 %

(b) SA 2 %

(c) SA 3 %

(d) SA 4 %

(e) SA 5 %

(f) SA 6 %

FIGURE 3.24: Modulation depth (dB) of the spectral comb profiles of the 3–QW material devices for various SA lengths.

for devices with SA≥4 %. However, they are concentrated within a relatively narrow range of the biasing parameters, just above threshold currents and V_{SA}=-2 – -3 V. There is a general trend of an increasing average TBP within the ML contour lines for devices with ≥3 % absorbers.

3.3.4 Radio Frequency Measurements

The amplitude of the RF signal at the cavity round trip frequency is mapped in Fig. 3.26. Clearly, the regions of high intensity peaks expand over much wider biasing ranges than the optimum ML contour lines. The ML operation produces RF signals with extinction

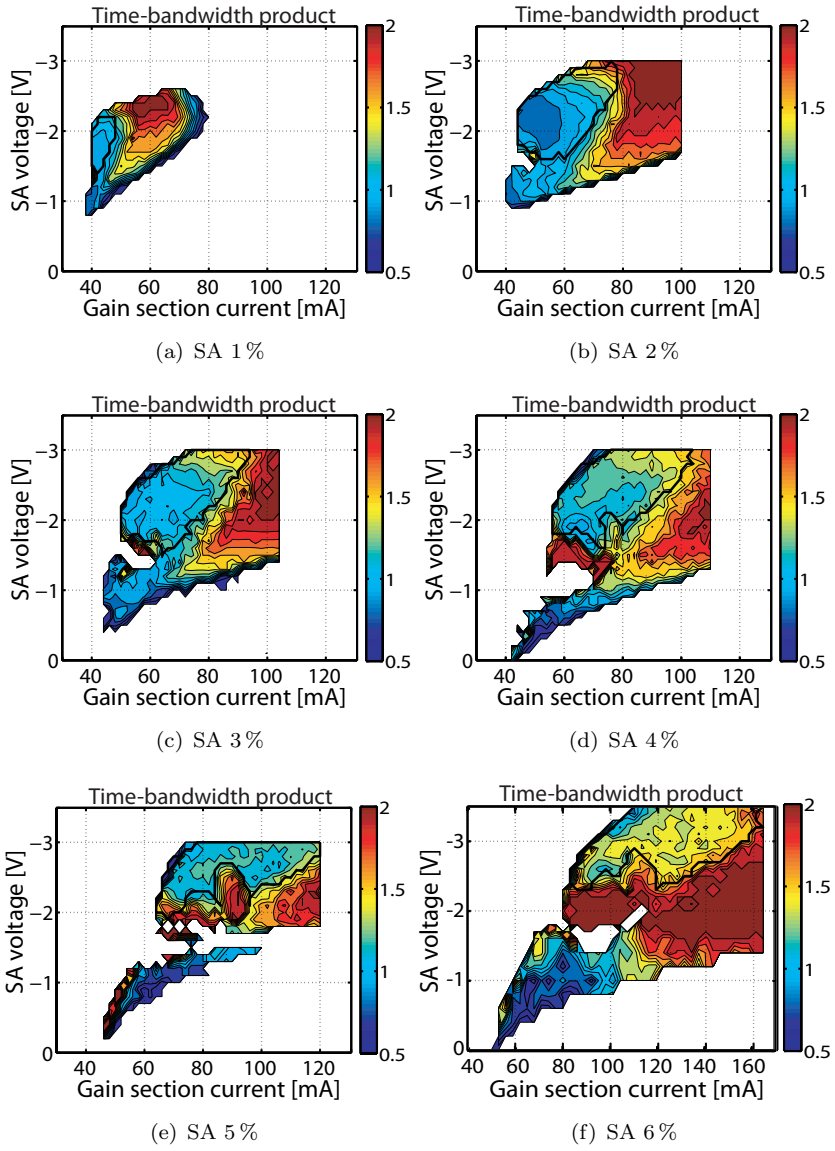

(a) SA 1 %

(b) SA 2 %

(c) SA 3 %

(d) SA 4 %

(e) SA 5 %

(f) SA 6 %

FIGURE 3.25: Time bandwidth product between the IAC and OS FWHM values measured on the 3–QW material devices for various SA lengths.

ratios (ERs) of over 30 dB. However, the highest peaks are mostly registered outside these regions, on the high-I_g side of the parametric maps. This is particularly evident in the case of devices with short SAs. The span of the RF amplitudes in the ML regions increases systematically with the absorber length and reaches over 60 dB on the 5 % SA device, as shown in Fig. 3.26(e). That proves their superiority to the short SA devices in the applications requiring wide repetition rate tunability ranges.

The fundamental repetition frequency (f_{rep}) of the SMLLs as a function of the biasing parameters is plotted in Fig. 3.27. There are two separate regions present in each figure. The region corresponding to low SA reverse bias (usually below 1 V), is much less sensitive to the biasing conditions than the upper regions, and display the highest

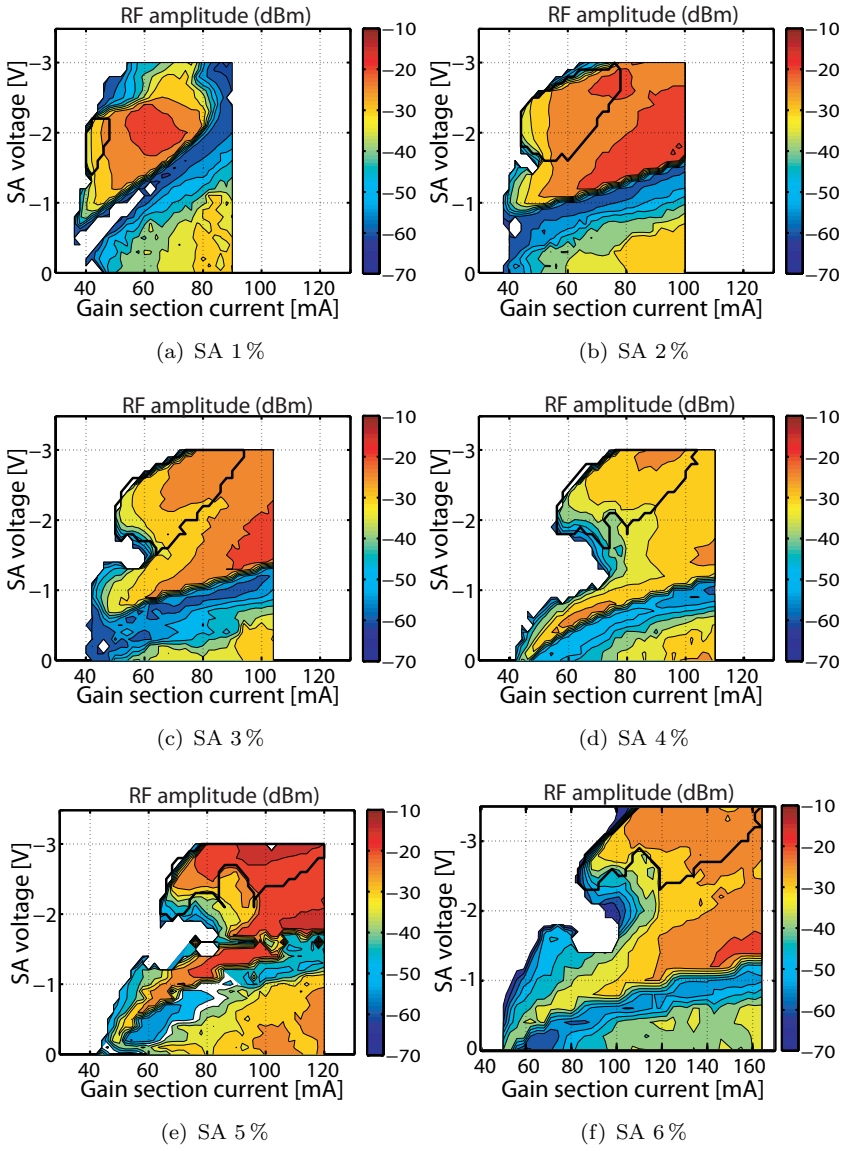

(a) SA 1 %

(b) SA 2 %

(c) SA 3 %

(d) SA 4 %

(e) SA 5 %

(f) SA 6 %

FIGURE 3.26: Peak intensity (dBm) of the RF spectrum at the cavity round-trip frequency measured on the 3–QW material devices for various SA lengths.

repetition rate values within the measurement ranges. The peak frequency in these biasing regions increases only slightly with the SA bias. A second region, with lower repetition rates, appears at higher V_{SA} and it is of greater interest, as it corresponds to stable ML operation. At low values of I_g, the repetition rate increases with V_{SA}. At higher gain section pumping, it first decreases and then increases with V_{SA} (e.g. at $I_g = 90\,\text{mA}$ in Fig. 3.27(d)). For a fixed absorber bias, the f_{rep} values decrease with increasing gain section current. Such a trend was well described in [97].

Basically, the refractive index change in the absorber, due to the electric-field-induced index variation, and in the gain section, through the carrier induced effects, alone cannot account for the complex tuning characteristics of the SMLLs. The electric field applied

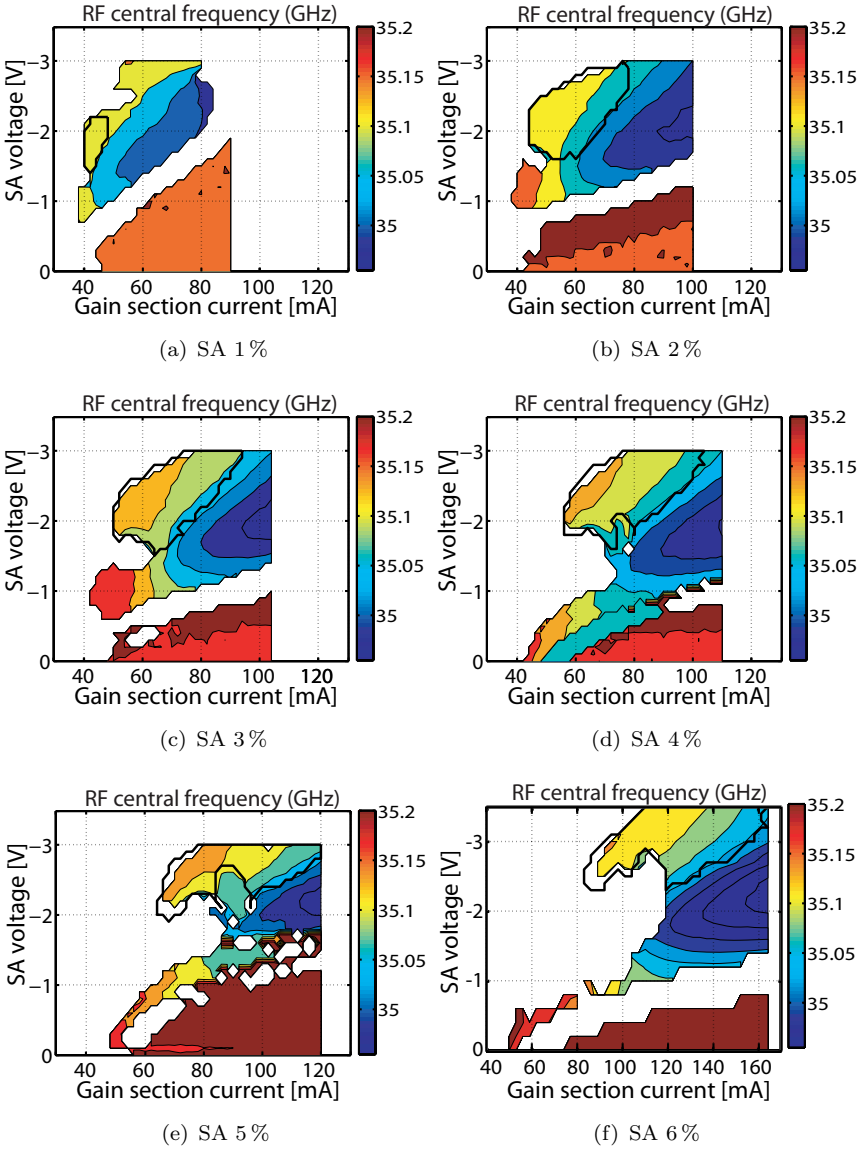

(a) SA 1 %

(b) SA 2 %

(c) SA 3 %

(d) SA 4 %

(e) SA 5 %

(f) SA 6 %

FIGURE 3.27: Repetition frequency (GHz) of ML of the 3–QW material devices for various SA lengths.

to the absorber section modifies the energy bandgap through the QCSE and shifts the absorption peaks towards the longer wavelength. This is accompanied by the refractive index variation, which takes negative values for wavelengths above the exciton absorption peak [98], i.e. in the spectral region corresponding to mode-locking. Similarly, the plasma effect (free-carrier absorption) always produces negative refractive index change. Also, the refractive index change due to the bandfilling effect is negative for the photon energies near and below the bandgap energy and changes sign to positive only well above the bandgap energy [77].

As all the phenomena produce a negative refractive index change with increased reverse voltage and forward biased current, respectively, the repetition frequency should increase

diagonally, from the bottom left to the top right corner in the plotted maps. However, the experimental results display a much more complicated relationship between the repetition frequency and the biasing conditions, which suggests that other processes governing the pulse repetition rate should be considered. If a device operates close to or in the ML condition, the saturation of the gain and absorption influences the repetition frequency by shifting the peak position of the pulse envelopes. Operating conditions of the laser play an important role in this shift, which varies with the pulse energy and initial level of saturation (before the pulse arrival). The repetition frequency of a ML laser can be described with by following expression:

$$f_{rep} = \frac{1}{T_{rep} - \delta t}, \tag{3.2}$$

where δt is the detuning time, defining the change in the round-trip time of the cavity from the nominal round-trip time, T_{rep}. δt has an approximated quadratic effect on the f_{rep} around its turning point.

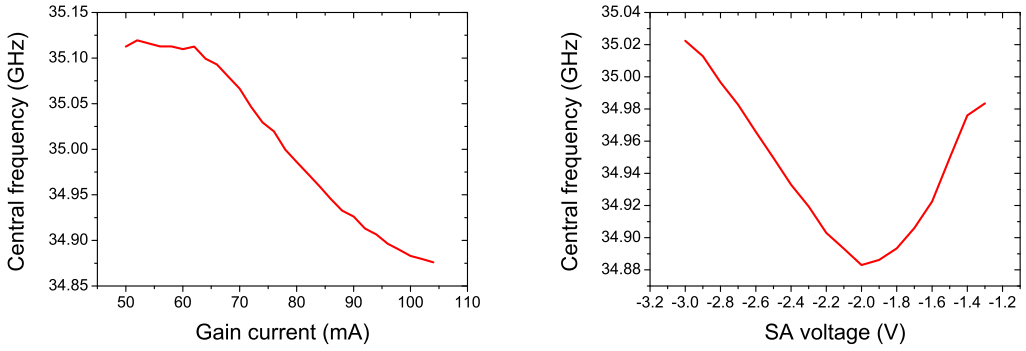

(a) (b)

FIGURE 3.28: Dependence of the repetition frequency on (a) the gain current (V_{SA}=-2 V) and (b) the SA reverse voltage (I_g=100 mA), measured on the 3 %-SA MLL.

These relationships can be observed in Fig. 3.27 and Fig. 3.28(a) as a function of both the gain current and absorber voltage. As I_g is increased, the pulse energy grows, which triggers a decrease in the repetition frequency. Due to the limited range of the gain current applied in the experiment, only the region below the detuning turning point is visible. A full dependence of f_{rep} on the detuning parameter can be seen with a sweep of V_{SA}. The variation in the SA bias not only influences the pulse energy, but also sets the unsaturated absorption and the recovery time of the absorber. The last effect is not significant as the recovery time values for V_{SA} <-1 V are already below the round trip time [88]. So, it is the level of unsaturated absorption that has the greatest impact on the repetition frequency detuning. Higher SA voltage reduces pulse energy, hence, for energies above the detuning turning point (low voltage), an increase in the

Relative SA length	I_g	V_{SA}	10 dB width
1 %	46 mA	-2.2 V	**708 kHz**
2 %	46 mA	-2.4 V	**270 kHz**
3 %	54 mA	-2.4 V	**290 kHz**
4 %	58 mA	-2.2 V	**291 kHz**
5 %	74 mA	-2.7 V	**250 kHz**
6 %	102 mA	-3.1 V	**475 kHz**

TABLE 3.1: Minimum 10 dB width values registered with 3-QW MLL with various SA lengths.

bias produces a reduction in f_{rep}. Above this point (higher SA bias values), a higher bias voltage results in an increasing f_{rep}. These effects are clearly evident in the graphs displayed in Fig. 3.27 and Fig. 3.28(b).

The graphs mapping the 10 dB-width of RF peaks are displayed in Fig. 3.29. The 10 dB-width very closely reproduce the ML trends presented in the autocorrelation and optical spectrum parametric maps and vary from 100 kHz to 6 MHz throughout the biasing regions. The most stable pulses deduced from the frequency linewidth measurements correspond to relatively high SA voltages and to the gain currents located close to the threshold. Clearly, excessive pumping increases the linewidth of the RF peak. The regions of narrowest linewidths also expand for longer absorber devices, which agrees with the observations described in [99]. A summary of the narrowest RF spectra for various SA lengths is presented in Table 3.1.

Finally, the RF spectra were analysed for their low frequency components. Observation of the spectra in this frequency range can provide crucial information about the emission noise and ML stability. The evolution of amplitude and peak frequency of the RF signal in the 0 – 5 GHz span is presented in Fig. 3.30 and Fig. 3.31. These experimental results agree with those presented in [90], where an increase in the absorber length triggered an expansion of the SP region. The low frequency modulations are enhanced by higher linear losses and higher carrier densities at threshold, with both effects being a direct consequence of a longer absorber. The regions with weak or no SP correlate well with the domains of optimum ML deduced from the IAC traces. As the absorber length increases, the SP tends to dominate the dynamical operation, as shown by the 6 % SA device, in which a strong, low frequency modulation is visible up to $V_{SA} = -3.0$ V.

The central frequency of the SP peak, f_{SP}, is strongly dependent on the gain section current. The observed self-pulsation can be attributed to two different effects: Q-switching effect, triggered by the saturable absorption, and undamped relaxation oscillations. The frequency of both phenomena increases with the average intensity, which explains the

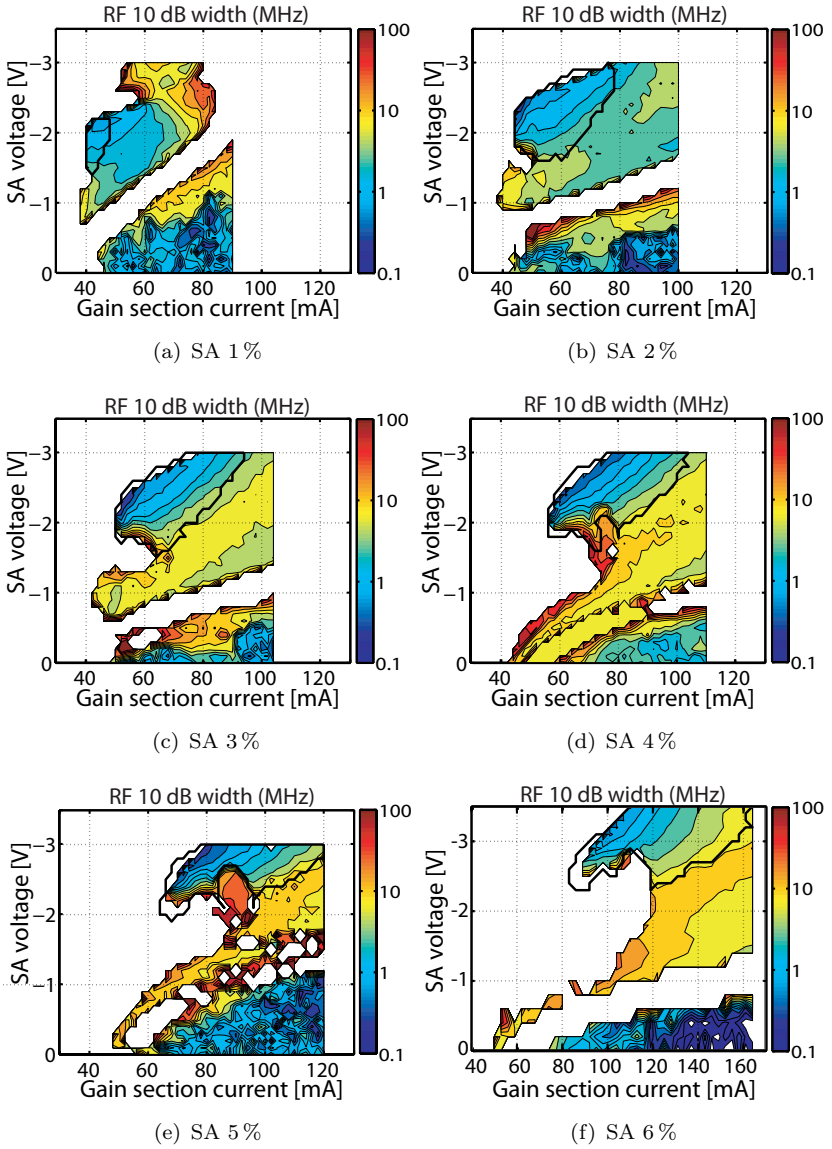

(a) SA 1 %

(b) SA 2 %

(c) SA 3 %

(d) SA 4 %

(e) SA 5 %

(f) SA 6 %

FIGURE 3.29: 10-dB width (MHz)of the fundamental RF peak of the 3–QW material devices for various SA lengths.

observed dependance of the SP peak on the gain pumping level [100]. Modulation frequencies as low as 200 MHz are observed for V_{SA} below the ML regions. Moreover, it can be seen that the rate of f_{SP} change with the gain current reduces with L_{SA}. The biasing point corresponding to the maximum frequency constantly shifts towards higher values of I_g and V_{SA}. For instance, the peak frequency of the 2 % SA device is reached at I_g=62 mA and V_{SA}=-1.7 V, whereas that of the 5 % SA device is reached at I_g=100 mA and V_{SA}=-2.1 V.

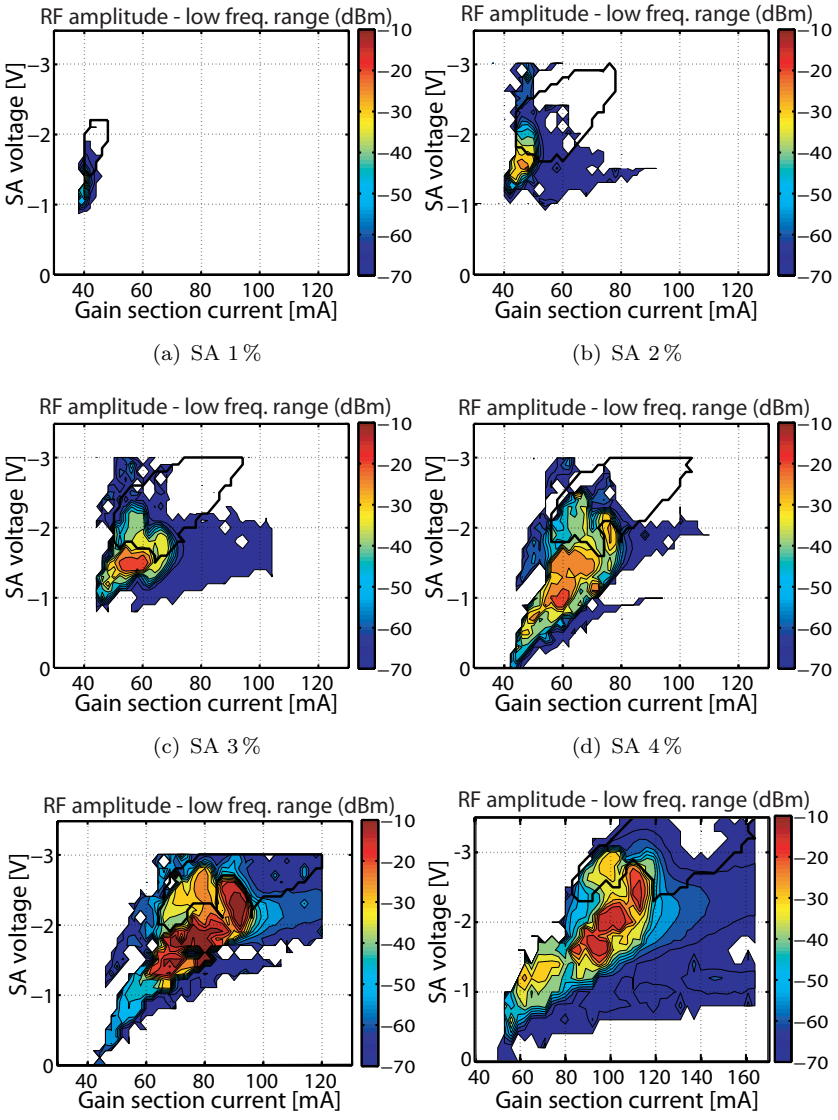

(a) SA 1 %

(b) SA 2 %

(c) SA 3 %

(d) SA 4 %

(e) SA 5 %

(f) SA 6 %

FIGURE 3.30: Amplitude (dBm) of the SP and RF noise peak of the 3–QW material devices for various SA lengths.

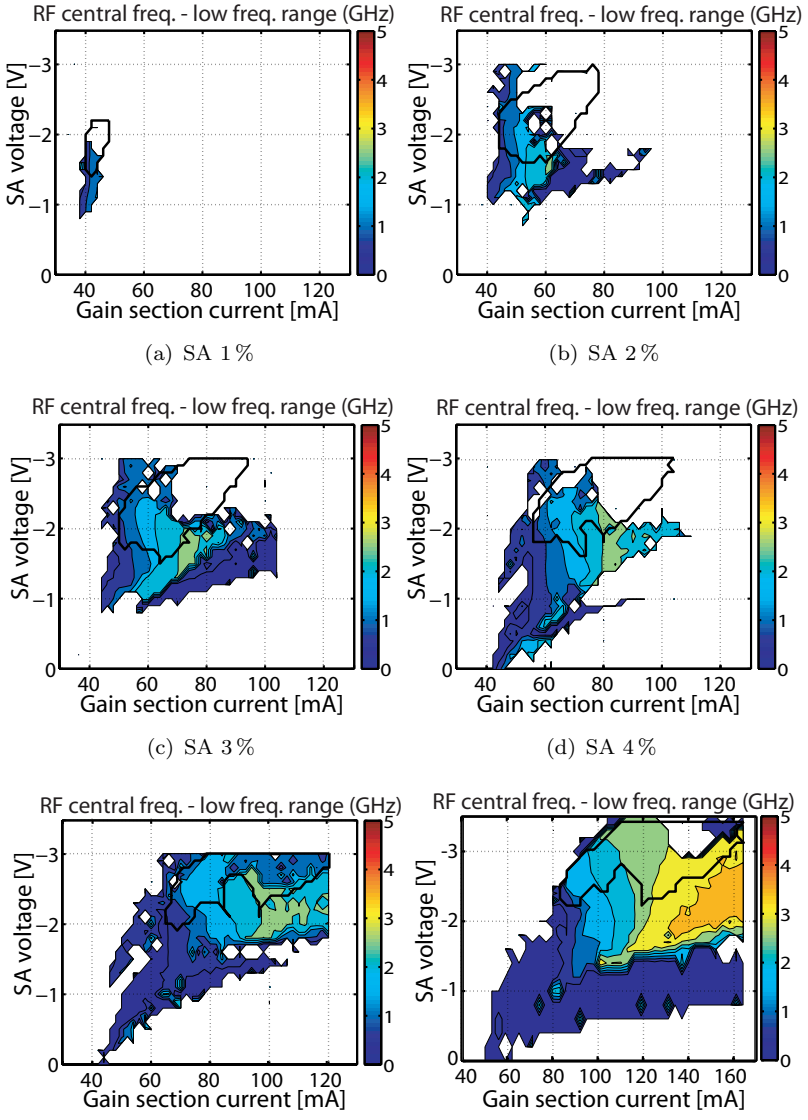

(a) SA 1 %

(b) SA 2 %

(c) SA 3 %

(d) SA 4 %

(e) SA 5 %

(f) SA 6 %

FIGURE 3.31: Central frequency (GHz) of the SP and RF noise peak of the 3–QW material devices for various SA lengths.

3.3.5 Jitter Measurements

The rms jitter measurements were performed on the 4 % SA device, using the procedures presented in Section 3.2.6. The parametric map in Fig. 3.32 shows a distribution of the jitter values across the ML region and demonstrates similar trends to those recorded in the RF and OS maps. The region with the lowest jitter occurs close to the low-I_g edge and takes a diagonal orientation across the biasing region. Typical values of jitter measured between 20 kHz and 320 MHz are between 1.2 ps to 2 ps, and reach 6 ps in the region affected by SP.

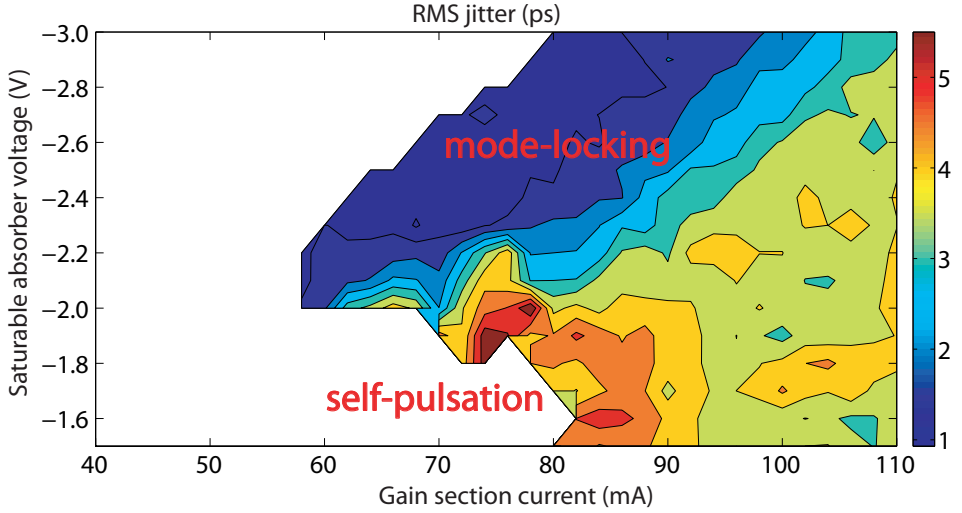

FIGURE 3.32: Parametric map of the rms jitter (ps) measured on the 4 % SA 3-QW device and integrated in the frequency offset range of 20 kHz – 320 MHz.

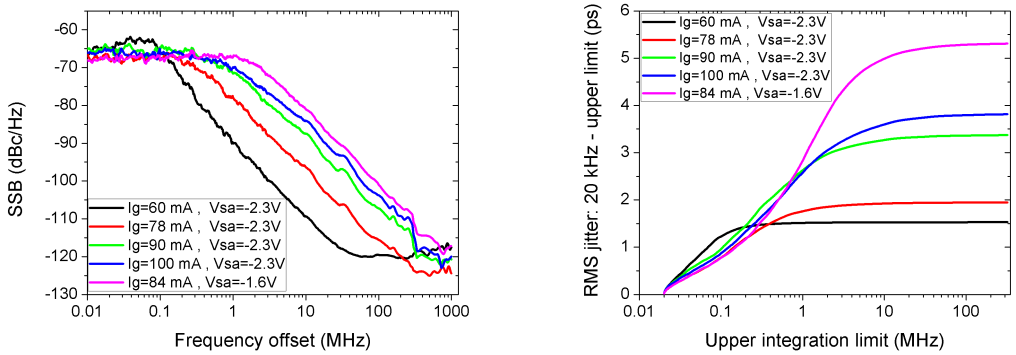

(a) (b)

FIGURE 3.33: (a) SSB phase noise spectrum at various regions of the ML region and (b) corresponding integrated rms jitter as a function of the upper integration limit.

Examples of the SSB spectra and integrated jitter, taken in the best ML region (V_{SA}=-2.3 V) and in the SP-affected region (V_{SA}=-1.6V), are presented in Fig. 3.33. The curve

corresponding to the lowest value of rms jitter displays a 3 dB roll-off frequency offset at around 130 kHz, while in case of the SP the roll-off frequency is more than 4 MHz away from the carrier frequency.

3.3.6 Saturable Absorber Photocurrent

The density of the photo-generated current in the saturable absorber, J_{abs}, measured with an ammeter connected between the voltage source and the absorber section, is presented in Fig. 3.34 for the entire biasing regions of all the six devices. A common feature of the graphs are the characteristic quarter-circular contours concentrated around the high I_g and V_{SA} values in the top-right corners. For the shortest absorber device (Fig. 3.34(a)) equally spaced contour lines can be observed. These become more distorted with longer SA as the SP regions start to dominate the emission on the low voltage side. It should be noted than for the devices with 2–6 % SA the ML operation corresponds to practically the same values of J_{abs}, which range from 8–20 kA/cm^2.

3.3.7 L-I Characteristics

The output light coupled from a single facet and monitored with a broad area photodetector is plotted in Fig. 3.35. The average power recorded within the ML regions systematically increases with L_{SA}, which is due to the fact that longer absorbers saturate at higher optical intensities, hence, the mode-locking region is systematically shifted towards higher gain pumping regions, and consequently, higher optical power. The 1 % SA device emits pulses with an average power below 2 mW, while the ML operation in the longest absorber device corresponds to power levels as high as 10 mW. In order to better visualise the influence of different SA lengths on the emission levels, several L-I curves corresponding to various absorber bias levels are presented in Fig. 3.36. For the 2 % device, the slope efficiency decreases gradually with absorber bias, from 0.2 mW/mA at V_{SA}=0 V to 0.07 mW/mA at V_{SA}=-3.0 V. As expected, the absorber attenuation is more distinct with longer SA sections.

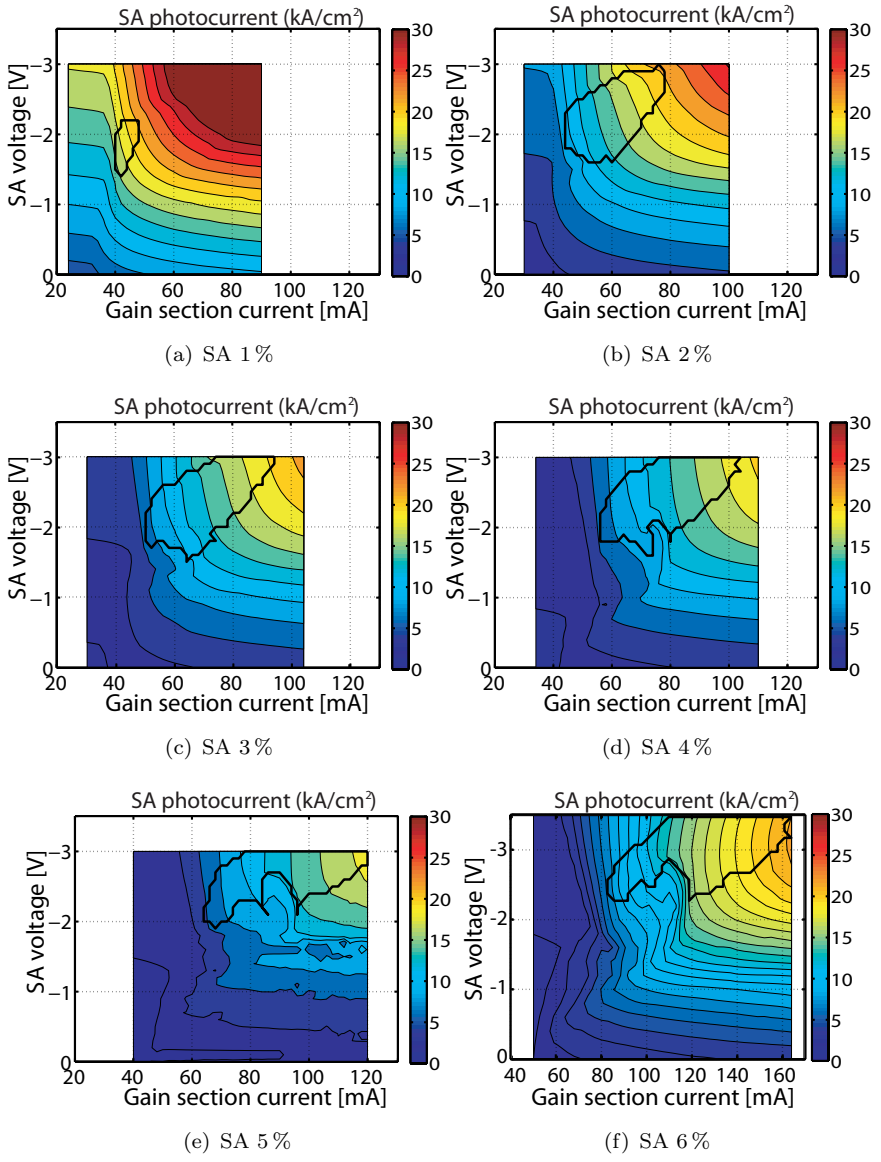

(a) SA 1 %

(b) SA 2 %

(c) SA 3 %

(d) SA 4 %

(e) SA 5 %

(f) SA 6 %

FIGURE 3.34: Photocurrent (kA/cm^2)induced in the saturable absorbers of the 3–QW material devices for various SA lengths.

3.3.8 Pulse Peak Power

The pulse peak power, P_{peak}, is estimated at each biasing point on the basis of the measured optical power and the autocorrelation traces. Only the approximate values of P_{peak} are presented in this analysis, since the method assumes an ideal sech^2 pulse shapes, and does not take any potential pulse deformation or incomplete mode-locking into account. The peak power is simply calculated with Eq. 3.3:

$$P_{peak} = 0.88 \cdot P_{avg}/(f_{rep} \cdot \tau), \tag{3.3}$$

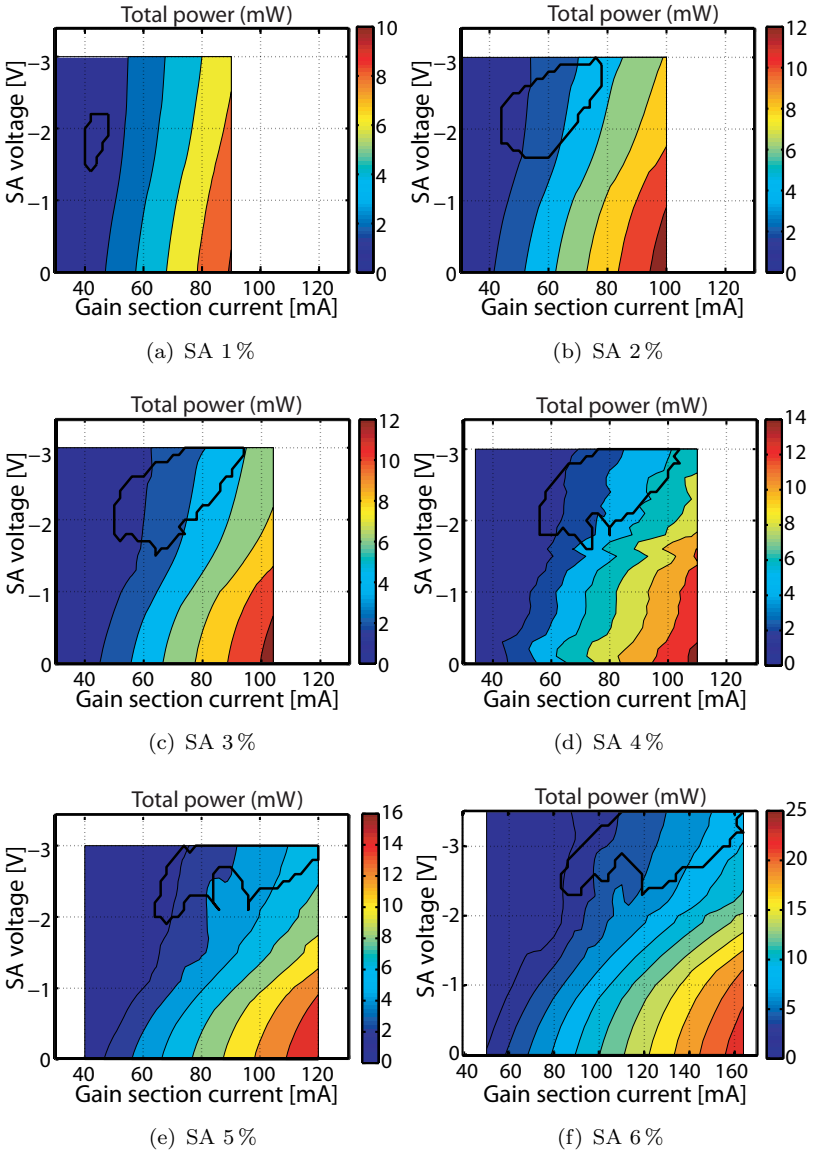

(a) SA 1 % (b) SA 2 %

(c) SA 3 % (d) SA 4 %

(e) SA 5 % (f) SA 6 %

FIGURE 3.35: Total power (mW) of a single facet emission from the 3–QW material devices for various SA lengths. The color scheme varies between the sub-figures.

where P_{avg}, f_{rep} and τ are the average power, repetition rate and the FWHM of the pulse, respectively. The results of this analysis are presented in Fig. 3.37. The regions of the highest peak power levels are located on the top-right side of the optimum ML regions. The shortest pulses correspond to relatively low I_g, usually close to threshold, and have low energy values. With increasing gain current the pulse energy increases, however, the stronger pumping also widens the pulses. Hence, the peak power is not directly related to the pulse energy and it begins to drop over a certain current biasing. The maximum peak power levels gradually increase with the absorber lengths and vary from 30 mW for the 1 % SA to 250 mW for the 6 % SA.

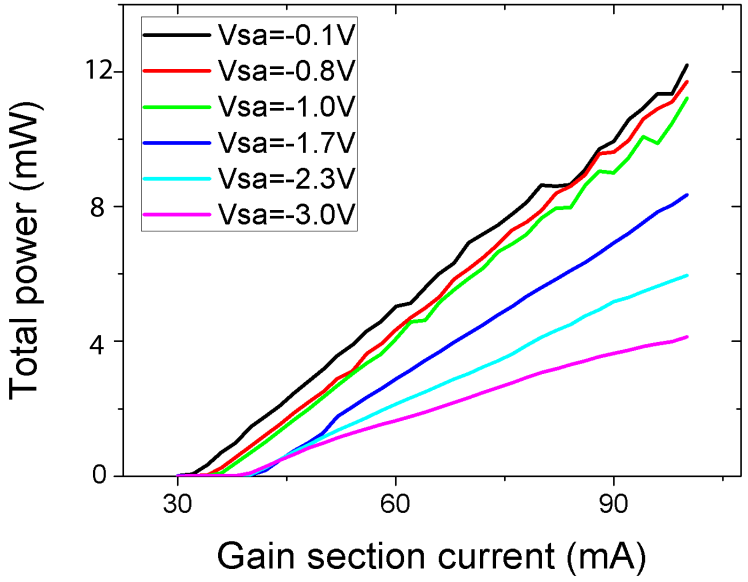

(a) SA 2 %

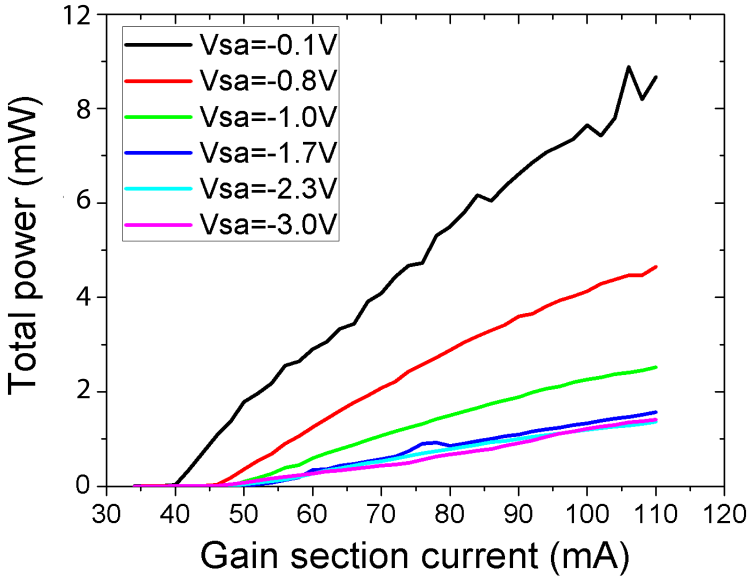

(b) SA 4 %

FIGURE 3.36: Output light vs. gain section current at various SA biasing levels measured on 2 % and 4 % SA devices.

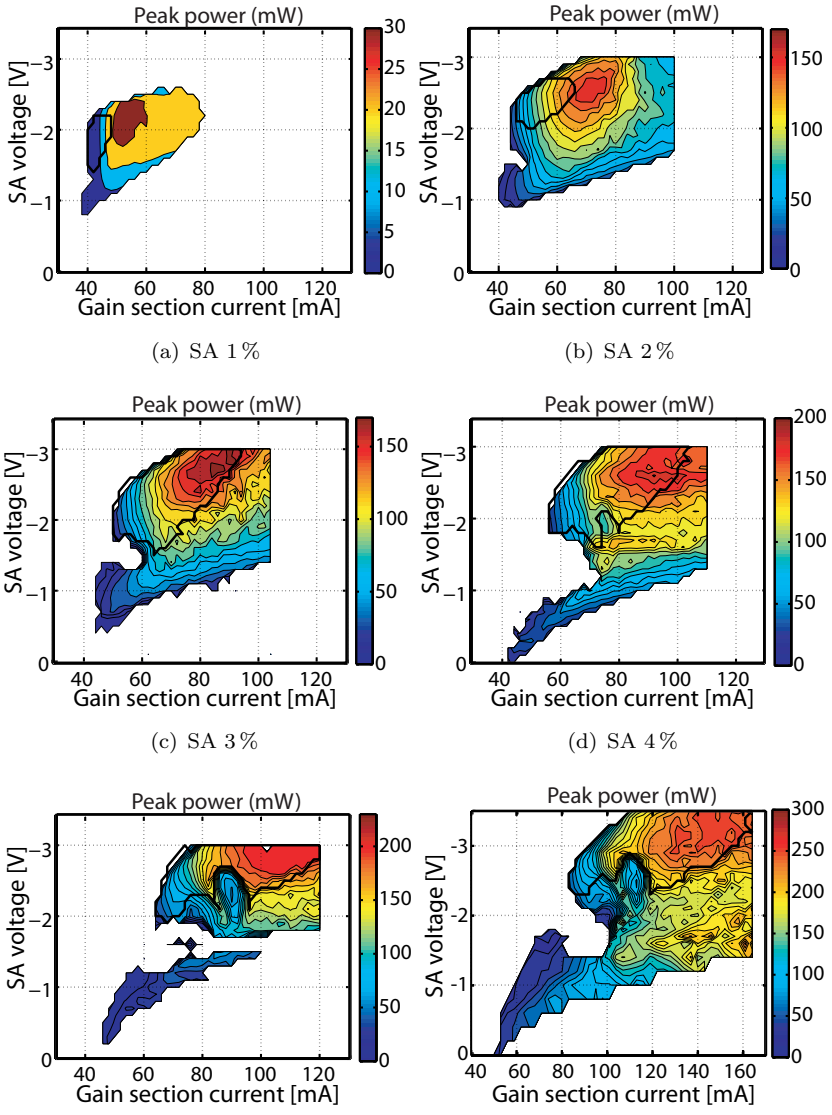

(a) SA 1 %

(b) SA 2 %

(c) SA 3 %

(d) SA 4 %

(e) SA 5 %

(f) SA 6 %

FIGURE 3.37: Peak power (mW) of the pulses emitted by the 3–QW material devices for various SA lengths. The color scheme varies between the sub-figures.

3.3.9 Summary of the 3-QW Devices

The comparative analysis between the 3-QW mode-locked lasers demonstrated the significance of the SA lengths on their dynamical behaviour. Although it can be problematic to identify a device with the optimum SA length, the best geometry can be selected by considering the requirements of the final application. A brief summary of the study is outlined below:

- The mode-locking biasing regions expand with L_{SA}. However, the largest region with pulses producing high-amplitude IAC traces, has been recorded on the 4 % SA device.
- The maximum achievable amplitude of the intensity autocorrelation systematically increases with L_{SA}.
- The minimum achievable intensity autocorrelation FWHM values decreases with L_{SA}, and reaches 0.7 ps on the 6 % SA device.
- The largest biasing region of coherence–spike–free autocorrelation traces has been realised on the 4 % SA device.
- The largest biasing region with the time-bandwidth product below the value of 1 has been recorded on the 2 % SA device.
- The minimum TBP achievable with a device decreases with L_{SA} and reaches a minimum value of 0.5 on the 5 % SA device. At the same time, the region with the lowest TBP values becomes more sensitive to the biasing parameters and shrinks with L_{SA}.
- The maximum spectral width of the pulses increases with L_{SA} (12 nm on the 6 % SA device).
- The wavelength range region with stable ML expands with L_{SA}.
- The most stable ML in terms of the minimum RF linewidth occurs on the 2–5 % SA devices.
- Regions of self-pulsation expand remarkably with L_{SA}, forcing the ML operation towards high I_g and V_{SA} values. The devices with the largest region of ML and minimum region of SP are those with the 2–4 % absorbers.
- The average and peak power scale with the absorber length. The maximum average and peak power values measured within the mode-locking operation of the 6 % SA device are equal to 10 mW and 250 mW, respectively.

Therefore, the SMLLs with short absorbers (up to 4 %) should be chosen for applications requiring stability and pure ML operation, whereas the long-SA devices are appropriate for the high peak and average power applications.

3.4 Comparison Between the 5-QW and 3-QW Devices

The analysis of the 3-QW devices demonstrated a significant improvement with respect to the MLLs fabricated on the 5-QW material. In order to illustrate the difference in performance of the devices fabricated on these two material platforms, the basic parameters have been summarised in Table 3.2, which presents the minimum values of IAC FWHM, TBP and jitter as well as the maximum spectral comb modulation measured on each device. Furthermore, it shows the gain current and SA voltage ranges corresponding to the ML and SP regimes. The mode-locking and self-pulsation have been distinguished based on the numerous features recorded during the pulse characterisation. Mode-locking is usually characterised by a clear intensity autocorrelation trace with subsequent peaks of similar amplitude, an RF spectrum with the fundamental peak at least 25 dB above the signal floor level and with no evidence modulation in the low frequency range (below 5 GHz), and a symmetrical, single-lobe optical spectrum, with a typical FWHM between 4 nm and 12 nm, and comb modulation depth above 10 dB. Self-pulsation, on the other hand, manifests itself in a wide peak dominating the autocorrelation trace, broad and shallowly modulated optical spectrum, usually blue-shifted with respect to the mode-locking spectral region, and finally the clear features on the RF signal occurring typically below 5 GHz. The comparison confirms that the 3-QW MLLs have a significant advantage over their 5-QW counterparts. They emit optical pulses that are ∼2 times shorter (down to 0.7 ps of IAC FWHM), less affected by chirp (TBP as low as 0.8) and more stable (rms jitter of 1 ps). The biasing ranges that produce mode-locking and self-pulsation are clearly distinct in the 3-QW MLLs, especially on short SAs devices (below 5 %). This feature gives pulse trains with no evidence of low-frequency modulations within a wide range of the biasing conditions. The 5-QW devices, on the other hand, are affected by SPs that are evident in a large fraction of the ML region. The presented findings confirm that the material modifications introduced in the 3-QW system indeed reduced the phase noise and jitter, improved mode-locking stability and increased the power emitted from the devices. This is due to the reduced number of QWs and decreased overlap of the optical mode with the cladding layer raised the level of saturated gain. The material improvements help increase the pulse energy, reduce the optical losses, and improve the optical resonator quality factor.

Parameter	5-QW		3-QW					
	SA:2.2 %	SA:3.1 %	SA:1 %	SA:2 %	SA:3 %	SA:4 %	SA:5 %	SA:6 %
Min. IAC FWHM (ps)	1.5	2.4	1.2	0.8	0.8	0.8	0.7	0.7
Min. TBP	1.1	1.4	0.9	0.8	0.7	0.6	0.5	0.5
Max. spectral comb height (dB)	23	20	22	22	22	23	23	23
Min. rms jitter (ps)	4	—	—	—	—	1	—	—
ML range I_g(mA)	60-130	60-110	40-54	45-82	50-100	46-110*	65-120*	80-130*
ML range V_{SA}(V)	2.1-3.4*	2.6-3.3*	1.4-2.3	1.5-3.0*	1.5-3.0*	1.5-3.0*	2.0-3.0*	2.0-3.3*
SP range I_g(mA)	40-100	40-100	38-42	40-50	45-65	40-80	60-100	50-120
SP range V_{SA}(V)	2.2-2.8	2.0-3.0	1.0-2.0	1.0-2.1	1.0-2.2	0-2.3	0-2.8	0-3.0

TABLE 3.2: Comparison between the vital parameters of the examined SMLLs.

3.5 Chapter Summary

Characterisation of the SMLLs fabricated on two material systems (3-QW and 5-QW) over a wide range of biasing parameters enabled the accurate map out of the different dynamical regimes of the devices, such as mode-locking, self-pulsation and continuous wave emission. A systematic study of the lasers with various lengths of the SA demonstrated the importance of careful geometry design for a desired mode–locking performance. The 3-QW MLLs proved superior to the 5-QW devices in terms of the pulse widths, emission stability and chirp. Pulses producing IAC traces with FWHM as low as 0.7 ps were measured with the 5 % SA laser fabricated with the 3-QW material. If a sech^2 pulse intensity profile was assumed, this autocorrelation width would correspond to a temporal FWHM of 450 fs. In order to investigate the actual pulse widths achievable with the devices, phase-sensitive measurements were performed, and will be presented in Chapter 6 of this thesis.

Chapter 4

Two-Photon Absorption Detectors

The TPA detector constitutes a crucial element of the sonogram measurement set-up and it decides on the type of optical pulses which can be characterised. The following device features were considered at the detector design stage:

- detection sensitivity covering the typical peak power levels of the investigated SMLLs, which are in the order of a few tens of milliwatts,
- ability to operate with pulse repetition rates of several tens of gigahertz,
- negligible chromatic (material and waveguide) dispersion for optical pulses down to 500 fs,
- covering the spectral region of 1520–1570 nm, without any significant variation in the detection sensitivity,
- negligible influence of single-photon absorption (SPA),
- low polarisation sensitivity,
- compact and easy to align.

TPA detectors were demonstrated in several material systems and geometries (see Table 4.1). However, these are usually optimised to satisfy only some of the criteria presented above, as most requirements are contradictory and therefore the device design requires a trade-off. For instance, the ultra low sensitivity achievable with GaAs PMTs [101] or InGaAsP laser diodes [102] comes at a price of bulky and expensive set-ups or multipath operation and polarisation sensitivity. Similar, the enhanced detection ability

Device	Sensitivity	Limitations
Silicon waveguide [47]	$1\,\mathrm{mW}^2$	Relatively long device (1.7 cm) and FP resonances
MQW GaAs laser [89]	$0.28\,\mathrm{mW}^2$	FP resonances
InGaAsP waveguide[48, 104]	$0.08\,\mathrm{mW}^2$	FP resonances
InGaAsP laser diode [102]	$1.5\times10^{-4}\,\mathrm{mW}^2$	FP resonances and polarisation sensitivity
Si avalanche photodiode [105]	$2\,\mathrm{mW}^2$	extensive SPA
Microcavity structure [106]	$9.3\times10^{-4}\,\mathrm{mW}^2$	Limited bandwidth (high cavity finesse) and multipath operation
GaAs PMT tube [101]	$1.7\times10^{-4}\,\mathrm{mW}^2$	Bulky and expensive

TABLE 4.1: Comparison between different approaches for TPA detection around $1.55\,\mu$m.

achieved in resonant microcavity structures [103] results in a strong wavelength dependence, both in terms of signal bandwidth and operating wavelength. Also, the multipath operation increases the dispersion accumulated by the pulses and makes the control of the spatial overlap between the interacting pulses rather difficult.

In this project, the TPA detection has been based on the approach from [48, 104], as it provides relatively high sensitivity and high detection bandwidth in a relatively cheap and compact system. The disadvantage of the FP resonances was eliminated by designing the structure to operate in a traveling-wave geometry. That would allow us to obtain relatively high sensitivity and high bandwidth detection in a reasonably cheap and compact system.

The chapter first introduces the TPA material system, the numerical simulations, and geometry of the designed waveguides. This is followed by the description of the fabrication procedures and the details of the main technology processes. The chapter concludes by presenting and discussing the results of the experimental tests performed with the fabricated detectors.

4.1 Material Considerations

The wafer structure for the TPA devices was based on a design proposed in [48], with an InGaAsP waveguide structure grown on a sulphur-doped InP substrate. An epitaxial structure with a bulk waveguide region was chosen in order to increase the polarisation insensitivity of the devices [107] compared to a QW system. The QW structure could also promote undesirable phase modulation mechanisms, such as space phase filling caused by the sub-picosecond-scale relaxation transitions of the excited carriers within the QWs

[108]. The designed bandgap energy of the absorption layer was a trade-off between the requirement for a high TPA coefficient, β_2, and a sufficient detuning between the energy of the bandgap and the photons, in order to minimise SPA. The theoretically predicted and experimentally confirmed [109] Van Stryland's scaling rule allows for an assessment of the spectral dependence of β_2 on the material bandgap:

$$\beta_2 = \frac{K \cdot \sqrt{E_p \cdot F_2(2E_{phot}/E_g)}}{n^2 \cdot E_g^3}, \tag{4.1}$$

where K=3100 is a constant independent from the material, E_p=21 eV is related to the Kane momentum parameter and is nearly material independent for a wide variety of semiconductors [110], E_{phot} and E_g are the photon and bandgap energies, n≈3.4 is the refractive index of the core, and F_2 takes the following form:

$$F_2(x) = \frac{(x-1)^{3/2}}{x^5}, \tag{4.2}$$

where $x = 2E_{phot}/E_g$. The calculated dependence of β_2 on the energy bandgap ranging 0.8 – 1.46 eV (1550 – 850 nm) and for E_{phot}=1550 nm, is displayed in Fig.4.1.

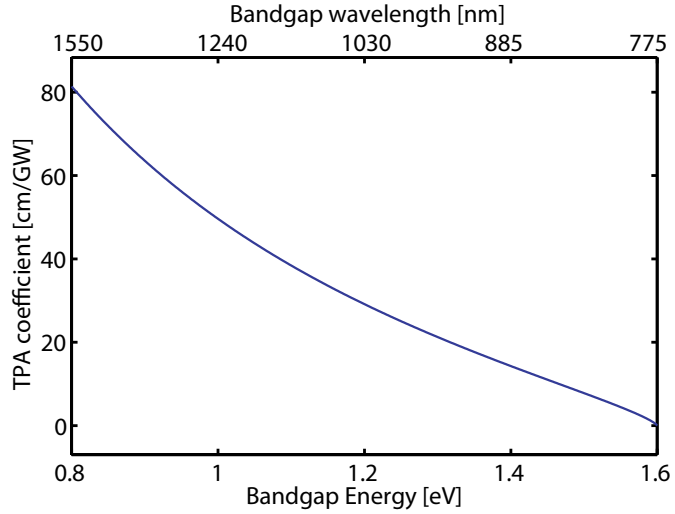

FIGURE 4.1: Theoretical prediction of the two photon absorption coefficient dependence on the active material bandgap energy for E_{phot}=1550 nm

In order to limit the amount of direct absorption, the material band-edge of 0.9185 eV (1350 nm), i.e. detuned by ∼120 meV with respect to the measured SMLL emission, has been selected. According to Fig. 4.1, such a choice of the band-edge value produces only a 10 % drop of β_2 compared to its maximum level available close to 1550 nm. The material composition for the guiding layer is derived with the Vegard's law for an $In_{1-x}Ga_xAs_yP_{1-y}$ lattice matched to InP [111], as presented in Eq. 4.3–4.4:

$$E_g(y) = 1.35 - 0.72y + 0.12y^2, \tag{4.3}$$

Thick.($\AA$)	Material	PL(nm)	Dop.	Type	Name	Conc.(cm^{-3})
1000	$In_{0.53}Ga_{0.47}As$	-	Zn	p	Cont. layer	1E+19
500	$In_{0.53}Ga_{0.47}As_{0.33}P_{0.67}$	1100	Zn	P	Cap layer	1E+18
6000	InP	-	Zn	P	P-clad. layer	1.5E+17
200	$In_{0.85}Ga_{0.15}As_{0.33}P_{0.67}$	1100	Zn	p	Wet etch stop	1E+17
2000	InP	-	i	–	InP layer	-
500	$In_{0.815}Ga_{0.185}As_{0.41}P_{0.59}$	1150	i	-	SHC layer	-
5000	$In_{0.68}Ga_{0.32}As_{0.68}P_{0.32}$	1350	i	-	Active layer	-
500	$In_{0.815}Ga_{0.185}As_{0.41}P_{0.59}$	1150	i	-	SHC layer	-
15000	InP	-	Si	N	Buffer layer	2.4E17
-	InP	-	Si	N	Substr. (100)	1.3E18

TABLE 4.2: TPA wafer epistructure

$$E_g(x,y) = 1.35 + 0.668x - 1.17y + 0.758x^2 + 0.18y^2 - 0.069xy - 0.322x^2y + 0.03xy^2. \quad (4.4)$$

The As composition, y, is used for the calculation of the material bandgap, E_g, while the lattice matching is realised by adjusting the Ga composition with the relation presented in Eq. 4.4. Solving these two equations for the desired band-edge level gives y=0.68 and x=0.32, bringing $In_{0.68}Ga_{0.32}As_{0.68}P_{0.32}$ as the quaternary compound for the absorption layer material.

The material refractive index, n=3.43, was calculated with the fitting parameters, A_1, A_2, and Eq. 4.5, as described in [112]:

$$n_y = \sqrt{1 + \frac{A_1}{1 - (\frac{E}{E_p + E_1})^2} + \frac{A_2}{1 - (\frac{E}{E_p + E_2})^2}}, \quad (4.5)$$

where E_1=2.5048 eV, E_2=0.1638 eV, A_1, and A_2 are the fitting parameters calculated from the PL wavelength, E_p:

$$A_1 = 13.3510 - 5.4554E_p + 1.23332E_p^2, \quad (4.6)$$

$$A_2 = 0.7140 - 0.3606E_p. \quad (4.7)$$

The schematic composition of the wafer structure is presented in Fig. 4.2. The absorption layer thickness is set to 0.5 μm and the waveguide structure is completed by two 50 nm thick intrinsic $In_{0.815}Ga_{0.185}As_{0.41}P_{0.59}$ separate confinement heterostructure (SCH) layers, with a PL wavelength of 1150 nm. The p-side has a 0.2 μm thick undoped InP layer and p-doped layers (0.67 μm thick), terminated with a highly-doped contact layer (0.1 μm thick). The p-i-n diode is realised for the high built-in electric field, allowing efficient collection of the photogenerated carriers without any external biasing [48, 104]. Further details on the epistructure can be found in Table 4.2. The wafer

FIGURE 4.2: Composition of the wafer structure used for the TPA detectors fabrication

was grown by the EPSRC National Centre for III-V Technologies at the University of Sheffield.

4.2 Design and Simulations

4.2.1 Waveguide Design

The lateral confinement in the TPA detectors is realised by index guiding through a ridge waveguide. Such guiding can be achieved with two etching geometries. In shallow etched structures ($\Delta n \leq 0.1$) the ridge is formed above the core layers in such way that the optical mode does not interact strongly with the ridge structure, and therefore sidewall scattering losses are minimal. As a result of the low lateral confinement the optical mode spreads out. The efficiency of the TPA detection strongly depends on the light intensity (quadratic dependence), so a strong lateral confinement is desired. By employing deeply etched structures, where the etching goes through the core layer, the horizontal confinement of the optical mode can be largely improved. Numerical calculations of the deeply etched structures were performed with the BeamPROP mode solver. The ridge height is 2.47 μm so that the etching reaches into the InP buffer layer, 1 μm below the bottom of the core layer. Example of the mode profiles (with TM polarisation) calculated in a 1 μm wide shallow and deep etch waveguides are shown in Fig. 4.3. As expected, a significant improvement in the mode lateral confinement in the deep etch structure compared to its shallow etch counterpart can be observed. The waveguide should operate in a single-mode regime, as multi-mode operation could decrease TPA efficiency (due to lower peak intensity levels), as well as introduce undesirable measurement errors caused by modal dispersion. Fig. 4.4(a) presents the effective refractive index, n_{eff}, of the simulated structures as a function of the waveguide ridge widths, calculated for the first three TM modes. The deeply etched waveguides become single-mode below a width of $\sim$2.5 μm.

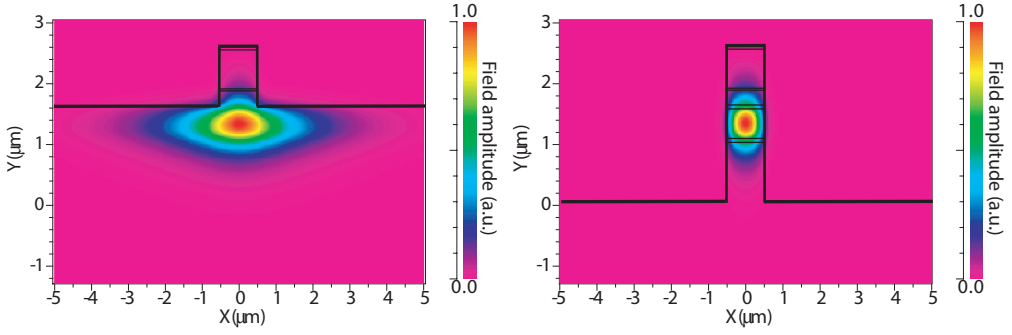

FIGURE 4.3: Modeled TM mode profiles in 1 μm wide (a) shallow and (b) deep etched waveguides.

The range of waveguide widths of 0.8 – 2 μm ensures single-mode operation and strong lateral mode guiding in the core layer. Fig. 4.4(b) plots the n_{eff} for the TE and TM fundamental modes and shows that the lowest polarisation sensitivity can be expected around the ridge width of 1.4 μm. However, there might be some discrepancies between the TPA response for the TE and TM polarisations due to the polarisation sensitivity of the TPA process. In zinc-blende semiconductors the third order susceptibility – hence, also the TPA – is dependent on the orientation of the polarisation to the crystal axes, even in a single-beam linearly polarised case. For instance, the anisotropy of the TPA coefficient between the polarisation orientations (related to the crystal axes) in GaAs can be as high as 70 % [113].

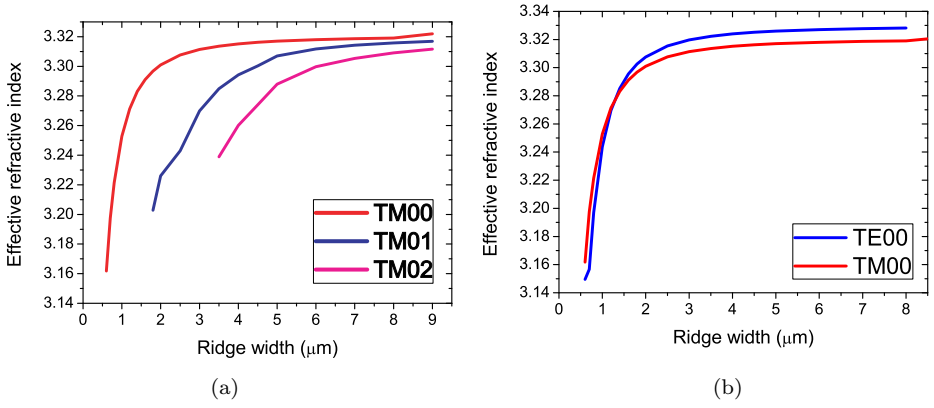

FIGURE 4.4: Calculated effective refractive index of deeply etched ridge waveguides as a function of the ridge width. (a) n_{eff} for the first three TM modes, (b) n_{eff} for the fundamental TE and TM modes.

4.2.2 Device Geometry Design

The devices were designed to operate in a traveling-wave mode by suppressing the FP cavity oscillations. The single-pass operation minimises the dispersion encountered by a pulse and allows precise control of the overlap between the cross-correlated pulses. An overview of the detector's geometry is sketched in Fig. 4.5.

FIGURE 4.5: Overview of the TPA detector geometry (not to scale).

The role of the adiabatically tapered input section is to maximise a coupling efficiency from free-space. A set of devices was fabricated and tested with input waveguide widths of 2 μm, 4 μm and 6 μm, and a straight detection waveguide widths changing from 0.5 μm to 2 μm. Finally, the output section is down-tapered and tilted (10°) to minimise back-reflection from the output facet. Each section is designed to have its own metal p-contact with gaps between the adjacent pads of at least 30 μm. Only the main section contact pad is used during the pulse characterisation, while the role of the contact above the input taper is to enable forward biasing in order to simplify the coupling and alignment procedures. Reverse biasing the output taper contact increases the optical absorption and therefore decreases even further the FP oscillations. The individual devices were fabricated on a single chip and were spaced by 200 μm, with additional mechanical support structures placed between them to protect the waveguide ridges from any lateral stress.

4.3 Fabrication of the Two-photon Absorption Detectors

4.3.1 Lithography and Etching Processes

All lithography steps were performed with Vistec VB6-UHR-EWF EBL 100 keV electron beam lithography (EBL) tool, due to its flexibility and high resolution, allowing efficient fabrication of prototype devices with sub-5 nm resolution [114]. Hydrogen silsesquioxane (HSQ) spin-on-glass negative tone resist was employed for direct definition of the waveguide etch mask because of its high-resolution (below 10 nm), small line edge roughness,

high sensitivity and high resistance to chemical etching [115]. Upon exposure of HSQ to high energy radiation, a chain of chemical reactions transforms the silicon hydride (Si-H) groups bounded to oxygen into siloxane (Si-O-Si) bonds, which are resistant to aqueous base developers [116]. The exposed patterns are then developed with tetramethylammonium hydroxide (TMAH) diluted with reverse osmosis (RO) water (1:1). The precise definition of the *p-i-n* waveguide etch mask is a critical step in the fabrication process and requires determining the optimum electron-beam (EB) parameters. Hence, a dose test was performed on a chip with several patterns, each comprising a set of waveguides of different widths. The exposure dose was gradually increased for each set from 200 μC/cm^2 to 1200 μC/cm^2 and the pattern was subsequently developed and inspected. Additionally, the proximity error correction (PEC) [82] was used in order obtain the same clear-out dose for all the patterned features. The *proximity effect* comes from the secondary electrons backscattered from the substrate, which contribute to the overall exposure. The extent of this effect is non-uniform across the written pattern and decreases towards the edges and corners, as the backscattered electrons have a limited range and these areas are eventually subjected to decaying levels of exposure. In order to achieve a more uniform distribution of the EB exposure and to avoid underexposed edges and corners (or overexposed areas) the PEC software adjusts the applied dose by accounting for the additional exposure of the backscattered electrons. Fig. 4.6(a) and Fig. 4.6(b) show the comparison between the dose tests performed without and with the PEC. Both figures present the thicknesses of the developed resists with various widths of the test waveguides. The results obtained without the correction show that the wider waveguides - 10 μm - are developed at much faster rates than the narrower - 4 μm patterns, as a result of more backscattered electrons. The narrowest shapes (0.5 μm) were underexposed even with the highest EB dose used in the non-PEC tests. A considerable improvement can be observed in Fig. 4.6(b), as a consequence of the PEC, which produced consistent exposure levels for all the structures. The dose of 330 μC/cm^2 was chosen for the optimum exposure level as it gives the best uniformity of residual resist thickness throughout the waveguide patterns. Higher doses, shown in the flat part of the the graph, correspond to an overexposure and produce wider waveguides.

Other EBL steps, such as the definition of the lift-off and contact window masks were performed with a high resolution positive tone poly(methylmethacrylate) (PMMA) resist. A usual double-layer stack of PMMA produces a uniform coating and undercut profiles are avoided if a lower sensitivity resist is chosen for the top layer [82]. The most critical aspect of the fabrication procedure was the waveguide etching. A first set of etching tests with an ET340 reactive ion etching (RIE) tool using a $CH_4/H_2/O_2$ gas mixture revealed inconsistencies in the etching depth between successive runs as well as extensive surface roughness. The unstable etch rate values of the test samples were

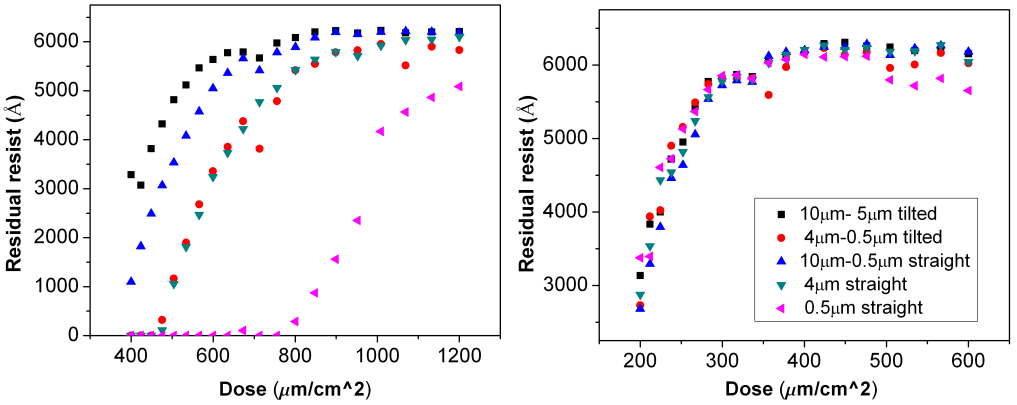

(a) (b)

FIGURE 4.6: HSQ resist thickness after development at various dose exposure levels, (a) with no proximity correction and (b) with the proximity correction.

caused by the formation of polymeric compounds in the etching tool chamber. Hence, an alternative technique, a Cl_2–based etch chemistry, was tested (recipe development and sample processing was done by the author's colleague Dr. Rafal Dylewicz). The inductively-coupled plasma (ICP) process based on a $Cl_2/Ar/N_2$ gas mixture allows for deep etchings with high aspect ratios, fast etch rates and anisotropic etch profiles in InP-related materials [117]. The role of the individual chemistry components are as follows: Cl_2 is the reactive gas, Ar acts as a sputtering component and N_2 passivates the surface of the treated sample. Before the actual etching process the sample was treated with O_2 plasma to increase the resistance of the HSQ mask. Fig. 4.7(a) and Fig. 4.7(b) show the scanning-electron microscope (SEM) pictures of the etched waveguide structures, taken after the ICP etching stage. Although highly vertical side-wall profiles have been achieved in the waveguides, a residual side-wall roughness is still present. In spite of this drawback, optical measurements showed that the fabricated waveguides exhibited low-loss performance and a high TPA coefficient. Hence, the ICP method along with the $Cl_2/Ar/N_2$ chemistry was used to fabricate the final TPA detectors.

4.3.2 Fabrication Steps

The fabrication process applied in development of the TPA detectors is based on the typical procedures and recipes used in the Optoelectronics Research Group at the University of Glasgow to fabricate InP-based semiconductor devices. The process can be be summarised in six basic stages, as visualised in Fig.4.8.

1. **Sample Preparation**

   The fabrication procedure begins by cleaving a two inch wafer into rectangular

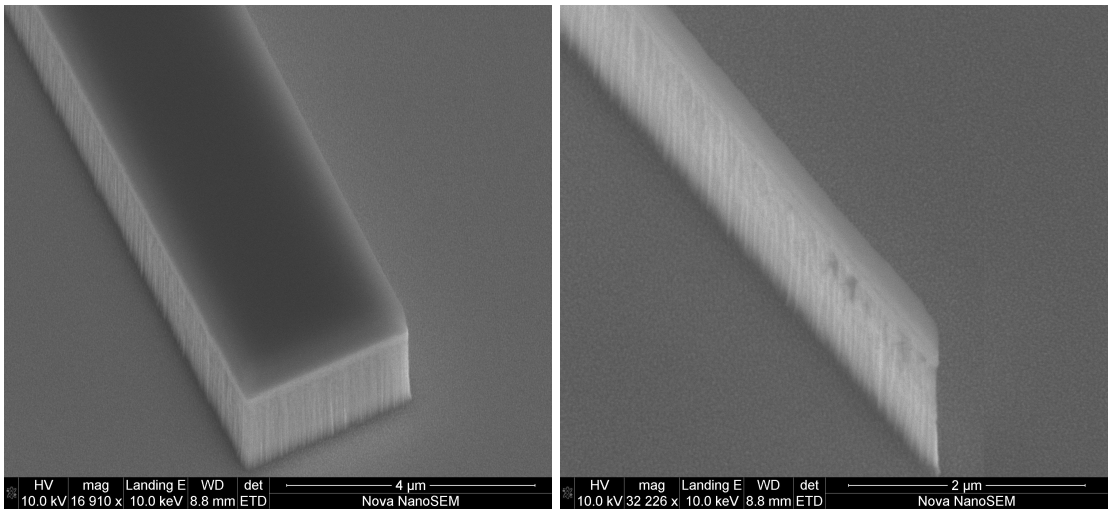

(a) (b)

FIGURE 4.7: SEM pictures of the etched test waveguides. (a) $3\mu m$-wide, straight waveguide and (b) the end of a down-tapered output.

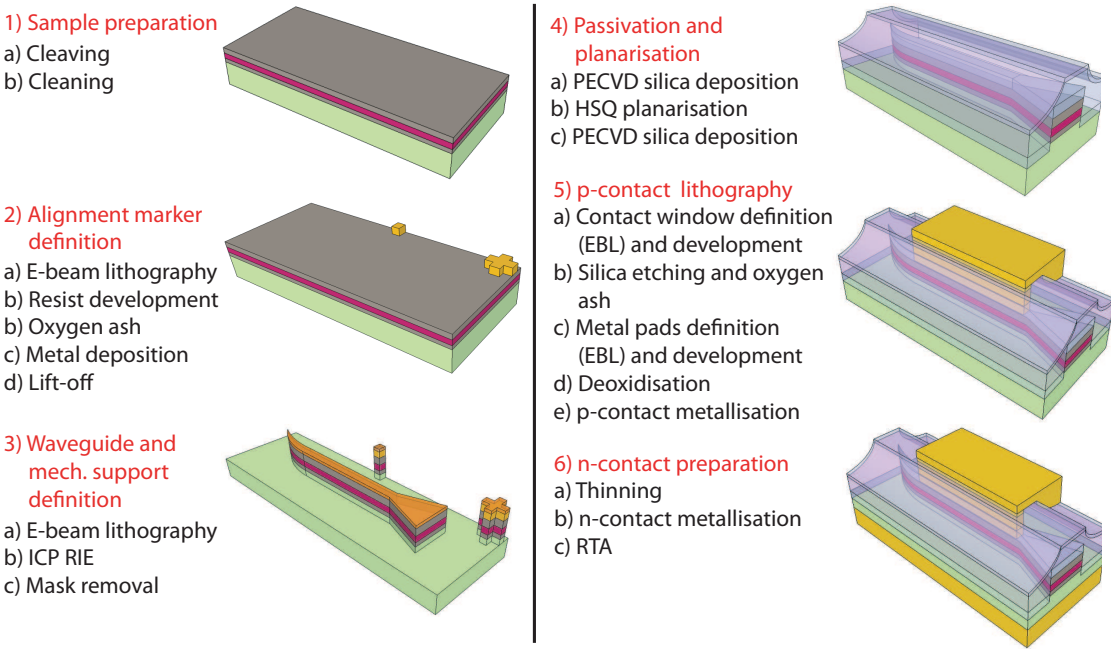

FIGURE 4.8: Visualisation of the main fabrication steps. For better clarity the alignment markers are displayed only up to the third stage.

samples (11×12 mm) with edges parallel to the (100) crystallographic plane. Subsequently, the sample is cleaned (inorganic and organic contaminants) in a three-stage ultrasonic bath of Opticlear, acetone and isopropyl alcohol (IPA), followed by drying with a nitrogen gun. Next, any residue of the solvents are removed with an oxygen plasma ash. Finally, the sample is dried with nitrogen and baked on a hot plate in order to remove water adsorbed on the surface.

The sample cleaning procedures are also implemented between subsequent fabrication steps but are usually limited to a rinse in acetone and IPA. To minimise the risk of the ridge structures breakage, no ultrasonic treatment is applied after the waveguide definition stage.

2. **Alignment Markers Definition**
   The entire fabrication process involves more than one lithography step, which imposes the definition of alignment markers to determine the precise location and orientation of the desired pattern. Gold markers are the best option as they provide a positive intensity contrast to the EBL tool and allow for high alignment accuracy. The procedure begins by spinning two layers of PMMA (methyl isobutyl ketone (MIBK)-diluted, 15 % and 4 %, respectively). The sample is subsequently exposed to EB patterning and developed in MIBK. At this stage it is important to check not only the quality of the developed pattern but also to confirm the accuracy of its rotational alignment (target alignment error below 0.5°). The Ti/Pt/Au deposition is followed by a lift-off process in hot acetone to remove the double-layer PMMA along with the metal stack deposited on the top of it. Finally, the sample is cleaned in ultrasonic IPA, dried and inspected under the optical microscope.

3. **Waveguide and Mechanical Support Definition**
   The waveguides and the supporting mesa etch masks are defined in a single lithographic step. A single layer of undiluted HSQ resist (FOX-16) is spun on the sample, which is next baked on a hot plate and exposed to the EB pattering. Next, the resist is developed, examined under the optical microscope and verified with a Dektak. The sample is processed with the ICP etch and examined with an SEM for quality, smoothness, verticality and dimensions of the etched waveguides. Finally, the resist is removed with HF:H_2O acid solution.

4. **Passivation and Planarisation**
   Before the deposition of the metallic contacts on the p and n side of the wafer a dielectric coating that fully covers the waveguide ridges is deposited on the p-side. It prevents an electric short between the p and n sides, increases the dielectric breakdown voltage and decreases the propagation losses by spatially separating the metallic electrodes from the guided light beam. The use of an extra layer of

HSQ ("spin-on-glass") reduces any height non-uniformities and step-like profiles across the sample. The height of this layer varies across the etched pattern as it is thinnest above the waveguide and becomes thicker away from it, creating a smoother surface above the transitions between the ridges and the trenches. This technique, known as a quasi-planarisation [82], improves the quality and robustness of the subsequent deposition of metal contacts. The complete process includes the deposition of 200 nm of plasma enhanced chemical vapour deposition (PECVD) silica as an isolation layer, followed by spinning and baking of a ∼450 nm thick layer of HSQ. The final 100 nm thick PECVD silica layer, deposited for improved adhesion of the *p*-contact metal, completes the dielectric stack.

5. **Preparation of the *p*-type Contacts**
   Separate contact windows are defined directly above the component of the TPA devices with EBL. After resist development and optical microscope inspection of the mask, the contact windows are etched with a CHF_3/Ar chemistry. Next, an oxygen plasma ash is used to remove resist residues in order to prepare the sample for a final lithographic step, in which the PMMA lift-off mask for the contact pads is defined. Before the metal deposition the contact windows are examined, cleaned with oxygen ash and deoxidised with a HCL:H_2O (1:4) etch. The stack of Ti, Pt and Au [118] is used for the *p*–type contact. A 30 nm thick Ti coating acts as an adhesion layer because of its high reactivity and oxidisation capability. A 60 nm thick Pt layer is deposited next, in order to prevent the atoms of the 240 nm thick top Au layer from diffusing into the semiconductor material. The metal contacts along with the contact pads and identification marks are shown in Fig. 4.9(a).

6. **Preparation of the *n*-type Contacts**
   The sample is first mounted top-side down on a glass slide with a S1818 photoresist spun, which protects the previously fabricated structures. Next, it is is thinned down to ∼200 μm by mechanical polishing in a 9 μm diameter Al_2O_3 colloid, cleaned, processed with oxygen ash, and deoxidised. Finally, a standard *n*-contact metal stack of Au/Ge/Au/Ni/Au [62, 119] is evaporated and alloyed by rapid thermal annealing (RTA) at 380 °C. The fabrication process is terminated by cleaving the processed chip into individual bars (device facet shown in Fig. 4.9(b)), which are glued *n*-side down on brass sub-mounts with conductive silver epoxy. This arrangement allows for convenient handling of the samples and stable mounting on the measurement set-ups.

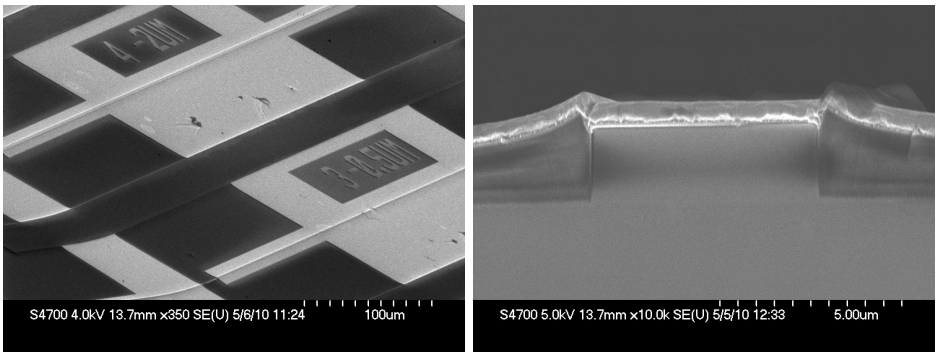

(a) (b)

FIGURE 4.9: SEM pictures of the completed TPA detectors. (a) View of the top side of the devices with the etched waveguides, *p*-contact pads, and mechanical trenches. (b) View on the detector facet with the contact window, passivation and planarisation layers and metal *p*-contacts.

4.4 Performance of the Two-photon Absorption Devices

4.4.1 Electrical Properties

Before optical characterisation, the devices underwent preliminary electrical tests. The value of the resistance of the forward-biased p-n junction was measured to be within 3.5 Ω and 5.0 Ω, which agrees well with the resistance of other InP devices of similar geometry [62, 82]. Also, the resistance between adjacent sections and between different devices (≈4 kΩ and 40 kΩ, respectively) proved to be a sufficient insulation against electrical cross-coupling. The average value of the dark current at a reverse bias level of -2 V stayed around a negligible value of a few pA.

4.4.2 Propagation Loss Measurements

The transmission losses of the TPA waveguides were characterised around the wavelength of 1550 nm to assess the optical quality of the waveguides. For loss measurements, the devices comprising of only two sections (i.e. a tapered input and a 2 mm long detection section), and having two cleaved mirrors, were fabricated. The measurement was performed with the FP resonance technique [120], in which the light emitted from an external tunable laser is transmitted through the ridge and the loss is deduced from the contrast ratio of the FP oscillations detected at the waveguide output. The measurement set-up is shown in Fig. 4.10, in which a commercial wavelength tunable LD source is used to scan through the spectrum from 1540 nm to 1570 nm. The light is next collimated, optically chopped, filtered with a PBS and coupled into the waveguide. Finally, the

output light is detected with a photodiode connected to a lock-in amplifier. The whole set-up is controlled by a PC with LabVIEW data acquisition software.

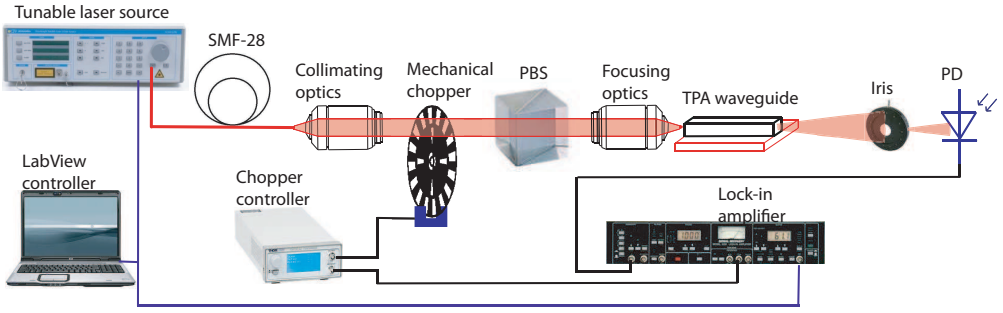

FIGURE 4.10: Test set-up for the measurements of transmission losses in the TPA waveguides.

To only measure the contribution of the direct band gap absorption without the influence of the TPA, the intensity of the emitted light from the tunable laser is kept below 100 μW. A typical transmission spectrum obtained in the loss measurements is shown in Fig. 4.11. The FP resonances maxima and minima, I_{max} and I_{min}, are related to the cavity transmission losses, α, mean facet reflectivity, R, and the cavity length, L, via:

$$\alpha = -\frac{1}{L} ln(\frac{K-1}{R(K+1)}), \tag{4.8}$$

and

$$K = \sqrt{\frac{I_{max}}{I_{min}}}. \tag{4.9}$$

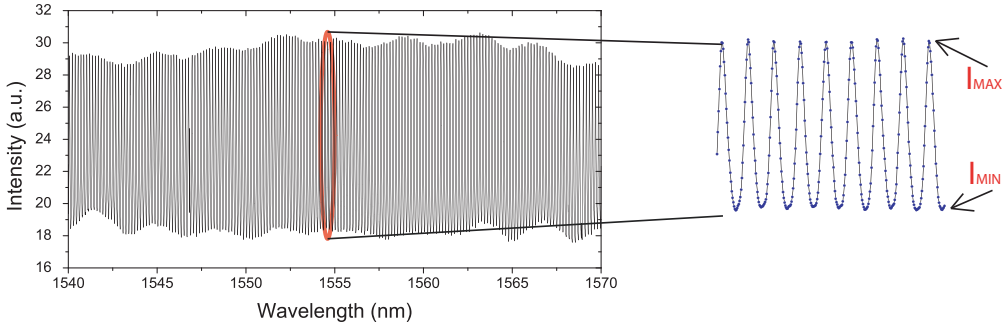

FIGURE 4.11: Transmission spectrum of a 6 μm wide waveguide ridge for TE linearly polarised light. On the right side a zooming of the FP modulation fringes around 1554 nm.

The transmission losses as a function of the wavelength measured on a 6 μm wide waveguide for TE and TM input polarisations are shown in Fig. 4.12(a). The graph shows that the TM-polarised light experienced higher attenuation than the TE state (~30 %), as expected from the higher confinement of the TE polarized light due to the modal birefringence caused by different effective indices for the both polarisations and, as a results, deeper penetration of the TM modal field into the doped layers. The loss figures

are quite uniform within the measured range and vary between 6.5–8 dB/cm and 8.5–10 dB/cm for the TE and TM polarisation, respectively, which compares favourably with the loss values presented in literature for similar InGaAsP/InP structures (>20dB/cm) [121]. Fig.4.12(b) presents the measured losses vs. the waveguide ridge width. The increase in the transmission losses with decreasing width is well fitted with an exponential curve and is due to scattering losses and substrate coupling. It should be noted that for the multimode waveguides (i.e. wider than 2.5 μm) the FP technique might be affected by measurement errors due to the screening effects, caused by the different transverse modes. This leads to a reduced modulation ratio and therefore to an overestimation of the losses.

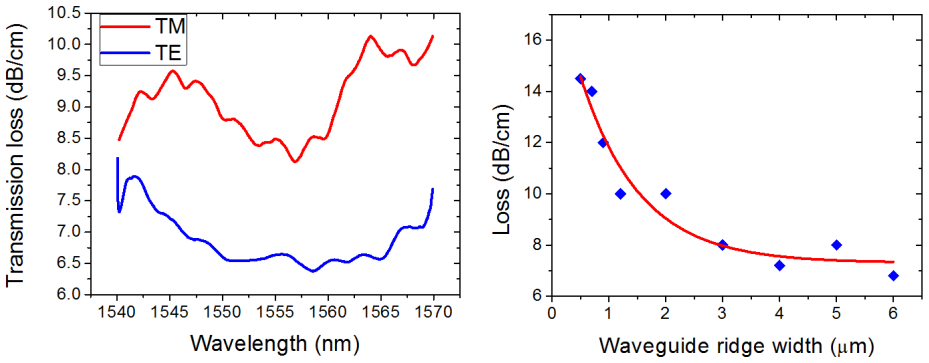

(a) (b)

FIGURE 4.12: (a) Transmission loss spectrum of a 6 μm wide detector measured with TE and TM polarisation states. (b) Transmission loss dependence on the waveguide ridge width measured with TE-polarised light.

4.4.3 TPA Response Measurements

A series of experiments have been performed to confirm the suitability of the detectors for the characterisation of optical pulses emitted by SMLLs. The TPA photo-response was measured on standard traveling-mode devices, with a 1 mm long detection section. A 2.5 ps-FWHM pulse train produced by a wavelength tunable actively mode-locked fiber laser (PriTel, Inc.), operating with a repetition frequency of 10 GHz, is coupled into the waveguide. The photocurrent generated in the detectors is directly measured with a lock-in amplifier and the power and polarisation of the light coupled into the detectors are controlled with a tunable optical attenuator and an all-fiber polarisation controller, as presented in Fig. 4.13. The test pulses are continuously monitored with an OSA, a Femtochrome autocorrelator and a power meter in order to monitor the pulse parameters, such as FWHM, average and peak power, and energy.

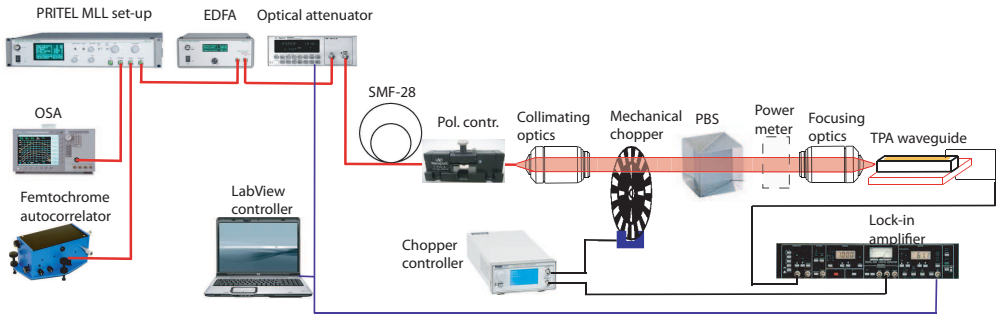

FIGURE 4.13: Test set-up for the measurements of the TPA response of the detecors.

Fig. 4.14 shows a typical photocurrent response of the TPA waveguide detector as a function of the pulse peak power, taken on a device with a 6 μm wide input and 1 μm wide detection waveguide. Three regions of operation can be identified in the photo-response characteristic. For a peak power above the value $\approx$5 mW (pulse energy of 11 fJ, detection sensitivity of 0.6 mW^2 and current response of 2.8 nA/mW^2) the detector exhibits clear quadratic response, indicating overwhelming TPA influence on the photo-generated carriers. A combined response, comprising of linear and quadratic behaviour, persists down to pulse peak power values $\approx$200 μW (pulse energy of 0.55 fJ and detection sensitivity of 1×10^{-3} mW^2). For even lower intensities, only a linear characteristic was recorded. The inset in Fig. 4.14 displays an interferometric autocorrelation trace taken with a pulse peak power corresponding to a clear quadratic response of the detector. The autocorrelation envelopes ratio of 7.6-to-1 confirms a prevailing presence of the TPA effect in the photocurrent response. The discrepancy between the measured envelopes ratio and an ideal 8-to-1 ratio is caused by the residual direct absorption and misalignments in the autocorrelator set-up.

The dependence of the photocurrent generated in the detection section on the peak power of the input pulses has been evaluated on a set of devices with various waveguide widths, for both TE and TM input polarisation states, and with the pulse optical spectrum centred at 1550 nm. The best performance was obtained on devices having the widest tapered input (6 μm), for which the coupling efficiency is optimised. The measured minimum pulse peak power producing a clear quadratic response as a function of the waveguide width is plotted in Fig. 4.15. Devices with a detection section width between 0.8 μm and 1.6 μm show the highest sensitivity for TM polarisation. This is due to the trade-off between the guiding capabilities of the rib waveguide structures, as they weaken with decreasing ridge width, and the maximum local intensities obtained in the waveguide, which scale down with the increased waveguide dimensions. The sudden loss in the sensitivity below the width of 0.8 μm corresponds to the drop in the effective refractive index for the fundamental transverse mode, as predicted by the numerical simulations (Fig. 4.4). The simulations show that waveguide would maintain its guiding

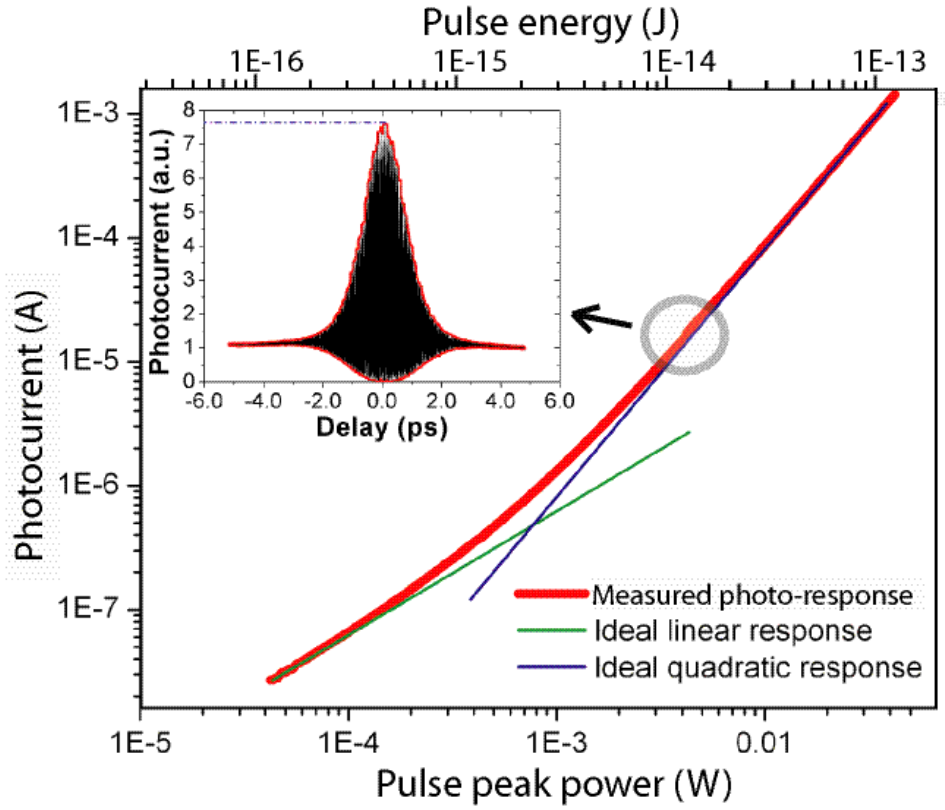

FIGURE 4.14: Photocurrent vs. pulse peak power response of 1 μm wide detector with TM-polarised light. Inset: the interferometric autocorrelation taken with pulses corresponding to the quadratic response region of the detectors.

properties for a slightly narrower ridge width with TM-polarised light. That explains why the detectors exhibit high sensitivity down to 0.7 μm for this polarisation state. For the devices with the ridge width between 0.8 μm and 1.6 μm, the minimum detectable pulse peak power is in the range of 6 – 13 mW. It should be noted that all the values of the pulse power levels presented in this work refer to the power before coupling the light into the TPA input waveguide and do not therefore take the insertion losses or coupling into account. With typical insertion losses in the range of 6 – 8 dB, the minimum in-waveguide peak pulse power is well below 1 mW. The minimum polarisation sensitivity was observed for waveguide widths between 1.0 μm and 1.2 μm.

Finally, the sensitivity (for TE polarisation) of the 1.0 μm wide detector was examined in the wavelength range of 1525 – 1570 nm (inset in Fig. 4.15) by varying the center wavelength of the pulses emitted from the fiber MLL. The sensitivity, defined as the minimum peak power producing a clear quadratic photocurrent response, ranges between 5 mW and 6 mW, which confirms a wide operating wavelength range of the devices. The obtained values of sensitivity are improved when compared with that of the TPA shallow etched waveguide detector fabricated in a similar material structure, and operating in a non-travelling wave mode, with a pulse peak power sensitivity of 29 mW [48].

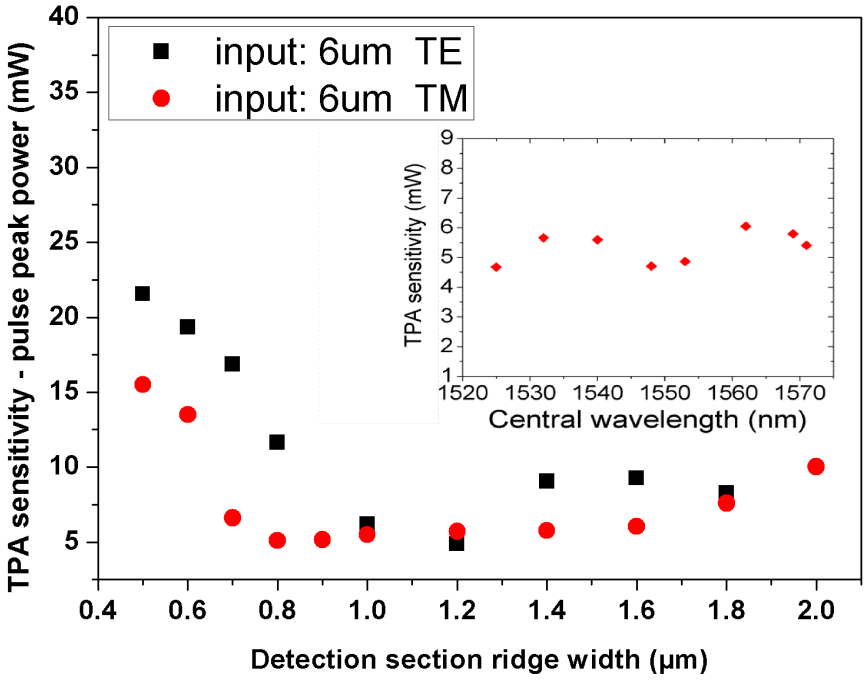

FIGURE 4.15: TPA sensitivity to TE and TM-polarised light as a function of the detection waveguide width for the devices with a 6 μm wide input. Inset: TPA sensitivity to TE polarised light of a 1 μm wide waveguide detector.

4.4.4 Dispersion in the Two-photon Absorption Detectors

The chromatic dispersion encountered by a pulse propagating in the TPA waveguides imposes a limit to the minimum temporal width of the pulse that can be characterised without introducing considerable measurement errors. The figure of merit applied for this analysis is the pulse critical pulsewidth, τ_c, which is defined as the width for which a pulse traveling in a dispersive medium of length L broadens by a factor of $\sqrt{2}$. As the fabricated detectors with the ridge widths below 2 μm operate in a single-mode regime, the two main contributions to the overall chromatic dispersion are material and waveguide dispersions. The critical pulsewidth can be calculated from the GVD with the following formula [75]:

$$\tau_c = \sqrt{|GVD|\frac{2ln(2)\lambda^2 L}{\pi c^2}}, \tag{4.10}$$

where λ is the pulse central wavelength.

The GVD is calculated in a similar manner as presented in Section 2.3.4. The longitudinal mode spacing is extracted from the FP modulation pattern measured on a single-mode waveguide section having a length of 2 mm and a width of 1.0 μm .

Experimental results presented in Fig. 4.16 indicate that the longitudinal mode separation has a similar trend for the TE and TM polarisation states. The effective refractive

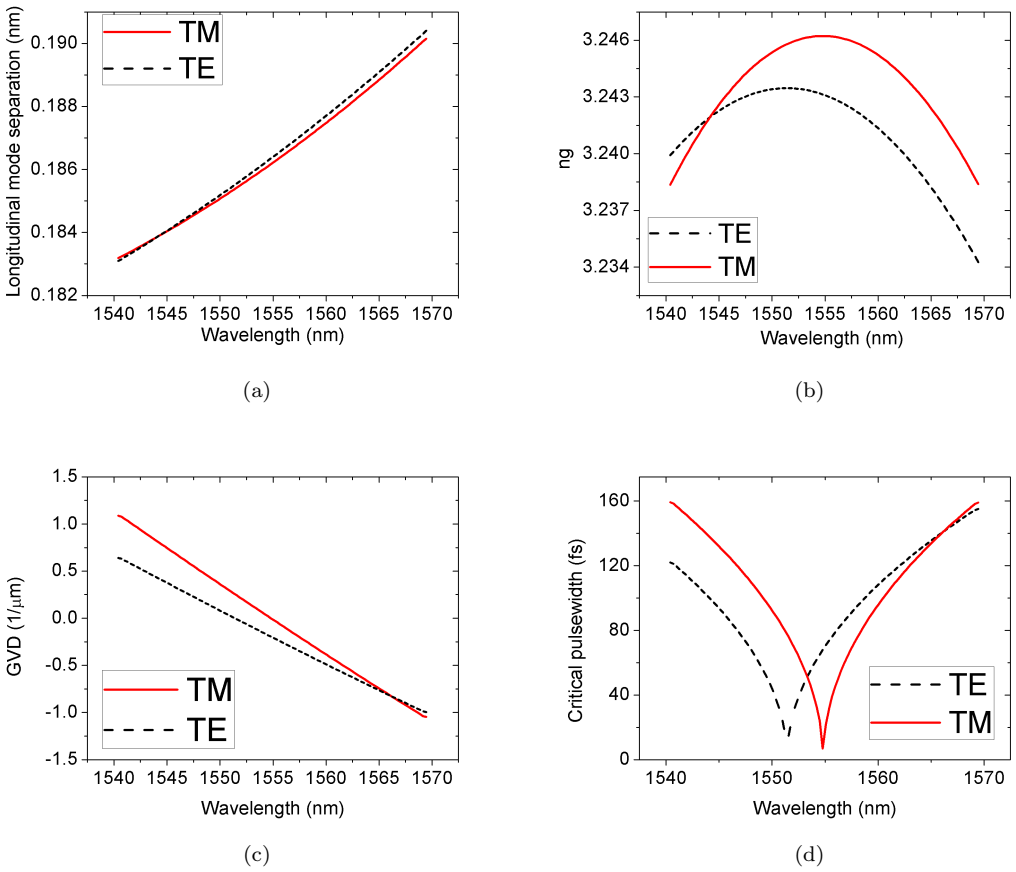

FIGURE 4.16: Results of the dispersion measurement in a 2 mm long and 1.0 μm wide TPA waveguide, performed with the TE and TM input polarisation states. (a) Measured longitudinal mode separation and calculated (b) effective refractive group index, (c) GVD, and (d) critical pulsewidth

.

group index, n_g was calculated with Eq. 2.14 and is shown in Fig. 4.16(b). The overall effect of the combined waveguide and material dispersions produces a monotonically decreasing characteristic, crossing the zero dispersion point around the wavelength of 1552 nm and 1557 nm for TE and TM polarisations, respectively. The maximum critical pulsewidth value obtained within the measured spectral range is equal to 160 fs for both the TE and TM states, as presented in Fig. 4.16(d). This confirms, that the maximum dispersion introduced by a single-pass propagation in the TPA waveguides does not introduce substantial dispersion, as the minimum pulse width produced by the SMLLs is expected to be around 500 fs. Furthermore, the detector employed in the sonogram set-up introduces even less dispersion, as the waveguide length is shorter than that of the device used for the GVD characterisation. (i.e. 1.2 mm vs. 2 mm).

4.5 Chapter Summary

In this chapter, the design, fabrication and testing of the TPA detectors was described. The chapter began by analysing the basic requirements imposed on the TPA device performance by the pulse characteristics to be measured. The chosen geometry was based on a traveling-wave semiconductor waveguide, fabricated on an InP–based epilayer with a bandgap of ∼1350 nm. The whole fabrication process was also described, along with the basic characterisation of the devices, such as electrical properties, transmission losses and TPA sensitivity. The experimental results showed that the fabricated devices are suitable for the characterisation of the investigated SMLLs within the whole range of emission spectra, repetition frequencies and power levels. A clear TPA response was registered with pulse peak power levels as low as 5 mW and a combined (linear and quadratic) response could be detected down to ∼200 μW (detection sensitivity of 1×10^{-3} mW^2). The devices were characterised by low linear loss, low polarisation sensitivity and flat response across the whole spectral region of interest. The traveling-wave operation of the detectors makes them suitable for high-repetition rate pulses, and also minimises dispersion which can add distortion to the pulses. The three-section device with a 6 μm wide input taper, a 1 mm long and 1.2 μm wide cavity has been chosen as a potentially optimum device to be used for the sonogram set-up due to the best trade-off between low-loss operation, high TPA sensitivity and low sensitivity to input polarisation.

Chapter 5

Sonogram Set–up

In this chapter, the experimental set-up that was developed for sonogram characterisation of ultrashort optical pulses is discussed. It begins with an overview of the theory behind the sonogram technique, in order to illustrate how the pulse information is encoded within the sonogram trace. Next, the key elements of the experimental set-up are presented, with particular attention paid to the spectrally tunable component. The subsequent section focuses on the measurement software and on the pulse retrieval algorithm. Finally, the experimental set-up is verified to be operating properly by performing measurements on the trial pulses.

5.1 Sonogram Method for Optical Pulse Measurements

The sonogram technique belongs to the spectrography/sonography family of pulse diagnostic methods. A sonogram trace is obtained by cross-correlating the spectrally filtered pulses with a pulse replica on a nonlinear detector. In order to achieve sufficient time resolution capable of detecting relative delays between the cross-correlated signals, a detector with an instantaneously responding optical medium has to be implemented. A full three-dimensional sonogram trace is built by acquiring the cross-correlation characteristics that were measured for successive central frequencies of the spectral filter. Such a procedure allows for the intensity and phase information of the optical pulses to be represented in a graphical manner, which can be subsequently processed with image processing algorithms.

A schematic of the sonogram arrangement developed in this work is presented in Fig. 5.1. The system is based on a Michelson interferometer geometry, with a variable delay line in one arm and a tunable band-pass filter (TBPF) in the other. The pulse is first

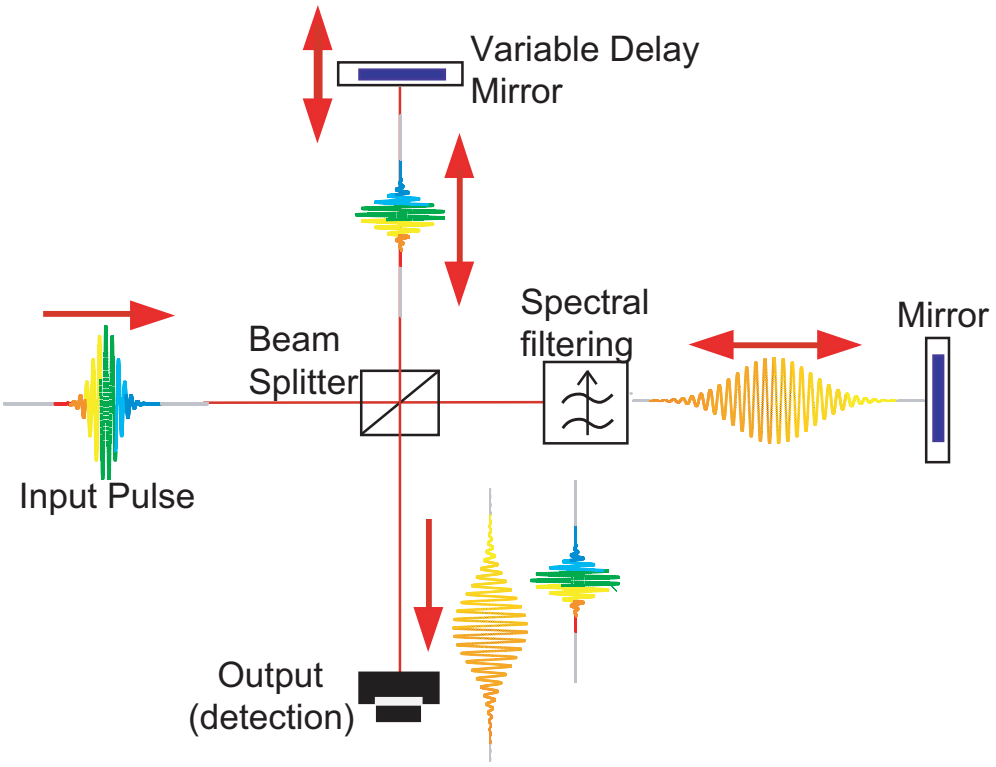

FIGURE 5.1: Schematic overview of the sonogram system. The replica of a time-delayed pulse is cross-correlated with a spectrally filtered pulse in an output detector. For the time-gating the detector has to be characterised by a quasi-instantaneous response.

processed by a time-stationary filter, i.e. the spectral filter, and next by a time-non-stationary filter, i.e. the TPA detector. This procedure, being the reverse of that utilised in the FROG technique, enables the time direction ambiguity to be eliminated, even if a second-order non-linearity is used. The sonogram trace is hence a time-frequency representation of the optical pulse and measures the group delay of each frequency component, i.e. the time of arrival of successive pulse spectral slices.

The concept of "true " sonogram, S_T, as presented in Eq. 5.1 assumes a measurement of temporal intensities of the filtered pulse at a range of the bandpass filter central frequencies, ω_c.

$$S_T(\omega_c, \tau) = |\int_{-\infty}^{\infty} E(\omega)G(\omega - \omega_c)e^{i\omega\tau}d\omega|^2, \tag{5.1}$$

where E, G, τ and ω denote the input spectral field, the filter transfer function, the delay between pulse replicas and the angular frequency, respectively. In order to accurately reconstruct the true sonogram, a very high temporal resolution [122] would need to be used. However, in the experimental sonogram, S_E, a replica of the input pulse, $I_{In}(t)$, acts as a temporal gate for the spectrally filtered pulse, $I_F(t)$. At the same time, $I_F(t)$ is the inverse Fourier Transform (FT) of the product of $I_{In}(\omega)$ and $G(\omega)$, at a specific centre frequency of the tunable filter. Hence, the product of the cross-correlations between these two pulses (first integral in Eq. 5.2), taken across the whole

pulse spectrum, is equivalent to the convolution of the true sonogram, S_T, with the temporal intensity of the input pulse (last part of Eq. 5.2):

$$S_E(\omega_c,\tau) = \int_{-\infty}^{\infty} I_F(t)\cdot I_{In}(t-\tau)dt = \int_{-\infty}^{\infty} I_{In}(t-\tau)\cdot\left|\int_{-\infty}^{\infty} E(\omega)G(\omega-\omega_c)e^{i\omega\tau}d\omega\right|^2 dt, \tag{5.2}$$

$I_{In}(t)$ acts as a δ-function inside the time integral, because it refers to a much shorter pulse. Under this condition, the final term in Eq. 5.2 can be reduced to that in Eq. 5.1 [123]. Similar to the FROG, the data is stored in a two-dimensional array. This means that the two complex fields (4 N-long vectors) are extracted from an N×N matrix. The usual sonogram trace arrays have the dimensions of 16×16, 24×24 or 32×32, so there is a data redundancy in the measured traces. The retrieval algorithm processing over-determined traces is more robust and immune to any random or systematic measurement errors [22].

5.1.1 Tunable Band-pass Element

A band-pass filter is a key element of the sonogram set-up and requires special attention at the system development stage. There are several approaches that can be used to realise the spectral filtering. The most popular geometry is based on a grating combined with a lens, a narrow slit, and a retroreflector [124–126]. This approach delivers high flexibility as the filter bandwidth and centre wavelength can be controlled by adjusting the width and position of the slit. However, it requires a mechanical positioner to precisely scan the Fourier plane of the lens, which imposes a substantial limitation on practically achievable data acquisition rates. A significant improvement in the spectral scanning speed can be obtained with an alternative technique based on a Fabry-Pérot filter [127]. Here, the frequency selection is realised by controlling the distance between two closely separated mirrors, forming a wavelength-selective etalon. The separation needs to be controlled within an optical wavelength by stable and accurate piezo-actuators. The system requires high mechanical stability in order to eliminate any vibrations and maintain parallelism between the mirrors. Furthermore, the mirrors' reflectivity values need to be carefully chosen in order to obtain the desired filter characteristics.

The alternative approach that has been used in this work is based on a commercially available acousto-optic (AO) bandpass filter [128]. Electronically controllable operation of such a filter allows for high-speed and mechanically stable measurements. The acousto-optic filters (AOFs) usually work in relatively wide wavelength ranges, which improves the versatility of the sonogram system. This method, however, does not provide easy tunability of the filter bandwidth (such as the grating-slit arrangement) nor

allows for controlling the full complex transfer function of the filter (such as the etalon-based set-up). The former issue can be partly addressed by driving the AOF with a superposition of two or more signals of different frequencies to broaden the bandwidth. The latter matter needs to be carefully evaluated in the sonogram measurements, as the transfer function of the bandpass filter has a direct effect on the sonogram trace. Preferably, a dispersionless filter should be used, as it simplifies the retrieval procedure and limits potential errors generated by the pulse retrieval algorithm. In the absence of such a filter, the complex transfer function of the filter needs to be determined and the gate signal characteristics generated by the sonogram retrieval algorithm has to be verified.

The free-space AOF (Gooch & Housego TF1450-500-1-1.5-CV1) with a wavelength tuning range of 1.2–1.75 μm and a spectral FWHM ~1.2 nm was chosen for the set-up. The AO medium of the filter is an anisotropic tellurium dioxide (TeO_2), transparent in a wide spectral range from 0.36 μm to 4.5 μm [129]. Preliminary tests were performed in order to characterise the operation of the filter around the optical wavelength of 1550 nm. First, the transmission spectra were investigated over a certain range of ultrasound frequencies with the experimental set-up presented in Fig. 5.2. A tunable laser (Photonetics 3642 HE Tunics Plus) is used as a narrow bandwidth light source from 1500 nm to 1640 nm. The polarisation of light coupled from the laser is adjusted with a fiber-based polarisation controller and the diffracted (filtered) beam is measured with a photodetector. The laser source, the RF driver, and the power meter are externally controlled with a PC for automatic data acquisition. The filtered beam intensity is measured as the central

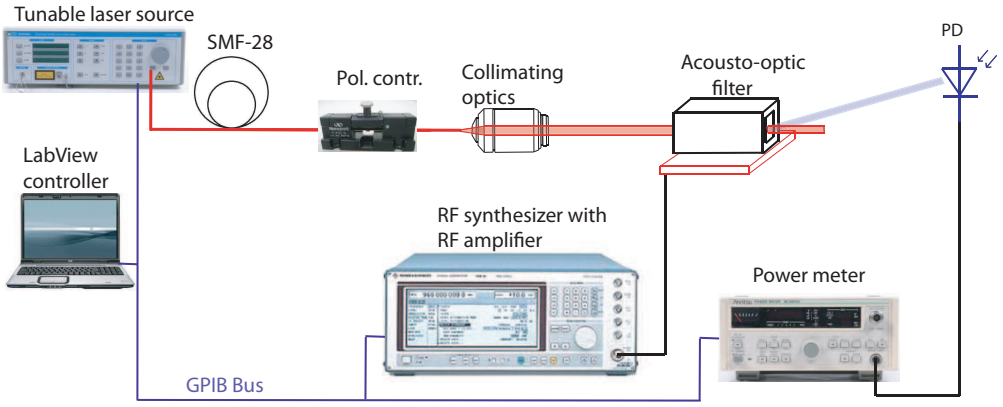

FIGURE 5.2: Experimental set-up for the acousto-optic filter transmission measurements.

wavelength of the tunable laser is scanned. The experiment was repeated for several ultrasound frequencies applied to the device. Fig. 5.3(a) presents an example of a transmission spectrum recorded with the driving frequency of 82.7 MHz, a FWHM of 1.26 nm (149 GHz), and a central wavelength of 1592 nm. Despite the high-quality performance

of the filter, there are two characteristic features which have to be considered when using the device for sonogram measurements. The first issue is a small side-lobe present on the long-wavelength side of the main lobe. This is a typical feature of AO devices caused by the acoustic transducers. However, the transducer of the tested device was designed to maximise the side-lobe suppression and to produce a Gaussian transmission characteristic. Although a side-lobe suppression of 0.04 (-14 dB) was recorded, the presence of this characteristic has to be taken into account when processing the results from the sonogram retrieval algorithm. The side-lobe of that filter can produce spurious features on the sonogram trace, which can be mistakenly attributed to some fluctuations in the pulse intensity envelope. The second issue evident in Fig. 5.3(b) is a residual dependence of the spectral bandwidth on the central wavelength of the bandpass filter. This needs to be addressed in the sonogram measurements, as the retrieval algorithm assumes a constant transfer function of the spectral gate. However, this problem is of low significance in case of relatively narrow bandwidth lasers. The investigated SMLLs emit pulses with spectral FWHM typically below 10 nm, which corresponds to an average 3-dB filter bandwidth variation of less than 1 %.

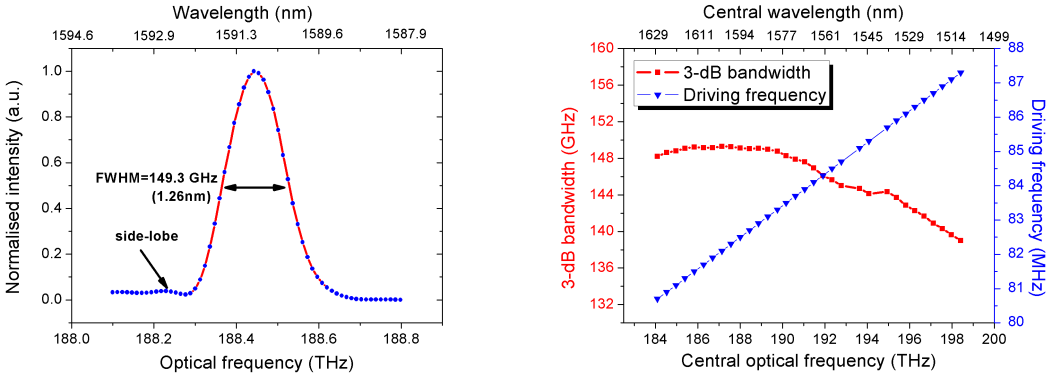

FIGURE 5.3: (a) Transmission spectrum of the AOF at a frequency of 82.7 MHz. (b) 3-dB bandwidth and driving frequency dependence on the central wavelength of the transmission spectrum.

The complete characterisation of the filter transfer function also requires the evaluation of the phase response. The applied measurement method is similar to that presented in [130], which is based on the group delay (GD) measurement with a phase shift technique. The experimental set-up is presented in Fig. 5.4. The light coupled from a tunable laser source is intensity modulated with an RF signal through a Mach-Zender modulator, driven with an Agilent E8257D signal generator at a repetition rate of 10 GHz. After the fiber amplifier stage the signal is split by a 10/90 % coupler into the reference and test paths. The test path contains a polarisation controller, collimating/coupling optics, and the device under test. The optical signals from the two paths are detected with two

65 GHz bandwidth photodiodes (Agilent 86116C) and the electrical signal is measured with a two-channel digital sampling oscilloscope (Agilent DCA-J 86100C).

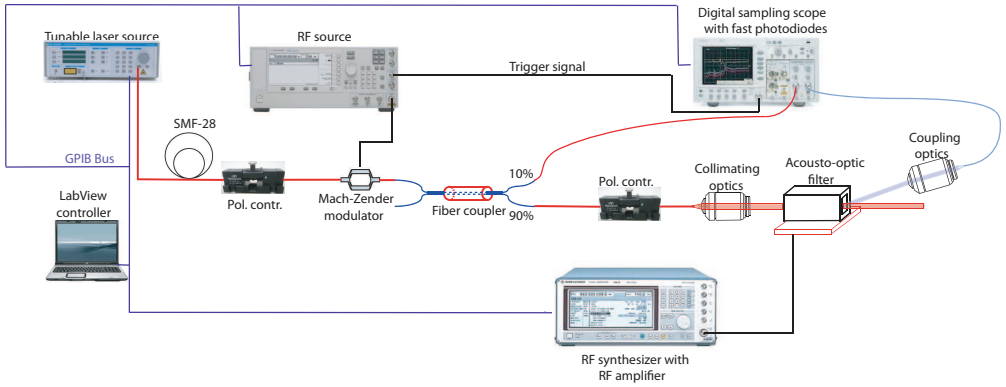

FIGURE 5.4: Experimental set-up for the acousto-optic filter group delay measurements.

The phase modulation of the test signal is measured relative to the reference path. If the investigated device introduces any group delay, $\Delta\tau$, this produces a corresponding shift in the modulation phase, $\Delta\phi$ (in degrees), as presented in Eq. 5.3:

$$\Delta\tau = \frac{\Delta\phi}{360} \cdot \frac{1}{f_m}, \tag{5.3}$$

where f_m is the modulation frequency. The central frequency of the laser is scanned across the transmission region of the filter and the relative group delay between the two signals is detected. The outcome of the group delay measurements for several frequencies inside the filter pass band is shown in Fig. 5.5(a). Also, a linear characteristic fitted to the scattered points and the calculated phase profile (i.e. the integrated group delay characteristic) are plotted in the same graph. The results show a normal dispersion introduced by the acoustic crystal, which needs to be considered in the retrieval algorithm verification process. Example of a full transfer function at a central wavelength ~1531 nm is plotted in Fig. 5.5(b). Similar group delay characteristics have been obtained with the filter central wavelength varying between 1520 nm and 1620 nm.

5.1.2 Delay Line

Another crucial element of the sonogram set-up is the delay line. Besides the requirement for precise control of the variable delay, it needs to deliver sufficient travel distance in order to scan the full length of the measured pulse. The spectral filtering in the sonogram temporally broadens the pulse, hence, a longer delay scanning range is required compared to other pulse characterisation techniques, e.g. FROG or intensity autocorrelation. The most accurate position control, with a resolution down to ~5 nm can be

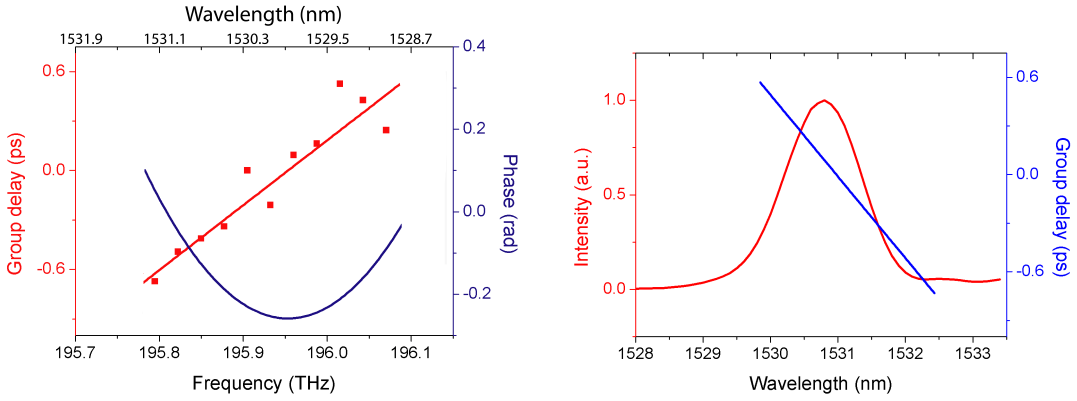

(a) (b)

FIGURE 5.5: (a) Measured group delay inside the transmission band of the filter (red scattered points) with a fitted linear characteristic and calculated phase profile (blue curve). (b) Full transfer function of the acousto-optic filter.

obtained with piezoelectric actuators. However, travel ranges of several millimeters are normally required for picosecond pulses, which are far above typical scanning ranges of piezoelectric positioners (Melles Griot 17 DRV 001), with a resolution of 50 nm and a travel distance of 8 mm. In a retro-reflecting geometry this corresponds to a temporal resolution and a delay range of 0.33 fs and 53 ps, respectively, which are largely sufficient for the developed system. The stepper motor is attached to a 6-axis flexure stage (17 MAX 601/L Nano-Max-HS) and is controlled with a 17 MST 001 modular driver. The x-, y-, θ_x-, θ_y-, and θ_z- axes of the positioning stage are adjustable with the micrometer actuators. Additionally, the x- and y- axes are controlled with the piezoelectric controllers with feedback (17 MPZ 001). All the modular controllers are installed in a 17 MMR 001 Main Rack with a CAN interface and internal communication modules. Such a configuration improves the flexibility of the optical system, simplifies the alignment procedure, and allows for remote control of the delay line. A low-frequency loudspeaker was mounted on the second arm of the Michelson interferometer to adjust the 0-delay position between the two arms in the alignment stage through the DC bias applied to its coil.

5.1.3 Sonogram Arrangement

The complete sonogram set-up is presented in Fig. 5.6. Light emitted from the MLL first passes through a fibre circulator in order to minimise any optical feedback from the measurement set-up. Next, it is optionally amplified by ∼8 dB with a low-dispersion EDFA to compensate for laser-to-fibre and fibre-to-free space coupling losses. A GRIN lens is then used to collimate the light into the free-space Michelson interferometer, with

the band-pass filter in one arm, the positioning delay stage in the second one, and the TPA waveguide detector at the output. The polarisation is adjusted with a fibre-based polarisation controller and a half-wave plate (HWP) to maximise the efficiency of the acousto-optic filter. Additionally, the filter modulates the optical signal at a frequency of 15 kHz and feeds the reference signal, LF, to the lock-in amplifier. The whole set-up is automated using LabView software, which performs the measurement and data acquisition routine. It communicates with the laser drivers, RF synthesizer, and lock-in amplifier through the GPIB bus and controls the movable mirror actuator through the CAN bus.

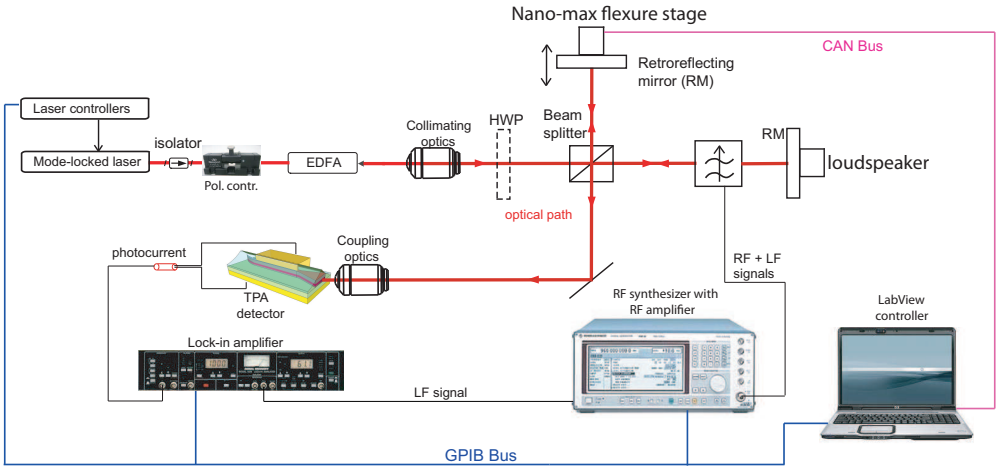

FIGURE 5.6: Schematic arrangement of the final sonogram set-up.

5.1.4 Dispersive Elements in the Sonogram Set-up

The optical elements in the sonogram set-up may affect the group delay profile of the measured pulse. It is therefore crucial to identify all the possible sources of dispersion present between the pulse source and the TPA detector. As there are no physical elements counteracting an inherent dispersion of the set-up, such as a dispersion-shifted fibre, these effects need to be analytically compensated for by modifying the phase profile of the retrieved pulse and recalculating the pulse characteristics.

Although the detector itself can be a source of dispersion, the prevailing material dispersion of the TPA detector can be neglected for pulses longer than 160 fs, as already discussed in Section 4.4.4.

The fibre patchcord used to deliver the optical signal from the MLL to the sonogram system input is a SMF-28 with a total length of ∼4 m. According to [131], the dispersion of the fibre, $D(\lambda)$, in the wavelength window of 1200–1600 nm can be approximated by the following formula:

$$D(\lambda) = \frac{s_0}{4}[\lambda - \frac{\lambda_0^4}{\lambda^3}], \tag{5.4}$$

where $\lambda_0 = 1310\,\text{nm}$ and $s_0 = 0.092\,\text{ps}/(nm^2 \cdot km)$ are the Zero Dispersion Wavelength and the Zero Dispersion Slope, respectively. The calculated dispersion characteristic in the 1500-1600 nm spectral range is presented in Fig. 5.7. It varies between ∼15–∼20 ps/nm·km, which corresponds to ∼60–∼80 fs/nm in a 4 m long patchcord. The calculated dispersion curve was used in the sonogram processing software to compensate for the group delay introduced by the optical fibre.

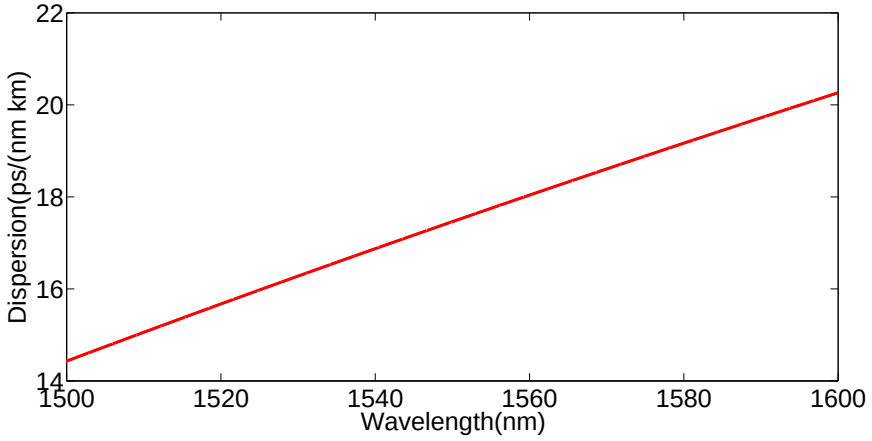

FIGURE 5.7: Dispersion in a SMF-28 optical fibre in the wavelength range 1500–1600 nm.

A second component with a potentially significant level of dispersion is the acousto-optic filter. The group delay profile presented in Fig. 5.5(b), independent of the filter central wavelength, is already included in the retrieval algorithm. However, in addition to the phase profile of the transfer function, the material dispersion of the crystal in the AOF has also to be considered. According to [132], the chromatic dispersion of the TeO_2 at 1550 nm is approximately -36 ps/nm·km. Even though the filtered beam passes through the ∼6 cm long crystal twice, the total dispersion introduced by this element is only -4 fs/nm and can therefore be neglected.

5.1.5 Measurement Software

The flow chart for the LabView software routine used for the measurement control and data acquisition is presented in Fig. 5.8. The routine starts by processing the measurement parameters applied to the experiment, e.g. sonogram grid size and wavelength step. Subsequently, the frequency values for driving the acousto-optic band pass filter

are calculated, and the corresponding delay steps and stage position points are determined. In order to sample the pulse with uniform steps in the time and frequency domain, the delay steps are computed with the following formula:

$$\Delta t = \frac{1}{N\Delta f}, \tag{5.5}$$

where Δt, Δf and N are the delay step, frequency step, and the grid size, respectively. After moving the delay line to the initial position the measurement process begins. The N x N sonogram trace is constructed by scanning the central wavelength of the spectral filter across the wavelength range at each position of the delay line. Afterwards, the trace is examined in order to verify the absence of any data truncation. If necessary, the scan parameters, e.g. the centre wavelength, grid size or stage initial position are adjusted and the measurement process is repeated. Finally, the sonogram trace is saved to a file for post-processing with the sonogram retrieval algorithm software.

5.2 Retrieval Algorithm

The major breakthrough in spectrography and sonography was the application of image processing methods to calculate the pulse field functions from the spectrogram and sonogram traces [30]. It can be shown that the spectrogram (or sonogram) should be represented by a rank 1 matrix (single non-zero eigenvalue) [133], which allows for an efficient singular value decomposition (SVD) method to be used to generate the pulse and gate fields in the iterative retrieval process. The inversion routine developed for the FROG and called the *principal components generalised projections alghorithm (PCGPA)* [134, 135] can also be adapted for retrieval of the sonogram traces [135]. Usually, the reconstructed traces are unique, so the method is free of any ambiguities. The sequence of time and frequency filtering in the sonogram technique is reversed with respect to the processing sequence of the FROG. As a consequence, the trace processing in the retrieval algorithm is performed on the frequency domain signal rather than on the time-domain characteristics. This provides an additional advantage as the spectral intensity of an investigated pulse, $E(\omega)$, can be experimentally verified on an OSA and used as a measurement constraint in case of a problematic algorithm convergence.

A schematic of the tasks used to process the sonogram traces is plotted in Fig. 5.9. It begins with an optional Fourier filtering in order to remove any high frequency noise [127]. Next, the background signal originating from the individual contributions of the filtered optical pulses to the TPA photocurrent is removed, by subtracting the signal measured at large temporal delay from the experimental trace. If the experimental delay/frequency steps do not strictly follow the condition of Eq. 5.5, the sonogram

trace is resampled by zero-padding the measured trace in a particular dimension and interpolating it at the correct delay-frequency points. The resampled sonogram trace is subsequently processed with a retrieval algorithm, which produces complex pulse and gate functions. After modifying the pulse group delay for the system dispersion, the temporal characteristics are recalculated and the second-order intensity autocorrelation function is evaluated. Finally, all the retrieved traces (i.e. the transfer function of the gate, the autocorrelation trace and the optical spectrum) are compared with the experimentally measured characteristics. An essential part of the sonogram processing software is the retrieval algorithm based on the PCGPA (Fig. 5.10). The algorithm is initially fed by trial guess functions for the pulse and gate. As the gate transfer function has been experimentally measured, it can be used as the initial trial input signal. The trial complex pulse is normally constructed with a sech^2 envelope and a constant phase profile. Next, the initial sonogram field and intensity are calculated with the procedure presented in Fig. 5.11. The sonogram intensity is normalised and compared with the experimental results by calculating the initial error. The subsequent iterative process minimises the error by modifying the filter and gate functions, so that the calculated sonogram converges to the experimental one. The procedure includes the replacement of the calculated sonogram intensity with the experimental trace while leaving the phase information unmodified, followed by the pulse and gate extraction (Fig. 5.11). To avoid the convergence to a wrong solution, additional constraints, such as the comparison with the experimental pulse spectrum, can be added to the algorithm. A new sonogram is next evaluated, normalised, and again compared with the measured trace. The iterative process continues until the maximum number of loops or a minimum value of error is reached. All the symbols used in the routines diagram have been defined in Fig. 5.12.

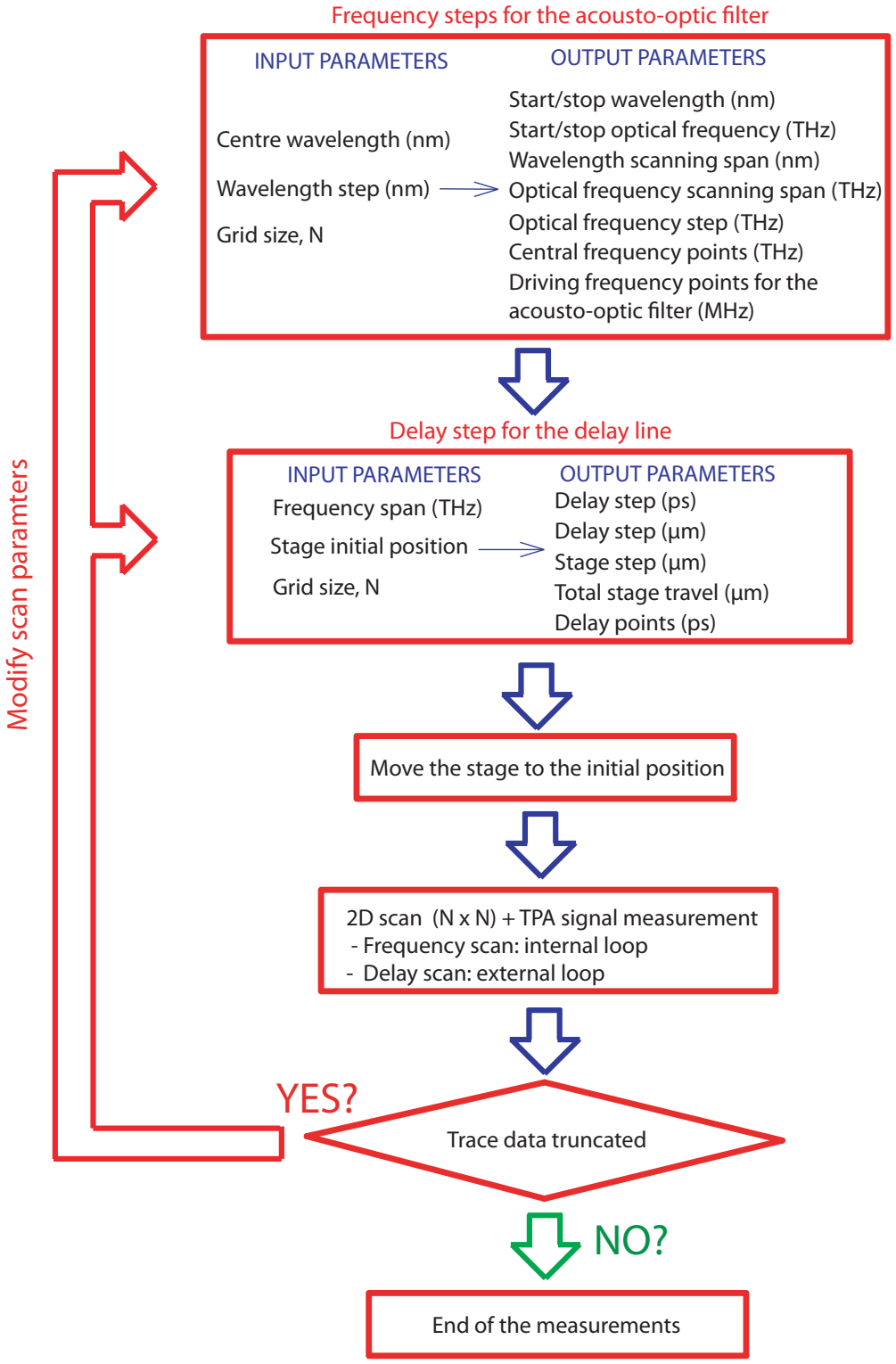

FIGURE 5.8: Routine for the sonogram data acquisition software.

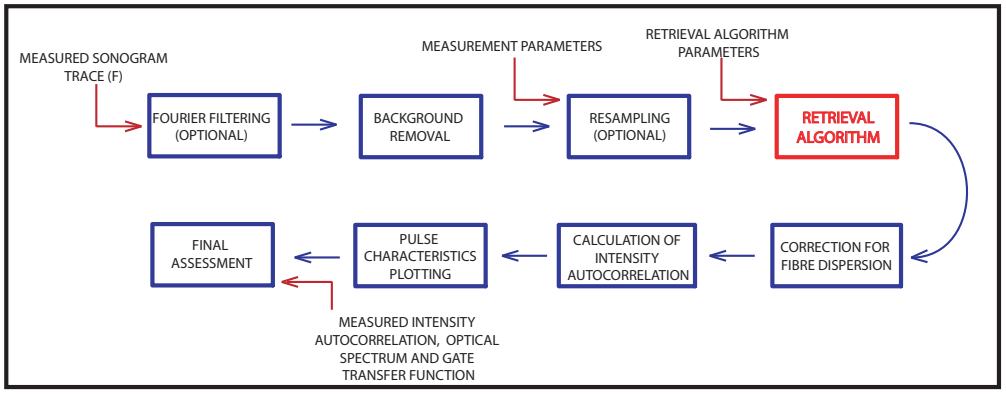

FIGURE 5.9: Routines for the sonogram data processing software.

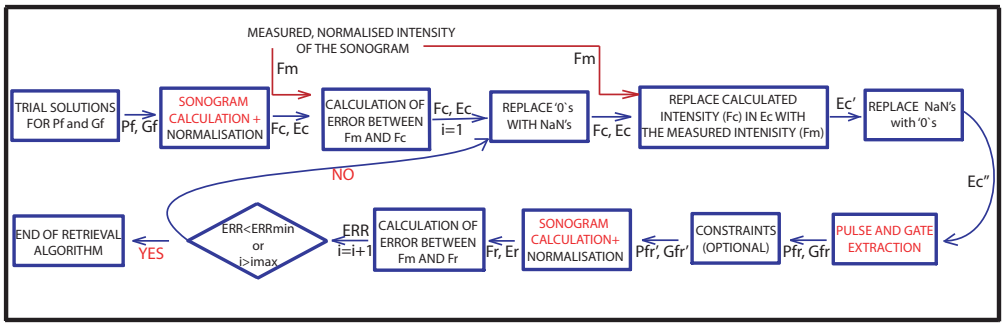

FIGURE 5.10: Routines of the PCGPA in the sonogram processing software.

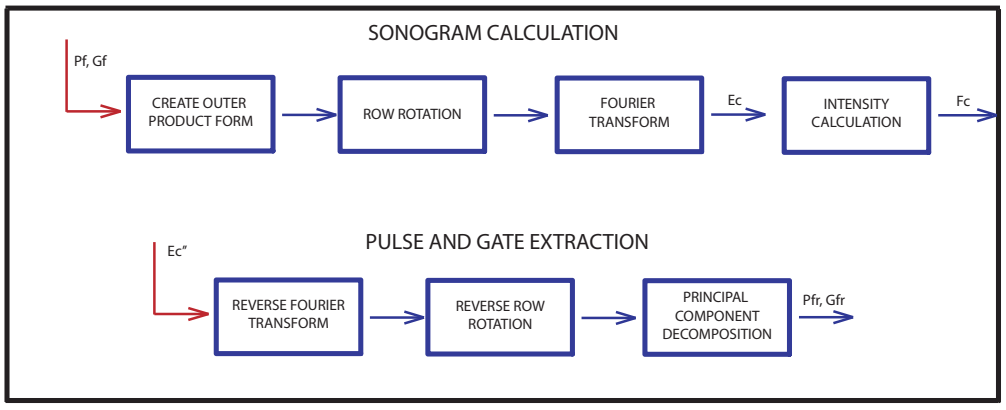

FIGURE 5.11: Routines for the sonogram calculation from the pulse and gate vectors and the sonogram inversion for the pulse and gate extraction.

Symbol	Description
F	Experimental sonogram matrix (real)
P_f, G_f	Trial solutions (complex vectors) for the pulse and gate function, used to initiate the algorithm routine ; input for the sonogram calculation routine
F_m	Experimental, normalised sonogram intensity matrix (real)
F_c, E_c	Sonogram calculation products: intensity (real) and field (complex) matrices
E_c'	Sonogram field matrix (complex) with the intensity replaced with F
E_c''	E_c' with NaN's replaced with 0's; input for the pulse and gate extraction routine
P_{fr}, G_{fr}	PCGPA-extracted pulse and gate vectors (complex)
P_{fr},' G_{fr}'	P_{fr}, G_{fr} with the measurement constraints applied (complex)
F_r, E_r	Retrieved sonogram intensity (real) and sonogram field (complex) matrices

FIGURE 5.12: Definitions of the sonogram symbols presented in the sonogram routine diagrams.

5.3 Verification of the Sonogram Set-up Operation

5.3.1 Set-up and Methodology of the Measurements

Before applying the developed sonogram system to the MLLs pulse characterisation, the set-up and the retrieval algorithm were evaluated with the reference pulses of known amplitude and phase profiles. The test set-up is presented in Fig. 5.13, in which an ultrafast fiber-based actively-MLL (PriTel, Inc) emitting transform-limited pulses around 1550 nm at a repetition rate of 10 GHz is used as a pulse source. In order to expand the range of trial pulses available for the experiment, the output pulses from the fiber laser are further transformed with a fiber based optical pulse compressor. The level of compression is controlled with the pump current applied to the EDFA amplifier, which precede the pulse compressor. The Er-doped optical amplifier from PriTel is dispersion–free and therefore does not affect the pulse shape within the whole range of available pumping current. The pulses from the compressor are transmitted through a long section of optical fiber (404 m–long SMF-28), in order to introduce a controlled amount of anomalous dispersion, which could then be verified with the sonogram system. Propagation of pulses in a material with anomalous dispersion leads to lower group velocity of the longer-wavelength components, hence it introduces a negative chirp. The test pulses are

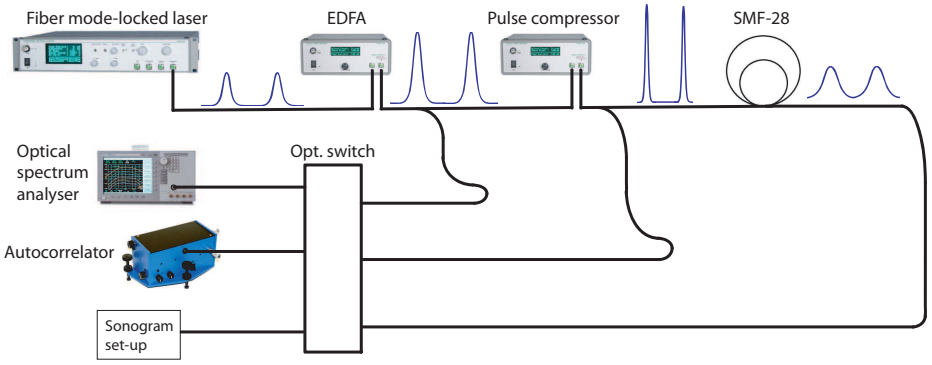

FIGURE 5.13: Test set-up for verification of the sonogram functionality.

first characterised with the SHG intensity autocorrelation and the OSA. Next, the sonogram measurements are performed and the retrieval algorithm is applied to the obtained traces. Various levels of pulse compression are applied to produce pulses with different spectral widths, temporal durations, and phase distortions. Fig. 5.14(a)–5.14(b) present the SHG intensity autocorrelation profiles of the initial pulse (i.e. before amplification and compression), along with the pulses transmitted through the fiber compressor for different values of the EDFA pump current (I_{EDFA}) levels. The pump current and the autocorrelation FWHM values corresponding to each pulse are also displayed in the graphs.

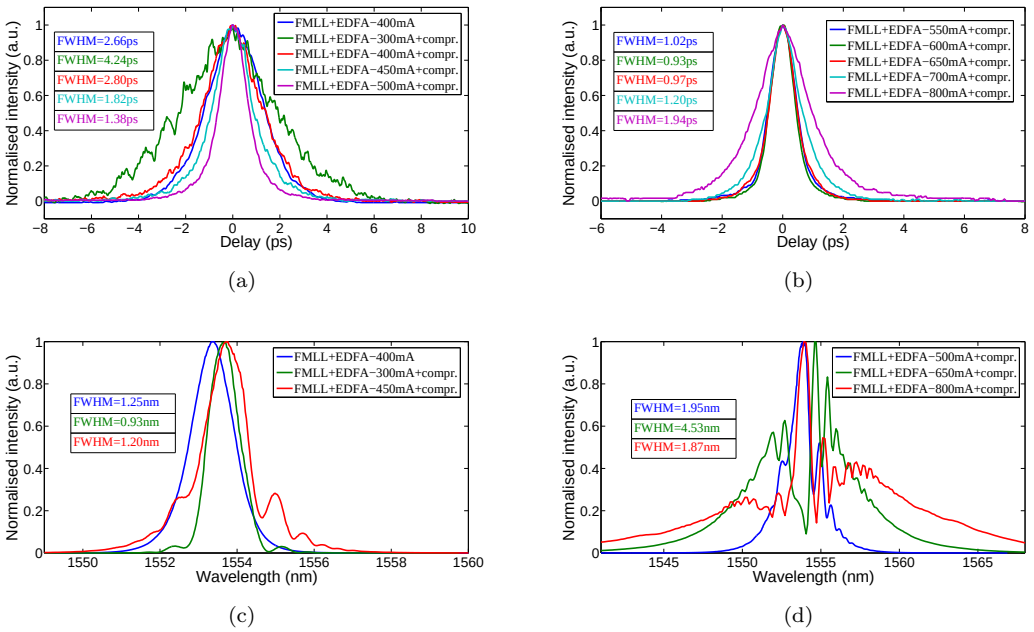

FIGURE 5.14: (a,b) Intensity autocorrelation traces and (c,d) normalised optical spectra of the uncompressed and compressed pulses.

The uncompressed pulse emitted from the fibre mode-locked laser (FMLL) produces an autocorrelation envelope with a FWHM of 2.66 ps. The pulse compression produces effective results only when the EDFA pumping exceeds 400 mA. Otherwise, pulse temporal spreading is evident, such as the case at I_{EDFA}=300 mA, in which the pulse width increases to 4.24 ps. For high amplification levels, the pulses are only compressed until a certain pumping limit. Fig. 5.14(b) demonstrates that too high a pulse intensity again leads to pulse expansion, which is evident from I_{EDFA}=650 mA upwards. These results are consistent with the corresponding optical spectra, plotted in Fig. 5.14(c)–5.14(d)

The best pulse compression is obtained for an EDFA pump current of 600 mA, that leads to the reduction in spectral FWHM from the initial 1.25 nm to 0.93 nm. As the initial pulse is transform-limited, any optical spectral shrinkage inevitably leads to a temporal expansion. Stronger compression induces spectral broadening, however, the spectra become irregular due to the nonlinearities introduced by the compressor fiber. Above a pump current of 650 mA the spectral width drastically decreases, again leading to temporal broadening of the trial pulses.

5.3.2 Sonogram Characterisation of the Test Pulses

The complex pulses produced with the pulse compressor were subsequently examined with the sonogram system. After applying the retrieval algorithm to the sonogram traces

and correcting for the dispersion in the fibre optic patch cords, the obtained spectra and autocorrelation traces were compared with previously measured characteristics. The examples of the experimental sonograms of Fig. 5.15 show the pulse profile evolution with increasing EDFA amplification level. The retrieved temporal pulse profiles are shown in Fig. 5.16

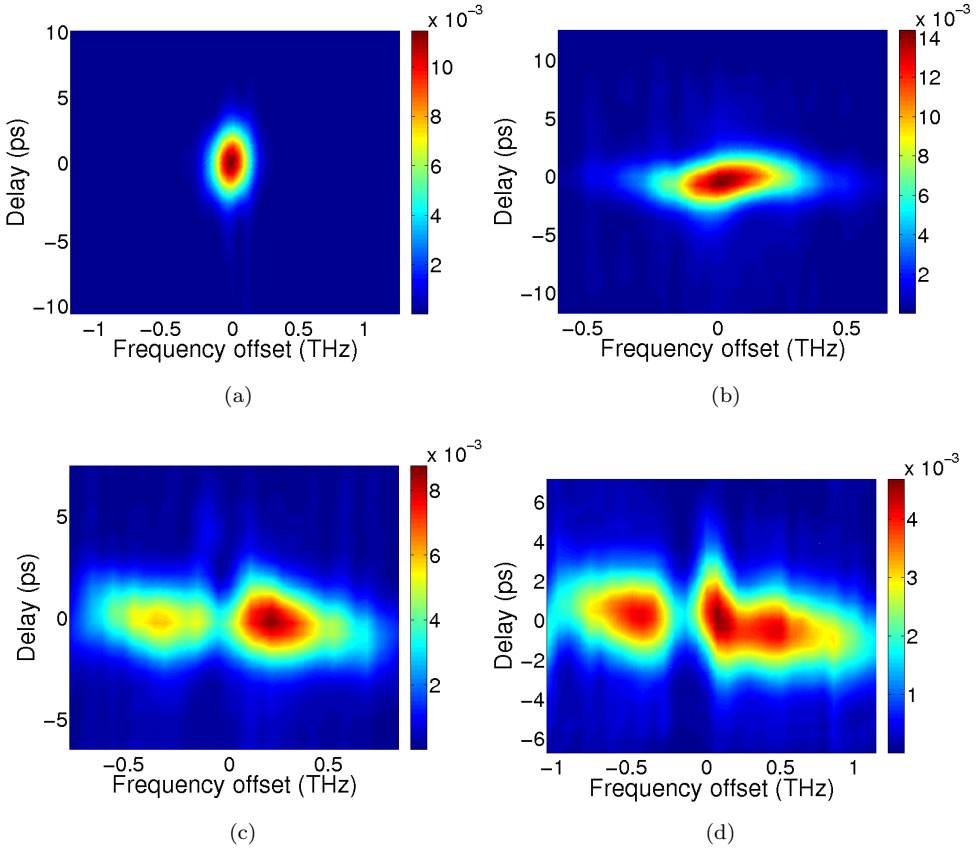

FIGURE 5.15: Sonogram traces of (a) the initial pulse and the pulses compressed at the EDFA pump current of (b) 550 mA, (c) 600 mA and (d) 800 mA.

The regular sonogram shape of the uncompressed pulse becomes more elaborate at higher EDFA pumping levels. At I_{EDFA}=550 mA the temporal compression is evident, with an indication of a chirp in the form of a slight tilt of the entire trace. With a stronger compression (600 mA) the sonogram trace develops an additional spectral component, which does not influence the smooth profile of the temporal pulse shape (Fig. 5.16(c)). Due to strong self-phase modulation (SPM) in the compressor fibre evident at the highest amplification levels, e.g. at I_{EDFA}=800 mA the sonogram trace exhibits three wide and almost independent spectral constituents, which produce a broad and strongly chirped pulse (Fig. 5.16(d)). Apart from the width of the main temporal peak at I_{EDFA}=800 mA being larger than at I_{EDFA}=600 mA, the extra spectral components also contribute to the pulse temporal profile in the form of significant substructures.

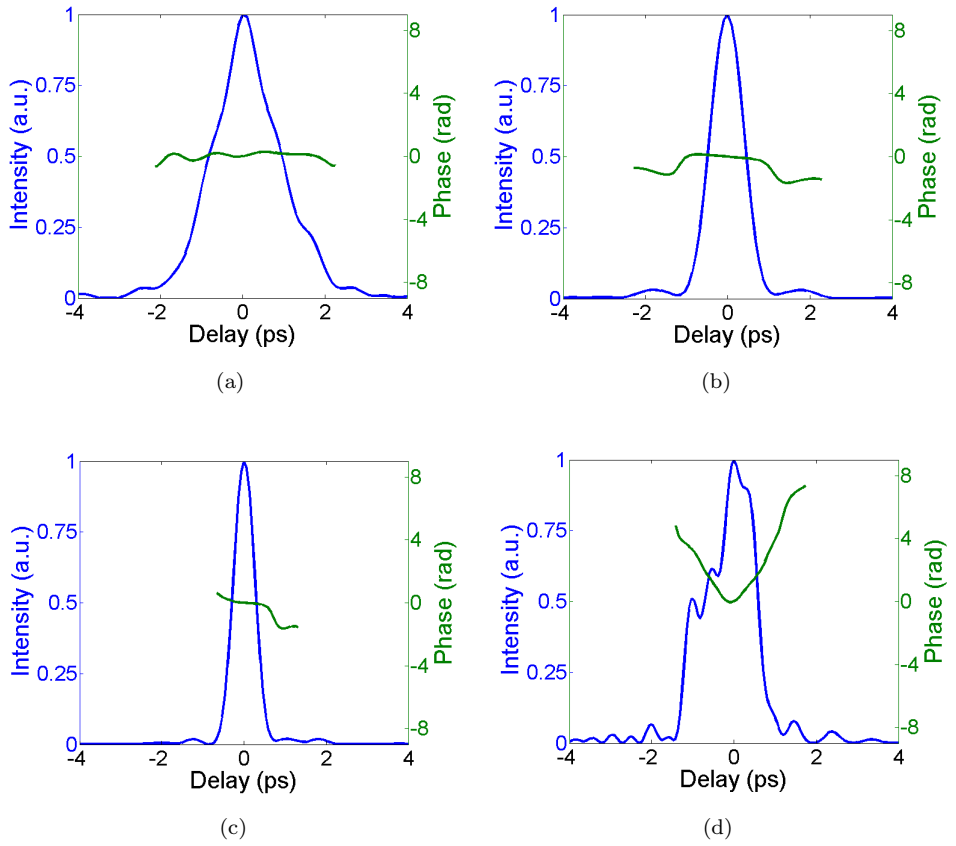

FIGURE 5.16: Retrieved temporal intensity and phase profiles of (a) the uncompressed pulse and the pulses compressed at an EDFA pump current of (b) 550 mA, (c) 600 mA and (d) 800 mA.

The spectral characteristics produced by the retrieval algorithm were in good agreement with the OSA-measured spectra. Also, the autocorrelation traces calculated from the pulse temporal intensities agreed with the SHG autocorrelation measurements. Example of comparison between the measured and retrieved (calculated) envelopes is presented in Fig. 5.17

In the last part of the experiment the demonstrated pulses are in turn coupled into an SMF-28 fibre. A 404 m–long non-dispersion-shifted single-mode fibre introduces dispersion of around 7 ps\nm·km at a wavelength of 1555 nm, so that a considerable increase in the temporal widths is expected. Similar to the previous tests, the fiber output is simultaneously coupled to the OSA, SHG autocorrelator and sonogram set-up.

The SHG intensity autocorrelation traces demonstrate a temporal spreading of the optical pulses in the dispersive fibre, as plotted in Fig. 5.19. Also, temporal overlapping between successive peaks in the pulse train caused by their excessive expansion was observed for compressed pulses with I_{EDFA} exceeding 500 mA. Hence, this current level was

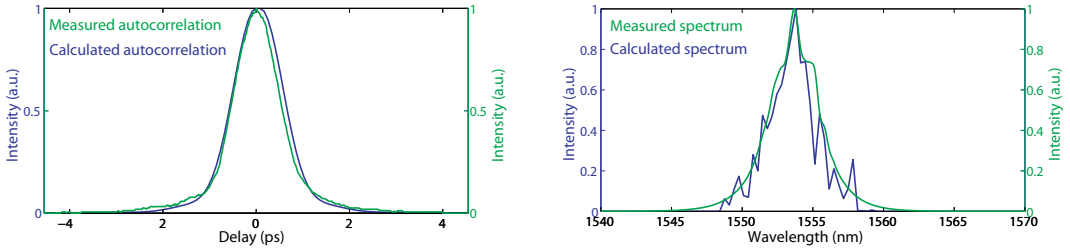

(a) (b)

FIGURE 5.17: Comparison of the measured and retrieved (a) second order intensity autocorrelation envelope and (b) the optical spectra of the pulse amplified at I_{EDFA}=550 mA and transmitted through a pulse compressor.

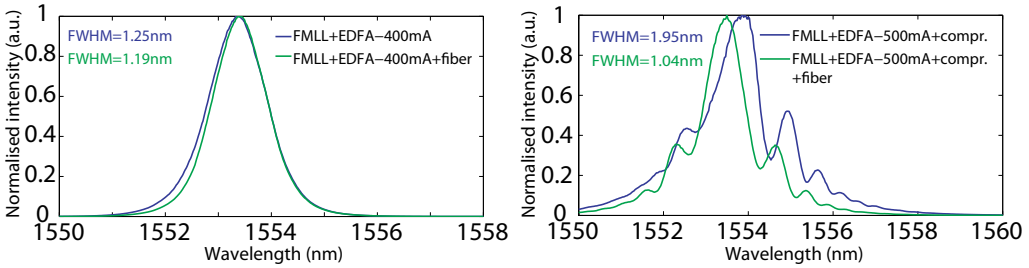

(a) (b)

FIGURE 5.18: Normalised optical spectral characteristics of the (a) uncompressed and (b) compressed pulses at the input and output of the 400 m long fiber.

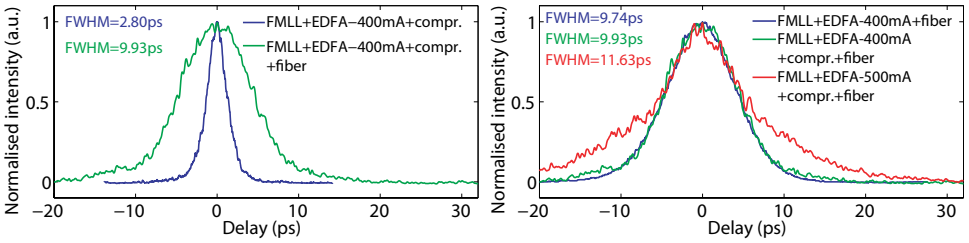

(a) (b)

FIGURE 5.19: Normalised intensity autocorrelation characteristics of various pulses compressed and subsequently transmitted through a 400 m long section of dispersive fiber.

set as a maximum limit for the sonogram measurements with the fibre. The examples of the obtained sonogram traces along with the corresponding IAC profiles are shown in Fig. 5.20. The figure also shows a good agreement between the algorithm-retrieved and experimentally measured IAC characteristics.

The most crucial feature of the measured pulses is the phase profile shaped by the introduction of anomalous dispersion. The temporal phase profiles corresponding to the

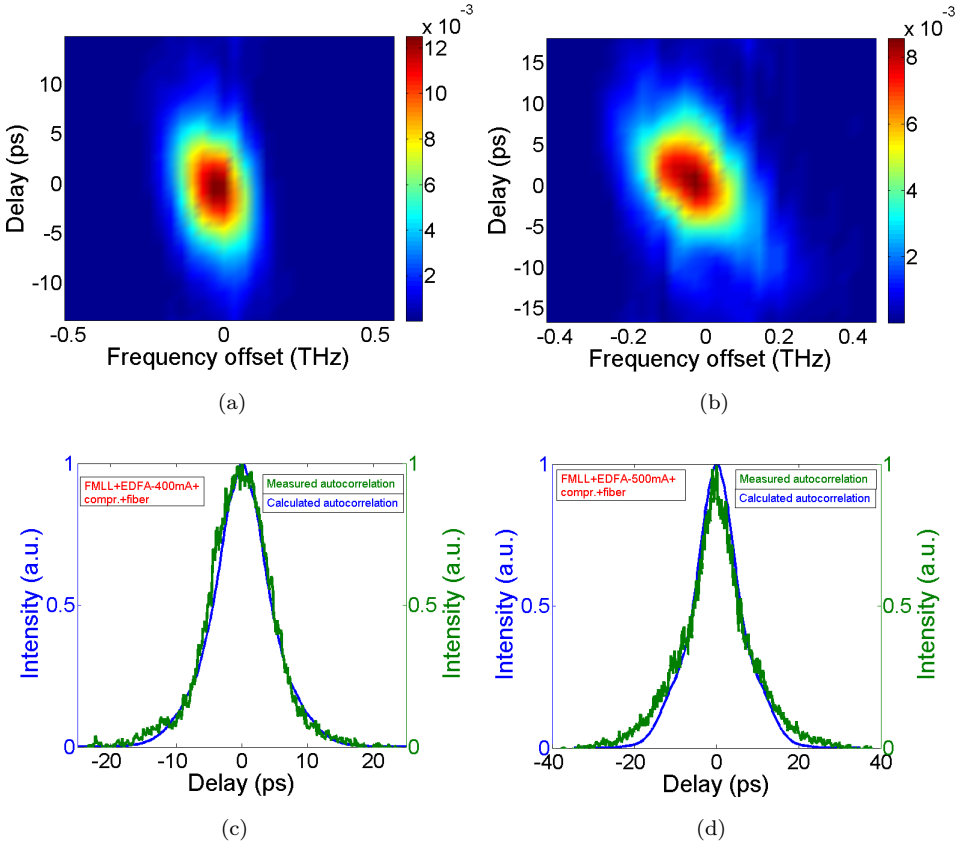

FIGURE 5.20: Sonogram and autocorrelation traces of the pulses compressed at I_{EDFA} equal to (a), (c) 400 mA and (b), (d) 550 mA and transmitted through a section of a dispersive fibre.

expected red-chirped pulses are shown in Fig. 5.21, along with the retrieved group delay profiles. They clearly show an almost linear chirp along the pulse spectrum, with a slope of 6.5 ps/nm, which agrees well with the expected dispersion introduced by the fibre. An inconsistency of 0.5 ps/nm from the expected figure of 7 ps/nm could be caused by SPM compensating for the anomalous dispersion.

5.3.3 Limitations of the Sonogram Set-up

The measurements performed with the trial pulses highlight some limitations of the sonogram set-up. In the examples presented so far, all the characteristics were obtained with the unrestricted algorithm, resulting in very satisfactory outcomes, as detailed in the previous section. However, while processing the data of pulses with spectral FWHM ~1 nm, serious inconsistency between the calculated and measured characteristics was encountered. Even though the algorithm was generating a proper profile for the filter transfer function, the retrieved pulses were much shorter and spectrally wider than those measured with the spectrum analyser and the autocorrelator. This case is illustrated in

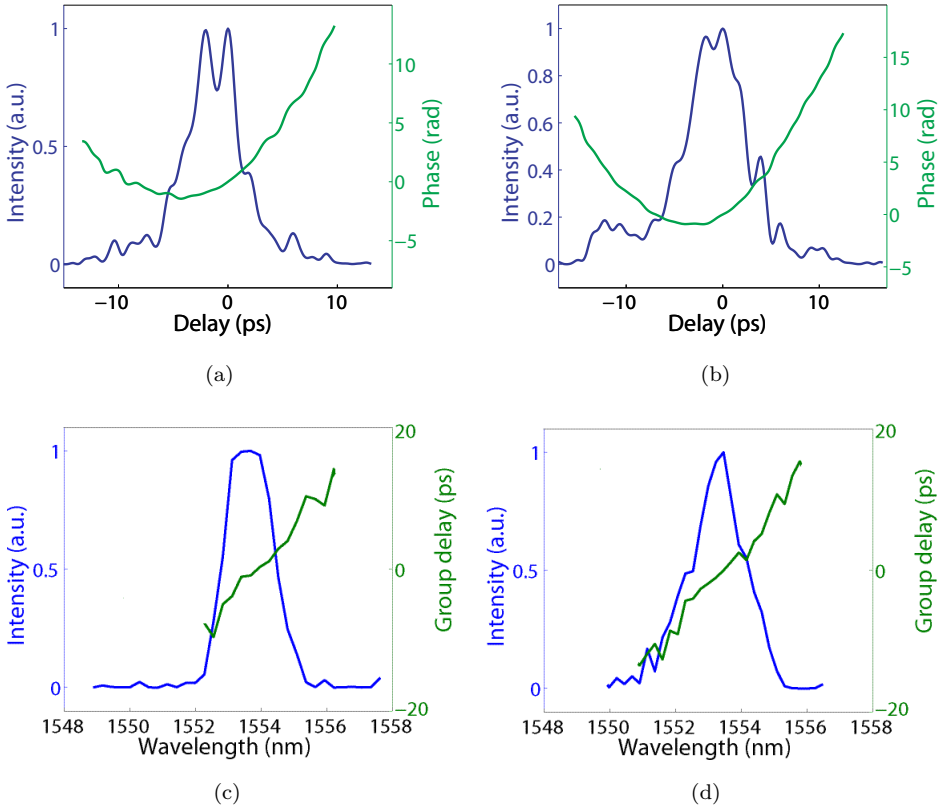

FIGURE 5.21: Retrieved time-domain intensity with phase profiles and spectral intensity with group delay of the pulses compressed at I_{EDFA} equal to (a), (c) 400 mA and (b), (d) 550 mA and transmitted through a section of a dispersive fibre.

Fig. 5.22, presenting a time-domain comparison between the calculated and measured narrow-bandwidth pulses. The retrieval algorithm is very accurate when characterising pulses spectrally broader than the bandwidth of the tunable filter. If the pulse spectrum approaches filter bandwidth, the retrieval algorithm may need some additional restrictions or the tunable filter may need some modifications.

Hence, in order to properly characterise such pulses, the existing set-up would need to be modified by substituting the existing band-pass filter with another, sub-nanometer pass-band filter. According to the theoretical investigations presented in [135], the installed filter should allow for precise measurements of pulses with spectral FWHM values between 2.4 nm and 12 nm, which is 2–10 times larger than the filter bandwidth. Too wide a bandwidth would cause insufficient temporal spread of the filtered pulse, and the unfiltered pulse will not act as a temporal gate. On the other hand, too wide a bandwidth would result in excessive broadening of the filtered pulse. Nonetheless, the range of spectral widths covered by the installed filter fully covers the scope of the SMLL pulses which are investigated in this project, as the typical spectral widths of these pulses

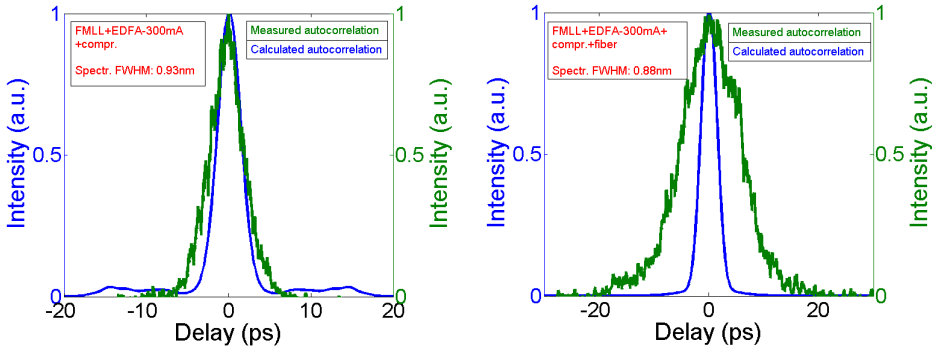

(a) (b)

FIGURE 5.22: Autocorrelation traces of the pulses with FWHM below 1 nm. (a) The pulse compressed at I_{EDFA}=300 mA. (b) The same pulse transmitted through a section of a dispersive fibre.

vary between 3 nm and 10 nm (see Chapter 3). Hence, neither set-up modifications nor retrieval algorithm restrictions are necessary for the characterisation the of SMLLs.

5.4 Chapter Summary

This chapter presented the development of the sonogram system for the characterisation of ultrashort optical pulses. The sonogram technique was briefly described and an overview of the implemented set-up was given. The main components of the system, i.e. the tunable filter and the delay line were examined with respect to their applicability to pulses emitted with the semiconductor mode-locked lasers. Also, the dispersion introduced by the various elements of the sonogram set-up was analysed, so that it could be incorporated in the retrieval algorithm in order to extract the correct intensity and phase profiles of the pulses. Next, the measurement routine and data processing software were presented, and finally, the experimental system and the algorithm were verified with a wide scope of trial optical pulses. The tests revealed some limitations of the system, arising mainly from a too large bandwidth of the tunable band pass filter. However, these restrictions do not apply to pulses emitted from the SMLLs, which have relatively wide optical spectra. Hence, the sonogram set-up can be employed to further investigate the mode-locking devices introduced in Chapter 3.

Chapter 6

Sonogram Characterisation of Optical Pulses from Semiconductor Mode-Locked Lasers

The study of the semiconductor mode-locked lasers presented in Chapter 3 indicated a significant impact of the devices' geometry, material and biasing conditions on the emission dynamics and pulse formation. This chapter provides a further insight into the ML operation, by extracting the phase profile of the optical pulses through sonogram measurements. Devices fabricated in both material systems are investigated and compared in terms of their group delay profiles and temporal intensity characteristics of the emitted pulses.

6.1 Measurement and Analysis Methodology

The 5-QW MLL with the 2.2 % absorber was selected for the sonogram evaluation, as it demonstrates stable mode-locking in a wider range of the operating conditions and shorter pulses than the 3.1 % SA device. For the analysis of the 3-QW MLLs, the sonogram measurements were performed on the lasers with the SA ranging between 2 % and 5 %, because these devices are characterised by large ML regions with a limited impact of SP. As discussed in the previous chapter, the sonogram traces allow to extract the GD profiles, which are direct indicators of the accumulated chirp, as well as the exact temporal profile of the pulses. These data will complement the characterisation of

Chapter 3 and will provide deeper understanding of the dynamical operation of SM-LLs. The integrity of the sonogram measurements were verified by comparison between the optical spectra and intensity autocorrelation traces calculated from the sonogram algorithm outcome and the experimentally obtained results. An example of excellent consistency between the experimentally measured and sonogram-retrieved traces is displayed in Fig. 6.1.

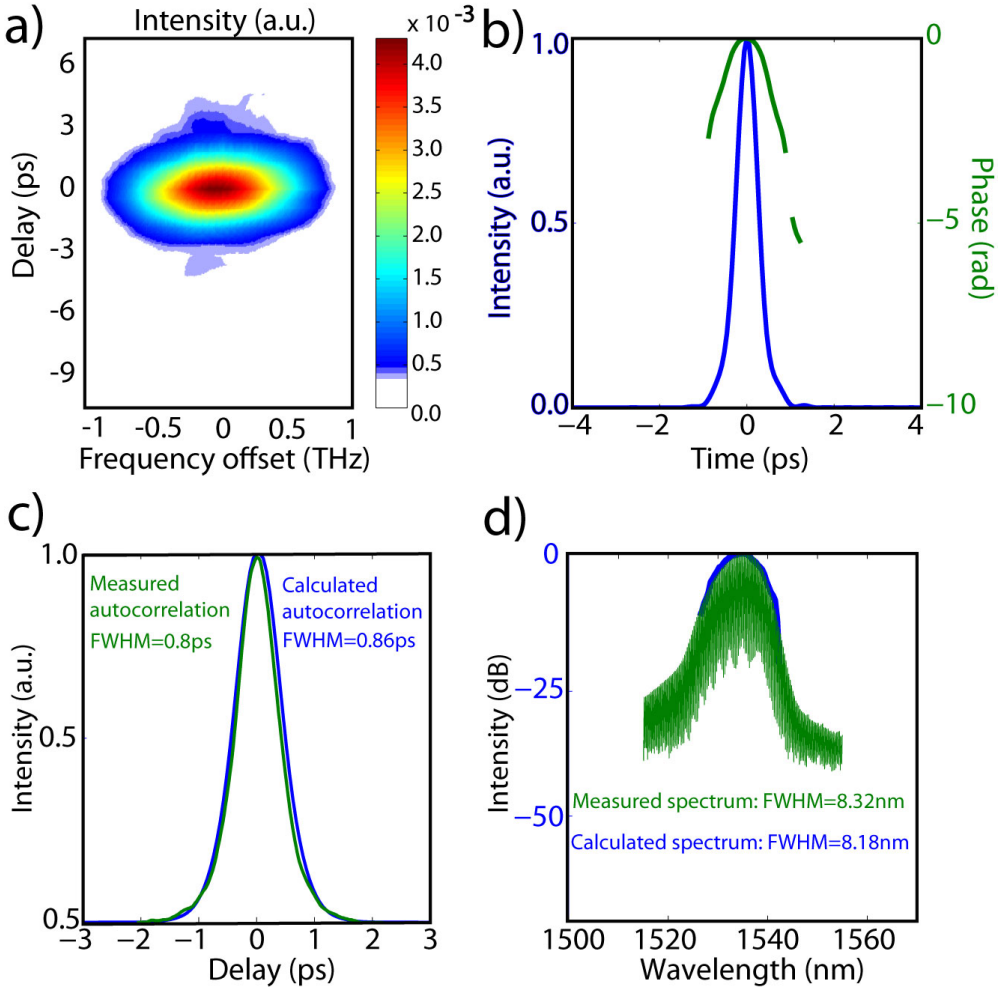

FIGURE 6.1: Example of the (a) experimental sonogram trace after the background removal, (b) retrieved time-domain pulse intensity and phase profiles, and comparisons between the experimental and sonogram-retrieved (c) autocorrelation and (d) optical spectrum traces. The measurement has been performed on the 2 %-SA device at V_{SA}=-2.4 V and I_g=52 mA.

However, the analysis of the sonographic measurements with the biasing corresponding to incomplete mode-locking or the mode-locking affected by self-pulsation revealed some discrepancies between the retrieved and experimentally measured optical spectral and intensity autocorrelation traces. An example of a disagreement between the pulse characteristics is presented in Fig. 6.2. The parametric maps presented in Chapter 3 indicate that at these laser driving conditions the device operates on the boundary of

ML and SP. Self-pulsations manifest themselves in the low intensity lobe present in the short-wavelength end of the optical spectrum in Fig. 6.2(d). The low-repetition rate pulsation corrupts both the experimental and sonogram-based autocorrelation traces. In the former case, it modulates the intensity autocorrelation peaks, and usually broadens the measured trace. In the latter case, the blue-shifted spectral components are usually not taken into account, as the frequency-domain sweep only scans the main lobe, hence, any broadening effects due to self-pulsation are not taken into account and the retrieved pulse produces narrower autocorrelation trace, as shown in Fig. 6.2(c). Similar discrepancies may occur in the case of incomplete mode-locking, as the sonogram algorithm assumes an ideal, noise-free optical pulse train.

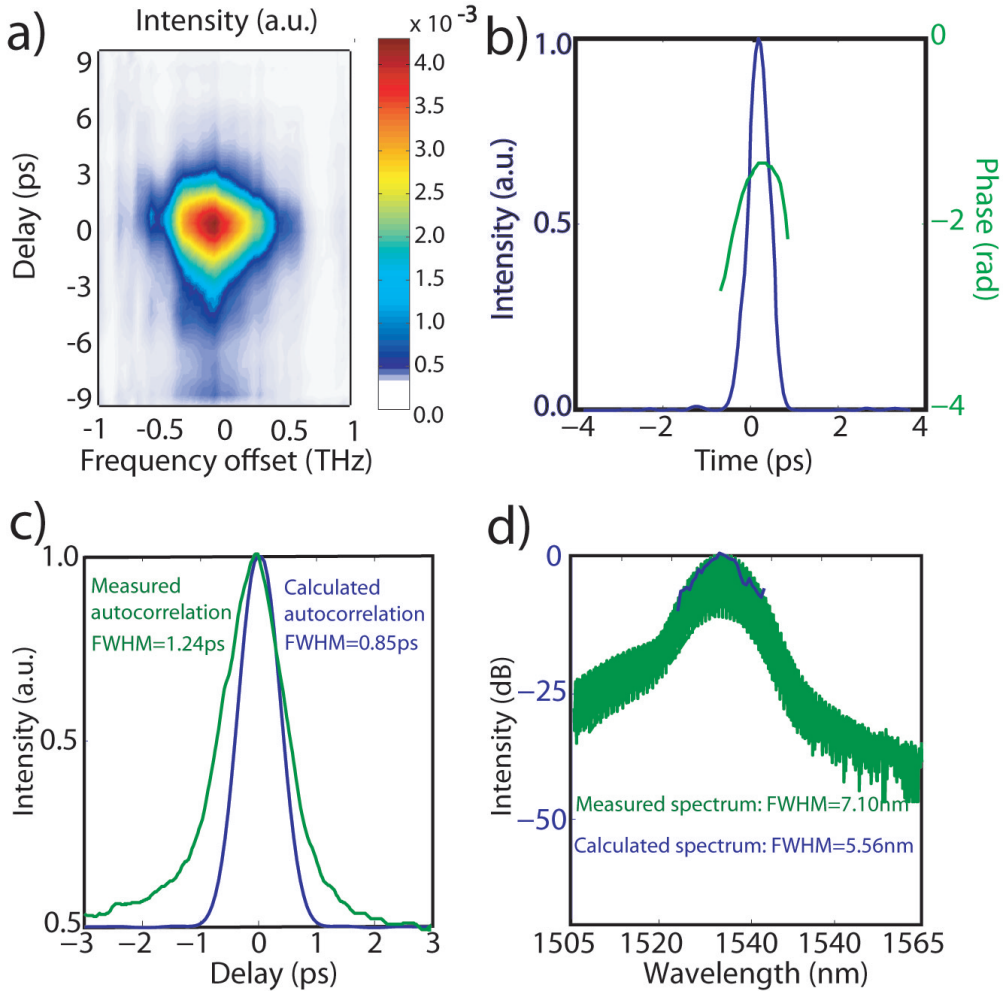

FIGURE 6.2: Example of the (a) experimental sonogram trace after the background removal, (b) retrieved time-domain pulse intensity and phase profiles, and comparisons between the experimental and sonogram-retrieved (c) autocorrelation and (d) optical spectrum traces. The measurement has been performed on the 2 %-SA device at V_{SA}=-1.8 V and I_g=60 mA.

The 5-QW devices show that major changes in the ML operation occur for the gain section current variations. Hence, the sonogram traces were taken along the I_g axis, at

several fixed values of V_{SA}. A stronger influence of the absorber biasing is apparent with on the 3-QW MLs, because regions of ML are usually characterised by constant values of the photocurrent in the absorber and tend to evolve diagonally on the I_g/V_{SA} maps. Therefore, the biasing points for the sonogram measurements were selected to selected at constant levels of I_{SA}. Fig. 6.3 and Fig. 6.9 display the IAC FWHM maps, as presented in Chapter 3, with the additional lines indicating the biasing ranges applied in the sonographic pulse characterisation.

6.2 5-QW Material Devices

6.2.1 Group Delay Characteristics

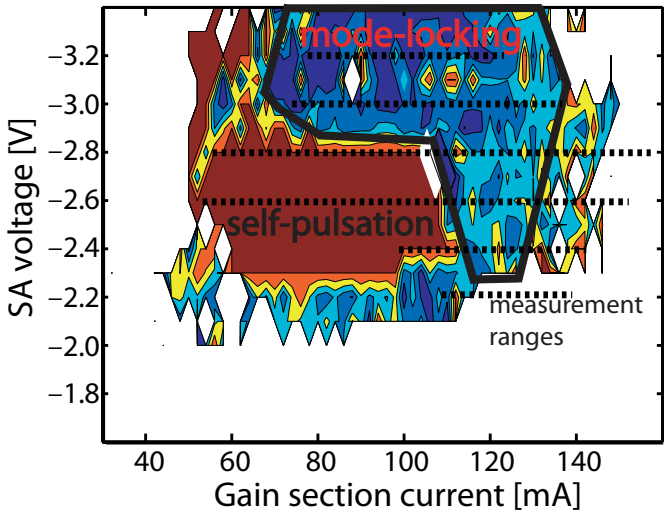

FIGURE 6.3: Sonogram measurement ranges – 5-QW MLL.

Examples of the group delay profiles measured on the 5-QW MLL are plotted in Fig. 6.4–6.5. The value of 0 ps in each characteristic is taken at the pulse central wavelength. To avoid noise and low intensity measurement errors, the GD characteristics are presented only for those wavelength ranges in which the spectral intensities are less than 10 dB below the amplitude peaks. Besides the two profiles measured at the low V_{SA} mode-locking boundary (Fig. 6.4(a)), all the presented characteristics show a general trend of positive (blue) chirp. The extent of accumulated chirp varies significantly with the gain section current. The influence of I_g is evident especially at relatively low levels of the absorber biasing, i.e. for V_{SA} ≤-2.6 V (Fig. 6.4(a)–6.4(d)). With higher voltage biasing the GD profiles appear to stabilise and become less affected by the gain current. The largest group delay variation within the pulse spectrum (over 5 ps) was measured at I_g=100 mA, V_{SA}=-2.4 V (Fig.6.4(b)), which corresponds to the boundary between the mode-locking and self-pulsation dynamics (see Fig. 6.3). Pulses least affected by chirp

are emitted at $V_{SA} = 2.6, V$, close to the lowest gain current (65 mA) and in the current range of I_g=110–120 mA (Fig. 6.4(c)–6.4(d)).

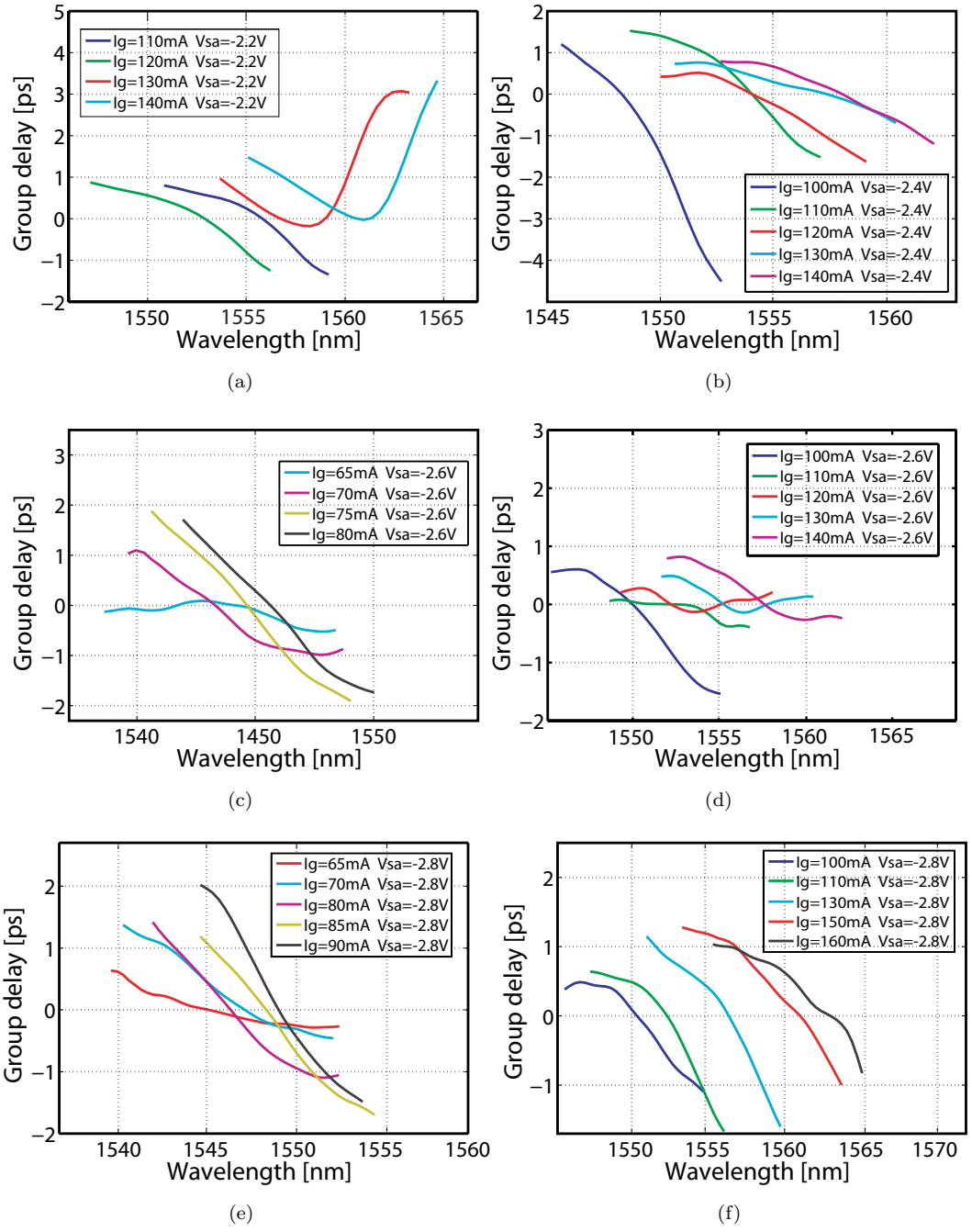

FIGURE 6.4: Group delay of the pulses taken at constant SA voltage bias for a 5-QW device with: (a) V_{SA}=-2.2 V and (b) V_{SA}=-2.4 V (c, d) V_{SA}=-2.6 V, and (e, f) V_{SA}=-2.8 V.

Examples of the group delay characteristics presenting at constant I_g and the varying absorber biasing are plotted in Fig. 6.6. At I_g=100 mA the profiles mostly overlap in the blue spectra part, and diverge slightly on the long-wavelength side (i.e. amount of

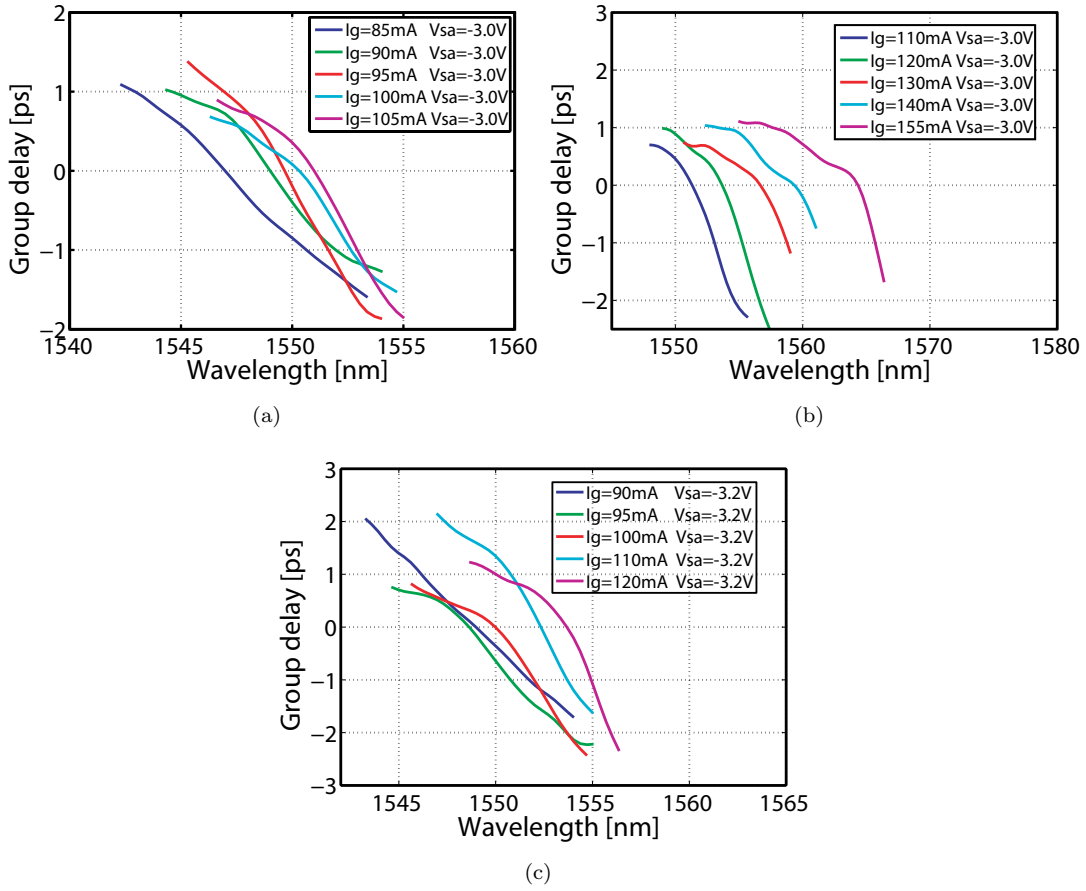

FIGURE 6.5: Group delay of the pulses emitted by a 5-QW device, taken at (a, b) V_{SA}=-3.0 V and (c) V_{SA}=-3.2 V.

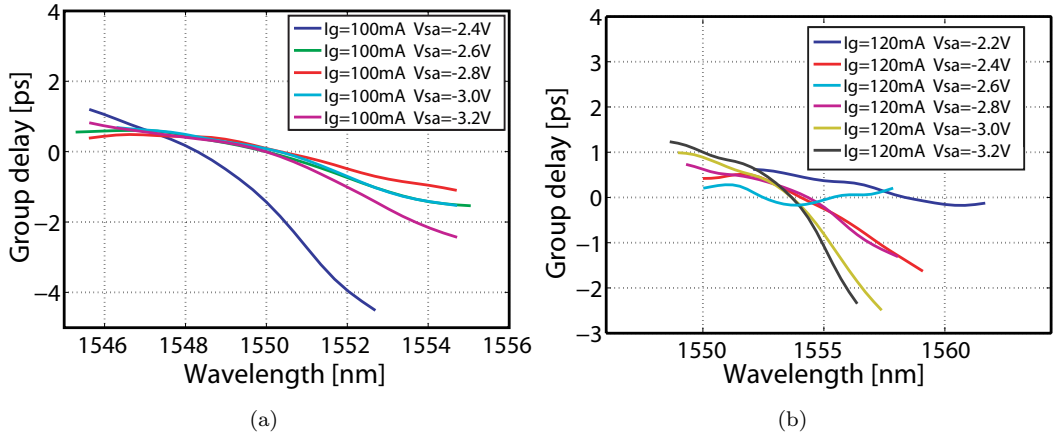

FIGURE 6.6: Group delay of the pulses taken at (a) I_{gain}=100 mA and (b) I_{gain}=120 mA.

chirp increases with V_{SA}). The only exception is the already mentioned group profile measured close to the SP region (V_{SA}=-2.4 V). A more evident influence of the SA biasing conditions appears at I_g=120 mA, where the slope of the GD characteristics

increases significantly between V_{SA}=-2.2 V and V_{SA}=-2.4 V, becomes almost flat at V_{SA}=-2.6 V, and increases again for V_{SA} <=-2.6 V.

To provide a better overview of the group delay profiles within the ML region, the coefficients of second degree polynomials fitted to all the retrieved characteristics are presented in Fig. 6.7. The linear coefficients (Fig. 6.7(a)) are dominated by negative values (meaning positive chirp), with an average magnitude that increases with V_{SA}. Besides the two regions of low linear chirp (indicated with yellow and orange markers) the typical values range from -0.2 ps/nm to -0.5 ps/nm. The highest chirps are measured on pulses affected by self-pulsation, e.g. at V_{SA}=-2.6 V, I_g=75–90 mA, as well as on the top right boundary of the ML region. The positive values measured at V_{SA}=-2.2 V (0.2 ps/nm) are caused by a highly nonlinear group delay characteristics (Fig. 6.4(a)). This is confirmed by the quadratic components of the GD profiles, plotted in Fig. 6.7(b). Besides this biasing point, another two regions are affected by quadratic chirp: pulses influenced by SP demonstrate positive quadratic chirp, and the pulses in the high–I_G and high–V_{SA} region have significant negative quadratic components.

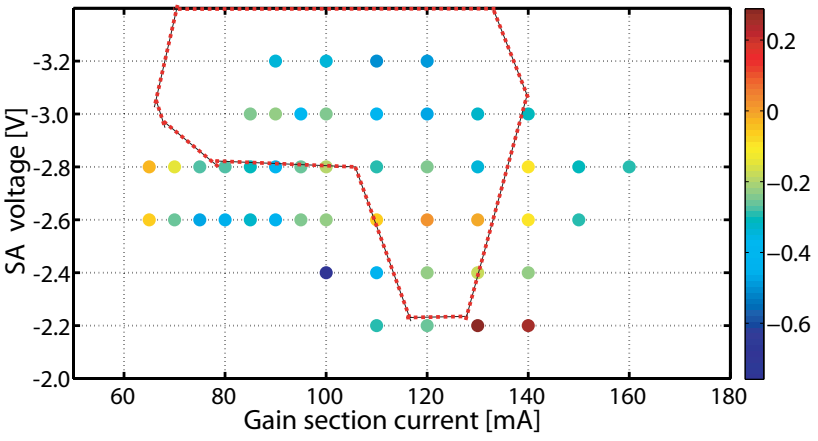

(a)

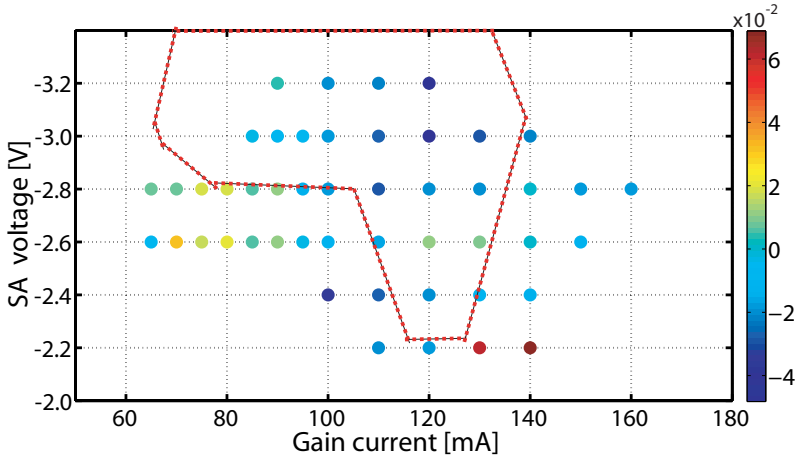

(b)

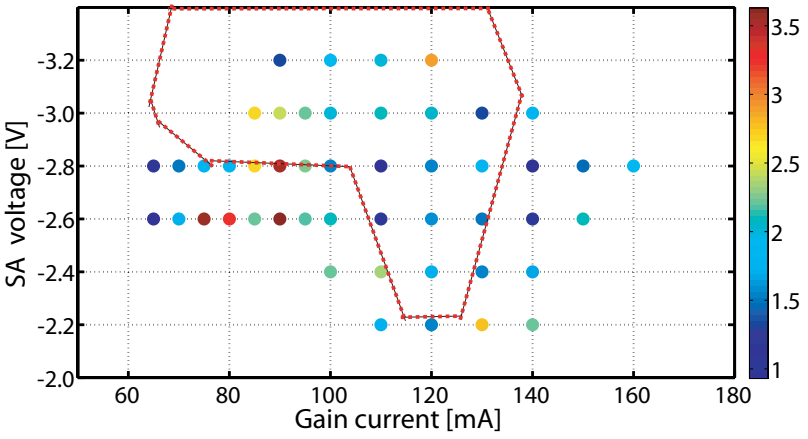

(c)

FIGURE 6.7: (a) Linear (ps/nm) and (b) quadratic (ps/nm^2) group delay profile coefficients, and (c) temporal FWHM (ps) values measured on the 2.2 % SA 5-QW MLL.

6.2.2 Temporal Intensity Profiles

In order to visualise the dynamics governing the pulse formation in the laser cavity at various biasing conditions, a parametric map displaying the temporal widths ($FWHM_P$) of the optical pulses is plotted in Fig. 6.7(c). The general tendency for the pulse width evolution follows the trend presented in Fig. 3.7(a), which plots the intensity autocorrelation widths values ($FWHM_{IAC}$) measured on the device. The shortest pulses are emitted near the low I_g ML boundary (∼1.1 ps) and in the central part of that region (e.g. ∼0.95 ps at V_{SA}=-2.6 – -2.8 V, I_g=110 mA and I_g=140 mA). The widest pulses are measured close to the boundary between ML and SP (e.g. 3.56 ps at V_{SA}=-2.6 V, I_g=75 mA). The FWHM values presented in Chapter 3 (Fig. 3.7) only depict non-deconvolved values of the IAC width. The actual temporal pulse width estimation based solely on these measurements would require an assumption on the pulse shape. Therefore, it would be encumbered with errors, as both the pulse shape and the structure evolve with the biasing conditions. To illustrate this point, a few examples of the sonogram-retrieved pulse temporal profiles are plotted in Fig. 6.8, along with the second order IAC characteristics, calculated from the pulse temporal traces. It clearly appears that most of the demonstrated pulses exhibit temporal asymmetry, with steeper trailing edge, and a low-intensity pedestal affecting the leading edge (e.g. Fig. 6.8(a)–6.8(c). The pulses become even more complex close to the SP region (Fig. 6.8(f)). Depending on the extent and amplitude of the pulse perturbations, the deconvolution factor (defined as the ratio between the FWHM values of the calculated autocorrelation trace, $FWHM_{IAC}$, and retrieved pulse, $FWHM_P$) takes values between 1.22 and 2.14. Such a complex pulse substructure in the pulse profile is impossible to identify in a simple IAC measurement, as the autocorrelation produces smoothly shaped characteristic. The low-intensity pulse instabilities, though, can be diagnosed even with the IAC traces, as the trace demonstrates a pedestal with a coherence spike (e.g. Fig. 6.8(a)). This ensemble of traces confirms the complexity of the pulse formation processes occurring in laser cavity, which vary dynamically with the biasing conditions.

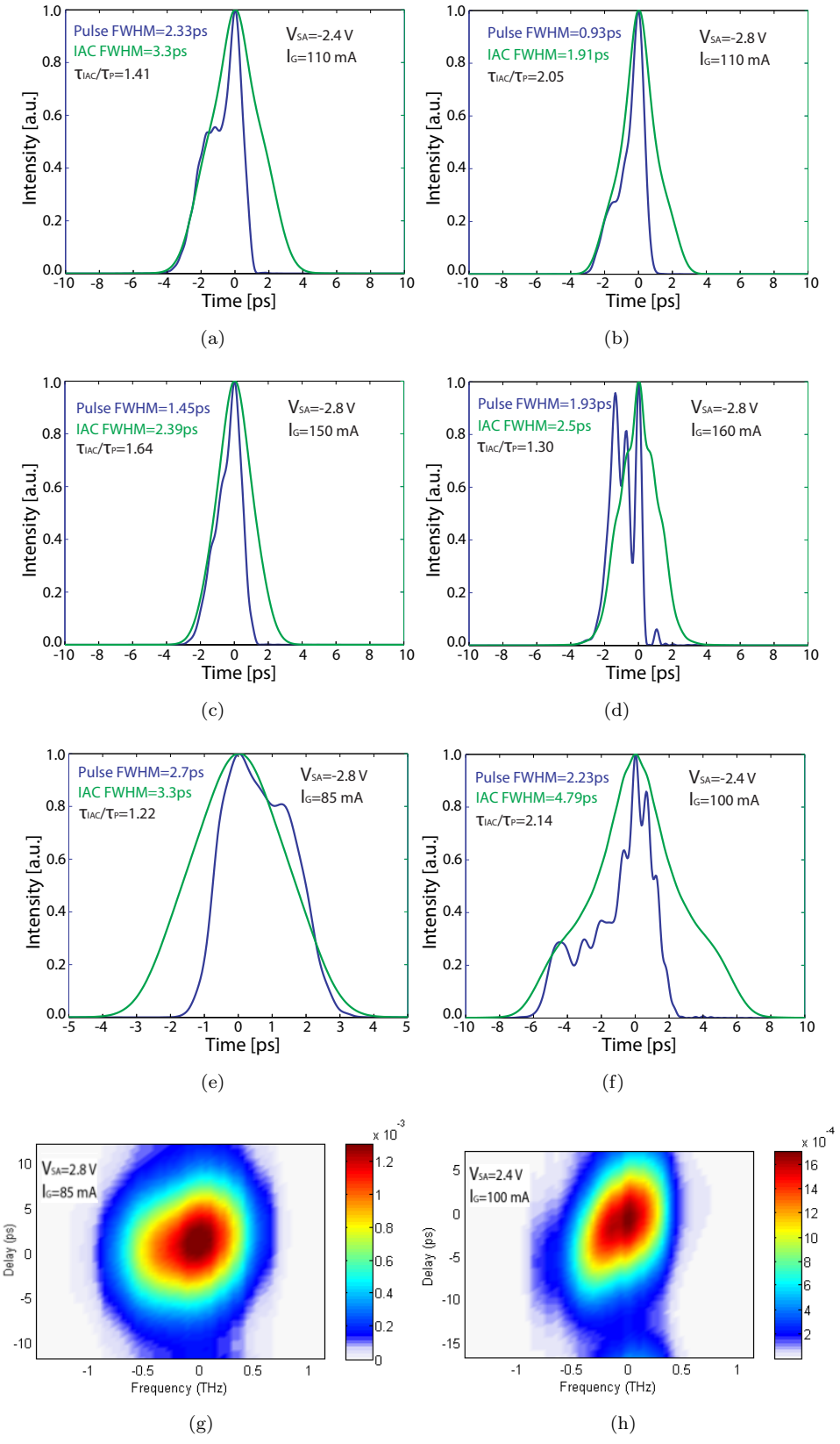

FIGURE 6.8: (a, f) Ensemble of time domain pulse profiles along with the calculated second order IAC traces at various biasing conditions within the ML region measured on the 2.2 % SA 5-QW MLL. (g, h) Sonogram traces measured on the pulses presented in (e) and (d).

6.3 3-QW Material Devices

6.3.1 Group Delay Characteristics

The sonogram measurements were performed on the 2–5 % SA devices within their mode-locking regions (Fig. 6.9). The characteristics plotted in Fig. 6.10 are examples of group delay profiles measured on the devices with different L_{SA}, at constant level of the gain current, absorber voltage and saturable absorber photocurrent. All the presented characteristics are dominated by positive chirp, with an average GD. However, depending on the laser geometry and on the biasing conditions the chirp profiles vary quite substantially. For instance, the characteristics in Fig. 6.10(c) display little differences between the chirp measured on the 4 % SA device at V_{SA}=-2.4 V. On the other hand, the gain section current applied to the 2 % MLL at V_{SA}=-1.6 V significantly modifies the pulse chirp characteristics (Fig. 6.10(d)). Also, the GD profiles taken at constant I_{SA} values vary differently between Fig. 6.10(e) and Fig. 6.10(f).

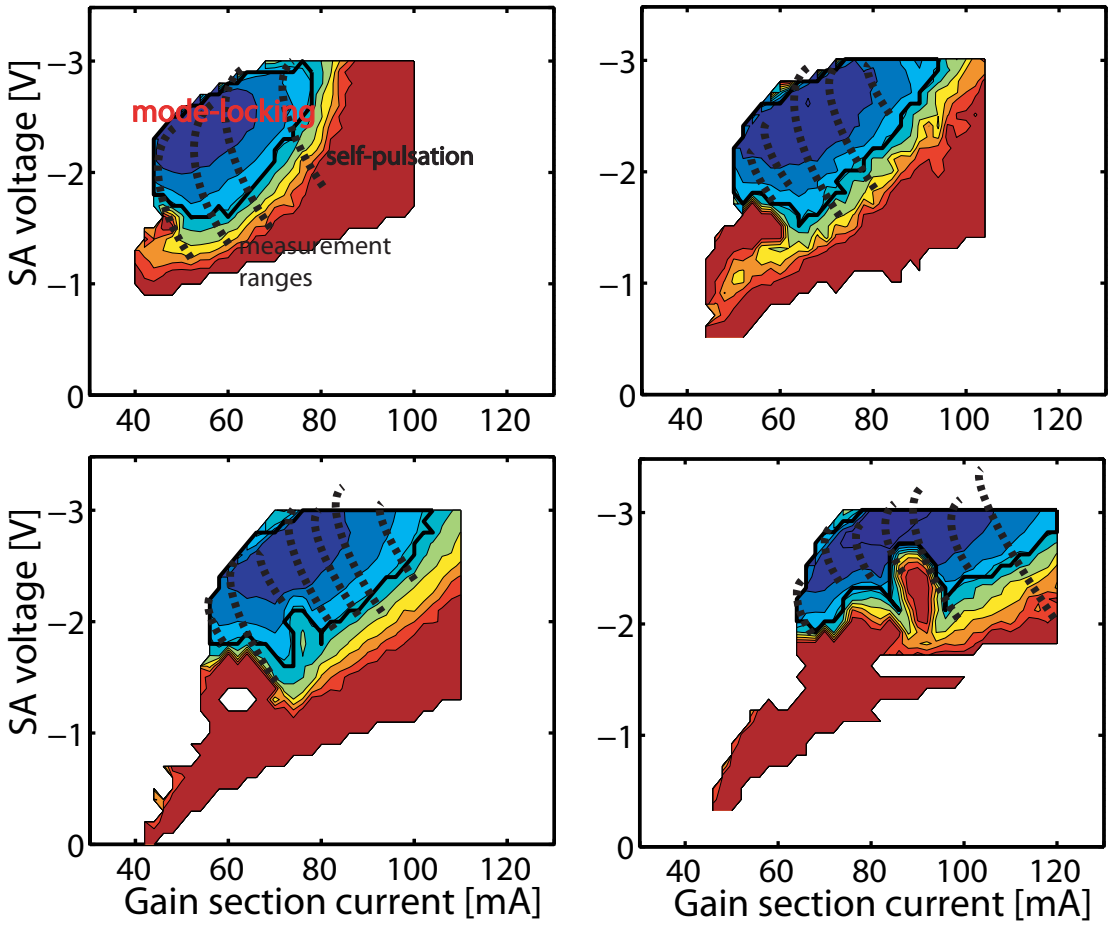

FIGURE 6.9: Sonogram measurement ranges – 5-QW MLL.

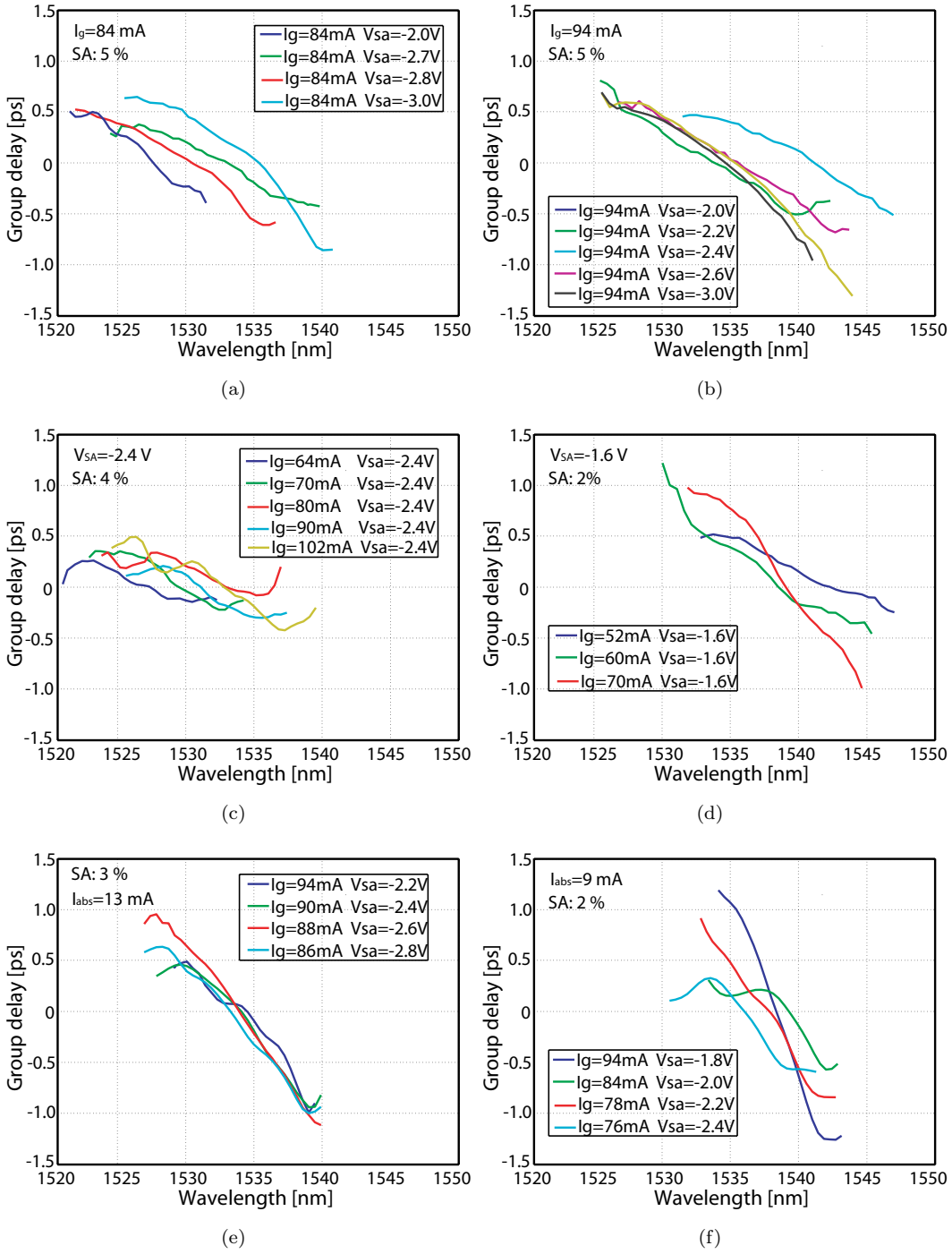

FIGURE 6.10: Group delay profiles of pulses measured on 3-QW MLLs for constant values of (a, b) gain current, (c, d) SA reverse voltage, and (e, f) absorber photocurrent.

The linear and quadratic coefficients of the polynomials fitted to the GD characteristics are shown in Fig. 6.11 – 6.12. The contour lines present in the plots indicate the regions of optimum ML and are based on the results presented in Chapter 3. It clearly appears that all the measured pulses are affected by positive chirp and the general trend for the linear component is similar on all the devices. The highest values are concentrated at the top right side of the ML regions, with values approaching -0.2 ps/nm. The linear chirp distribution covers a wider range with increasing absorber length. Also, the range of amplitudes of the linear coefficient scales with L_{SA}. Pulses with the flattest GD profiles are emitted by the 4 % SA MLL, at the low I_g ML boundary, e.g. at I_g=75 mA, V_{SA}=-3.0 V. On devices with L_{SA}=2–3 % the quadratic components in the ML regions limited are negligible, ranging from -0.8×10^{-2} ps/nm^2 to 0.3×10^{-2} ps/nm^2. The extent of the quadratic chirp intensifies with increasing L_{SA}, reaching 2.5×10^{-2} ps/nm^2 and -2.8×10^{-2} ps/nm^2 at the boundaries for the ML regions of the 4 % and 5 % SA devices. Hence, it appears that the short saturable absorber devices are suitable for applications requiring negligible amount of nonlinear chirp to be present in the optical pulses. Such chirp is simple to be compensated for, if transform-limited pulses have to be obtained. On the other hand, if pulses with low linear chirp are preferred and the nonlinear contribution to the chirp can be accepted, the longer SA devices are more favourable.

6.3.2 Temporal Intensity Profiles

The distribution of the pulse temporal FWHM values is plotted in Fig. 6.13. It is apparent from this figure that the average pulse width within the ML regions does not vary substantially as a function of L_{SA}.

On the 2 % SA the uniform region with the shortest pulses is concentrated within the boundaries of I_g=40 – 60 mA and V_{SA}=-1.6 – -2.4 V. Examples of pulses from this biasing region, along with calculated second order intensity autocorrelation characteristics, are presented in Fig. 6.14. The pulses at I_g=48 mA are characterised by smooth and symmetric pulse profile. However, the $FWHM_{IAC}/FWHM_P$ ratio is equal to 1.64, which is higher than the deconvolution factor for an ideal sech^2 pulse shape (i.e. 1.54). Additional substructures are apparent at higher gain section biasing (I_g=62 mA), and the pulses outside the optimum ML region are even more strongly affected by the trailing edge instabilities, resulting in pulse widths exceeding 2 ps, as shown in Fig. 6.14 (c, d). Also, examples of two sonogram traces measured on the 3 % SA device are plotted in Fig. 6.14.

On the 3 % SA device, most of the pulses located within the contoured region have temporal widths below 0.8 ps (Fig. 6.13 (b)). There is a significant improvement in the

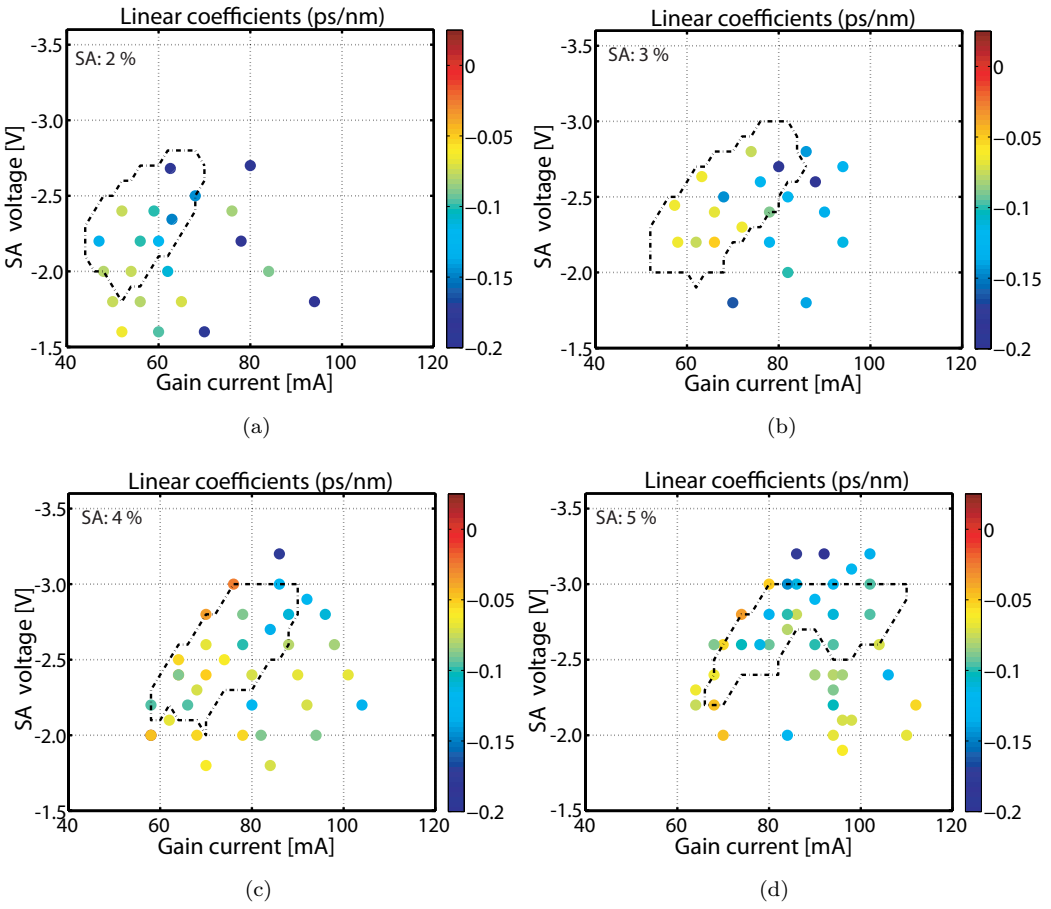

FIGURE 6.11: Linear group delay coefficients (ps/nm) of pulses measured on the 3-QW MLLs.

quality of the emitted pulses compared to the 2 % SA MLL, which also exhibit an almost ideal sech^2 pulse, e.g. at I_g=58 mA and V_{SA}=-2.2 V (Fig. 6.15). The figure shows that the pulses outside the optimum ML region produce pulses only weakly affected by temporal profile instabilities, as no additional substructures nor pulse envelope instabilities are visible within a wide range of the biasing parameters applied to the device.

A similar trend can be observed with the 4 % SA MLL (Fig. 6.13 (c)). The pulse widths are the narrowest of all the measured devices and span from 0.5 ps to 0.9 ps, as shown by the temporal profiles plotted in Fig. 6.16. The deconvolution factor of the shortest pulse (I_g=70 mA, V_{SA}=-2.4 V) is relatively high (1.67), which is caused by a slight asymmetry between the pulse edges. Much lower $FWHM_{IAC}/FWHM_P$ ratios, although with wider pulses, correspond to the low I_g boundary of the ML region. For instance, the virtually symmetric, 0.74 ps wide pulse in Fig. 6.16 (d) has a Gaussian-shaped envelope, with a $FWHM_{IAC}/FWHM_P$ ratio of 1.46.

A wider variety of optical pulses was recorded with the longest (5 %) SA device. There

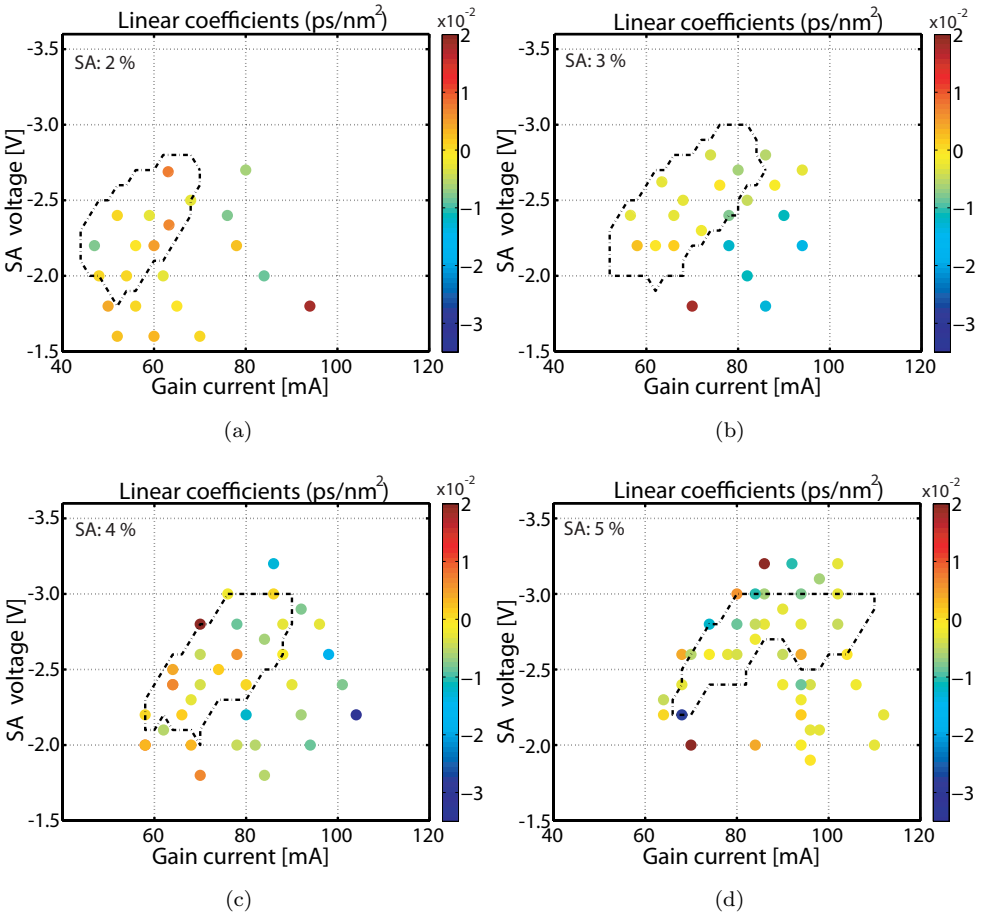

FIGURE 6.12: Quadratic group delay coefficients (ps/nm^2) of pulses measured on the 3-QW MLLs.

is a large ML region with pulses below 0.8 ps, located in the contoured biasing area at I_g <90 mA. An example of such pulse is presented in Fig. 6.17(a), with FWHM of 0.51 ps and a deconvolution factor of 1.68. All these pulses are characterised by smooth and pedestal-free time profiles. Also, the region of I_g=90 – 100 mA and V_{SA}=-2.0 – -2.5 V produces stable pulses, only weakly affected by the leading edge instabilities.

In conclusion, the pulses emitted by the device with the shortest saturable absorber are vastly affected by intensity instabilities. These temporal substructures gradually decrease with L_{SA}. The shortest pulse width (0.5 ps) is recorded with the 4 % SA MLL, while the pulses closest to the sech^2 profile are emitted with the 3 % device. The most stable emission, in terms of the temporal FWHM is measured on the 2–3 % saturable absorber MLLs.

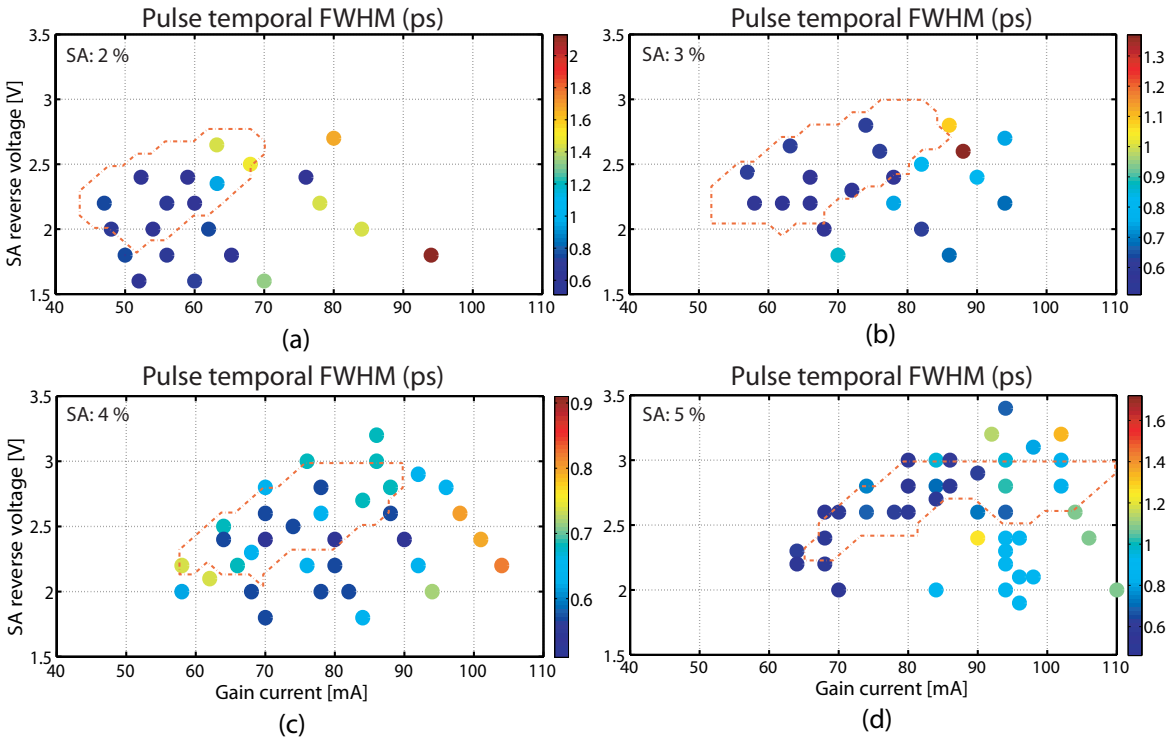

FIGURE 6.13: Distribution of the FWHM values (ps) of the temporal profiles of pulses emitted from (a) 2 %-SA, (b) 3 %-SA, (c) 4 %-SA and (d) 5 %-SA 3-QW MLLs.

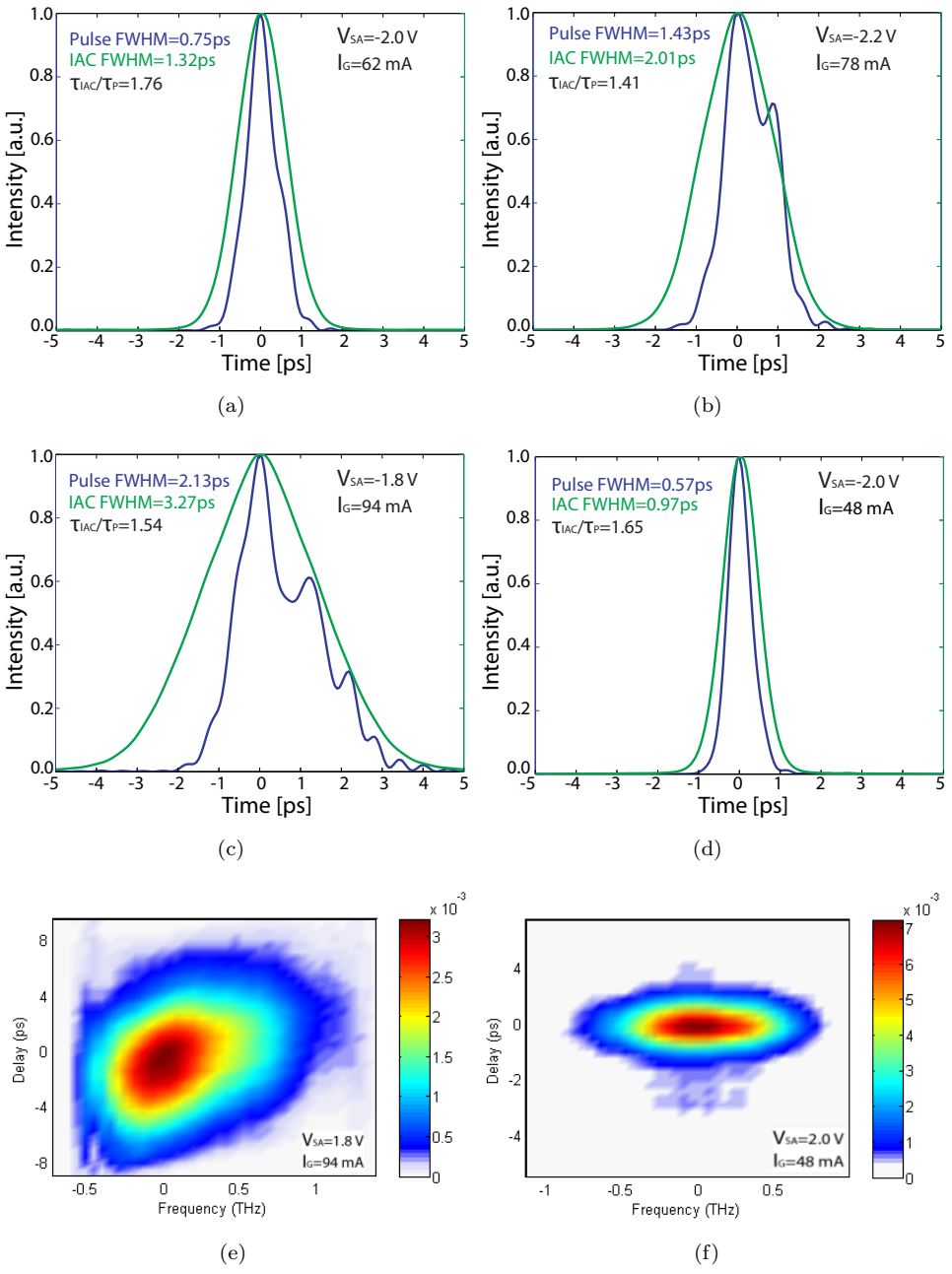

FIGURE 6.14: ((a-d) An ensemble of time domain pulse profiles along with their second order IAC traces at various biasing conditions within the ML region of the 3-QW laser with a 2 % SA. (e, f) Sonogram traces measured on the pulses presented in (c) and (d).

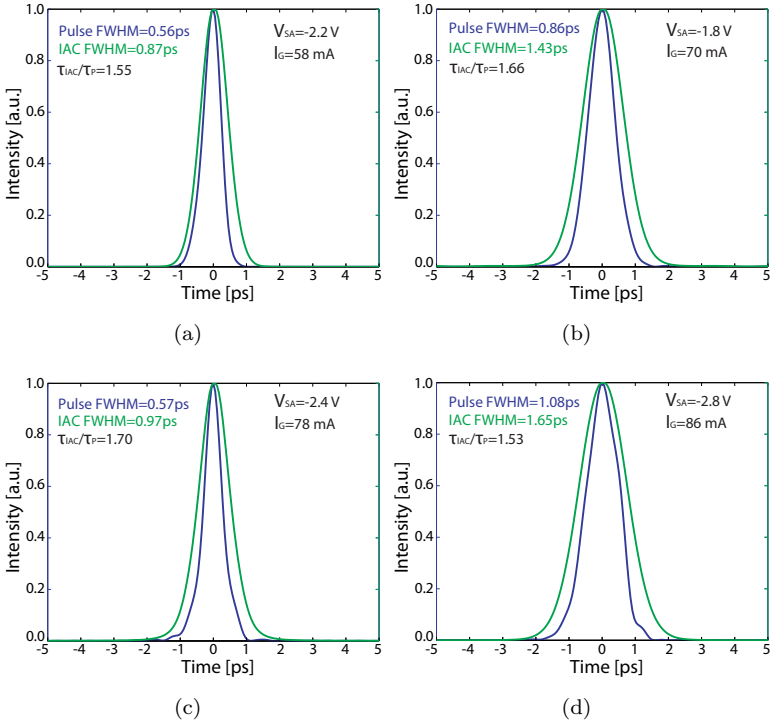

FIGURE 6.15: An ensemble of time domain pulse profiles along with their second order IAC traces at various biasing conditions within the ML region of the 3-QW laser with a 3 % SA.

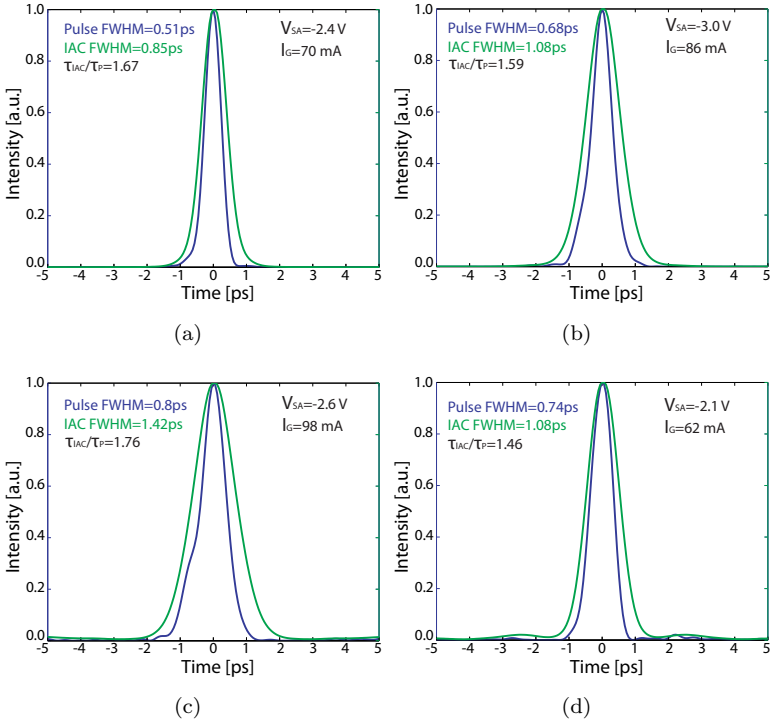

FIGURE 6.16: An ensemble of time domain pulse profiles along with their second order IAC traces at various biasing conditions within the ML region of the 3-QW laser with a 4 % SA.

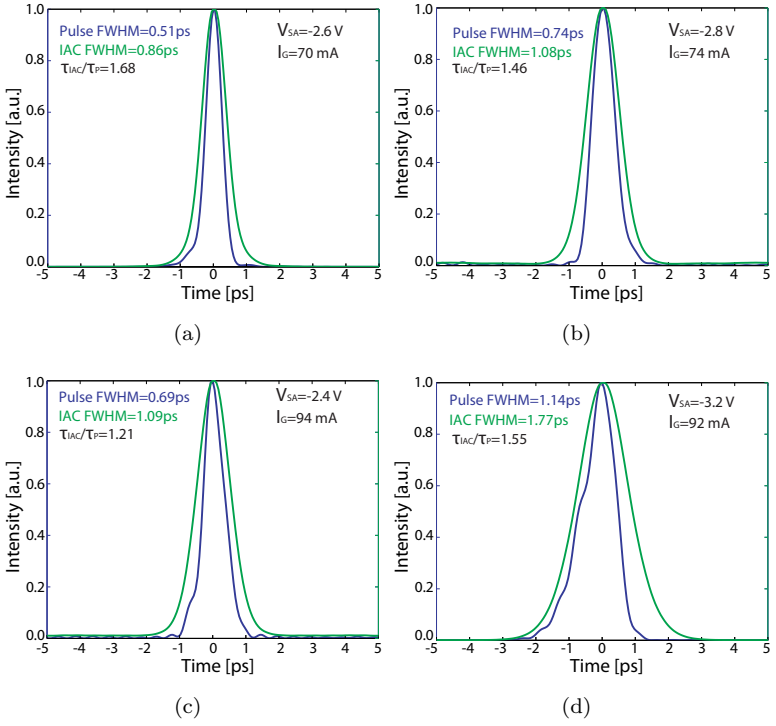

FIGURE 6.17: An ensemble of time domain pulse profiles along with their second order IAC traces at various biasing conditions within the ML region of the 3-QW laser with a 5 % SA.

6.4 Comparison Between the 5-QW and 3-QW Devices

The presented results confirm a significant improvement in the 3-QW devices over their 5-QW counterparts in terms of intensity and phase profiles of the emitted optical pulses. This confirms the conclusion drawn from the analysis reported in Chapter 3. The group delay profiles show a dominant positive chirp present in pulses from both the 5-QW and 3-QW devices. The former device, though, shows higher values of average chirp, typically ranging between -0.2 ps/nm and -0.4 ps/nm, whereas the group delay variation in the 3-QW MLL pulses rarely exceeds -0.2 ps/nm. Also, the extent of nonlinear chirp is much wider with the 5-QW MLL. Furthermore, all the parametric maps indicate that the linear chirp component can be minimised by proper adjustment of the laser biasing parameters. In terms of the temporal intensity profiles, pulses from the 5-QW device are vastly affected by various types of instabilities that are present on both the leading and trailing edges. The 3-QW lasers, on the other hand, produce symmetrical, smooth and pedestal free pulses over wide ranges of biasing conditions. The distortions in the time profile usually occur only at the boundaries of the ML operation or close to the SP regions. The minimum pulse widths measured with the 5-QW and 3-QW MLLs are equal to 1 ps and 500 fs, respectively.

6.5 Discussion on the Chirp and Temporal Profiles

The pulse generation in passive SMLLs with slow SA is based on the saturation of both the gain and the absorber sections. Changes in the optical gain triggered by the traveling pulse induce material-generated phase shift [136], governed by the linewidth enhancement factor, α-factor. The α-factor describes the relation between the variations in real, χ_r, and imaginary, χ_i, part of the material optical susceptibility with the carrier density, N:

$$\alpha = -\frac{d\chi_r}{dN} / \frac{d\chi_i}{dN} \tag{6.1}$$

The refractive index change due to the carrier depletion and gain/absorption nonlinearity caused by the saturation leads to the modification of the pulse optical frequency. These effects, along with the cavity dispersion shape both the spectral intensity and phase of the pulse and are the main contributors to the chirp. The effect of the phase modulation in the SA (due to the absorption saturation) has an opposite sign to that induced by the gain saturation. Hence, it is possible to some extent to compensate the chirp by balancing the nonlinearities in both sections. The sign of the final pulse chirp depends strongly on the mutual relation between the linewidth enhancement factors in the gain and absorption sections. In terms of the carrier density, the two sections operate in very

different regimes. The gain section operates with high carrier density levels, whereas in the reversely biased SA the band states are close to empty. In the theoretical discussion presented in [137] this difference has a major impact on the pulse chirp, as the blue chirp was obtained if the SA α-factor was set to the typical and realistic values below 1.5. The authors also emphasise a direct connection between the ML stability and the pulse chirp characteristics. This relation has been also observed in the chirp profiles presented in this chapter, where high values of the linear and quadratic coefficients appear close to the SP regions. An uncompensated and excessive chirp prevents from stable ML operation and triggers the temporal instabilities and SP.

The temporal characteristics plotted in Fig. 6.8 and Fig. 6.13 show that the pulse intensity characteristics can be affected by additional substructures or satellite pulses. The appearance of such distortions can be explained by two mechanisms. The first is caused by the presence of positive net gain at the pulse leading edge. In the ideal case, the positive gain window should be opened only at the time of the pulse arrival [6]. However, if the net gain becomes positive before that, any existent low intensity perturbations will be amplified. The dynamical evolution of these instabilities depends on the mutual relation between their group velocity, gain relaxation time and absorber recovery time. They can either be absorbed by the main peak or destabilise the pulse train and create substructures on the leading edge [138]. The second mechanism triggers similar deformations on the trailing edge, and is caused by the gain section saturation energy being larger than the absorber saturation energy [5]. In this case, the net gain window opens periodically after the main peak and the satellite pulses may develop.

6.6 Chapter Summary

In this chapter, the outcome of the sonogram measurements performed on the semiconductor mode-locked lasers was presented. The pulses on both the 5-QW and 3-QW SMLLs were studied with respect to their group delay profiles and temporal intensity characteristics. The results demonstrated superior performance of the 3-QW devices, in terms of both the accumulated chirp and temporal width of the pulses. The majority of pulses were affected by positive (blue), mostly linear chirp, the extent of which can be minimised with careful adjustment of the biasing conditions. The highest linear and nonlinear group delay characteristics were usually apparent close to the self-pulsation regions, proving a direct relation between the pulse train instabilities and the chirp formation. Examples of various pulse shapes and intensity envelope distortions were presented and discussed.

Chapter 7

Conclusions and future work

7.1 Summary of the project

This thesis dealt with the characterisation of semiconductor passively mode-locked lasers that emit picosecond and sub-picosecond optical pulses at repetition rates of ∼40 GHz and wavelengths around 1.55 μm. Such devices find applications, for instance, in optical communication systems, security, imaging and sensing. The first objective of the work was to investigate the dynamical behaviour of the AlGaInAs/InP SMLLs, by performing an extensive study of their properties at various biasing conditions, as well as for different geometries and epistructure compositions. Furthermore, the project aimed at developing a measurement system, which could evaluate both the amplitude and phase profiles of the emitted pulses, so to gather a deeper understanding on the pulse formation mechanisms. This proved to be a challenging task due to the high repetition rates, ultrashort temporal structures, low energy, and lack of synchronisation of these pulses. Hence, the sensitivity of the existent self-referenced indirect measurement techniques had to be improved to accomplish the task.

The following sections summarise the major findings and results obtained throughout the course of this research work.

7.1.1 Chapter1: Introduction

The introductory chapter gave some background on the concept of passive mode–locking, mode–locked laser diodes and ultrashort optical pulses. Various pulse characterisation approaches were analysed in terms of their advantages and drawbacks, especially with respect to their suitability for measuring pulses from SMLLs. The sonogram technique

with a TPA detection was selected as the optimum method, because it does not require any reference pulses or ultrafast modulation, and is virtually ambiguity–free. Furthermore, the TPA detection allows to achieve high sensitivity, and can be used with high–repetition pulses and over extensive spectral regions.

7.1.2 Chapter 2: Al-quaternary Material Systems

This chapter investigated the properties of the two semiconductor materials systems (5–quantum well and 3–quantum well) used to fabricate the MLLs. Material features, such as the gain, absorption and group velocity dispersion profiles, all having significantly an impact on the mode–locking operation, were examined over a wide range of the biasing conditions. Two material characterisation techniques, namely the three-section and Hakki–Paoli methods were compared, and the latter method was used to analyse the material properties. The obtained results highlighted the differences in the gain and absorption spectra between the two materials, and also demonstrated the biasing conditions' influence on typical phenomena taking place in semiconductor devices, such as the QCSE or carrier induced effects.

7.1.3 Chapter 3: Dynamics of Al-quaternary Mode-Locked Laser Diodes

The first project objective was completed by a detailed characterisation of the SMLLs fabricated in the two material systems, performed over a wide range of biasing parameters. The study was based on the analysis of the optical and RF spectra, as well as on the intensity autocorrelation traces. It provided an extensive overview of the different dynamical regimes of the devices, such as mode-locking, self-pulsation and continuous wave emission. The dynamical behaviour of different material structures and device geometries (i.e. the saturable absorber relative length) was evaluated. The 3–QW MLLs proved superior to the 5–QW devices in terms of the pulse widths, emission stability and lower influence of self-pulsation. Pulses producing IAC traces with FWHM as low as 0.7 ps were measured with the 5 % SA laser fabricated in the 3-QW material system.

7.1.4 Chapter 4: Two-Photon Absorption Detectors

This chapter described the design, fabrication and testing of the TPA detectors intended for the sonogram pulse characterisation system. The detectors were based on semiconductor waveguides, operating in a traveling-wave mode and were fabricated with standard III–V semiconductor processing technologies. The desired sensitivity was achieved by maximising the intensity inside the optical waveguide through the use of narrow and

deep waveguides. The experimental tests confirmed that the fabricated devices were suitable for the characterisation of the SMLLs within the whole range of emission spectra, repetition frequencies and power levels. A TPA response was measured with pulse peak power levels as low as 5 mW and ∼200 μW in the pure quadratic and combined (linear and quadratic) detection regimes, respectively. The three-section devices with a 6 μm wide input taper, 1 mm long and 1.2 μm wide detection section proved optimum design for the sonogram set-up due to the best trade-off between low-loss operation, high TPA efficiency and low sensitivity to the input polarisation.

7.1.5 Chapter 5: Sonogram Set–up

This chapter detailed the concept of optical pulse measurements with the sonogram technique and discussed the features of the main optical components required for the development of the system, i.e. the tunable bandpass filter and the delay line. The data acquisition process and the iterative pulse retrieval algorithm were next explained. The final arrangement with the TPA detector was subsequently verified with a wide range of different trial optical pulses, generated with a fiber-based mode-locked laser. These tests were very successful and only showed a few minor limitations of the system, caused mostly by the fixed resolution of the tunable filter. However, the developed set-up proved suitable for ultrashort pulses emitted from SMLLs.

7.1.6 Chapter 6: Sonogram Characterisation of Optical Pulses

The results presented in this chapter concluded the second objective of the project, by investigating the chirp and temporal profiles of the pulses from the ML laser diodes. The sonogram system was used to study the evolution of the pulse characteristics with varying biasing conditions and on different devices. The obtained results confirmed that the devices fabricated in the 3-QW material produce pulses with superior features, i.e. with weaker chirp, smoother temporal profiles and narrower widths. The majority of the pulses were affected by a positive chirp, which usually could be minimised with careful adjustment of the applied biasing. The minimum pulse widths calculated from the sonogram traces measured on the 5-QW and 3-QW devices were equal to 1 ps and 500 fs, respectively.

7.2 Conclusion

The work presented in this thesis demonstrated an improved approach to the characterisation of unsynchronized, ultrashort, low energy optical pulses, such as those emitted from semiconductor mode-locked lasers. It has been shown, that the sonogram technique provides a capability for retrieving both pulse intensity and phase profiles and combined with the optimised two-photon absorption detector can be applied to low intensity optical pulses. The proposed detector also benefits from a traveling-mode type of operation and negligible dispersion, which makes it suitable for high repetition rate sub-picosecond pulses. The operation of the developed sonogram set-up has been successfully verified with the test pulses of a known chirp. Also, some limitations of the developed system have been demonstrated, caused mainly by the fixed-bandwidth tunable filter, but also by the vulnerability of the sonogram method to optical pulses emitted from purely phase-locked or SP-affected lasers.

The measurement system has been used to examine picosecond and sub-picosecond optical pulses emitted from the 1.5 μm AlGaInAs/InP semiconductor passively mode-locked lasers. Combined with an extensive characterisation of the lasers' dynamics, this work demonstrates a comprehensive study of such devices. It has been shown how the modifications introduced in the laser material structure, e.g. the lower number of quantum wells in the active region or decreased cavity losses, influence the devices' performance and improve their output power, phase noise, or optical pulse intensity and phase profiles. Furthermore, various benefits stemming from the saturable absorber size have been demonstrated, so that the future devices can be designed for the maximum average power, minimum self-pulsation region, low phase noise, highly linear chirp, etc.

7.3 Future work

Suggestions for future work as a continuation of this project are as follows:

- Investigation of other semiconductor epistructures for the fabrication of the two-photon absorption detectors. For instance, the ratio between the quadratic and linear photo-response could be optimised by the careful selection of the material bandgap.

- Optimisation of the spectral filter employed in the sonogram set-up in terms of achievable resolution, bandpass tunability and introduced phase distortion. For instance, an etalon-based bandpass filter could be used to used in order to gain control of all those parameters. Minimised phase distortion introduced by the filter would improve the pulse retrieval algorithm convergence. The capability to modify the bandwidth would increase the scope of potential optical pulses, which could be characterised with the sonogram system.

- Miniaturisation of the sonogram system and development of a portable and a plug-and-play device. For instance, a sonogram system comprising the commercially available bandwidth variable fibre-based tunable filter, fiber-based delay line, and butt-coupled TPA detector could be implemented in order to achieve alignment free sonogram system.

- Investigation of the routes for the full integration of the sonogram system. For example, the silicon-on-insulator ring resonators provide robust tunable spectral filter and tunable delay line components. Also, silicon is a semiconductor material suitable for TPA detection at 1550 nm.

- Study of mode-locked laser diodes with more complex structures, for instance comprising chirped distributed Bragg reflectors, or devices fabricated on quantum-dot materials.

Bibliography

[1] A. C. Bryce, "High power, high frequency mode-locked semiconductor lasers," September 2007, EP/E065112/1. [Online]. Available: http://gow.epsrc.ac.uk/ViewGrant.aspx?GrantRef=EP/E065112/1

[2] R. Paschotta and U. Keller, "Passive mode locking with slow saturable absorbers," *Applied Physics B: Lasers and Optics*, vol. 73, pp. 653–662, 2001.

[3] R. Koumans and R. Van Roijen, "Theory for passive mode-locking in semiconductor laser structures including the effects of self-phase modulation, dispersion, and pulse collisions," *IEEE J. Quantum Electron.*, vol. 32, no. 3, pp. 478–492, Mar 1996.

[4] W. Koechner, *Solid-State Laser Engineering*. New York, NY; London: Springer, 2006.

[5] H. Haus, "Mode-locking of lasers," *Selected Topics in Quantum Electronics, IEEE Journal of*, vol. 6, no. 6, pp. 1173 –1185, Nov/Dec 2000.

[6] G. New, "Pulse evolution in mode-locked quasi-continuous lasers," *Quantum Electronics, IEEE Journal of*, vol. 10, no. 2, pp. 115 – 124, Feb 1974.

[7] S. Arahira, Y. Matsui, and Y. Ogawa, "Mode-locking at very high repetition rates more than terahertz in passively mode-locked distributed-bragg-reflector laser diodes," *Quantum Electronics, IEEE Journal of*, vol. 32, no. 7, pp. 1211 –1224, Jul 1996.

[8] A. Schmitt-Sody, A. Velten, Y. Liu, L. Arissian, and J.-C. A Diels, "High-Power Hybrid Mode-Locked External Cavity Semiconductor Laser Using Tapered Amplifier with Large Tunability," *Research Letters in Optics*.

[9] N. Onodera, "Optical beat frequency generation up to 40.6 THz by mode-locked semiconductor lasers," *Electronics Letters*, vol. 32, no. 18, p. 1727, Aug 1996.

[10] M. Shirane, Y. Hashimoto, H. Yamada, and H. Yokoyama, "A compact optical sampling measurement system using mode-locked laser-diode modules," *Photonics Technology Letters, IEEE*, vol. 12, no. 11, pp. 1537 – 1539, Nov 2000.

[11] L. A. Jiang, E. P. Ippen, and H. Yokoyama, "Semiconductor mode-locked lasers as pulse sources for high bit rate data transmission," vol. 3, pp. 21–51, 2007.

[12] A. Clausen, H. Poulsen, L. Oxenlowe, A. Siahlo, J. Seoane, and P. Jeppesen, "Pulse source requirements for OTDM systems," in *Lasers and Electro-Optics Society, 2003. LEOS 2003. The 16th Annual Meeting of the IEEE*, vol. 1, Oct 2003, pp. 382 – 383 vol.1.

[13] F. Quinlan, S. Ozharar, S. Gee, and P. J. Delfyett, "Harmonically mode-locked semiconductor-based lasers as high repetition rate ultralow noise pulse train and optical frequency comb sources," *Journal of Optics A: Pure and Applied Optics*, vol. 11, no. 10, p. 103001, 2009. [Online]. Available: http://stacks.iop.org/1464-4258/11/i=10/a=103001

[14] M. Strain, P. Stolarz, and M. Sorel, "Passively mode-locked lasers with integrated chirped bragg grating reflectors," *Quantum Electronics, IEEE Journal of*, vol. 47, no. 4, pp. 492 –499, Apr 2011.

[15] K. A. Williams, M. G. Thompson, and I. H. White, "Long-wavelength monolithic mode-locked diode lasers," *New Journal of Physics*, vol. 6, no. 1, p. 179, 2004. [Online]. Available: http://stacks.iop.org/1367-2630/6/i=1/a=179

[16] W. Yang and A. Gopinath, "Study of passive mode locking of semiconductor lasers using time domain modeling," *Applied Physics Letters*, vol. 63, no. 20, pp. 2717 –2719, Nov 1993.

[17] J. Palaski and K. Y. Lau, "Parameter ranges for ultrahigh frequency mode locking of semiconductor lasers," *Applied Physics Letters*, vol. 59, no. 1, pp. 7 –9, Jul 1991.

[18] J. C. Diels and W. Rudolph, *Ultrafast Optics Textbook,*.

[19] C. Iaconis, V. Wong, and I. Walmsley, "Direct interferometric techniques for characterizing ultrashort optical pulses," *Selected Topics in Quantum Electronics, IEEE Journal of*, vol. 4, no. 2, pp. 285 –294, Mar/Apr 1998.

[20] J. Paye, "The chronocyclic representation of ultrashort light pulses," *Quantum Electronics, IEEE Journal of*, vol. 28, no. 10, pp. 2262 –2273, Oct 1992.

[21] J. K. Ranka, A. L. Gaeta, A. Baltuska, M. S. Pshenichnikov, and D. A. Wiersma, "Autocorrelation measurement of 6-fs pulses based on the two-photon-induced

photocurrent in a GaAsP photodiode," *Opt. Lett.*, vol. 22, no. 17, pp. 1344–1346, Sep 1997. [Online]. Available: http://ol.osa.org/abstract.cfm?URI=ol-22-17-1344

[22] R. Trebino, *Frequency-resolved optical gating: the measurement of ultrashort laser pulses*. Boston, MA; London: Kluwer Academic, 2000.

[23] K. Naganuma, K. Mogi, and H. Yamada, "Time direction determination of asymmetric ultrashort optical pulses from second harmonic generation autocorrelation signals," *Applied Physics Letters*, vol. 54, no. 13, pp. 1201 –1202, Mar 1989.

[24] N. Naganuma, K. Mogi, and H. Yamada, "General method for ultrashort light pulse chirp measurement," *Quantum Electronics, IEEE Journal of*, vol. 25, no. 6, pp. 1225 –1233, Jun 1989.

[25] J. W. Nicholson, M. Mero, J. Jasapara, and W. Rudolph, "Unbalanced third-order correlations for full characterization of femtosecond pulses," *Opt. Lett.*, vol. 25, no. 24, pp. 1801–1803, Dec 2000. [Online]. Available: http://ol.osa.org/abstract.cfm?URI=ol-25-24-1801

[26] D. A. Bender, J. W. Nicholson, and M. Sheik-Bahae, "Ultrashort laser pulse characterization using modified spectrum auto-interferometric correlation (MOSAIC)," *Opt. Express*, vol. 16, no. 16, pp. 11 782–11 794, Aug 2008. [Online]. Available: http://www.opticsexpress.org/abstract.cfm?URI=oe-16-16-11782

[27] B. Yellampalle, R. D. Averitt, and A. J. Taylor, "Unambiguous chirp characterization using modified-spectrum auto-interferometric correlation and pulse spectrum," *Opt. Express*, vol. 14, no. 19, pp. 8890–8899, Sep 2006. [Online]. Available: http://www.opticsexpress.org/abstract.cfm?URI=oe-14-19-8890

[28] D. A. Bender and M. Sheik-Bahae, "Modified spectrum autointerferometric correlation (MOSAIC) for single-shot pulse characterization," *Opt. Lett.*, vol. 32, no. 19, pp. 2822–2824, Oct 2007. [Online]. Available: http://ol.osa.org/abstract.cfm?URI=ol-32-19-2822

[29] A. Sharma, P. Naik, and P. Gupta, "Simple and sensitive method for visual detection of temporal asymmetry of ultrashort laser pulses," *Opt. Express*, vol. 12, no. 7, pp. 1389–1396, Apr 2004. [Online]. Available: http://www.opticsexpress.org/abstract.cfm?URI=oe-12-7-1389

[30] I. A. Walmsley and C. Dorrer, "Characterization of ultrashort electromagnetic pulses," *Adv. Opt. Photon.*, vol. 1, no. 2, pp. 308–437, Apr 2009.

[31] R. Trebino and D. J. Kane, "Using phase retrieval to measure the intensity and phase of ultrashort pulses: frequency-resolved optical gating," *J. Opt.*

Soc. Am. A, vol. 10, no. 5, pp. 1101–1111, May 1993. [Online]. Available: http://josaa.osa.org/abstract.cfm?URI=josaa-10-5-1101

[32] A. Baltuska, M. Pshenichnikov, and D. Wiersma, "Second-harmonic generation frequency-resolved optical gating in the single-cycle regime," *Quantum Electronics, IEEE Journal of*, vol. 35, no. 4, pp. 459 –478, Apr 1999.

[33] B. A. Richman, M. A. Krumbügel, and R. Trebino, "Temporal characterization of mid-IR free-electron-laser pulses by frequency-resolved optical gating," *Opt. Lett.*, vol. 22, no. 10, pp. 721–723, May 1997. [Online]. Available: http://ol.osa.org/abstract.cfm?URI=ol-22-10-721

[34] B. Kohler, V. V. Yakovlev, K. R. Wilson, J. Squier, K. W. DeLong, and R. Trebino, "Phase and intensity characterization of femtosecond pulses from a chirped-pulse amplifier by frequency-resolved optical gating," *Opt. Lett.*, vol. 20, no. 5, pp. 483–485, Mar 1995. [Online]. Available: http://ol.osa.org/abstract.cfm?URI=ol-20-5-483

[35] J. N. Sweetser, D. N. Fittinghoff, and R. Trebino, "Transient-grating frequency-resolved optical gating," *Opt. Lett.*, vol. 22, no. 8, pp. 519–521, Apr 1997. [Online]. Available: http://ol.osa.org/abstract.cfm?URI=ol-22-8-519

[36] P. O'Shea, M. Kimmel, and R. Trebino, "Increased phase-matching bandwidth in simple ultrashort-laser-pulse measurements," *Journal of Optics B: Quantum and Semiclassical Optics*, vol. 4, no. 1, p. 44, 2002. [Online]. Available: http://stacks.iop.org/1464-4266/4/i=1/a=307

[37] J. L. Chilla and O. E. Martinez, "Frequency domain phase measurement of ultrashort light pulses. Effect of noise," *Optics Communications*, vol. 89, no. 5-6, pp. 434 – 440, 1992.

[38] D. Reid, B. Thomsen, J. Dudley, and J. Harvey, "Sonogram characterisation of picosecond pulses at 1.5 μm using waveguide two photon absorption," *Electronics Letters*, vol. 36, no. 13, pp. 1141 –1142, Jun 2000.

[39] D. N. Fittinghoff, J. L. Bowie, J. N. Sweetser, R. T. Jennings, M. A. Krumbügel, K. W. DeLong, R. Trebino, and I. A. Walmsley, "Measurement of the intensity and phase of ultraweak, ultrashort laser pulses: erratum," *Opt. Lett.*, vol. 21, no. 16, pp. 1313–1313, Aug 1996. [Online]. Available: http://ol.osa.org/abstract.cfm?URI=ol-21-16-1313

[40] C. Iaconis and I. Walmsley, "Spectral phase interferometry for direct electric-field reconstruction of ultrashort optical pulses," *Opt. Lett.*, vol. 23, no. 10, pp. 792–794, May 1998. [Online]. Available: http://ol.osa.org/abstract.cfm?URI=ol-23-10-792

[41] M. Beck, M. G. Raymer, I. A. Walmsley, and V. Wong, "Chronocyclic tomography for measuring the amplitude and phase structure of optical pulses," *Opt. Lett.*, vol. 18, no. 23, pp. 2041–2043, Dec 1993. [Online]. Available: http://ol.osa.org/abstract.cfm?URI=ol-18-23-2041

[42] F. Laughton, J. Marsh, D. Barrow, and E. Portnoi, "The two-photon absorption semiconductor waveguide autocorrelator," *Quantum Electronics, IEEE Journal of*, vol. 30, no. 3, pp. 838 –845, Mar 1994.

[43] J. M. Roth, T. E. Murphy, and C. Xu, "Ultrasensitive and high-dynamic-range two-photon absorption in a GaAs photomultiplier tube," *Opt. Lett.*, vol. 27, no. 23, pp. 2076–2078, Dec 2002.

[44] K. Taira, Y. Fukuchi, R. Ohta, K. Katoh, and K. Kikuchi, "Background-free intensity autocorrelator employing Si avalanche photodiode as two-photon absorber," *Electronics Letters*, vol. 38, no. 23, pp. 1465 – 1466, Nov 2002.

[45] R. Salem and T. E. Murphy, "Polarization-insensitive cross correlation using two-photon absorption in a silicon photodiode," *Opt. Lett.*, vol. 29, no. 13, pp. 1524–1526, Jul 2004. [Online]. Available: http://ol.osa.org/abstract.cfm?URI=ol-29-13-1524

[46] D. Reid, W. Sibbett, J. Dudley, L. Barry, B. Thomsen, and J. Harvey, "Commercial Semiconductor Devices for Two Photon Absorption Autocorrelation of Ultrashort Light Pulses," *Appl. Opt.*, vol. 37, no. 34, pp. 8142–8144, Dec 1998.

[47] T. K. Liang, H. K. Tsang, I. E. Day, J. Drake, A. P. Knights, and M. Asghari, "Silicon waveguide two-photon absorption detector at 1.5 μm wavelength for autocorrelation measurements," *Applied Physics Letters*, vol. 81, no. 7, pp. 1323 –1325, Aug 2002.

[48] L. Chan and H. Tsang, "Two photon absorption InGaAsP waveguide autocorrelator for pulsewidth measurement of low power 1.55 μm wavelength pulses," in *Electron Devices Meeting, 1995. Proceedings., 1995 IEEE Hong Kong*, Jul 1995, pp. 47 –50.

[49] H. K. Tsang, R. V. Penty, I. H. White, R. S. Grant, W. Sibbett, J. B. D. Soole, H. P. LeBlanc, N. C. Andreadakis, R. Bhat, and M. A. Koza, "Two-photon absorption and self-phase modulation in InGaAsP/InP multi-quantum-well waveguides," *Journal of Applied Physics*, vol. 70, no. 7, pp. 3992 –3994, Oct 1991.

[50] P. Stolarz, J. Javaloyes, G. Mezosi, L. Hou, C. Ironside, M. Sorel, C. Bryce, and S. Balle, "Spectral dynamical behavior in passively mode-locked semiconductor lasers," *Photonics Journal, IEEE*, vol. 3, no. 6, pp. 1067–1082, Dec 2011.

[51] Y. Qian, A. Hohl-AbiChedid, J. Li, F. Ye, F. Yang, A. Rice, X. Chen, S. D. Solimine, R. J. Bhat, M. H. Hu, and et al., "High-performance AlGaInAs/InP 14xx-nm semiconductor pump lasers for optical amplifications," *Proceedings of the SPIE The International Society for Optical Engineering*, vol. 4905, pp. 37–46, 2002. [Online]. Available: http://axiom.iop.org/fmtprt?VdkVgwKey=7704705&fmt=H&emailed=1

[52] S. C. W. J. L. Y. Xiong Bing, Xu Jianming, "High speed electro-absorption modulators for digital and analog optical fiber communications," *China Communications*, vol. 6, no. 3, p. 72, 2009. [Online]. Available: http://www.chinacommunications.cn:8080/zgtx/EN/abstract/article_7546.shtml

[53] T.-C. Peng, Y.-H. Huang, C.-C. Yang, K.-F. Huang, F.-M. Lee, C.-W. Hu, M.-C. Wu, and C.-L. Ho, "Low-cost and high-performance 1.3 μm AlGaInAs-InP uncooled laser diodes," *Photonics Technology Letters, IEEE*, vol. 18, no. 12, pp. 1380 –1382, Jun 2006.

[54] L. Hou, M. Haji, B. Qiu, J. Akbar, A. Bryce, and J. Marsh, "10-GHz AlGaInAs/InP 1.55-μm Passively Mode-Locked Laser With Low Divergence Angle and Timing Jitter," *IEEE Photonics Technol. Lett.*, vol. 23, no. 15, pp. 1079–1081, Aug 2011.

[55] K. Yvind, D. Larsson, L. Christiansen, C. Angelo, L. Oxenlwe, J. Mrk, D. Birkedal, J. Hvam, and J. Hanberg, "Low-jitter and high-power 40-GHz all-active mode-locked lasers," *Photonics Technology Letters, IEEE*, vol. 16, no. 4, pp. 975 –977, Apr 2004.

[56] C. Henry, "Theory of the linewidth of semiconductor lasers," *Quantum Electronics, IEEE Journal of*, vol. 18, no. 2, pp. 259 – 264, Feb 1982.

[57] D. Henderson and A. Roddie, "A comparison of spectral and temporal techniques for the measurement of timing jitter and their application in a modelocked argon ion and dye laser system," *Optics Communications*, vol. 100, no. 56, pp. 456 – 460, 1993. [Online]. Available: http://www.sciencedirect.com/science/article/pii/003040189390244Y

[58] L. Hou, M. Haji, J. Akbar, B. Qiu, and A. C. Bryce, "Low divergence angle and low jitter 40 GHz AlGaInAs/InP 1.55 μm mode-locked lasers," *Opt. Lett.*, vol. 36, no. 6, pp. 966–968, Mar 2011. [Online]. Available: http://ol.osa.org/abstract.cfm?URI=ol-36-6-966

[59] M. A. S. M. Dutta, *Advances in semiconductor lasers and applications to optoelectronics*. Singapore: World Scientific, 2000.

[60] J. D. Thomson, H. D. Summers, P. J. Hulyer, P. M. Smowton, and P. Blood, "Determination of single-pass optical gain and internal loss using a multisection device," *Applied Physics Letters*, vol. 75, no. 17, pp. 2527–2529, 1999. [Online]. Available: http://link.aip.org/link/?APL/75/2527/1

[61] M. Jain and C. Ironside, "A multi-section technique for the electroabsorption measurements in waveguide semiconductor electroabsorption modulators," *IET Optoelectronics*, vol. 1, no. 4, pp. 163–168, 2007. [Online]. Available: http://link.aip.org/link/?OPT/1/163/1

[62] S. McMaster, "Monolithically Integrated Mode-Locked Ring Lasers and Mach-Zender Interferometers in AlGaInAs," *PhD Thesis, University of Glasgow*, May 2010.

[63] H. Okamoto, "Optical properties of superlattice and MQW laser diode," *Journal of Vacuum Science and Technology B: Microelectronics and Nanometer Structures*, vol. 3, no. 2, pp. 687–693, 1985. [Online]. Available: http://link.aip.org/link/?JVB/3/687/1

[64] M. Korbl, A. Groning, H. Schweizer, and J. L. Gentner, "Gain spectra of coupled InGaAsP/InP quantum wells measured with a segmented contact traveling wave device," *Journal of Applied Physics*, vol. 92, no. 5, pp. 2942–2944, 2002. [Online]. Available: http://link.aip.org/link/?JAP/92/2942/1

[65] D. A. B. Miller, D. S. Chemla, T. C. Damen, A. C. Gossard, W. Wiegmann, T. H. Wood, and C. A. Burrus, "Electric field dependence of optical absorption near the band gap of quantum-well structures," *Phys. Rev. B*, vol. 32, no. 2, pp. 1043–1060, Jul 1985.

[66] A. Moseley, D. Robbins, A. Marshall, M. Kearley, and J. Davies, "Quantum confined Stark effect in GaInAs/InP single quantum wells grown by low pressure MOVPE," *Electronics Letters*, vol. 24, no. 21, pp. 1301 –1302, Oct 1988.

[67] J. S. Weiner, D. A. B. Miller, D. S. Chemla, T. C. Damen, and C. A. Burrus, "Strong polarization-sensitive electroabsorption in gaas/algaas quantum well waveguides," *Applied Physics Letters*, vol. 47, pp. 1148–1150, Dec 1985.

[68] E. Zielinski, F. Keppler, S. Hausser, M. H. Pilkuhn, R. Sauer, and W. T. Tsang, "Optical gain and loss processes in GaInAs/InP MQW laser structures," *IEEE Journal of Quantum Electronics*, vol. 25, pp. 1407–1416, Jun 1989.

[69] R. O. Miles, M. A. Dupertuis, F. K. Reinhart, and P. M. Brosson, "Gain Measurements in InGaAs/InGaaAsP Multiquantum-Well Broad-Area Lasers," *IEE Proceedings J : Optoelectronics*, vol. 139, no. 1, pp. 33–38, 1992.

[70] B. W. Hakki and T. L. Paoli, "Gain spectra in GaAs double-heterostructure injection lasers," *Journal of Applied Physics*, vol. 46, pp. 1299–1306, Mar 1975.

[71] H. Wang and D. T. Cassidy, "Gain Measurements of Fabry Pérot Semiconductor Lasers Using a Nonlinear Least-Squares Fitting Method," *IEEE Journal of Quantum Electronics*, vol. 41, pp. 532–540, Apr 2005.

[72] D. Miller, J. Weiner, and D. Chemla, "Electric-field dependence of linear optical properties in quantum well structures: Waveguide electroabsorption and sum rules," *Quantum Electronics, IEEE Journal of*, vol. 22, no. 9, pp. 1816 – 1830, Sep 1986.

[73] P. Claxton, M. Hopkinson, J. Kovac, G. Hill, M. Pate, and J. David, "Quantum-confined Stark effect in InGaAs/InP multiple quantum wells grown by solid source molecular beam epitaxy," *Journal of Crystal Growth*, vol. 111, no. 1-4, pp. 1080 – 1083, 1991. [Online]. Available: http://www.sciencedirect.com/science/article/pii/002202489191137Y

[74] L. Novotny and C. Hafner, "Light propagation in a cylindrical waveguide with a complex, metallic, dielectric function," *Phys. Rev. E*, vol. 50, pp. 4094–4106, Nov 1994. [Online]. Available: http://link.aps.org/doi/10.1103/PhysRevE.50.4094

[75] K. Hall, G. Lenz, and E. Ippen, "Femtosecond time domain measurements of group velocity dispersion in diode lasers at 1.5 μm," *Lightwave Technology, Journal of*, vol. 10, no. 5, pp. 616 –619, May 1992.

[76] H. Burkhard, "Effective phase and group indices for $In_{1-x}Ga_xP_{1-y}As_y$/InP waveguide structures," vol. 55, no. 2, pp. 503–508, 1984. [Online]. Available: http://dx.doi.org/doi/10.1063/1.333054

[77] B. R. Bennett, R. A. Soref, and J. A. Del Alamo, "Carrier-induced change in refractive index of InP, GaAs and InGaAsP," *IEEE Journal of Quantum Electronics*, vol. 26, pp. 113–122, 1990.

[78] F. Stern, "Dispersion of the Index of Refraction Near the Absorption Edge of Semiconductors," *Physical Review'*, vol. 133, pp. 1653–1664, Mar 1964.

[79] B. Jensen and A. Torabi, "Temperature and intensity dependence of the refractive index of a compound semiconductor," *J. Opt. Soc. Am. B*, vol. 2, no. 9, pp. 1395–1401, Sep 1985. [Online]. Available: http://josab.osa.org/abstract.cfm?URI=josab-2-9-1395

[80] T. Numai, *Fundamentals of Semiconductor Lasers*. Springer-Verlag, 2004.

[81] H. Bissessur, R. Ettinger, F. Fernandez, and J. Davies, "The influence of temperature on the eigenmodes of a semiconductor laser," *Photonics Technology Letters, IEEE*, vol. 5, no. 7, pp. 764 –766, july 1993.

[82] G. Mezosi, "Semiconductor ring lasers for all-optical signal processing," *PhD Thesis, University of Glasgow*, Aug 2010.

[83] L. Hou, P. Stolarz, J. Javaloyes, R. Green, C. Ironside, M. Sorel, and A. Bryce, "Subpicosecond Pulse Generation at Quasi-40-GHz Using a Passively Mode-Locked AlGaInAs-InP 1.55-μm Strained Quantum-Well Laser," *IEEE Photonics Technol. Lett.*, vol. 21, no. 23, pp. 1731–1733, Dec 2009.

[84] "FR-103XL Rapid Scanning Auto/Crosscorrelator," product Information. [Online]. Available: http://www.femtochrome.com/Datasheets/FR-103XL%20Datasheet.pdf

[85] J. Leegwater, "Theory of mode-locked semiconductor lasers," *Quantum Electronics, IEEE Journal of*, vol. 32, no. 10, pp. 1782 –1790, Oct 1996.

[86] E. J. R. Kelleher, J. C. Travers, E. P. Ippen, Z. Sun, A. C. Ferrari, S. V. Popov, and J. R. Taylor, "Generation and direct measurement of giant chirp in a passively mode-locked laser," *Opt. Lett.*, vol. 34, no. 22, pp. 3526–3528, Nov 2009. [Online]. Available: http://ol.osa.org/abstract.cfm?URI=ol-34-22-3526

[87] H. A. Haus, J. G. Fujimoto, and E. P. Ippen, "Structures for additive pulse mode locking," *J. Opt. Soc. Am. B*, vol. 8, no. 10, pp. 2068–2076, Oct 1991. [Online]. Available: http://josab.osa.org/abstract.cfm?URI=josab-8-10-2068

[88] R. P. Green, M. Haji, L. Hou, G. Mezosi, R. Dylewicz, and A. E. Kelly, "Fast saturable absorption and 10 GHz wavelength conversion in Al-quaternary multiple quantum wells," *Opt. Express*, vol. 19, no. 10, pp. 9737–9743, May 2011. [Online]. Available: http://www.opticsexpress.org/abstract.cfm?URI=oe-19-10-9737

[89] D. Duchesne, L. Razzari, L. Halloran, R. Morandotti, A. J. S. Thorpe, D. N. Christodoulides, and D. J. Moss, "Two-photon photodetector in a multiquantum well GaAs laser structure at 1.55 μm," *Opt. Express*, vol. 17, no. 7, pp. 5298–5310, 2009. [Online]. Available: http://www.opticsexpress.org/abstract.cfm?URI=oe-17-7-5298

[90] D. Jones, L. Zhang, J. Carroll, and D. Marcenac, "Dynamics of monolithic passively mode-locked semiconductor lasers," *Quantum Electronics, IEEE Journal of*, vol. 31, no. 6, pp. 1051 –1058, Jun 1995.

[91] D. Derickson, R. Helkey, A. Mar, J. Karin, J. Wasserbauer, and J. Bowers, "Short pulse generation using multisegment mode-locked semiconductor lasers," *Quantum Electronics, IEEE Journal of*, vol. 28, no. 10, pp. 2186 –2202, Oct 1992.

[92] G. Agrawal and N. Olsson, "Self-phase modulation and spectral broadening of optical pulses in semiconductor laser amplifiers," *Quantum Electronics, IEEE Journal of*, vol. 25, no. 11, pp. 2297 –2306, Nov 1989.

[93] R. Poore, "Phase Noise and Jitter," 2001, application Note. [Online]. Available: http://www.home.agilent.com/upload/cmc_upload/All/phase_noise_and_jitter.pdf?&cc=GB&lc=eng

[94] R. B. Marcus, *Measurement of High-Speed Signals in Solid State Devices*. United Kingdom: Academic Press Limited, 1990.

[95] F. Kefelian, S. O'Donoghue, M. Todaro, J. McInerney, and G. Huyet, "RF Linewidth in Monolithic Passively Mode-Locked Semiconductor Laser RF Linewidth in Monolithic Passively Mode-Locked Semiconductor Laser," *Photonics Technology Letters, IEEE*, vol. 20, no. 16, pp. 1405 –1407, Aug 2008.

[96] A. Weiner, *Ultrafast optics*. Wiley, 2009.

[97] S. Arahira and Y. Ogawa, "Repetition-frequency tuning of monolithic passively mode-locked semiconductor lasers with integrated extended cavities," *Quantum Electronics, IEEE Journal of*, vol. 33, no. 2, pp. 255 –264, Feb 1997.

[98] M. Pantouvaki, C. Renaud, P. Cannard, M. Robertson, R. Gwilliam, and A. Seeds, "Fast tuneable ingaasp dbr laser using quantum-confined stark-effect-induced refractive index change," *Selected Topics in Quantum Electronics, IEEE Journal of*, vol. 13, no. 5, pp. 1112 –1121, sept.-oct. 2007.

[99] R. Maldonado-Basilio, S. Latkowski, F. Surre, and P. Landais, "Linewidth analysis of 40-GHz passively mode-locked multi-mode semiconductor lasers," *Optics Communications*, vol. 283, no. 2, pp. 299 – 303, 2010. [Online]. Available: http://www.sciencedirect.com/science/article/pii/S0030401809009614

[100] C. Mirasso, G. Van Tartwijk, E. Hernandez-Garcia, D. Lenstra, S. Lynch, P. Landais, P. Phelan, J. O'Gorman, M. San Miguel, and W. Elsasser, "Self-pulsating semiconductor lasers: theory and experiment," *Quantum Electronics, IEEE Journal of*, vol. 35, no. 5, pp. 764 –770, may 1999.

[101] J. M. Roth, T. E. Murphy, and C. Xu, "Ultrasensitive and high-dynamic-range two-photon absorption in a GaAs photomultiplier tube,"

Opt. Lett., vol. 27, no. 23, pp. 2076–2078, Dec 2002. [Online]. Available: http://ol.osa.org/abstract.cfm?URI=ol-27-23-2076

[102] L. Barry, B. Thomsen, J. Dudley, and J. Harvey, "Autocorrelation and ultrafast optical thresholding at 1.5 μm using a commercial InGaAsP 1.3 μm laser diode," *Electronics Letters*, vol. 34, no. 4, pp. 358 –360, Feb 1998.

[103] T. Krug, M. Lynch, A. L. Bradley, J. F. Donegan, L. P. Barry, H. Folliot, J. S. Roberts, and G. Hill, "High-Sensitivity Two-Photon Absorption Microcavity Autocorrelator," *IEEE Photonics Technology Letters*, vol. 16, pp. 1543–1545, Jun 2004.

[104] H. Tsang, L. Chan, J. Soole, H. LeBlanc, M. Koza, and R. Bhat, "High sensitivity autocorrelation using two-photon absorption in InGaAsP waveguides," *Electronics Letters*, vol. 31, no. 20, pp. 1773 –1775, Sep 1995.

[105] K. Kikuchi, "Highly sensitive interferometric autocorrelator using Si avalanche photodiode as two-photon absorber," *Electronics Letters*, vol. 34, no. 1, pp. 123 –125, Jan 1998.

[106] T. Krug, M. Lynch, A. Bradley, J. Donegan, L. Barry, H. Folliot, J. Roberts, and G. Hill, "High-sensitivity two-photon absorption microcavity autocorrelator," *Photonics Technology Letters, IEEE*, vol. 16, no. 6, pp. 1543 –1545, Jun 2004.

[107] C. Holtmann, P.-A. Besse, T. Brenner, and H. Melchior, "Polarization independent bulk active region semiconductor optical amplifiers for 1.3 μm wavelengths," *Photonics Technology Letters, IEEE*, vol. 8, no. 3, pp. 343 –345, Mar 1996.

[108] H. K. Tsang, R. V. Penty, I. H. White, R. S. Grant, W. Sibbett, J. B. D. Soole, H. P. Leblanc, N. C. Andreadakis, R. Bhat, and M. A. Koza, "Two-photon absorption and self-phase modulation in InGaAsP/InP multi-quantum-well waveguides," *Journal of Applied Physics*, vol. 70, pp. 3992–3994, Oct 1991.

[109] E. W. Van Stryland, S. Guha, H. Vanherzeele, M. Woodall, M. Soileau, and B. Wherrett, "Verification of the scaling rule for two-photon absorption in semiconductors," *Optica Acta: International Journal of Optics*, vol. 33, no. 4, pp. 381–386, 1986. [Online]. Available: http://www.tandfonline.com/doi/abs/10.1080/713821955

[110] E. W. V. Stryland, M. A. Woodall, H. Vanherzeele, and M. J. Soileau, "Energy band-gap dependence of two-photon absorption," *Opt. Lett.*, vol. 10, no. 10, pp. 490–492, Oct 1985. [Online]. Available: http://ol.osa.org/abstract.cfm?URI=ol-10-10-490

[111] R. E. Nahory, M. A. Pollack, W. D. Johnston, and R. L. Barns, "Band gap versus composition and demonstration of Vegard's law for $In_{1-x}Ga_xAs_yP1_{1-y}$ lattice matched to InP," vol. 33, no. 7, pp. 659–661, 1978. [Online]. Available: http://dx.doi.org/doi/10.1063/1.90455

[112] C. Henry, L. Johnson, R. Logan, and D. Clarke, "Determination of the refractive index of InGaAsP epitaxial layers by mode line luminescence spectroscopy," *Quantum Electronics, IEEE Journal of*, vol. 21, no. 12, pp. 1887 – 1892, Dec 1985.

[113] D. C. Hutchings and B. S. Wherrett, "Theory of anisotropy of two-photon absorption in zinc-blende semiconductors," *Phys. Rev. B*, vol. 49, pp. 2418–2426, Jan 1994. [Online]. Available: http://link.aps.org/doi/10.1103/PhysRevB.49.2418

[114] JWNC University of Glasgow, "Electron beam lithography/nanolithography." [Online]. Available: http://www.jwnc.gla.ac.uk/electronbeamlithography.html

[115] A. Grigorescu, M. van der Krogt, C. Hagen, and P. Kruit, "10 nm lines and spaces written in HSQ, using electron beam lithography," *Microelectronic Engineering*, vol. 84, no. 5-8, pp. 822 – 824, 2007. [Online]. Available: http://www.sciencedirect.com/science/article/pii/S0167931707000408

[116] I. Junarsa, M. P. Stoykovich, P. F. Nealey, Y. Ma, F. Cerrina, and H. H. Solak, "Hydrogen silsesquioxane as a high resolution negative-tone resist for extreme ultraviolet lithography," *Journal of Vacuum Science Technology B: Microelectronics and Nanometer Structures*, vol. 23, no. 1, pp. 138 –143, Jan 2005.

[117] R. Dylewicz, R. M. D. L. Rue, R. Wasielewski, P. Mazur, G. Mezosi, and A. C. Bryce, "Fabrication of submicron-sized features in InP/InGaAsP/AlGaInAs quantum well heterostructures by optimized inductively coupled plasma etching with Cl2/Ar/N2 chemistry," vol. 28, no. 4, pp. 882–890, 2010. [Online]. Available: http://dx.doi.org/doi/10.1116/1.3466811

[118] A. Katz, B. E. Weir, and W. C. Dautremont?Smith, "Au/Pt/Ti contacts to p-$In_{0.53}Ga_{0.47}As$ and n-InP layers formed by a single metallization common step and rapid thermal processing," vol. 68, no. 3, pp. 1123–1128, 1990. [Online]. Available: http://dx.doi.org/doi/10.1063/1.346706

[119] M. Islam and P. J. McNally, "A comparative study of Pd/Sn/Au, Au/Ge/Au/Ni/Au, Au-Ge/Ni and Ni/Au-Ge/Ni ohmic contacts to n-GaAs," *Microelectronic Engineering*, vol. 40, no. 1, pp. 35 – 42, 1998. [Online]. Available: http://www.sciencedirect.com/science/article/pii/S0167931797001846

[120] R. Walker, "Simple and accurate loss measurement technique for semiconductor optical waveguides," *Electronics Letters*, vol. 21, no. 13, pp. 581 –583, 1985.

[121] A. Beaurain, S. Dupont, H. W. Li, J. P. Vilcot, C. Legrand, J. Harari, M. Constant, and D. Decoster, "Characterization and fabrication of InGaAsP/InP deep-etched micro-waveguides," *Microwave and Optical Technology Letters*, vol. 40, no. 3, pp. 216–218, 2004. [Online]. Available: http://dx.doi.org/10.1002/mop.11333

[122] C. Dorrer and I. A. Walmsley, "Concepts for the temporal characterization of short optical pulses," *EURASIP J. Appl. Signal Process.*, vol. 2005, pp. 1541–1553, Jan 2005. [Online]. Available: http://dx.doi.org/10.1155/ASP.2005.1541

[123] V. Wong and I. A. Walmsley, "Ultrashort-pulse characterization from dynamic spectrograms by iterative phase retrieval," *J. Opt. Soc. Am. B*, vol. 14, no. 4, pp. 944–949, Apr 1997. [Online]. Available: http://josab.osa.org/abstract.cfm?URI=josab-14-4-944

[124] J. L. A. Chilla and O. E. Martinez, "Direct determination of the amplitude and the phase of femtosecond light pulses," *Opt. Lett.*, vol. 16, no. 1, pp. 39–41, Jan 1991. [Online]. Available: http://ol.osa.org/abstract.cfm?URI=ol-16-1-39

[125] V. Wong and I. A. Walmsley, "Ultrashort-pulse characterization from dynamic spectrograms by iterative phase retrieval," *J. Opt. Soc. Am. B*, vol. 14, no. 4, pp. 944–949, Apr 1997.

[126] I. G. Cormack, W. Sibbett, and D. T. Reid, "Rapid measurement of ultrashort-pulse amplitude and phase from a two-photon absorption sonogram trace," *J. Opt. Soc. Am. B*, vol. 18, no. 9, pp. 1377–1382, Sep 2001.

[127] I. G. Cormack, W. Sibbett, R. Ortega-Martinez, and D. T. Reid, "Ultrashort pulse characterization using a scanning Fabry – Perot etalon enabling rapid acquisition and retrieval of a sonogram at rates up to 1.52 Hz," *Review of Scientific Instruments*, vol. 72, no. 11, pp. 4071–4079, Nov 2001.

[128] T. Hori, N. Nishizawa, T. Goto, and M. Yoshida, "Wideband and nonmechanical sonogram measurement by use of an electronically controlled, wavelength-tunable, femtosecond soliton pulse," *J. Opt. Soc. Am. B*, vol. 20, no. 11, pp. 2410–2417, Nov 2003. [Online]. Available: http://josab.osa.org/abstract.cfm?URI=josab-20-11-2410

[129] J. Ward, C. N. Pannell, E. S. Wachmann, and W. Seale, "Applications of acousto-optic devices for spectral imaging systems." [Online]. Available: http://www.neostech.com/PDFs/aotf.pdf

[130] G. Genty, T. Niemi, and H. Ludvigsen, "New method to improve the accuracy of group delay measurements using the phase-shift technique,"

Optics Communications, vol. 204, no. 1-6, pp. 119–126, 2002. [Online]. Available: http://www.sciencedirect.com/science/article/B6TVF-458WXCS-1/2/57748c2b87623c50dcd712408a7bf893

[131] "Corning SMF-28 Optical Fiber," Apr 2002, product Information. [Online]. Available: http://ece466.groups.et.byu.net/notes/smf28.pdf

[132] G. Ghosh, "Sellmeier Coefficients and Chromatic Dispersions for Some Tellurite Glasses," *Journal of the American Ceramic Society*, vol. 78, no. 10, pp. 2828–2830, 1995. [Online]. Available: http://dx.doi.org/10.1111/j.1151-2916.1995.tb08060.x

[133] D. J. Kane, "Principal components generalized projections: a review [Invited]," *J. Opt. Soc. Am. B*, vol. 25, no. 6, pp. A120–A132, Jun 2008.

[134] D. J. Kane, G. Rodriguez, A. J. Taylor, and T. S. Clement, "Simultaneous measurement of two ultrashort laser pulses from a single spectrogram in a single shot," *J. Opt. Soc. Am. B*, vol. 14, no. 4, pp. 935–943, Apr 1997. [Online]. Available: http://josab.osa.org/abstract.cfm?URI=josab-14-4-935

[135] D. T. Reid, "Algorithm for complete and rapid retrieval of ultrashort pulse amplitude and phase from a sonogram," *Quantum Electronics, IEEE Journal of*, vol. 35, no. 11, pp. 1584–1589, Nov 1999.

[136] R. Salvatore and A. Yariv, "Demonstration of down-chirped and chirp-free pulses from high-repetition-rate passively mode-locked lasers," *Photonics Technology Letters, IEEE*, vol. 7, no. 10, pp. 1151 –1153, Oct 1995.

[137] M. Schell, M. Tsuchiya, and T. Kamiya, "Chirp and stability of mode-locked semiconductor lasers," *Quantum Electronics, IEEE Journal of*, vol. 32, no. 7, pp. 1180 –1190, Jul 1996.

[138] U. Bandelow, M. Radziunas, A. Vladimirov, B. Hüttl, and R. Kaiser, "40 GHz mode locked semiconductor lasers: Theory, simulation and experiments," in *Frontiers in Optics*. Optical Society of America, 2004, p. FMD1. [Online]. Available: http://www.opticsinfobase.org/abstract.cfm?URI=FiO-2004-FMD1

AML: active mode-locking
AO: acousto-optic
AOF: acousto-optic filter
ASE: amplified spontaneous emission
COMD: catastrophic optical mirror damage
CW: continuous-wave
DBR: distributed Bragg reflector
DFB: distributed feedback
DWDM: dense wavelength division multiplexing
EA: electro-absorption
EB: electron-beam
EBL: electron beam lithography
EDFA: erbium-doped fibre amplifier
EO: electro-optic
EPSRC: Engineering and Physical Sciences Research Council
ER: extinction ratio
FFP: far-field pattern
FMLL: fibre mode-locked laser
FP: Fabry-Pé rot
FRAC: fringe-resolved autocorrelation
FRL: far-field reduction layer
FROG: frequency-resolved optical gating
FT: Fourier Transform
FWHM: full-width half maximum
GC: graded composition
GD: group delay
GRENOUILLE: grating-eliminated no-nonsense observation of ultrafast incident laser light e-fields
GRIN: graded-index
GVD: group velocity dispersion
GVM: group velocity mismatch
HP: Hakki-Paoli
HSQ: hydrogen silsesquioxane
IAC: intensity autocorrelation
ICP: inductively-coupled plasma
IPA: isopropyl alcohol
LD:laser diode
MIBK: methyl isobutyl ketone
ML: mode-locking

MLL: mode-locked laser
MOCVD: metal-organic chemical vapour deposition
MOSAIC: modified-spectrum auto-interferometric correlation
MQW: multi-quantum-well
NFP: near-field pattern
OCDMA: optical-code division multiple access
OS: optical spectrum
OSA: optical spectrum analyser
OTDM: optical time-division multiplexing
PBS: polarising beam splitter
PCGPA: principal components generalised projections alghorithm
PCGPs: principal-components generalised projections
PEC: proximity error correction
PECVD: plasma enhanced chemical vapour deposition
PG: polarisation-grating
PICASO: phase and intensity from correlation and spectrum only
PL: photoluminescence
PML: passive mode-locking
PMLL: passive mode-locked laser
PMMA: poly(methylmethacrylate)
PMT: photomultiplier tube
PSK: phase-shift keying
QAM: quadrature-amplitude modulation
QCSE: quntum confined Stark effect
QW: quantum-well reconstruction
RF: radio-frequency
RFA: radio-frequency analyser
RFS: radio-frequency spectrum
RIE: reactive ion etching
rms: root-mean-square
RO: reverse osmosis
RTA: rapid thermal annealing
SA: saturable absorber
SCH: separate confinement heterostructure
SD: self-diffraction
SEM: scanning-electron microscope
SH: second harmonic
SHG: second-harmonic generation
SI: spectral interferometry

SMLL: semiconductor mode-locked laser

SP: self-pulsation

SPA: single-photon absorption

SPIDER: spectral phase interferometry for direct electric field

SPM: self-phase modulation

SRI: self-reference interferometry

SSB: single-sideband

SVD: singular value decomposition

TADPOLE: Temporal Analysis by Dispersive a Pair of Light E-fields

TBP: time-bandwidth product

TBPF: tunable band-pass filter

TE: transverse electric

TG: transient-grating

THG: third-harmonic generation

TM: transverse magnetic

TMAH: tetramethylammonium hydroxide

TNSF: time-non-stationary filter

TPA: two-photon absorption

TPRI: test-pulse-reference interferometry

TROG: time-resolved optical gating

TSF: time-stationary filter

Journal publications

P. M. Stolarz, G. Mezosi, M. J. Strain, A. C. Bryce, and M. Sorel, "Highly-Sensitive Sonogram for Assessment of Chirp in Semiconductor Mode-Locked Lasers," *Quantum Electronics, IEEE Journal of*, Accepter for publication on 7 April 2012 (Author's contribution: Fabrication and characterisation of the TPA detectors, development and testing of the sonogram set-up, dynamical and sonographic characterisation of the semiconductor mode-locked lasers; and manuscript preparation).

P. M. Stolarz, J. Javaloyes, G. Mezosi, L. Hou, C. N. Ironside, M. Sorel, A. C. Bryce, and S. Balle, "Spectral Dynamical Behavior in Passively Mode-Locked Semiconductor Lasers", *Photonics Journal*, IEEE , vol. 3, no. 6, pp. 1067-1082, Oct 2011 (Author's contribution: Characterisation of the presented laser material structure - gain and absorption measurements; experimental characterisation of the mode-locked lasers' dynamics; and manuscript preparation).

M. J. Strain, P. M. Stolarz, and M. Sorel, "Passively Mode-Locked Lasers With Integrated Chirped Bragg Grating Reflectors," *Quantum Electronics, IEEE Journal of*, vol. 47, no. 4, pp. 492-499, Apr 2011

L. Hou, R. Dylewicz, M. Haji, P. Stolarz, B. Qiu; and A. C. Bryce, "Monolithic 40-GHz Passively Mode-Locked AlGaInAs-InP 1.55–μm MQW Laser With Surface-Etched Distributed Bragg Reflector" *Photonics Technology Letters, IEEE* , vol. 22, no. 20, pp. 1503-1505, Oct 2010

L. Hou, P. Stolarz, R. Dylewicz, M. Haji, J. Javaloyes, B.Qiu, and A. C. Bryce, "160-GHz Passively Mode-Locked AlGaInAs 1.55–μm Strained Quantum-Well Compound Cavity Laser," *Photonics Technology Letters, IEEE* , vol. 22, no. 10, pp. 727-729, May 2010

L. Hou, P. Stolarz, J. Javaloyes, R. P. Green, C. N. Ironside, M. Sorel, and A. C. Bryce, "Subpicosecond Pulse Generation at Quasi-40-GHz Using a Passively Mode-Locked AlGaInAs-InP 1.55–μm Strained Quantum-Well Laser," *Photonics Technology Letters, IEEE* , vol. 21, no. 23, pp. 1731-1733, Dec 2009

Peer reviewed international conference publications:

M. J. Strain, P. Stolarz, and M. Sorel, "Intra-Cavity Dispersion Control in Passively Mode-Locked Semiconductor Lasers," *IEEE Photonics 2011 Conference*, awaiting publication

M. J. Strain, P. Stolarz, and M. Sorel, "Semiconductor mode-locked lasers with integrated dispersion control," *Lasers and Electro-Optics Europe (CLEO EUROPE/EQEC), 2011 Conference on and 12th European Quantum Electronics Conference*, May 2011

J. Javaloyes, P. Stolarz, L. Hou, M. Sorel, A. C. Bryce, and S. Balle, "Passive mode-locking in quantum well Fabry-Perot lasers," *Lasers and Electro-Optics Europe (CLEO EUROPE/EQEC), 2011 Conference on and 12th European Quantum Electronics Conference*, May 2011

L. Hou, J. Akbar, M. Haji, P. Stolarz, R. Dylewicz, A. E. Kelly, M. Sorel, J. H. Marsh, A. C. Bryce, and B. Qiu, "40 GHz AlGaInAs/InP 1.55 μm passively mode-locked laser with low divergence angle and timing jitter" *Lasers and Electro-Optics (CLEO), 2011 Conference on*, May 2011

A. C. Bryce, L. Hou, M. Haji, R. Dylewicz, and P. Stolarz, "High frequency mode-locking of diode lasers" *Optoelectronic and Microelectronic Materials and Devices (COMMAD), 2010 Conference on*, pp. 3-4, Dec 2010

P. Stolarz, M. J. Strain, L. Hou, A. C. Bryce, and M. Sorel, "Chirp characterization of semiconductor mode-locked laser pulses with a high-sensitivity TPA waveguide detector sonogram," *IEEE Photonics Society, 2010 23rd Annual Meeting of the* , pp. 114-115, Nov 2010

J. Javaloyes, P. Stolarz, L. Hou, M. Sorel, A. C. Bryce, and S. Balle, "Passive Mode-Locking in AlGaInAs 1.55–μm strained quantum well lasers: Modeling and experiment" *Optical Communication (ECOC), 2010 36th European Conference and Exhibition on* , pp. 1-3, Sep 2010

L. Hou, M. Haji, R. Dylewicz, P. Stolarz, A. E. Kelly, J. M. Arnold, J. H. Marsh, R. M. De La Rue, M. Sorel, A. C. Bryce, and B. Qiu, "Monolithic 40 GHz passively mode locked AlGaInAs/InP 1.55 μm MQW laser with surface-etched Bragg gratings" *Lasers and Electro-Optics (CLEO) and Quantum Electronics and Laser Science Conference (QELS), 2010 Conference on*, pp. 1-2, May 2010

A. C. Bryce, P. Stolarz, J. Javaloyes, L. Hou, M. Sorel, and S. Balle, "Passive mode-locking of AlGaInAs quantum well laser, modelling and experiment," *LEOS Annual Meeting Conference Proceedings, 2009. LEOS '09. IEEE*, pp. 515-516, Oct 2009

J. Javaloyes, L. Hou, P. Stolarz, R. P. Green, C. N. Ironside, M. Sorel, J. M. Arnold, A. C. Bryce, and S. Balle, "Wide range 40-GHz Passive Mode-Locking operation of an AlGaInAs 1.55-μm Strained Quantum Well laser," *Lasers and Electro-Optics 2009 and the European Quantum Electronics Conference. CLEO Europe - EQEC 2009. European Conference on*, pp. 1, Jun 2009

L. Hou, P. Stolarz, C. N. Ironside, M. Sorel, and A. C. Bryce, "High temperature and wide range 40-GHz passive mode-locking operation of an AlGaInAs 1.55-μm strained

quantum well laser," *IEEE Lasers and Electro-Optics Society, 2008. LEOS 2008. 21st Annual Meeting of the* , pp. 679-680, Nov 2008

Other publications:

P. M. Stolarz, M. J. Strain, and M. Sorel, "Sonogram characterization of semiconductor mode-locked lasers with chirped Bragg grating reflectors," *European Semiconductor Lasers Workshop (ESLW) 2010*, Pavia, Italy, Sep 2010

J. Javaloyes, P. M. Stolarz, L. Hou, M. Sorel, A. C. Bryce, and S. Balle, "Passive mode-locking in quantum-well lasers," *European Semiconductor Lasers Workshop (ESLW) 2010*, Pavia, Italy, Sep 2010

P. Stolarz, J. Javaloyes, L. Hou, M. Sorel, and A. C. Bryce, "40- and 160-GHz passive mode-locking of AlGaInAs strained quantum well lasers - modelling and characterisation," *Rank Prize Funds symposium on Ultrashort Pulse Sources*, Aug 2009

P. M. Stolarz, G. Mezosi, M. J. Strain, A. C. Bryce, and M. Sorel, "Highly-Sensitive Sonogram for Assessment of Chirp in Semiconductor Mode-Locked Lasers," *Quantum Electronics, IEEE Journal of*, awaiting revision (Author's contribution: Fabrication and characterisation of the TPA detectors, development and testing of the sonogram set-up, dynamical and sonographic characterisation of the semiconductor mode-locked lasers; and manuscript preparation).